Space Radiation Environment Impacts on High Power Amplifiers and Solar Cells On-board Geostationary Communications Satellites

by

Whitney Quinne Lohmeyer

Submitted to the Department of Aeronautics & Astronautics
in Partial Fulfillment of the Requirements for the Degree of

Doctor of Philosophy

at the

MASSACHUSETTS INSTITUTE OF TECHNOLOGY

June 2015

Signature of Author Signature redacted
.....
Department of Aeronautics and Astronautics
March 19, 2015

Certified by Signature redacted
.....
Kerri Cahoy
Assistant Professor of Aeronautics and Astronautics
Thesis Supervisor

Certified by Signature redacted
.....
Daniel Hastings
Professor of Aeronautics and Astronautics

Certified by Signature redacted
.....
Gregory Ginet
Senior Staff, MIT Lincoln Laboratory

Accepted by Signature redacted
.....
Paulo Lozano
Associate Professor of Aeronautics and Astronautics
Chair, Graduate Program Committee

Space Radiation Environment Impacts on High Power Amplifiers and Solar Cells On-board Geostationary Communications Satellites

by

Whitney Quinne Lohmeyer

Submitted to the Department of Aeronautics and Astronautics
On March 19, 2015 in Partial Fulfillment of the Requirements for the Degree of Doctor of Philosophy in Aeronautics and Astronautics

ABSTRACT

Communications satellite operators maintain archives of component telemetry to monitor system function. Operators generally do not typically use the telemetry data for scientific analysis of the space radiation environment effects on component anomalies or performance. We partnered with four geostationary (GEO) operators, acquired >1 million hours of telemetry, and combined these data with space weather observations to investigate relationships between space weather and hardware performance.

We focused on the effects of space weather on two component types: solar cells and high power amplifiers. For solar cells, by augmenting >20 years of GEO telemetry with separate GEO space weather measurements, we calculated both on-orbit degradation of Si and GaAs solar cells in an annual average sense, and also quantified the degradation of cells during severe solar proton events (SPEs) of 10 MeV protons > 10,000 pfu. A functional relationship between the amount of degradation and proton fluence is also considered. We used the calculated degradation to evaluate several combinations of space weather environment models with solar cell degradation models and found that predicted performance is within 1% of the observed degradation. These models had not previously been validated using multiple on-orbit GEO datasets. We did not find a model pairing that consistently outperformed the others over all of the datasets.

For high power amplifiers, through the use of statistical analysis,

simulations, and electron beam experiments we conducted a root-cause analysis of solid state power amplifier (SSPA) anomalies on-board eight GEO satellites. From the statistical analysis, we identified that the occurrence of anomalies was not random with respect to the space weather environment, but that there appeared to be a relationship to high-energy electron fluence for periods of time between 10 – 21 days before the anomalies. From the simulations and electron beam lab tests, we demonstrated that internal charging occurs in the amplifier chain, potentially identifying a cause for the observed anomalies.

We substantiated an approach toward understanding space weather effects on space components by obtaining and using long-duration archives of standard commercial telemetry for scientific analysis. The analysis of large telemetry data sets of similar components over long periods of time improves our ability to assess the role of different types of space weather events in causing anomalies and helps to validate models. The findings in this work that relate deep dielectric charging to component anomalies and solar proton events to solar cell degradation make use of only a small fraction of the potentially available commercial geostationary satellite telemetry. Expansion of this work would provide additional insights on the role of space weather to the science community and to the satellite design and operator community.

Thesis Supervisor: Kerri Cahoy
Title: Professor of Aeronautics and Astronautics

Acknowledgments
I would first like to acknowledge and thank my advisor and role-model, Kerri Cahoy. I aspire to one day be as successful as her. I would also like to thank my parents, Melody and Bill Lohmeyer, for always being there for me, giving me perspective, and bringing a smile to my face.

I would like to acknowledge my committee, Dan Hastings and Greg Ginet, and other inspiring professors with whom I have worked or had conversations during my time at MIT. I sincerely thank Inmarsat, Telenor and ARABSat, for their willingness to contribute the telemetry data used throughout the entirety of this work, and specifically Marcus Vilaca, Mark Dickinson, David Bath, the Satellite Operators. I would also like to thank Dr. Fred DeJarnette, Dan Baker, Scott Messenger, Paul Bauer, Marilyn Good, Beth Marois, and Hamza Baig.

Lastly, I would like to thank my friends and family. To name only a few of the many who have provided support over the years – Raichelle Aniceto, Natalya Brikner, Ashley Carlton, Todd Sheerin, Carolann Belk, Emily Brune, Emily Clements, Leonard Bouygues, Abhi Butchibabu, Mark Sanchez Net, Annie Marinan, as well as The Cheung's (Zoe-Beth, Lilly-Rose, Zachary, Rowena, and Andrew).

Thank you.

Outline

List of Figures

Figure 26 (a-h): The distribution of *Kp* Index for (a,b) every measurement, (c,d) two day average, (e,f) three day average, and (g,h) two-week average with *Kp* index at the time of the SSPA anomalies.

Figure 27: Local time for the twenty-six SSPA anomalies onboard (red circles) Fleet A and (black asterisk) Fleet B. The radial distance from the center of the plot is an offset for clarity and has no other significance

Figure 28(a-d): The distribution of the $\log_{10}$ of 1.8-3.5 MeV Electron fluxes in units of #/(cm2 s st keV) from 1996-2009 for (a) every measurement, (b) two day average, (c) three day average, and (d) two-week average with electron flux at the time of the SSPA anomalies on Fleet A (green squares) and Fleet B (cyan circles)

Figure 29(a,b): Twenty-one individual $\log_{10}$(1.8–3.5 MeV electron flux) 0–21 days before the SSPA anomalies, represented by the thin gray curves, and the daily average shown in the dashed black curve in Figure 29(a). Figure 29(b) shows the same average $\log_{10}$(1.8–3.5 MeV electron flux) 0–21 days before the SSPA anomalies, as shown in black in Figure 29(a), but with higher resolution

Figure 30(a-d): >2 MeV electron flux during SSPA anomaly for 2 weeks before and after four anomalies

Figure 31: Daily >2 MeV Electron Fluence and the time of SSPA Anomalies

Figure 32: Percentage of >2 MeV Electron Fluence Measurements from 1996 to 2012 over periods of 1, 3, 7, 10 14, and 21 day periods

Figure 33: Percentage of SSPA Anomalies that occur for a given total >2 MeV electron fluence over periods of 1, 3, 7, 10, 14 days and 21 day periods prior to the twenty-six SSPA anomalies

Figure 34: Ratio of the anomaly %'s from Figure 3 to the measurement %'s shown in Figure 2 for each >2 MeV electron fluence and each time period (1, 3, 7, 10, 14, and 21 days)

Figure 35: Percentage of 1000 random trials of twenty-six random days that occurred for a given >2 MeV electron fluence of 1 day, 3 days, 7 days, 10 days, 14 days and 21 days prior to the randomly selected twenty-six days

Figure 36: Voltage reached for thirty-five simulated scenarios of seven temperatures (0 to 50 degrees C) and five resistivity values (1E+18 to 1E+22 ohm-cm) for a single GEO orbit (1 day)

Figure 37: Test configuration for electron experiments for DC blocking capacitor and coaxial cable. Dashed lines are probes where data is read by the scope

Figure 38(a,b): High magnification of (a) pre-test and (b) post-test articles. No burn marks appear on the post-test article

List of Tables

Table 35: Accumulated Electric Field over periods of 1, 3, 7, 10, 14 and 21 days in a worst-case GEO orbit – The calculated average electric field exceeded the 1E+07 V/m breakdown threshold for the majority of the 3, 7, 10, 14, and 21 day simulations

Table 36: Accumulated Voltage over a period of 1, 3, 7, 10, 14, and 21 days – The voltage threshold of the DC Blocking capacitor (50 V) was exceeded for all of the simulations except for four of the 1 day accumulated voltage simulations

Table 37: RF Performance Summary of Pre and Post Charging Test

List of Acronyms

ACE	Advanced Composition Explorer
ADCS	Attitude Dynamics and Control Systems
AE	Auroral Electrojet
CCD	Charge coupled device
CIR	Corotating Interaction Region
CME	Coronal mass ejection
COMSAT	Communications satellite
COTS	Custom-off-the-shelf
CRAND	Cosmic ray albedo neutron decay
CRRESPRO	Combined release and radiation effects satellite proton model
CSDA	Continuous-slowing-down approximation
DDD	Displacement damage dose
DICTAT	Dielectric Internal Charging Threat Analysis Tool
Dst	Disturbance Storm Time Index
EDAC	Error detection and correction algorithm
ELDRS	Enhanced low dose rate sensitivity
ELF	Extremely Low Frequency
EMI	Electromagnetic interference
EOL	End of life
EPC	Electronic Power Conditioner
EPEAD	Energetic proton, electron and alpha detectors
ESA	European Space Agency
ESD	Electrostatic discharge
ESP	Energetic sensor for particles
ESP	Emission of solar protons
FLUMIC	Flux model for internal charging
GaAs	Gallium arsenide
GCR	Galactic cosmic rays
GEO	Geostationary orbit
GOES	Geostationary Operational Environment Satellite
GSE	Geocentric solar eclipse
GSFC	Goddard Space Flight Center
GSM	Geocentric solar magnetosphere
HEPAD	High-energy proton and alpha detector
IMF	Interplanetary Magnetic Field
IMP	International Monitoring Platform
JPL	Jet Propulsion Laboratory
LANL	Los Alamos National Labs
LATRM	Low altitude trapped radiation model
LEO	Low earth orbit
LET	Linear energy transfer

MAD	Median absolute deviation
MAGED	Magnetospheric electron detector
MAGPD	Magnetospheric proton detector
MARECS-A	Maritime European Communications Satellite A
MOSFET	Metal oxide semiconductor field effect transistor
MTQ	Magnetorquers
NOAA	National Oceanic and Atmospheric Administration
NSREC	Nuclear and Space Radiation Effect Conference
NRC	National Research Council
POLE	Particle ONERA-LANL electron
RAND	Research ANd Development
RF	Radio frequency
SAA	South Atlantic Anomaly
SEB	Single event burn out
SEE	Single event effects
SEGR	Single event gate rupture
SEL	Single event latchup
SEM	Space Environment Monitor
SET	Single event transient
SEU	Single event upsets
SIDC	Solar Influences Data Analysis Center
SPE	Solar Proton Event
SSB	Space Studies Board
SSC	Sudden storm commencement
SSPA	Solid state power amplifiers
TID	Total ionizing dose
TMR	Triple-module redundancy
TPM-1	Trapped proton model
TWTA	Traveling wave tube amplifiers
VLF	Very Low Frequency
V_{oc}	Open circuit voltage

List of Variables

AE Auroral Electrojet Index

a_i Least-Square Fits for GaAs degradation equation

AL Auroral Lower

AU Auroral Upper

$\vec{B}$ Magnetic Field

C The decrease in I_{sc} per decade in radiation fluence in the logarithmic region

dE_{ele} Electronic energy loss

Dst Disturbance Storm Time Index

dx Depth of distance

$\vec{E}$ Electric Field

E_0 Average Electric Field

$\vec{F}_B$ Magnetic Lorentz Force

$\vec{F}_E$ Electrostatic force

g the number of sunspot groups

I_{sc} Short Circuit Current

I_{sco} Initial Short Circuit Current

k the correction factor that allows for differences in observing equipment and conditions for determining sunpot number

Kp Kp index

LET Linear Energy Transfer

$L_{m,e}$ Mass LET due to ionization

m degree of polynomial

m_p Particle mass

n Number of days

P_{max} Maximum Power

q Particle charge

R	Sunspot number
s	the number of individual sunspots
TID	total ionizing dose
$\vec{v}$	Velocity vector of particles
$v_{\perp}$	Velocity component perpendicular to the magnetic field
V_{oc}	Open Circuit Voltage
Δt	Orbit duration
ρ	Density
ρ_p	Cyclotron or gyro radius
ϕ_x	The radiation fluence at which I_{sc} starts to change to a linear function of the logarithm of the fluence
ϕ	Fluence
ϕ	1 MeV Electron Fluence
τ	Charging time
Ω_p	Cyclotron frequency

Chapter 1. Introduction

1.1 Context

In 2008, the National Research Council (NRC) published the "Severe Space Weather Events – Understanding Societal and Economic Impacts Workshop Report" which documented findings from the National Academies Space Studies Board (SSB), which was charged to assess the nation's ability to manage the effect of space weather events and their societal and economic impacts [*NRC*, 2008]. The NRC report highlighted concerns about the impact of space weather on the satellite telecommunications industry.

At the time of the 2008 NRC workshop, there were more than 250 communications satellites in geostationary Earth orbit (GEO). GEO is a circular equatorial orbit at 35,786 km in altitude with an orbital period equal to a sidereal day (Earth's rotation period). Collectively, these GEO satellite assets were valued at more than $75B and delivered an annual revenue of $25B in 2008 This was a substantial increase from 1999, when there were 123 GEO satellites insured at $1.7B [*Baker,* 2000]. GEO communications satellite revenue is primarily generated by leasing satellite transponder services. The lease fees depend on the satellite and transponder type, and the geographic market served by the satellite. The estimated revenue of transponders in the early 2000's ranged from $4M/year for K-band and $500k/year for C-band European Markets [*Oldenwald and Green,* 2007]. Demand for high capacity communications services has continued to grow, and improving GEO communications satellite system performance has become a top design and maintenance priority. It is important to validate and improve modeling tools used in both spacecraft design and operation as well as important to try to identify possible failure mechanisms related to the space environment.

1.1.1 Importance of Geostationary (GEO) Communications Satellites (COMSATs)

Beyond the economic impact of commercial GEO communications satellites, satellites in general are critical infrastructure because of the services they provide. In addition to providing information to aid scientists' understanding of the space environment, GEO satellite observations are also used to actively monitor weather, geological

processes, agricultural development, and the evolution of natural and man-made hazards. Defense agencies depend on GEO satellite services for communication in remote locations, and reconnaissance and intelligence. Both commercial and government users rely on GEO communication satellites to provide backup communication in the event of a disaster that damages ground based communications systems, provide news, education, and entertainment to remote areas, and connect global businesses for information distribution and fast electronic monetary transactions [*Galvin et al.,* 2014]. There would be a significant impact to society if space weather interrupted these services or, worse, if space weather events damaged these assets permanently.

1.1.2 Importance of Understanding Space Weather

Space weather is defined as the dynamic, variable conditions in the space environment including those on the sun, in the interplanetary medium, and in the magnetosphere-ionosphere-thermosphere system [*Baker,* 1998]. While it is widely known that space weather impacts the performance of satellite systems and can lead to anomalous satellite behavior [e.g. *Baker*, 2000; *Fennell et al.*, 2001; *Iucci et al.,* 2006; *Allen,* 2010], there are still major gaps in our ability to understand the mechanisms by which specific components and satellite systems are affected by the plasma environment of space and space weather events [*Gubby and Evans,* 2002]. Understanding the causal relationship between space weather and component health is critical to improving the robustness of satellite hardware and strengthening the services that satellite operators provide to their customers.

The complexities of space weather have been studied for hundreds of years, dating back to before 2000 B.C. with documentation the aurora in both Chinese and Greek literature [*Kivelson and Russell,* 1995]. The dynamic space environment continues to be researched, and knowledge of new phenomena continues to be gained through the investment of agencies in space weather monitoring missions like Deep Space Climate Observatory (DSCOVR). DSCOVR, launched on February 11, 2015 will maintain the nation's real-time solar wind monitoring capabilities used in NOAA's space weather alerts and forecasting system [*Burt and Smith,* 2012].

1.1.2.1 Historical Effects of Space Weather

Space weather not only affects geostationary communication satellite hardware, but also impacts the productivity of the satellite engineers, satellite operators, and satellite customers. Space weather can cause electrical and computational upsets, hardware anomalies, and solar array degradation [*Koons et al.,* 2000; *Gubby and Evans,* 2002]. The potential consequences of severe space weather have become more critical given the development of complex and interconnected continental electrical power grids, GPS, and other satellite technology such as weather monitoring satellites and communications satellites [*Brekke et al.,* 2013].

As a result of space weather, satellite operators are occasionally forced to manage satellites with reduced capabilities or fully decommission satellites, amounting to social and economic losses of several tens of millions of dollars per year [*Baker,* 1998; *Wilkinson et al.,* 2000; *Barbieri and Mahmot,* 2004]. For instance, *Oldenwald and Green* [2007] concluded that a large 1859-caliber storm, like the one that caused the Hydro Quebec power system in Canada to shut down for more than eight hours in 1989 [*Baker,* 2002], could result in a $30B revenue loss. This analysis was based on a model of transponder capacity and leasing with simplified assumptions on replacement rates, hardware and launch costs, and revenue generation.

In another example, a major solar wind event in 1994 coincided with a satellite anomaly for Canadian Telesat. It was later determined that their ANIK E2 satellite went off-air due to an energetic electron induced discharge to the momentum wheel control circuitry [*Shea and Smart,* 1998]. As a result, more than 100,000 dish owners and 1,600 remote communities were affected. Fortunately, the $290M satellite was restored after an intensive six month, $70M recovery effort [*Gubby and Evans,* 2002]. Other examples of satellites that have suffered anomalies due to the space environment include ANIK E1, Galaxy IV, and Galaxy 15 [*Baker,* 1998; *Balcewicz et al.,* 1998; *Allen,* 2010]

Due to the demands for increased capability, satellite components are progressively evolving, and the effects of space weather on state of the art components are often unknown until after they have flown.

Advances in technology, particularly smaller electrical component feature sizes, have increased complexity and reduced the overall size of the systems. These advances may have also inadvertently increased susceptibility to the effects of space weather, since effects vary with depth of penetration through materials [*Wilkinson et al.*, 1991, 2000; *Baker*, 2000; *Gubby and Evans*, 2002].

1.2 Identifying the Research Problem and Opportunity

Satellite engineers work to ensure that redundancy and adequate shielding measures for protecting their spacecraft from the spacecraft's mission environment are incorporated into their designs. Knowing mission susceptibility, and designing contingency plans that define preventative measures for mitigating risks associated with those susceptibilities should also be required prior to the commencement of operations [*Barbieri and Mahmot,* 2004]. Space weather effects are a primary cause of mission susceptibilities, and are thus accounted for, integrated in the design phase and often tracked with NOAA's Space Weather Now warning system during operations to monitor the difference between the initial predictions and the on-orbit observations.

The challenge for creating more efficient yet robust spacecraft designs lies in understanding how to quantify the physical nature and effects of space weather on satellite components, and how to improve confidence in determining whether the space environment positively correlates with anomaly occurrences [*Baker,* 2000; *NRC,* 2008]. At LEO, it is becoming more common to follow a Custom-off-the-shelf (COTS) design approach that results in less expensive satellites, but with a higher risk than if radiation tolerant or radiation hardened parts were used. At GEO, the low-energy electron radiation environment is orders of magnitude more intense than that at LEO and so the luxury of the COTS approach is not possible. The impacts of radiation at GEO must be taken seriously, as it is cost-intensive to reach and maintain geostationary orbit.

The implementation of redundancy, shielding and the quantification of risks related to a GEO mission's susceptibilities should be conducted in a more efficient manner through the use of additional analyses

incorporating on-board telemetry from operational GEO satellites. **This concept is directly in line with the root-cause anomaly investigation presented in this thesis, which simultaneously assesses satellite telemetry and space weather data, physics based models, and high-energy electron-beam experiments.** More root-cause anomaly investigations like the one presented in this thesis, enabled by the access to proprietary satellite telemetry and the availability of environment data at the location of the satellite, will also lead to satellite designs that are less susceptible to failure, that have higher capacity, and that are reduced in mass.

1.2.1 Access to Space Weather Data and Satellite Telemetry

One of the primary conclusions from the 2008 NRC Report [*NRC*, 2008] was that ***access to space weather data as well as satellite telemetry is the first step in better understanding to what extent space weather is related to the cause of satellite anomalies.***

The quantification of space weather effects requires analysis of both space weather and satellite anomaly data [*Baker*, 2002; *Tretkoff*, 2010]. Unfortunately, it is often challenging, if not impossible, to gain access to both space weather data and satellite telemetry from the affected spacecraft and components at the same time. Access to space weather data is publically available, but generally limited in utility because the closest space weather monitoring satellite may be located more than 100 degrees in longitude from the affected satellite. Access to satellite telemetry is rarely made public due to concerns about competitive advantage and export control [*Oldenwald and Green*, 2007].

Some satellites incorporate on-board dosimeters or environmental monitoring sensor suites to better understand the impacts of the environment on their components. It would be strategic and ideal if everyone incorporated dosimeters into their satellite designs, but this would not solve the problem of high-fidelity data availability since dosimeters would only provide a measure of accumulated dose. Dosimeters would not provide a means to discriminate against the individual particle populations and energies of the particle populations.

Without a means for better measuring the environment in the vicinity of the satellite, root-cause analyses of space weather related anomalies of satellite component is challenging. In 2014, the RAND Corporation published a report titled, "Satellite Anomalies: Benefits of a Centralized Anomaly Database and Methods for Securely Sharing Information among Satellite Operators" [*Galvan et al.,* 2014]. The report was written in light of satellite anomaly investigations conducted over several decades, including early publications of the work upon which this thesis is based. The report defines satellite anomalies as any mission degrading event affecting on-orbit operational spacecraft. The root cause of anomalies may include poor quality design or manufacturing of satellite hardware and software, repeated use and age, poor workmanship, impacts with micrometeoroids or space debris, operator error, or radiation from extreme space environment [*Galvan et al.,* 2014]. The RAND report validated that the goals of this research were topics of importance for the nation, and posed research questions consistent with the work in this thesis:

- What are satellite anomalies and how do they affect the functionality of spacecraft?
- What phenomena cause satellite anomalies?
- How can cataloging these anomalies in a centralized database aid satellite designers and operators?

1.2.2 Commercial Satellite Telemetry

Telemetry comes from the Greek words tele (remote) and metron (measure), meaning to measure from a distance. Telemetry data are acquired and monitored by ground operators, and anomaly alarms are sounded should the component health stray outside pre-defined nominal operational thresholds. The proprietary spacecraft health data are largely used in real time to help mitigate the effect of anomalies on the overall system performance and minimize impact to customers. The cause of an anomaly is generally not immediately obvious. Once the "fire" has been put out, operators may use the telemetry data for fault investigations, ground-based anomaly re-creation and modeling, and summaries of lessons learned. After a period of approximately a week, the telemetry is generally stored in archives.

Prior to this dissertation, decades of spacecraft anomaly data sat unused in the electronic telemetry archives of major geostationary communications satellite manufacturers and operators. The extensive databases of on-orbit anomalies from commercial spacecraft operators are generally not used for scientific investigations. This is partly because scientific analyses of these anomaly data, beyond the engineering analyses for prompt detection and mitigation strategies, are not in the immediate interest of these businesses.

Commercial communications operators often continue nominal operation during periods of increased solar activity due to the challenge in predicting the effect of space weather events on communications satellites. These companies use real-time space weather predictions and observations for fleet operations (such as the impact of solar particle events on solar array degradation). Satellite operators are interested in translating the complicated metrics used to quantify space weather activity into meaningful and detailed potential impacts on their systems.

1.3 Problem Statements and Objectives

Detailed analyses of cumulative or single-event space weather impacts on components on-orbit are rare, due to the complexity of understanding the dynamic space environment and due to the difficulties in acquiring space weather data near affected spacecraft and components.

Substantial work remains to achieve an in-depth understanding of the specific types of space weather events that impact component health, and the necessary methods for mitigating component failures [*Violet and Frederickson*, 1993]. Understanding the causal relationship between space weather and component health is critical in improving the robustness of satellite hardware and improving the services that satellite operators provide to their customers. When analyzing the effects of space weather on satellite systems, it is of utmost importance to understand the satellite systems and components under investigation.

The barrier of acquiring proprietary data from commercial satellite operators has limited the scale and depth of studies that seek to understand the environmental mechanisms that cause satellite anomalies. For this study, we have established innovative and strategic partnerships with three geostationary communications satellite operators, Inmarsat, Telenor, and ARABSat, headquartered in the United Kingdom, Norway and Saudi Arabia, respectively. A similar partnership with Intelsat was recently established, but the ongoing analysis of the Intelsat data is not included in this work. The specific types of satellite component anomaly data are analyzed to more accurately quantify the effect of space weather on geostationary communications satellites. More than 665,112 operational hours of on-orbit component telemetry and anomaly data were acquired and analyzed from Inmarsat (our first partner for this effort), along with 344,496 operational hours from Telenor, and 271,560 operational hours from ARABSat. Table 1 summarizes the acquired telemetry used in this work including data for solid state power amplifiers (SSPAs) and traveling wave tube amplifiers (TWTAs).

Table 1. Acquired Telemetry

	Inmarsat	Telenor	ARABSat
Headquarters	United Kingdom	Norway	Saudi Arabia
Number of Satellites	10	4	3
Number of Bus Types	3	3	2
Data Time Range	1991 – 2012	1997 - 2012	1996 - 2011
Years of Data	22	16	17
Telemetry Obtained	SSPA current and temperature; solar panel current, total bus power; anomaly and SEU list	TWTA current and temperature; solar panel current and total bus power; anomaly and SEU list	Solar panel current and total bus power

The focus of this work is on understanding the impacts of the space environment on solar arrays and high power amplifiers on-board geostationary satellite components. Solar arrays and high power amplifiers are responsible for providing the primary power supply, or

heart-beat of satellites in general, and the means to send data (news, media and emergency-response data) for communications satellites, respectively.

The specific research questions that will be addressed in this work are:

1. Can geostationary communications satellite telemetry be used to improve our understanding of the impact of solar particle events on solar cell degradation during solar proton events (SPEs)?
2. Can geostationary communications satellite telemetry be used to validate current methods for modeling the expected solar cell degradation for a given mission?
3. Can we use long duration telemetry data archives for multiple spacecraft to better understand the effects of space weather on key components?

O'Brien et al. [2013] discuss the difference in priorities between space scientists and satellite operators. Among other observations, *O'Brien et al.* [2013] state that the scientific community places higher priority on space weather forecasting and understanding the underlying physics while placing a significantly lower priority on understanding how the phenomena and particle populations of interest affect the satellite operators. The proposed research questions will directly address this priority mismatch, and focus on investigating the space environment and understanding its effects on satellite systems with a goal of improving the design of components and satellite operations. These results will also inform how satellite engineers can build in protective mechanisms and structures for improving satellite lifetimes and performance.

1.4 Thesis Overview

The content of this thesis is summarized in this section. Chapter 2 provides an overview of the space environment and plasma physics that govern particle interactions in space. The chapter begins by discussing the Sun as the origin of what is commonly thought of as "space weather". We consider how a particle that has been emitted in a coronal mass ejection (CME), speeds towards the Earth via the solar wind, interacts

with the bow shock, magnetopause and ultimately enters the Earth's magnetosphere through magnetotail injections. Next, a description of the trapped particle populations present in low earth orbit (LEO) and geostationary orbit (GEO) is given, along with the space weather hazards of these orbits including total ionizing dose (TID), surface and internal charging, single event effects (SEEs). We also outline how to model and estimate the potential risk a spacecraft may face during the mission lifetime.

Chapter 3 provides an assessment of the GEO space weather environment in terms of both environmental metrics (such as *Kp* and *Dst* indices, both used to measure geomagnetic activity) and in situ measurements (such as >2 MeV electrons and >10 MeV protons). Operators subscribe to environment warning systems, which include some of these metrics for advance or real-time warnings, but have expressed concern that the difficulty in interpreting and understanding the meaning of the metrics and in situ measurements limits their usefulness. Operators also do not typically have a clear understanding of the potential effects the different metrics could have on their space assets. The baseline provided in this work can be used as a reference for operators to help facilitate operational decisions in the event of warnings.

Chapter 4 describes space-based photovoltaic power systems. An explanation of the primary solar cell performance parameters used in this work is provided along with a description of the physics behind the mechanisms of solar cell radiation damage. This chapter next provides a description of environmental models used to calculate solar cell degradation, which is required to design satellites to supply power throughout end-of-life. Finally, the chapter concludes with a description of the solar array telemetry and radiation environment data acquired for the analysis presented in Chapter 5.

The first half of Chapter 5 quantifies the annual degradation experienced onboard eleven geostationary satellites equipped with either Si or GaAs cells, and determines whether solar cell degradation increases during solar proton events (SPEs). An investigation of the relationship between the magnitude of particle flux during SPEs and solar cell degradation is conducted. The second half of Chapter 5

analyzes nine combinations of geostationary environment models that are required as input for predicting solar cell degradation to determine which combination of models most accurately predicts the on-board solar cell degradation of the eleven aforementioned satellites.

Chapter 6 provides background information on GEO communications satellite power amplifiers: solid state power amplifiers (SSPAs) and traveling wave tube amplifiers (TWTA). This chapter describes the current and future planned capabilities for SSPAs and TWTAs, provides detail on the underlying technology and physics behind these two types of amplifiers, and discusses the advantages and disadvantages of both technology types. The data acquisition and management of the GEO commercial satellite amplifier telemetry is also described in this chapter.

Chapter 7 compares sixteen years, or 665,112 operational hours, of housekeeping telemetry from two generations of Inmarsat satellites (Fleet A and Fleet B) with space environment observations at the time of the anomalies to better understand the relationship between the environment and satellite performance. Environment data was acquired from OMNI2 database, Geostationary Operational Environmental Satellites (GOES), the Advanced Composition Explorer (ACE) Satellite, Los Alamos National Laboratory (LANL) GEO observations, the sunspot number and the *Kp* index. Most satellite anomaly studies analyze recorded spacecraft anomalies, determine the time of the anomaly, and then compare the space environment for a period during and prior to the anomaly to determine if a relationship exists [*Violet and Frederickson,* 1993]. This dissertation follows in a similar manner for the analysis, and is expanded in Chapter 7 to help the commercial satellite communications industry and space weather science communities understand the sensitivity of key components to the changes of the space environment [*O'Brien et al.,* 2013].

In Chapter 7 we also describe how anomalies occur at a rate higher than just by chance when the >2 MeV electron fluence accumulated over fourteen and twenty-one days is elevated. To try to understand why, the amplifier subsystem is modeled to assess whether the dielectric material in the RF coax cables, which are the most exposed part of the system, is liable to experience electrical breakdown due to internal charging.

Analysis shows that the accumulated electric field over the fourteen and twenty-one days leading up to the anomalies is high enough to cause the dielectric material in the coax to breakdown. Further, the accumulated voltages reached are high enough to compromise components in the amplifier system, for example, the DC blocking capacitor. An electron beam test using a representative coaxial cable terminated in a blocking capacitor showed discharges could occur with peak voltages and energies sufficient to damage active RF semiconductor devices. This chapter ultimately describes methodology for progressing from space weather and telemetry-based anomaly investigations, through targeted modeling and experimental testing efforts, to reach plausible root-cause explanations.

1.5 High Level Review of Contributions

The contributions of this thesis begin with the acquisition of more than a million operational hours of telemetry from geostationary communications satellites. As previously mentioned, this data is generally kept behind locked doors and rarely released for outside scientific and engineering analysis. Space weather data was also collected. Both data required considerable management and conditioning before any investigations could begin.

With the acquired telemetry and space weather data, the variability of five space weather observations (*Kp, Dst, AE,* 10 MeV Protons, and $\log_{10}$(1.8-3.5 MeV electrons) throughout Solar Cycles 20 – 23 is first quantified. We then quantify the likelihood of increased activity for the use of satellite operators, engineers and the space weather community to better understand the dynamic nature of the space environment.

We next quantify the annual solar cell degradation experienced on-board eleven GEO COMSATs with either Si or GaAs solar cells. We find that increased degradation occurs in years of extreme solar particle events (SPEs), and as a result we can determine if a functional relationship exists between the degradation experienced over the SPEs. This analysis is similarly useful for both the scientific and satellite operator community.

After we quantified the solar cell degradation over the SPEs, we determined the deviation in the solar cell degradation experienced on-board the eleven GEO COMSATs and the predicted solar cell deviation using nine different combinations of commonly used environment models. Improving the models used for solar cell degradation prediction are of utmost importance to the community. Interestingly, all nine model combinations came within 1% of the observed on-orbit degradation for both GaAs and Si cells.

Lastly a root-cause anomaly investigation of twenty-six SSPAs onboard eight of Inmarsat's geostationary communications satellites is conducted. We begin by investigating several plausible space weather hazards (surface charging, internal charging, and the timing of the anomaly with respect to eclipse periods) and statistically rule out causes that appear to show no sign of relationship with the occurrence of the anomalies. We ultimately find a relationship between high-energy electrons over a period of seven to fourteen days prior to the anomalies, which motivates the further pursuit of investigations of internal charging as a possible cause of the anomalies.

We continue the root-cause anomaly investigation by (1) performing additional statistics on high-energy electron fluence measurements, (2) modeling a variety of internal charging simulations of the coaxial cable leading to the SSPA, which could have experienced internal charging that caused an arc to damage components further down the RF front end chain, and (3) conducting high-energy electron beam radiation tests on an RF circuit with a coaxial cable and DC blocking capacitor similar to the components in front of the SSPA on the Inmarsat payload.

In summary, this work improves the state of the art of GEO satellite design and operation through the following contributions:

- The formation of a strategic academic-satellite operator partnership that led to the acquisition of >1 million operational hours of satellite telemetry.
- The quantification of annual solar cell degradation on-board eleven GEO COMSATs that will aid future design and on-orbit power management.
- The validation of solar cell degradation models to within <0.5% of the observed on-orbit degradation at GEO.

- The characterization of the functional relationship between solar cell degradation and extreme Solar Proton Events for both GaAs and Si cells.
- The substantiation of a plausible relationship between amplifier anomalies and internal charging through statistics of high-energy electron fluence measurements, internal charging simulations, and high-energy electron beam radiation experiments.
- Suggested modification of NASA Internal Charging Guidelines

Chapter 2. The Space Environment: Observations and Models

The purpose of this chapter is to first provide an introduction to the space environment – starting with the Sun and transitioning like a particle that is racing towards Earth and that enters the Earth's magnetosphere. The Inner and Outer Van Allen Belts are also described along with low earth orbit (LEO) and geostationary orbit (GEO). The impacts of radiation on satellite components in LEO and GEO are then discussed with a focus on total ionizing dose (TID), spacecraft charging and single event upsets. Modeling tools used to predict the impact of the space environment during a spacecraft mission are then explained. This is followed by a description of space environment observations such as the Disturbance Storm Time Index (*Dst*) and the *Kp* Index. The last section of this chapter describes the approach used to acquire and manage the space environment data used for this research.

2.1 Solar Activity

With the exception of galactic cosmic rays (GCRs), space weather originates from the Sun, a G-type main sequence star with a core temperature of approximately 15.7 million Kelvin [*Kivelson and Russell*, 1995; *Baker*, 2002]. At such high temperatures, the sun is physically in the plasma phase – the phase in which energetic outer-shell electrons are capable of escaping their atomic nucleus causing the formation of ionized gas.

The sun emits plasma in two primary forms:

1. Variable low energy plasma known as solar wind, and massive explosions of high energy plasma in the form of solar flares, and
2. Coronal mass ejections (CMEs), and corotating interaction regions (CIRs) [*Hastings and Garrett*, 1996].

Solar wind was first measured in 1951 with instrumentation developed by Konstantin I. Gringauz for the Soviet *Luna* probes [*Kivelson and Russell*, 1995]. Solar wind varies in density, temperature, and pressure. Solar wind density and speed are two of the key factors that affect the response of the magnetosphere to geomagnetic disturbances. Solar wind speeds are approximately 500 km/s on average, with density of a few particles per cm^{-3} [*Hastings and Garrett*, 1996]. As the high-speed solar wind approaches Earth, it leads to intense magnetic field strength and

causes the injection of solar plasma. Combined, these effects form geomagnetic storms that are capable of causing hazardous anomalies (noise or even loss in telemetry, degradation to solar cells, and electrical upsets) and can also drastically diminish the quality of science data [e.g. *Baker,* 2002; *Cole,* 2003; *Barbieri and Mahmot*, 2004].

Solar flares and CMEs result from large explosions of the sun's electromagnetic material and charged particles (primarily protons and electrons), which cause strong interplanetary shock waves that also lead to major geomagnetic storms [*Baker*, 1998]. CMEs and solar flares are often thought to occur simultaneously, but have been observed to occur independently. CIRs form in response to fast solar wind interacting with slower solar wind, and generally reoccur every 27-days [e.g. *Tsurutani et al.,* 1995; *Denton et al.,* 2006].

CMEs and CIRs are the primary source of geomagnetic storms, which are intense disturbances in the Earth's magnetosphere that are initially driven by changes in the solar wind [*Kamide et al.,* 1998]. This phenomena was interestingly coined "geomagnetic storm" in the mid-1800s [*Chapman and Bartels,* 1940].

Although they have some similarities in origin, CMEs and CIRs uniquely alter the space environment. CIRs cause fluctuations in solar wind (particularly the Bz component of interplanetary magnetic field (IMF)) and are more effective at causing strong increases in high-energy electrons in the outer radiation belt [*Li et al.,* 2005; Denton et al., 2006; *Miyoshi et al.*, 2008]. The relativistic electrons of the CIRs are known to produce higher levels of deep dielectric charging than CMEs [*Denton et al.,* 2006]. Deep dielectric charging, also known as bulk or internal charging, is of particular importance to this research and will be covered in Section 2.3.2.2.

2.1.1 The Solar Cycle

The sunspot number is the longest available quantitative record of solar activity, and serves as the primary metric for monitoring the overall strength/variability of solar activity and for defining the solar cycle [*Clette et al.*, 2007]. The sunspot number, R, is determined from eye- and camera-based observations of relatively cooler and darker regions

of enhanced magnetic field strength on the sun, termed sunspots [*Vaquero,* 2007]. The Wolf or Zurich sunspot number is calculated as

$$R = k(10g + s) \tag{1}$$

Where g is the number of sunspot groups, s is the number of individual sunspots, and k is a correction factor that allows for differences in observing equipment and conditions [*Hastings and Garrett,* 1996].

The increase and decrease in the sunspot number defines the maximum and minimum of the solar activity cycle, a period of approximately eleven years that was first discovered by Schwabe in 1843 [*Schwabe and Schwabe,* 1844]. At solar maximum, solar activity causes temperatures in the upper atmosphere to increase, and in turn causes the upper atmosphere to expand [*Hastings and Garrett,* 1996]. At solar maximum there is also an increased chance of solar flares and CMEs, yet even at solar minimum, the Sun can produce damaging storms [*Baker,* 1998; *Denton et al.,* 2006].

The actual cause of the eleven year solar cycle is suspected to be related to the polarity of the sun's magnetic field, which reverses every eleven years and returns to its original magnetic configuration every twenty-two years [*Goldman,* 2005]. Figure 1 depicts the monthly smoothed and non-smoothed International Sunspot Number, monitored at the Royal Observatory of Belgium's Solar Influences Data Analysis Center [*SIDC,* 2003].

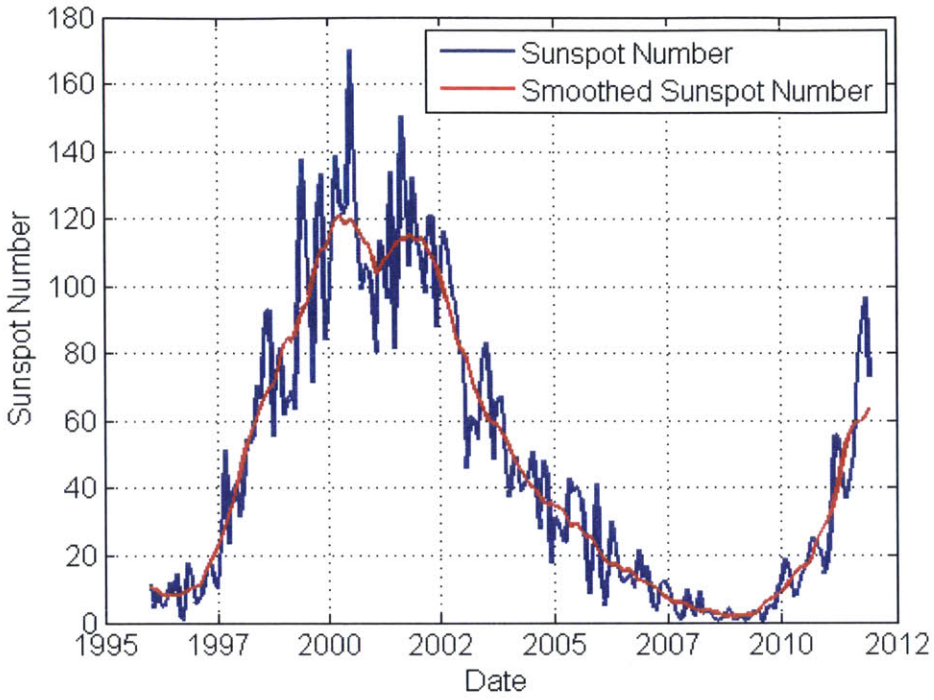

Figure 1. The 11-year Solar Cycle

2.2 The Earth's Magnetosphere

The Earth's magnetosphere shields the Earth's surface and the majority of Earth orbiting spacecraft from hazardous charged particles originating from flares, CMEs and CIRs. Energetic solar particles are capable of entering the magnetosphere at the cusp, near the north and south magnetic poles, forming a constant stream of incoming particles at high latitudes that collide with the atmosphere and form the aurora.

The mechanism formally known as cosmic ray albedo neutron decay (CRAND) explains how neutrons produced in the earth's atmosphere by cosmic ray bombardment, escape and decay into protons and electrons trapped in the Inner Van Allen Radiation Belt [Singer, 1958, Armstrong, 1973, *Heynderickx,* 2002]. The evolution of the Outer Van Allen Radiation Belt is a subject of research, but is believed to originate from the acceleration of low-energy electrons through radial diffusion and wave-particle interactions. Radial diffusion is the process of accelerating low-energy electrons at high altitudes via inward radial transport, and is generally deemed the main acceleration mechanism [*Schulz and*

Lanzerotti, 1974]. Lower-energy electrons can also be energized by wave-particle interactions with various very-low frequency (VLF) and extremely-low frequency (ELF) waves such as whistler-mode chorus waves [*Baker and Daglis,* 2007; *Su et al.,* 2011].

The Inner and Outer Van Allen Radiation Belts are separated from the by a region of fewer electrons, known as the "slot region" [*Daly et al.,* 1996; *Heynderickx,* 2002]. The slot region is formed due to enhanced wave-particle interactions that cause pitch-angle scattering as well as an incoherent and structureless whistler-mode emission known as hiss waves [*Lyons and Thorne,* 1973; *Abel and Thorne,* 1998; *Thorne,* 2010; *Meredith et al.,* 2006].

As previously mentioned, solar flares, CMEs and CIRs drive high-speed solar winds that contain the solar and interplanetary magnetic field (IMF) structure. The sun and solar wind jointly contribute to form the interplanetary magnetic field (IMF), which is the dominant field outside of the Earth's approximately dipolar magnetic field [*Galvin et al.,* 2014].

When the z-component of the IMF is southward, the IMF field lines connect with the Earth's magnetic field lines, and grant entrance to the Earth's magnetosphere. In this process, energetically charged particles travel along the magnetospheric field lines and transfer energy from the solar wind, through reconnection in the magnetotail, ultimately to the radiation belts of the Earth's magnetosphere [*Cole,* 2003]. Energetic solar protons can reach near-terrestrial altitudes within tens of minutes and peak within hours [*Baker,* 1998]. Figure 2 highlights the different regions of the magnetosphere including the bow shock, magnetopause, and radiation belts. These portions of the Earth's magnetosphere will be discussed in detail in this section.

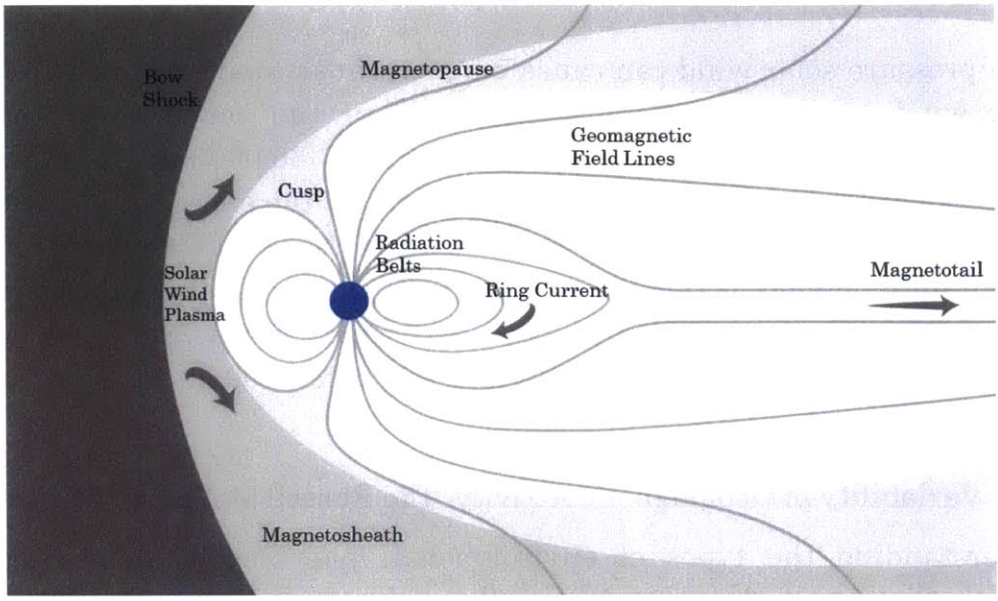

Figure 2. The Earth's magnetosphere including the solar wind (pictured to the left), bow shock, magnetosheath and magnetopause

In the early 1960s it was clear from spacecraft measurements that solar wind experiences a sudden transition, or a shock, before reaching the magnetopause. This shock, more formally known as bow shock, occurs as the solar wind encounters the earth, and reacts to the Earth's electric and magnetic fields, which alter the motion of the particles, and cause the solar wind to be slowed, heated and deflected around the Earth [*Kivelson and Russell,* 1995]. Close to the earth the plasma is cold and dense, but decreases in density with increasing altitude until the magnetosphere is exited and the plasma transitions into solar-wind plasma [*Hastings and Garrett,* 1996].

In 1961, the battery powered *Explorer 10* was the first spacecraft to measure the magnetopause, the boundary between the solar wind and the earth's magnetic field [*Kivelson and Russell,* 1995]. The complex interaction of the high speed solar wind plasma along with the strong southward IMF and movement of the charged particles along the field lines compresses the magnetosphere on the sunward "day" side, and stretches the magnetosphere behind the earth on the "night" side, forming the magnetotail. The dayside of the magnetopause generally lies at 10 Earth radii (R_E), approximately 63,700 km, whereas the night side magnetotail stretches hundreds of R_E [*Singer et al.,* 1996].

High-pressure solar wind can cause magnetopause compression. When solar wind compresses the magnetopause, or the boundary of the magnetosphere, past GEO, or to less than 6.6 R_E (36,000 km), it leaves geostationary orbits exposed to direct influence of the energetic particle populations that are present in the solar wind. Long duration spaceflights outside of the Earth's magnetosphere are also subject to galactic cosmic rays and high-speed solar wind, which can threaten successful operability of satellite electronics [*Baker,* 1998].

2.2.1 Variability in Geomagnetic Activity: The Russell McPherron Effect

Understanding the types of environmental phenomena, their time scales/variability and the resulting influence on spacecraft is important to predict how a satellite will perform. The Russell McPherron Effect describes that semiannual variation in geomagnetic activity exists due to semiannual variation in the polarity of the IMF, specifically the southward component of the IMF (Bz). The controlling factor in the Russell McPherron Effect is the angle, theta, between the IMF Bz in the geocentric solar magnetospheric (GSM) coordinate system and the IMF By in the geocentric solar equatorial (GSEQ) coordinate system. The probability of a southward, or a negative, Bz component of the IMF increases when theta (which is smaller than 90 degrees) decreases. The southward Bz enables more efficient dayside reconnection, which conveys more energy into the magnetosphere [*Zhao and Zong,* 2012]. *Russell et al.,* [2003] show that the tilt of the dipole axis controls the reconnection rate, the size of the dayside reconnection region and geomagnetic activity [*Zhao and Zong,* 2012]

Long-term averages of geomagnetic activity indices peak near the equinoxes during spring and fall (March/April and October), and reach minimums near the solstices in the winter and summer (January and June/July). Geomagnetic activity is enhanced during the spring and fall equinox because the direction of the IMF is "toward and away" from the Sun, respectively [*Russell and McPherron,* 1973; *Miyoshi and Kataoka,* 2008]. The variability of other space environment observations, such as the *Kp* and *Dst* Indices, the auroral electrojet (*AE*), energetic proton and energetic electron flux, will be discussed in Chapter 3.

2.2.2 Particle Motion

Understanding particle motion is a critical aspect of this research, as the analysis depends on particle energy and trapping. Particles physically move as a result of two primary electromagnetic forces: the electrostatic force and the magnetic (Lorentz) force. The electrostatic force is defined as:

$$\vec{F}_E = q\vec{E} \tag{2}$$

The magnetic Lorentz force is defined as:

$$\vec{F}_B = q(\vec{v} \times \vec{B}) \tag{3}$$

where q is the particle charge, v is the velocity vector of the particle, and $\vec{B}$ and $\vec{E}$ are the magnetic and electric field in vector space. When the electric field is zero, the Lorentz force implies that the force on a charged particle is always perpendicular to the magnetic field vector and the particle's instantaneous velocity vector. Thus in the presence of a uniform $\vec{B}$, the particle moves in a circle around the plane perpendicular to the magnetic field.

The radius of the gyrating particle, known as the cyclotron or gyro radius, ρ_p, is quantified in Equation 4 for non relativistic particles, by setting the Lorentz force equal to the centripetal force, $m_p v_\perp^2/\rho_p$ where m_p is the particle mass and $v_\perp$ is the velocity component perpendicular to the magnetic field.

$$\rho_p = \frac{m_p v_\perp}{qB} \tag{4}$$

The gyro radius of an electron in a plasma is less than the gyro radius of an ion in a plasma by a factor equal to the ratio of the particle masses. The cyclotron frequency, Ω_p, quantifies the frequency at which the particle gyrates and is equal to qB/m_p.

A particle's motion consists of a component that is parallel to the magnetic field, $v_{||}$, and a component that is perpendicular to the magnetic field, $v_\perp$. The motion of a particle is described in terms of the

angle between the particle's motion and the magnetic field direction. This angle is referred to as the pitch angle and is defined in Equation 5 for non-relativistic particles.

$$\alpha = \cos^{-1}\left(\frac{v_{||}}{v_{\perp}}\right) \tag{5}$$

A particle's pitch angle determines at what point the particle will mirror and reverse the direction in which it is traveling along the magnetic field. Particles with pitch angles of 90 degrees experience a mirror force that causes a mirror point at the equator, and particles with pitch angles of 0, or 180 degrees theoretically mirror at the poles. In reality, the particles that mirror at the poles are absorbed in the Earth's atmosphere. One can determine the likelihood of a particle striking the atmosphere and no longer remaining trapped by analyzing the particle's geomagnetic equatorial pitch angle, the angle that defines the loss cone of the particle. At angles inside the loss cone the particle will no longer remain trapped, and for angles outside of the loss cone the particle will continue to be trapped.

In the presence of an electric field, ion acceleration occurs during part of the orbit, and ion deceleration occurs for the remainder of the orbit. This acceleration and deceleration lead to a distorted circle with a net displacement in the direction perpendicular to the electric field. If the distortion persists over the course of several gyration orbits then the drift velocity can be determined using Equation 6.

$$v = \frac{\vec{E}\times\vec{B}}{B^2} \tag{6}$$

This velocity is commonly referred to as the drift E-cross-B drift velocity, which is important in establishing the ring current, described in Section 2.2.2.1.

The Grad-B drift describes a particle's velocity due to the variation of the magnetic field over one period of gyration, or gyroperiod. The Grad-B drift is particularly important in regards to the Van Allen Belts because it pertains to the curvature of the particle's motion in a magnetic field.

The three adiabatic invariants are another important aspect of charged particle motion. An adiabatic invariant is a property of a system that stays constant while other changes in the system slowly take place. In plasma physics, the first adiabatic invariant is the magnetic moment, μ. The magnetic moment of a gyrating particle is conserved when the length scale of the variation in the magnetic field is much greater than the cyclotron radius of the motion. The first adiabatic invariant ensures that the magnetic field at the mirror points remains constant [*Gurnett and Bhattacharjee*, 2005]. The second adiabatic invariant is the longitudinal invariant, J. The longitudinal invariant of a particle trapped in a magnetic mirror, or with the bounce motion between two mirror points on a magnetic line, is constant as long as the geomagnetic field and drift velocity vary on time-scale longer than the bounce period. The bounce period for MeV protons and electrons generally peaks at a few seconds. The third adiabatic invariant is the magnetic flux enclosed in a particle's drift surface. The procession of particles around the Earth is conserved provided that the variation in the Earth's magnetic field is on time-scales longer than the drift period (this is typical during relatively quiet geomagnetic periods) [*Schulz and Lanzerotti*, 1974].

The term L-shell is related to the third adiabatic invariant and is associated with azimuthal drift motion of a particle. The collection of all field lines with the same magnetic mirror field, B_m, and integral invariant, I, define an L-shell. When particles drift around the Earth they remain on the same L-shell. The L-parameter, or L-value, of an L-shell, corresponds to the equatorial radial distance measured in R_E of a field line in a dipole field with the same values of B_m and I [*Gurnett and Bhattacharjee,* 2005].

Interestingly, adiabatic theory suggests that radiation belt particles would remain trapped indefinitely, yet in actuality geomagnetic storms lead to particle diffusion and eventual particle loss.

In summary, the motion of the energetic charged particles that enter the Earth's magnetosphere consists of three components:

- Gyration: the particles spiral along magnetic field lines
- Bounce Motion: the gyration center moves up and down the magnetic field lines, between "mirror-points"

- Drift: there is a slow longitudinal drift of the guiding center around the Earth. Ions (protons and oxygen ions) drift westward from midnight to dusk and 10 – 300 keV electrons drift eastward from midnight to dawn, giving rise to the ring current.

The combined result of these three motions trap particles on surfaces known as drift shells, which are centered on the Earth's dipole center.

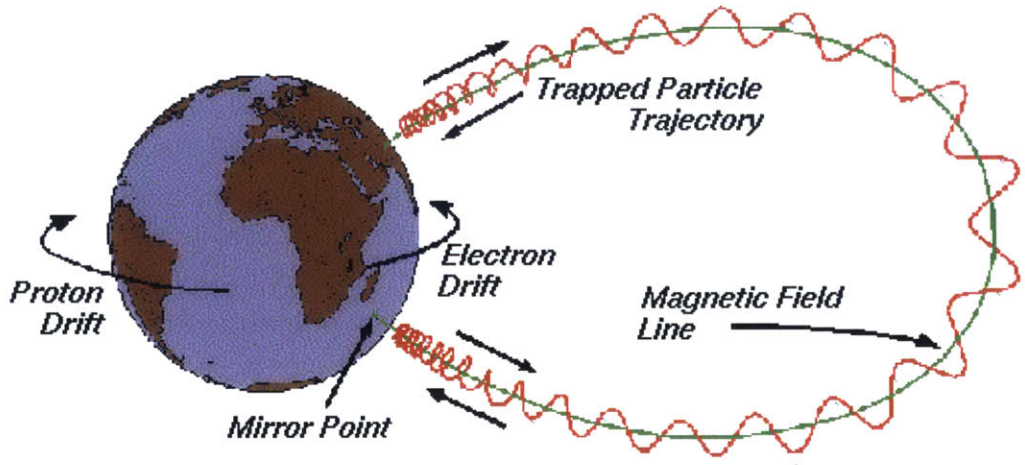

Figure 3. Representation of the composite motion of charged particles trapped in the Earth's magnetic field [*Heynderickx*, 2002]

2.2.2.1 The Ring Current

The equatorial ring current is the result of the drift of 1 – 200 keV ions due to the magnetic field gradient and curvature, as well as gyration. This drift induces a magnetic field disturbance that is opposite to the direction of Earth's magnetic dipole field, which in turn linearly weakens the Earth's magnetic field as a function of the total energy of the ring current particles. Interesting, the largest energy consumer in the Earth's magnetosphere is the buildup of the storm time ring current [*Singer et al.,* 1996; *Baker*, 1998].

The defining property of geomagnetic storms is the formation of an enhanced ring current, generally between 2-7 R_E (approximately 12,700 km to 44,600 km) that peaks between 3-4 R_E (19,000 km and 25,500 km). Large geomagnetic storms generally begin when an energetic stream of solar plasma interacts with the magnetosphere, causing a shock that charges currents in the magnetotail, and leads to large magnetic

disturbances and increased particle flux [*Hastings and Garrett,* 1996; *Baker*, 1998].

2.2.2.2 Particle Flux and Fluence Definition

Flux is the rate of the number of particles that pass through a unit of cross-sectional area in units of particles/cm^2/s. Fluence (Φ) is the number of particles that pass through a unit of cross-sectional area over a finite period of time. Fluence is the integral of flux over the radiation exposure duration, measured in particles/cm^2.

Additionally, particle energy is measured with electron volts (eV), the energy that a particle carrying a charge *e* gains in falling through a potential drop of 1 V, where 1 eV = 1.6022 x 10E-19 J.

2.2.3 The Van Allen Belts

James Van Allen and his co-workers established the existence of the Earth's radiation belts in 1958 using a Geiger counter onboard the Explorer-1 spacecraft [*Kivelson and Russell,* 1995; *Heynderickx*, 2002]. High-energy solar wind causes variability in the intensities of energetic particles (MeV electrons to tens of MeV protons) and variability in the boundary of the radiation belts [*Lanzerotti*, 2001]. However, because the inner belt is dominated by the Earth's magnetic field, the inner zone is relatively stable in comparison to the outer belt, which is heavily influenced by the temporal fluctuations in the geomagnetic tail [*Hastings and Garrett,* 1996]. Recently, with the launch of the Van Allen Probes, formerly known as the Radiation Belt Storm Probes (RBSP), there has been discovery of what some have identified as a third radiation belt [*Baker et al.,* 2013].

2.2.3.1 Inner Van Allen Radiation Belt

In calm solar wind conditions, the inner belt is generally located between 1.2 and 2 R_E (approximately 7645 km to 12700 km) [*Schulz and Lanzerotti*, 1974]. However, at the South Atlantic Anomaly (SAA) the Inner Van Allen Belt dips down to 200 km with an L-value of 1.2 – 1.5, and causes an increase in particle flux. The Inner Van Allen belt is

notorious for trapping high energy protons (energies < 1 GeV) and energetic electrons (less than 0.8 MeV) [*Fennell et al.,* 2015]. Albedo neutrons and solar energetic protons are credited for causing the intense proton and electron fluxes observed in the inner belt [*Hastings and Garrett,* 1996].

The Inner Van Allen Belt is home to hundreds of satellites operating in low earth orbit (LEO). Fortunately, the Earth's magnetic field acts as a shield, and deflects low-energy particles from reaching LEO spacecraft. In polar-regions, particles enter along the magnetic field lines causing danger to LEO polar spacecraft. Spacecraft traversing the SAA are also at risk [*Hastings and Garrett,* 1996]. The SAA and the dangerous particle populations in the Inner Van Allen belt are discussed in more detail in the following three subsections

2.2.3.1.1 High-Energy Protons

Energetic protons, with energies reaching up to hundreds of MeV are the most hazardous component of the Inner Van Allen Belt [*Daly et al.,* 1996]. The high-energy proton population originates from two primary sources. CRAND is thought to be the primary source of >100 MeV protons, while protons of <100 MeV are solar energetic protons from solar phenomena like CMEs, which drive interplanetary shock waves that accelerate protons to high energies [*Thomsen et al.,* 2007]. In less than two days after a CME, these particles penetrate the Earth's magnetic field at the poles, crash into atmospheric particles, and produce ion and electron pairs that temporarily increase the plasma density in the lowest regions of the ionosphere [*Baker*, 2000; *Baker*, 2002]. This causes absorption of short wave radio signals and widespread blackout of communications, sometimes called a polar cap absorption event.

Dangerous levels of high-energy particle radiation accumulate below 20,000 km in the Inner Van Allen Belt [*Heynderickx*, 2002]. Energetic protons coming from the west gyrate from above a particular point, whereas protons coming from the east gyrate from below [*Daly et al.,* 1996]. Particles coming from below encounter increased atmospheric density and tend to become lost in collisions. Thus, the particle flux from the west is greater than the particle flux from the east, which causes

proton anisotropy, known as the East-West effect. Particle anisotropy depends on gyro-radius (higher energy particles display larger anisotropy) and on atmospheric density (anisotropy decreases with increasing altitude). Particles in the South Atlantic Anomaly also contribute to low-altitude anisotropy because the particles are all near their mirror points, strongly biased towards 90 degrees (mirroring at the equator). While the atmosphere absorbs lower particles from the inner edge of the South Atlantic Anomaly, CRAND and diffusion replenish the population [*Daly et al.,* 1996].

The radiation from high-energy protons can damage spacecraft microelectronics and pose a serious threat to the safety of astronauts [*Baker,* 1998]. Energetic proton events can also cause increased noise in photonics, total dose problems, single event upsets, and solar panel degradation. Solar cell degradation occurs primarily from radiation damage of solar protons, and is one of the leading causes of decreased satellite performance (along with charging and single event upsets (SEUs)) [*Koons et al.,* 2000]. One design approach to compensate for this degradation is to oversize the solar arrays, yet this solution is wasteful in terms of material and cost [*Hastings and Garrett,* 1996]. Thus relationship between high-energy protons and solar cell degradation is of particular interest to the communications satellite industry as these interactions drive cost and limit available power and fuel to sustain mission operation [*Barbieri and Mahmot,* 2004].

2.2.3.1.2 Energetic Electrons

Electrons on the orders of tens of keV are accelerated and delivered into the inner magnetosphere from magnetotail injections and drift eastward into the night portion of the magnetosphere [e.g. *Wrenn,* 1995; *Allen,* 2010]. Low-energy electrons can eject hazardous secondary electrons and can be reflected from spacecraft surfaces [*Davis et al.,* 2008]. Low-energy electrons deposit on the surface of the satellite, but do not possess enough energy to penetrate shielding materials [*Hastings and Garrett* 1996].

In general, trapped electrons are confined to two zones: the inner zone, located below 1 R_E, and the outer zone, located above 2 R_E. A region of fewer electrons, known as the "slot region", separates the two zones

[*Daly et al.,* 1996; *Heynderickx,* 2002]. The slot region is formed due to enhanced wave-particle interactions that cause pitch-angle scattering, which ultimately deplete the region between the inner and outer zone [*Daly et al.,* 1996]. Specifically hiss waves, an incoherent and structureless whistler-mode emission, are responsible for the formation of the slot region [*Lyons and Thorne,* 1973; *Abel and Thorne,* 1998; *Thorne,* 2010; *Meredith et al.,* 2006].

2.2.3.1.3 South Atlantic Anomaly

The South Atlantic Anomaly (SAA) is the region near Brazil, where the Earth's magnetic field is weakest, and the energetic proton component of the Inner Van Allen Belt dips closest to the Earth's surface. The SAA at 560 km, taken by the ROSAT satellite, is depicted in Figure 4. A deviation in the Earth's magnetic field dipole axis and the Earth's geographic N-S axis of 11.2 degrees, as well as an offset in the Earth's first-order dipole center and the Earth's geographic center of approximately 500 km jointly contribute to the formation of the SAA [*Daly et al.,* 1996; *Olson and Deguen*, 2012].

The secular changes in the geomagnetic field influence the geographic location of the SAA. The SAA slowly drifts westward at a rate of 0.3 degrees/year, or ~2.5 km/year. The SAA intensifies the radiation environment for orbital altitudes up to ~1000 km and orbital inclinations of 35-60 degrees. Satellite operators and satellite mission designers typically have protective management strategies for their systems when they are in proximity of the SAA [*Heynderickx*, 2002; *Barbieri and Mahmot*, 2004]. High-energy particles in the SAA are all near their mirror points; otherwise the particles would be quickly absorbed by the atmosphere as they approached lower altitudes.

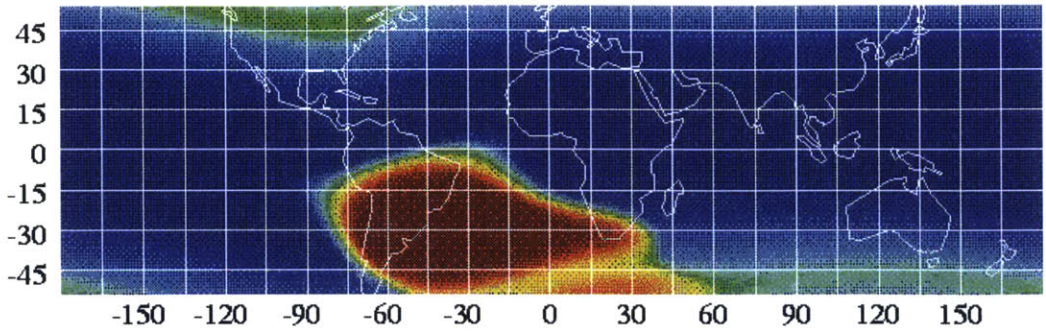

Figure 4. The South Atlantic Anomaly. Image credit: ROSAT; MPE; S.L. Snowden, NASA/GSFC.

2.2.4 Outer Van Allen Belt

In calm solar wind activity, the outer radiation belt, which traps energetic electrons with energies up to ~10 MeV, is located between ~2.5 and 7 R_E (approximately 15,900 km to 44,600 km) [*Schulz and Lanzerotti*, 1974]. The Outer Van Allen Belt can extend to approximately 10 R_E (approximately 63,700 km) with a maximum flux of >1 MeV electrons occurring at 4 R_E (approximately 25,500 km). This belt tends to be more dynamic than the inner belt, and varies in intensity by orders of magnitude over periods of several hours [*Heynderickx,* 2002].

The source of the outer radiation belt is the subject of research, and is the prime science objective of the Van Allen Probes mission [*Mauk et al.,* 2013; *Baker et al.,* 2013]. The outer belt is thought to exist due to the acceleration of low-energy electrons through radial diffusion and wave-particle interactions. As previously mentioned, the main acceleration mechanism is radial diffusion (the process of accelerating low-energy electrons at high altitudes via inward radial transport) [*Schulz and Lanzerotti,* 1974]. Lower-energy electrons can also be energized by wave-particle interactions with various very-low frequency (VLF) and extremely-low frequency (ELF) waves such as whistler-mode chorus waves [*Baker and Daglis,* 2007; *Su et al.,* 2011].

2.2.4.1 High-Energy Electrons

CMEs and CIRs, which drive geomagnetic storms, control high-energy electron flux enhancement in the outer belt. The high-energy electrons trapped in the outer belt peak during the declining phase of the solar cycle, when high-speed solar wind streams from CIRs tend to occur [*Shea and Smart*, 1998; Miyoshi and Kataoka, 2008]. High-energy electrons also emit secondary electrons upon collisions with solid material [*Alig and Bloom*, 1975].

At high latitudes, the outer electron belts reach down to low altitudes and can affect high-inclination satellite missions [*Heynderickx,* 2002]. After large geomagnetic storms, high fluxes of energetic electrons have been seen at altitudes between three and four R_E (~25,500 km). After a period of a day, these energetic electrons diffuse to GEO where they remain for numerous days (the actual period over which the electrons remain in GEO is not known) [*Vampola et al.*, 1985]. These hazardous high-energy electrons are capable of penetrating spacecraft shielding and contributing to internal charging, a failure mechanism that will be investigated in Chapter 7. Interestingly, *Wrenn et al.,* [2002] showed the occurrence of 214 phantom commands from January 1991 to December 2000, attributed to 2-day >2 MeV electrons fluence at GEO correlated with the declining phase solar cycle.

2.2.4.2 GEO Environment

Approximately half of the satellites launched are either GEO Earth observing satellites or GEO communications satellites. Geostationary orbit is a circular equatorial orbit with an altitude of 35,786 km, and a period of 1,436 minutes. The period of GEO, 1436 minutes (23.93 hours) is equal to the sidereal day, which is the rotation speed period of the Earth relative to the fixed starts [*Wertz et al.,* 2011]. Thus, at GEO a satellite will remain fixed over a specific longitude on the Earth's equator.

Geostationary orbit moves in and out of the outer radiation belt, a region dominated by high-energy electrons and bombarded with energetic protons from solar events [*Baker*, 1998]. The GEO environment is subjected to injections of high-energy plasma near local midnight,

known to be a major source of surface charging. Components onboard geostationary satellites are at high risk to TID induced anomalies along with both surface and internal charging anomalies, which is relevant to the analysis on geostationary communications satellite component anomalies presented in Chapter 7. Specific examples of GEO satellite anomalies related to TID and internal charging can be found in *Farthing et al.,* 1982; *Vampola,* 1987; *Violet and Frederickson,* 1993; *Wrenn et al.,* 1993; *Wrenn and Smith,* 1996; *Wilkinson,* 1990; *Balcewicz et al.,* 2000; *Baker,* 2000; *Fennell et al.,* 2001; *Bhat et al.,* 2005; *Davis et al.,* 2008; *Bodeau,* 2010.

Plasma at GEO, unlike plasma at LEO that is sufficiently collisional, is rarefied and collision-less. LEO plasma is said to follow a Maxwellian distribution function, but this distribution is not appropriate for GEO, as it under estimates the number of low energy electrons and both low and high energy ions at GEO. A double Maxwellian fit that uses four variables rather than two is suggested to align more closely with the actual distribution function of particles in GEO [*Hastings and Garrett,* 1996].

As previously mentioned, high solar wind pressure can compress the magnetopause to within GEO, leaving satellites in this orbit outside of the Earth's magnetospheric shield. When spacecraft cross the magnetopause, serious effects particularly related to magnetic torque coils can occur. Magnetic torque coils at GEO (unlike at LEO where the magnetic field is strong enough to use magnetorquers (MTQ) for Attitude Dynamics and Control Systems (ADCS)) are used to adjust satellite momentum changes induced by solar radiation pressure. Some satellite operators turn magnetorquers off during magnetopause crossings due to the large deviation from the modelled magnetic field of the Earth and the space environment outside of the magnetosphere [*Singer et al.,* 1996]

2.2.5 Galactic Cosmic Rays (GCRs)

GCRs result from supernova explosions that spread highly energetic particles throughout the galaxy. GCRs consist mostly of protons (84% hydrogen), alpha particles (15% helium), and less than 1% of heavier nuclei (e.g. C, N, O, Fe) [*Baker,* 2000; *Wilkinson et al.,* 1991]. Galactic

cosmic rays have energies of up to 10^{14} MeV, which in combination with the heavy ions (ions of any element heavier than helium) leads to severe tissue damage in humans and major SEUs in electronics. These high energies also make detection with scientific instruments onboard satellites challenging. Thus, GCRs are monitored with cosmic ray detectors, which are usually ground-based neutron monitors [*Wilkinson et al.,* 2000].

GCRs occur out of phase with the eleven year solar cycle – the radiation from GCRs peaks at solar minimum and reaches a minimum at solar maximum [*Wilkinson et al.*, 1991, 2000; *Riley*, 2012]. At solar minimum, the solar wind is low, so GCRs are capable of reaching the Earth's magnetosphere. This does not tend to occur at solar maximum when the high-speed solar wind speeds towards the earth act as a shield, prohibiting GCRs from entering a trajectory towards the magnetosphere. The earth's magnetic field and neutral atmosphere shield GCRs from reaching the equatorial region of Earth's surface, but GCRs have more direct access to polar-regions and high equatorial altitudes [*Baker*, 1998].

2.3 Radiation Effects on Components

It is important to understand the impacts of radiation and the associated failure mechanisms on components in analyzing solar cell degradation (presented in Chapter 5) and attempting a root-cause study of amplifier anomalies (presented in Chapter 7) on-board geostationary communications satellites. The relevancy of one or more particular radiation effects is not always clear when starting a root-cause anomaly analysis. Specifically, this was the case for the root-cause anomaly investigation presented here. Therefore, additional research work is involved to determine which of the causes and effects are particularly relevant.

Satellite systems face five primary hazards in the space radiation and plasma environment: total ionizing dose (TID), displacement damage dose (DDD), surface charging, internal charging, and single event effects (SEE) [*O'Brien et al.,* 2013]. These hazards can decrease a subsystem's efficiency (solar panel degradation), cause temporary service outages

(electromagnetic interference (EMI) or charging), to complete mission failure. Table 2 summarizes the environmental hazards, describes the particle populations which are generally identified as causing these hazards, and the impacts of the hazards on satellite systems. Each hazard, along with a discussion of the impacts of the hazards, will be discussed in detail in the next three sections.

Table 2. Summary of Environmental Hazards and Spacecraft Impacts

Hazard	Particle Type	Impact
Total Ionizing Dose (TID)	High-energy electrons and protons, heavy ions, secondary particles	Reduced expected life of satellite components
Displacement Damage Dose (DDD)	Low-energy protons	Impacts solar cells and optical detectors such as charge coupled devices (CCDs)
Surface Charging	Low-energy electrons	Electrostatic Discharge (ESD)
Internal Charging	High-energy electrons	ESD, component anomalies
Single Event Effects (SEE)	High-energy protons and cosmic heavy ions	Single event upsets (SEUs), Single event latchup (SELs)

Figure 5 shows the range of penetration depth for protons and electrons between zero and fifty MeV in silicon. The range of electrons and protons is material dependent. For example, the range of a 100 MeV proton in aluminum is approximately 40 mm, whereas the range of a 3 MeV electron is approximately 3 mm in aluminum [*Lanzerotti,* 2001].

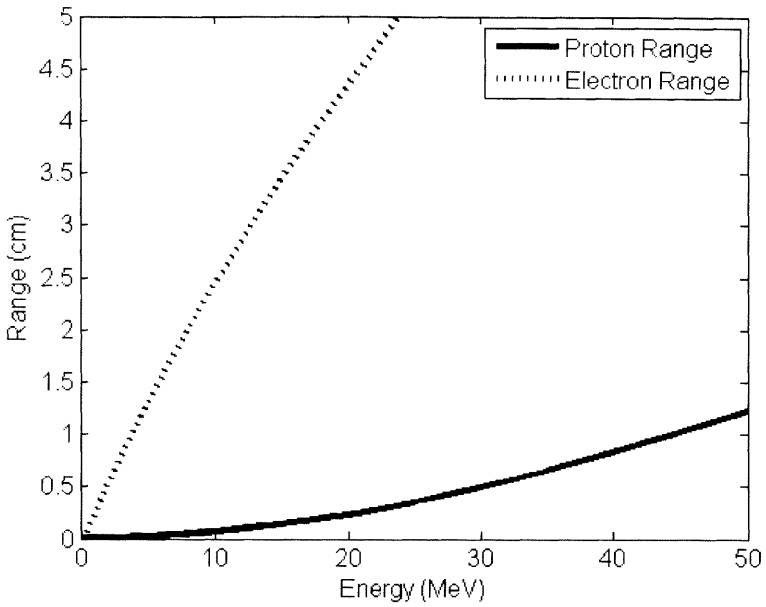

Figure 5. Range of protons and electrons in silicon

2.3.1 Total Ionizing Dose (TID)

Ionization occurs when the bombardment of radiation causes the removal of orbital electrons from an atom or molecule, and in the case of semiconductors the creation of electron-hole pairs [*Alig and Bloom*, 1975]. Ionizing radiation can exist in the form of alphas, betas, x-rays, gamma rays, neutrons, high-energy electrons and protons, and heavy ions from GCRs. For spacecraft, the trapped high-energy electrons and protons, as well as the solar protons, contribute most to TID [*O'Brien et al.*, 2013]. Accurate measurements of accumulated dose throughout a satellite mission is necessary to optimize radiation shielding design for electronic components [*Bhat et al.*, 2005]

Active semiconductor spacecraft components, such as metal-oxide semiconductor field effect transistors (MOSFETs), are particularly susceptible to ionizing radiation dose. One susceptible part of these components is the insulating SiO_2 layers present in MOS transistors. The energy required to generate an electron hole pair in SiO_2 is ~17 eV, which is low. The bombardment of ionizing radiation in the oxide layer leads to the production of electron hole pairs and charge trapping in the gate oxide of the less mobile holes (positive charges). The trapped charge alters the electrical characteristics of the device by specifically shifting

the gate threshold voltage. As such, one of the main approaches for radiation hardening devices is to thicken the oxide layer to limit the amount of charge trapping.

Ionization can also cause the development of color centers, which darkens adhesives and solar cell coverglass, and thus reduces the transmittance of the solar cell coverglass [*Bailey and Raffaelle*, 2003]. Ionizing radiation is not the largest contributor to solar cell degradation, as it only accounts for approximately 4% of cell degradation over the mission lifetime [*Messenger et al.,* 2011].

To understand TID and radiation penetration into matter, it is important to first understand the concept of linear energy transfer (LET). LET is the energy per unit path length absorbed/transferred locally by/to the target material through the process of ionization. LET is often erroneously deemed synonymous with stopping power, the total energy lost by a particle per unit distance travelled in a material, but it is indeed different. LET is generally normalized by the material density and referred to as the mass LET, with units of MeV-cm^2/mg

$$L_{m,e} = LET = \frac{1}{\rho}\frac{dE_{ele}}{dx} \tag{7}$$

dE_{ele}/dx is the electronic energy loss, which is due to inelastic collisions with electrons, known as ionization. LET is also used to define a critical level, that once exceeded induces an upset, which is defined further in Section 2.3.3. Single Event Effects.

TID is the total energy per unit mass of material, transferred to the material via ionization from all ionizing radiation. Mathematically, TID is the integral over all of the ionizing particle fluence (ϕ) of the LET, with units of rads or radiation-absorbed dose (1 Gy = 1 joule/kg = 100 rad = 10^4 ergs/g) [*Srour and McGarrity,* 1988].

$$TID = \int_{\phi} L_{m,e} = \int_{\phi} \frac{1}{\rho}\frac{dE_{ele}}{dx} \tag{8}$$

It is common practice to state these values with specific designation of absorbing material, since the energy transferred by a given particle flux varies with the material (e.g. rad(Si)). The energy delivered per rad(Si)

is independent of the type of radiation, but the damage incurred is not independent of the type of radiation.

The unit conversions to arrive at the dose are shown below:

$$Dose = LET\left[\frac{MeV \cdot cm^2}{mg}\right] \cdot Fluence\left[\frac{particles}{cm^2}\right] \cdot \left[\frac{10^6 eV}{MeV}\right] \cdot \left[\frac{1.602 \times 10^{-19} J}{eV}\right] \cdot \left[\frac{10^6 mg}{kg}\right] \cdot \left[\frac{0.1\ krad}{J/kg}\right] \quad (9)$$

After canceling units and collecting factors the equation becomes

$$Dose = LET\left[\frac{MeV \cdot cm^2}{mg}\right] \cdot Fluence\left[\frac{particles}{cm^2}\right] \cdot 1.602 \times 10^{-8} krad \quad (10)$$

2.3.2 Spacecraft Charging

Spacecraft charging is one of the primary causes of anomalies for spacecraft components due to the plasma environment. Charging occurs when surrounding plasma particles bombard the satellite and deposit charge onto the surface of the satellite, or even penetrate the satellite shielding and deposit in the internal components. The potential of the ambient space plasma is traditionally defined to be zero, and the spacecraft potential is defined relative to the ambient plasma potential. When a spacecraft potential is nonzero, the spacecraft is charged, and a potential sheath forms around the vehicle [*Lai,* 2012].

The sheath region is often complex in shape and is highly dependent on spacecraft motion, plasma properties, spacecraft surface materials, and spacecraft activity such as thruster firings. This region also becomes distorted due to charge on the spacecraft [*Baker,* 2000]. It is important to note that negatively charged spacecraft repel electrons and positively charged spacecraft attract electrons [*Davis et al.,* 2008].

A spacecraft in a plasma generally strives to follow Kirchhoff's law, which states that at every node in equilibrium the sum of all current coming in equals the sum of all currents going out. Once a deviation from equilibrium occurs and a build-up of charge accumulates beyond the material's breakdown potential an electrostatic discharge (ESD) occurs and emits lightning-like energy that can cause single event

upsets (SEUs) or component anomalies in electronic systems [*Hastings and Garrett,* 1996; *Fennell et al.,* 2001, *Baker*, 2002; *Bodeau,* 2010].

2.3.2.1 Surface Charging

Electrons with energies in the few to ten keV range can lead to charge build up on the surface of spacecraft materials resulting in a phenomenon known as surface charging. The amplitude of charging is determined by the balance of currents (the currents of ambient electrons/ions and secondary and backscattered electrons) on the surface of the spacecraft [*Baker,* 2000]. The photoemission current, which generates photoelectrons in the presence of sunlight must also be considered [*Lai,* 2012].

Surface charging is most likely to occur between shadowed and sunlit surfaces, because photoemission due to solar ultraviolet radiation ejects low-energy electrons on sunlit surfaces [*Vampola et al.,* 1985]. Electric fields due to differential charging of spacecraft surfaces can trap photoelectrons and make it difficult for charge balance to occur [*Whipple,* 1976; *Mandell et al.,* 1978; *Olsen et al.,* 1981].

When a spacecraft is immersed in a cool, dense plasma these currents all balance, producing a low net spacecraft potential. In a hot tenuous plasma, like that in GEO, large potential can build as it is difficult to achieve current balance in these conditions, and surface charging can occur [*Baker,* 2000]. It is widely acknowledged that surface charging anomalies generally occur between local midnight and dawn at geostationary orbit due to the eastward drift of electrons. It is also known that surface charging occurs at highly inclined low earth orbits [e.g. *Vampola et al.,* 1985; *Wrenn,* 1995; *Fennell et al.* 2001; *Lanzerotti et al.,* 1998] Anomalies attributed to surface charging also peak at solar maximum [*Kamide et al.,* 1998; *Denton et al.,* 2006].

Several geostationary satellites have experienced anomalies due to surface charging; for example, the Maritime European Communications Satellite A (MARECS-A) experienced an uncommanded switching anomaly from a sudden increase in moderate energy electrons [*Wrenn,* 1995; *Baker,* 2000; *Koons et al.,* 2000]. Figure 6 depicts the local time of surface charging anomalies, showing the tendency to occur between

local midnight and dawn, as measured from onboard the GOES-4 and GOES-5 geostationary spacecraft. Anomalies are also likely to occur soon after a spacecraft transitions from being in the Earth's shadow to becoming illuminated by the sun [*Vampola et al.,* 1985].

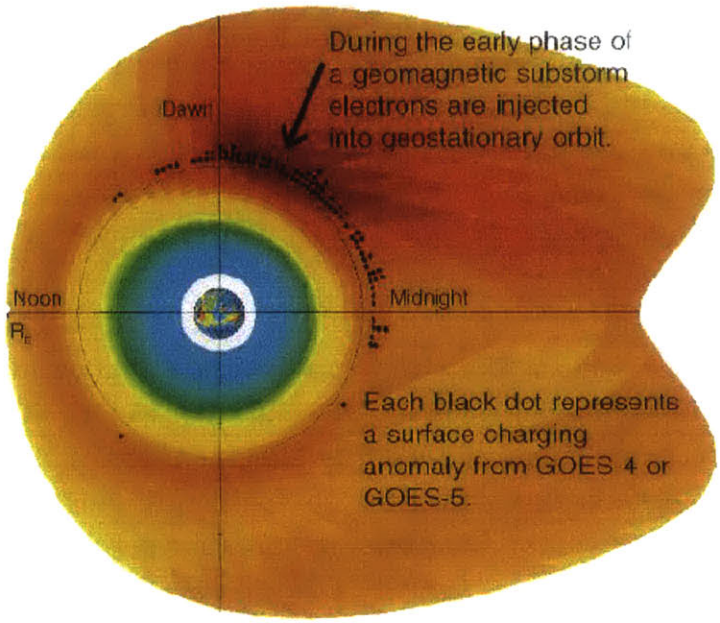

Figure 6. Local Time Dependence of Surface Charging [*Freeman,* 2001]

2.3.2.2 Internal Charging

High-energy electrons (e.g. a few hundred keV to ~2 MeV) that are accelerated during geomagnetic storms penetrate satellite shielding, and deposit into the dielectric materials including coaxial cables, semiconductors and circuit boards [*Vampola et al.,* 1985]. Depending on the conductivity of the satellite components, particularly if the component's resistivity is high, the rate of charge build-up can exceed the rate at which charge leaks from the internal components. When this occurs, the induced electric field can exceed the breakdown threshold for the material, causing electrostatic discharges (ESDs) in the insulating material [*e.g., Hastings and Garrett*, 1996; *Shea and Smart*, 1998; *Baker,* 2000; *Fennell et al.,* 2001; *Bodeau*, 2010; *Lai,* 2012]. The resulting discharge is potentially hazardous directly to the material, or

indirectly to other spacecraft components, causing spacecraft component malfunctions and satellite component failures.

Internal charging, commonly referred to as deep dielectric charging, generally occurs one to several days after a major magnetic storm [*Baker,* 2000; *Koons et al.,* 2000]. The >2 MeV electron channel is commonly used as the representative portion of the electron spectrum capable of penetrating spacecraft structures [e.g. *Love et al.,* 2000; *Gubby and Evans,* 2002]. While surface charging is known to peak between midnight and dawn, studies show that internal charging peaks near local noon [*Fennell et al.,* 2001]. Unfortunately, deep dielectric charging is difficult to predict and determine because charge build-up takes time to accumulate, during which other particle populations may fluctuate [*Thomsen et al.,* 2007].

The anomalies on ANIK E1, ANIK E2, the Japanese BS-3a satellite, Intelsat K, Galaxy 4, and Telstar 401 have been attributed in previous studies to internal charging [*Baker,* 2000; *Love et al.*, 2000; *Allen*, 2010; *Horne et al.*, 2013]. However, at the time of the ANIK and Telstar anomalies the >2 MeV electron flux was very weak [*Baker,* 2000]. These anomalies experienced periods of high flux levels of energetic electrons one to two weeks before the anomalies occurred [*Shea and Smart,* 1998; *Love et al.,* 2000]. This finding is particularly interesting, and relevant to this research and analysis presented in Chapters 6 and 7.

To prevent future internal charging anomalies from occurring (1) all conductors in cables and circuit boards should be terminated/grounded at both ends, even if unused, and (2) at least 35 mils of aluminum should shield dielectric materials from the space environment [*Vampola et al.,* 1985; *Fennell et al.,* 2001]. These preventative design guidelines are particularly relevant for the analysis of solid state power amplifier anomalies on-board geostationary communications satellites, presented in Chapter 7. These preventative design guidelines are not always implemented and as a result can cause anomalies onboard satellite payloads, and in internal satellite electronics boxes.

2.3.3 Single Event Effects

Heavy ions from galactic cosmic rays and high-energy protons from GCRs, the Van Allen radiation belts or solar proton events with energies > 10 MeV can cause single event effects (SEEs) in satellite electronics [*Baker*, 1998]. SEEs that occur in the inner belt are generally caused from high-energy protons, as the geomagnetic field shields particles from GCRs and solar proton events at low altitudes [*Heynderickx,* 2002]. Types of SEEs include non-destructive effects such as single event upsets (SEUs) and single event transients (SET), as well as destructive effects like single event latchup (SEL), single event gate rupture (SEGR), and single event burn out (SEB).

SEUs occur when a high energy particle deposits sufficient energy in the sensitive volume of an electronic device to change a logic state of a circuit [*Baker*, 1998]. Upon collision with the spacecraft components, these high energy particles leave ionization tracks in the microminiaturized electronic devices [*Baker*, 2002]. The highly ionizing Fe nuclei are considered the most damaging form of GCR for SEUs because they are the heaviest and a relatively abundant element in the cosmic ray and solar flare environment [*Srour and McGarrity,* 1988; *Baker*, 2000].

The critical level, that once exceeded induces an upset, is generally quantified in terms of LET. The LET threshold (LET_{th}) is the minimum LET above which a particle will cause an upset [*Hastings and Garrett*, 1996]. SEUs include bit flips, which is when a high-energy particle impacts a solid-state memory device, which can lead to incorrect computations that result in loss of attitude or pointing control, or anomalous telemetry [*Baker,* 2002].

SEL occurs when a low impedance conduction path forms between the supply and ground of a device. Power cycling the device is a typical mitigation strategy, yet this type of SEE is destructive when excessive current is drawn from the power supply; this phenomena is known as single-event burnout (SEB), which is formally defined as a formation of a conductive path, other than the channel, that forms from the source to the drain of a transistor [*Edmonds et al.,* 2000]. SEGR, a conductive path formed across the gate oxide, and SET, one or more voltage pulse/glitch that propagates through a circuit, will not be described in detail.

It is often impossible to shield against heavy ions, yet shielding and radiation hardening devices can limit the impact of solar particles and help reduce the risk of SEEs [*Baker*, 1998]. Software techniques, such as error detection and correction algorithms (EDACs) can be implemented to detect and repair SEUs. One such approach is triple-module redundancy (TMR). TMR consists of three processors that perform the same calculation, and compare answers. If one processor computes a value different from the other two, the value computed by the majority of processors would be selected, and the "incorrect" process would be rebooted or corrected [*Wertz and Larson,* 1999].

2.4 Space Radiation Environment Modeling Tools

Mission designers and architects use models based on their orbital locations and spacecraft shielding to quantify and predict the expected radiation environment to which their satellites will be exposed [*Daly et al.,* 1996]. Three models are used to calculate the expected TID for a particular mission orbit and duration. These three models (trapped particle, solar particle, and TID) are explained in more detail in this section. The next few subsections introduce several space environment models including trapped particle models, long term solar particle models, and total ionizing dose models that will be used in later sections of this thesis. A complete list of existing space environment models can be found in Appendix C of *Garrett and Whittlesey* [2011]. In this thesis we focus on a subset of the models, which are most commonly used.

2.4.1 Trapped Particle Models

Since the beginning of the space age, the trapped radiation belts have posed hazards to successful space mission performance. As a result, tremendous efforts were put forth to build models of the trapped particle populations, so that satellite designers could better prepare for the harsh space environment [*Heynderickx,* 2002]. The standard trapped particle models developed from these efforts, known as AP-8 and AE-8, were released in 1976 and 1983, respectively. These two models contain data from thirty-eight satellites, dating back to as early as 1958. While the large number of satellites combine to create an intricate map of the

trapped particle environment, the diversity of the instruments on-board these satellites leads to errors in the models from a lack of inter-satellite calibration of the instruments [*Laurenstein and Barth,* 2005].

AP-8 and AE-8 provide omni-directional (integrated over 4π solid angle, not isotropic where particle fluxes come uniformly from all directions) trapped particle fluxes based on the McIlwain (B/B_o, L) coordinate system [*Heynderickx,* 2002]. In the McIlwain coordinate system, B is the magnetic field strength at the position in question, Bo is the magnetic field strength at the geomagnetic equator, and L is the radius (measured in earth radii, R_E) where the magnetic field line crosses the equator [*Vette,* 1991]. An L-shell defines the drift shells for trapped particles in the magnetosphere, and is formed by rotating the magnetic field lines azimuthally about the dipole axis.

The trapped particle models are also based on an internal geomagnetic field model, and must be run with the same internal geomagnetic field model originally used in the development of the trapped particle models. Jensen and Cain 1960 (JC-60) should be used for all models, except for AP-8MAX when the GSFC-12/66 model extrapolated to 1970 should be used [*Daly et al.,* 1996]. As a result of having the radiation models based on these magnetic field models, secular changes in the location of the SAA are not accounted for, leading to incorrect flux estimations at low altitudes [*Laurenstein and Barth*, 2005].

The models consist of three regions: the inner zone for L of 1.2-2.4, the outer zone for L of 3-11 and the transition region for L between 2.4 and 3 [*Vette,* 1991]. AP-8 has an energy range of 100 keV to 400 MeV protons, whereas AE-8 models energies that span 40 keV to 4.5 MeV for electrons in the inner region and 40 keV to 7 MeV for electrons in the outer region [*Laurenstain and Barth*, 2005]. For each region there are two versions that refer to either solar maximum or solar minimum [*Vette,* 1991]. During solar maximum, the atmosphere expands and absorbs energetic protons, causing a decrease in particle flux, thus AP-8MIN is considered worst case [*Daly et al.,* 1996].

AE-8 and AP-8 are static models and provide long-term averages for the expected levels of the trapped particle environment throughout user defined mission durations. The long term averaging prevents the user

from conducting a worst-case analysis, and from understanding the impacts of solar wind variation and storm injections. Additionally, due to the dynamic behavior of the trapped particle environment, numerous authors have identified shortcomings with the static nature of the models [e.g. *Daly et al.,* 1996; *Heynderickx*, 2002; *Laurenstein and Barth*, 2005]. For low altitudes, problems exist with the models due to the SAA, east-west asymmetries and solar cycle variations. At high altitudes problems exist with models due to the highly dynamic electron environment.

Since the release of AP-8 and AE-8, several other trapped proton and electron models have been developed. Examples of trapped proton models include PSB97, Low Altitude Trapped Radiation Model (LATRM), Trapped Proton Model (TPM-1), Combined Release and Radiation Effects Satellite Proton Model (CRRESPRO), and examples of trapped electron models include CRRESELE, Flux model for internal charging (FLUMIC) and the International Geosynchronous Electrons (IGE)-2006 model.

The IGE-2006 model is the latest version of the Particle ONERA-LANL Electron (POLE) model, and has become the standard for geostationary (GEO) missions, as it is based on data from thirteen LANL GEO satellites from 1967 to 2001 [*Laurenstein and Barth*, 2005]. This model covers energies from approximately 1 keV to 5.2 MeV, and is solar cycle dependent. The unique lower energy bound expands the relevancy of dose calculations for spacecraft surfaces and surface materials [*Guild et al.,* 2009].

Recent efforts have been put forth to improve the current AE8/AP8 de facto trapped particle models, with an updated version called AE9/AP9. The updates to these models include the quantification of uncertainty from the dynamic space environment and errors across instruments/calibration, and more detailed spatial resolution. The AE9/AP9 series also consists of new data sets and updates to the statistical approach enabling a Monte-Carlo estimation of flux thresholds for a user specified percentile level [*Ginet et al.,* 2013].

2.4.2 Long-term Solar Particle Fluence Models

Long-term solar particle fluence models predict fluences outside the magnetosphere over the duration of the mission lifetime. Solar particle fluence modeling had progressed to the point where many models agree on the long-term SPE spectra to within a factor of approximately two in fluence [*Xapsos et al.,* 2004]. Commonly used solar particle fluence models include: Emission of Solar Protons - (Prediction of Solar particle Yields for CHaracterizing Integrated Circuits (ESP-PSYCHIC), Jet Propulsion Lab JPL-91, the Rosenquist et al., (2005, 2007) model, and the King model. The ESP-PSYCHIC model [*Xapsos et al.,* 1999] is suggested for long-term solar particle fluence modeling by the Aerospace Corporation with a confidence of 90% for GEO and 80% for LEO missions [*Guild et al.,* 2009].

The ESP-PSYCHIC model includes measurements out to > 100 MeV protons that extend to > 327 MeV with extrapolation using GOES data [*Guild et al.,* 2009]. This model is based three solar cycles (Solar Cycle 20 – 22) of historical event observations to quantify the likelihood of exceeding a mission-integrated fluence threshold. The intensity of > 10 MeV Protons throughout Solar Cycles 20 - 22 will be described in further detail in the next chapter. In brief, Solar Cycle 20 had one anomalously large event, Solar Cycle 21 was rather quiet with no large events, and Solar Cycle 22 was active, with several large solar proton events (SPEs).

The ESP-PSYCHIC model incorporates the statistical Maximum Entropy Principle to estimate the initial distribution of SPE fluences over a wide range of SPE fluences and Extreme Value Theory to estimate the worst case fluences. The initial distribution is a truncated power law, which smoothly approaches zero at maximum fluence, and thus establishes an appropriate upper limit for the magnitude of peak flux during an SPE [*Xapsos et al.,* 1999]. This statistical approach is notably different between previous models [*King,* 1974; *Feynman et al.,* 1993].

The ESP-PSYCHIC confidence level, 90% for GEO as suggested by *Guild et al.,* [2009], means that for ten "reasonable projections" of the space environment of a given mission length, one of the projections will exceed the mission fluence levels specified.

JPL-Extended is another long-term solar particle fluence model that is less commonly used in comparison to ESP-PSYCHIC. This model was originally constructed in 1985, and since then has been improved. The data set in JPL-Extended includes a nearly continuous record of daily average fluxes of > 1, >4, >10, >30, and >60 MeV protons, along with solar proton event data. The statistical nature of particle events during active phases of the solar cycle are handled differently than during quiet periods, as the model assumes no significant proton fluence occurs during quiet phases of the solar cycle. Due to the large population of the JPL data set pure Poisson statistics are applied. The model is thus based on a set of probability curves of exceeding a given fluence during a mission lifetime [*Feynman et al.,* 1993].

2.4.3 Total Ionizing Dose (TID) behind Aluminum Shielding

Satellite engineers use space radiation TID models to predict the amount of total ionizing dose exposure a satellite will experience over the mission lifetime for a given orbit. Once the expected radiation environment is analyzed, a determination can be made of which satellite components are best suited for a mission, including determining whether they can sustain the mission estimated dose. SHIELDOSE-2 is the primary model used to estimate TID. SHIELDOSE-2, originally released in 1980 as SHIELDOSE, determines the absorbed dose behind a range of aluminum shielding thicknesses on different detector materials from user-input electron and proton fluences for a given orbit [*Seltzer,* 1980; *Seltzer,* 1994].

The code references pre-calculated, mono-energetic dose-depth distributions for an isotropic fluence source incident on an aluminum plane medium. The distributions were smoothed in depth and incident energy yielding an estimated uncertainty of 10% for the model output. SHIELDOSE-2 is capable of analyzing the expected dose for three aluminum shield geometries: a finite Al shield, in a semi-infinite Al medium, and at the center of a solid sphere shown in Figure 7.

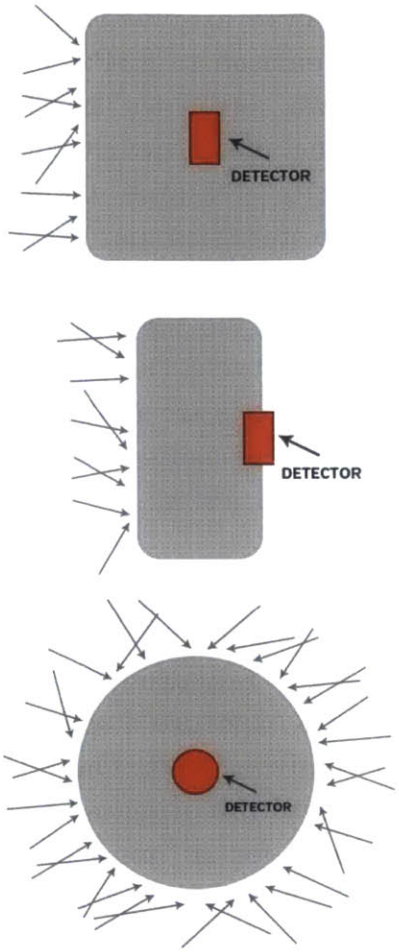

Figure 7. SHIELDOSE-2 shield geometries (from top to bottom semi-infinite medium, finite-thickness slab, and solid-sphere). The gray solid is aluminum material [*Seltzer,* 1980]

The electron and bremsstrahlung calculations in SHIELDOSE use the Monte Carlo code ETRAN, which accounts for (1) the electron energy loss due to inelastic scattering by atomic electrons and to the emission of bremsstrahlung photons, (2) angular deflection of electrons, (3) penetration and diffusion of the secondary bremsstrahlung photons, and (4) penetration and diffusion of secondary electrons produced from electron-electron knock-on collisions (delta rays) and interactions of bremsstrahlung photons with the medium (pair, Compton and photoelectrons) [*Berger and Seltzer,* 1968, and 1970]. Proton calculations are limited to Coulomb interactions, but the simplification is suggested to incur error of no more than 20% for shielding thickness of up to 30 g/cm^2. Additionally the proton contribution utilizes the

straight-ahead, continuous-slowing-down approximation (CSDA) using the stopping power and range data of *Barkas and Berger* [1964].

On-orbit dose rates are generally consistent with dose rates less than or equal to 10 mrad/s, which is specified in the Enhanced Low Dose Rate Sensitivity (ELDRS) radiation test procedure in MIL-STD-883H [*Bogorad et al.,* 2010].

2.4.4 Low Earth Orbit (LEO) TID Environment and Radiation Requirements

The main focus of this work pertains to GEO communications satellites, yet the increase in CubeSats and LEO spacecraft [*Buchen and DePasquale*, 2014] suggests the utility of analysis and cohesive documentation of TID radiation requirements for LEO spacecraft. In the communications world, the implementation of LEO communications constellations would result in decreased latency, compared to GEO satellites, which have a single hop time delay of at least 0.25 seconds due to speed of light transmission [*Comparetto and Ramirez*, 1997].

At LEO, particle fluxes, and TID, increases steeply with altitude, so small errors in computing locations could result in large inaccuracies for the expected TID. Disagreements between the models and flight data at low altitudes are expected because of differences between solar cycles. Additionally, particle flux measurements taken on the shuttle suggest that the ratio of the measured to predicted flux in the SAA is 1.55 [*Daly et al.,* 1996]. A typical rule of thumb is to include a factor of two margin on the expected TID predicted for a mission, so at the shuttle altitude (~420 km) this margin would help reduce the impact of the 1.55 discrepancy over the SAA. For orbits above the shuttle the margin of twice the expected TID is likely insufficient to overcome the deviation in the predicted TID value and the actual TID experienced. This is particularly expected in LEO with the steep increase in TID for increasing altitude that was previously mentioned.

Radiation hardened components, like geostationary communications satellite components, are often rated to a dose of 100 krad to > 1 Mrad, and among other qualities do not suffer from SEL. "Radiation tolerant" components are commercial or industrial parts that are not

manufactured with the space radiation environment in mind, but that have been found to function to a certain dose [*Sinclair and Dyer*, 2013]. Most commercial parts are tolerant to 5 krad, some can withstand 20 krad or more, yet some parts fail before 1 krad. Radiation testing is required to predict the dose at which a part will fail. Numerous databases (Nuclear and Space Radiation Effects Conference (NSREC) Radiation Effects Data Workshop, Jet Propulsion Laboratory's (JPL) RAD Archive, and Goddard Space Flight Center (GSFC) Radiation Data Base) and papers of radiation test results for components exist [*Kingsbury et al.,* 2013; *Sinclair and Dyer,* 2013].

For LEO CubeSat and MicroSat missions the term Careful COTS has been coined as an alternative approach to radiation hardened/space grade design philosophy. Lot control and screening is required in the Careful COTS approach, because commercial vendors often change manufacturing processes, or the foundries that produce the parts. These differences may cause unexpected radiation susceptibilities. Additionally, *Sinclair and Dyer* [2013] suggest that the Careful COTS approach is appropriate when the total lifetime dose is less than 30 krad.

Figure 8(a-d) contains four plots that depict the TID for one-year missions launched January 1, 2017, at altitudes of 200 – 1300 km, inclinations of 0, 15, 30, 45, 60, 75, and 90 degrees, as well as sun-synchronous orbit, for shielding thicknesses of (a) 1.0 mm Al, (b) 1.5 mm Al, (c) 2.0 mm Al, and (d) 2.5 mm Al. AP8-MIN and AE8-MAX were used to model the trapped particles and ESP-PSYCHIC with an 80% confidence level was used to model long-term solar proton fluence. Year 2017 is considered an active year and the geomagnetic shielding was turned on in this analysis. Appendix A contains tables of the accumulated TID for altitudes of 200 – 2000 km, along with 0.5 mm Al and 3.0 mm of Al shielding thicknesses. The figures below do not show altitudes up to 2000 km because, as seen in Appendix A, above 1300 km the expected TID for a one-year mission increases rapidly above the Careful COTS 30 krad limit.

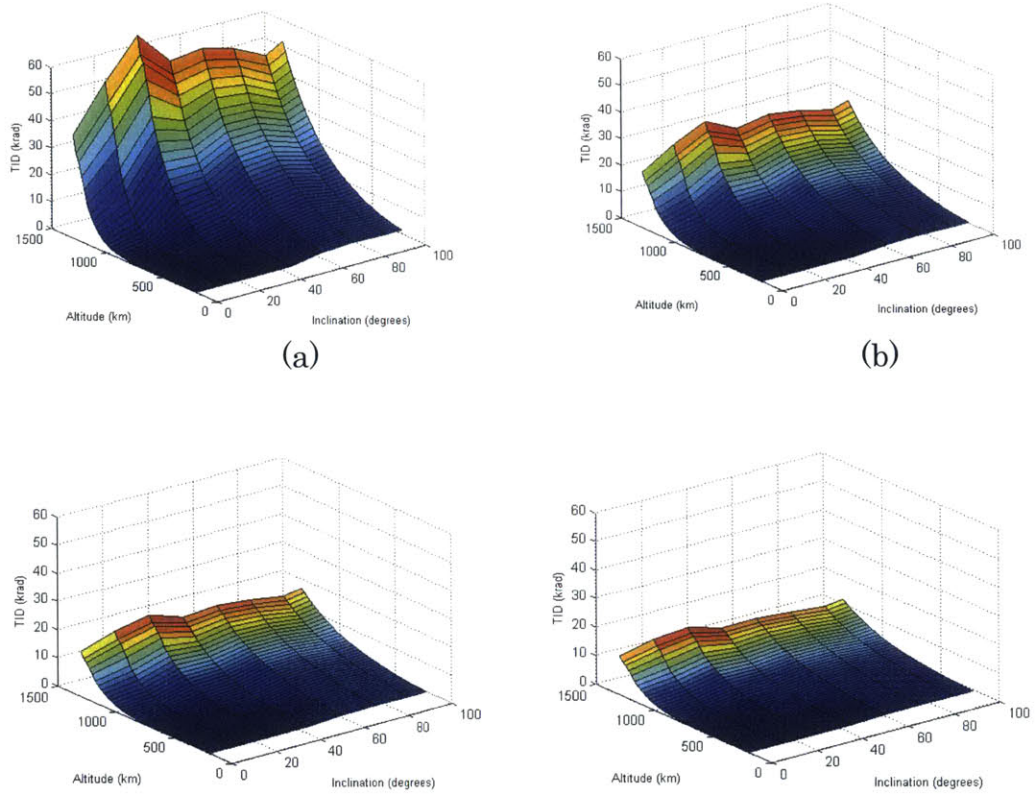

Figure 8(a-d). TID (krad) at altitudes of 200 – 1300 km and inclinations of 0 – 90 degrees in increments of 15 degrees as well as sun synchronous orbit for shielding thicknesses of (a) 1.0 mm Al, (b) 1.5 mm Al, (c) 2.0 mm Al, and (d) 2.5 mm Al

As expected, the magnitude of TID decreases as the Al shielding thickness increases. For Al shielding thicknesses of 0.5 mm, 1.0 mm and 1.5 mm, the altitude at which the 30 krad limit is occurs is considerably different for a given inclination. For example, for 1.0 mm of Al shielding at 0 degrees inclination, the 30 krad limit for Careful COTS lies between 1250 and 1275 km. However, for an inclination of 75 degrees the 30 krad limit occurs between 1050 and 1075 km. This is likely because the shielding thickness does not provide substantial absorbance of incoming radiation, and at the equator (inclination of 0 degrees) the geomagnetic field lines are parallel to Earth's surface – so all but the most energetic ions are deflected away [*Benton and Benton*, 2001]. Figure 9 shows curves above which the 30 krad Careful COTs limit is violated for

aluminum shielding thicknesses of 0.5 – 2.0 mm for altitudes up to 1400 km.

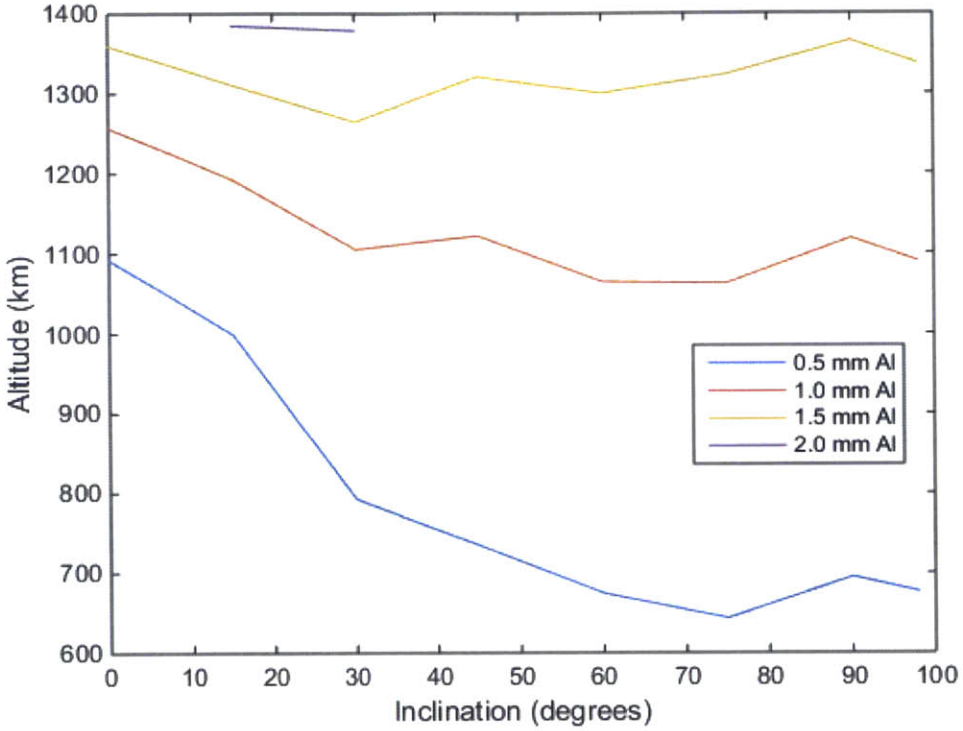

Figure 9. The 30 krad Careful COTS Design Approach Limit for aluminum thicknesses of 0.5 – 2.0 mm, for altitudes up to 1400 km, and inclination of 0 – 90 degrees in increments of 15 degrees as well as sun synchronous orbit

For higher shielding thicknesses, such as 1.5 or 2 mm of Al, the altitudes above which the 30 krad limit is exceeded is less dependent on inclination. For 1.5 mm of Al the 30 krad limit is exceeded between 1260 and 1350 km, and for 2.0 mm of Al the 30 krad limit is exceeded between 1375 and 1500 km. It is important to remember that Figure 8(a-d) only plots up to 1300 km, so this boundary is not evident.

Several modern satellite start-ups decide not to perform any radiation testing on Custom-Off-The-Shelf (COTS) parts for several reasons:

1. The TID environment at LEO is relatively benign below 600 km (as shown in Figure 8 above).

2. There have been numerous tests of COTS components on-board the International Space Station (ISS), for example laptops, that have worked without significant issues.
3. The expense and lengthy time associated with radiation testing of electronic components.
4. The complexity of accurately replicating the LEO radiation environment in ground-based radiation tests.
5. A level of redundancy may be incorporated into satellite design at the component or satellite level that renders testing unnecessary.

Solar cells are, however, one component for which radiation testing is often deemed worthwhile. The outcomes of the solar cell radiation tests are required to accurately predict degradation over a mission lifetime and to evaluate different types of protective encapsulates and cover material.

2.4.5 The Modelled GEO Radiation Environment

The GEO environment's dynamic nature of the outer electron belt, makes modeling the particle population particularly difficult, unless one is interested in long-term averages over a mission lifetime. For this work, understanding the expected particle population at geostationary orbit over given mission durations is required for predicting and assessing solar cell degradation as well as for analyzing potential root-cause hypotheses for amplifier failures.

The trapped particle models, AE-8, AP-8, and IGE2006 ONERA/DESP-LANL (previously known as Particle ONERA-LANL Electron (POLE) model) is intended specifically for GEO. It is important to note that AE-8 MIN and AE-8 MAX don't differ for geostationary orbit [*Laurenstein and Barth,* 2005], and that the IGE2006 is intended specifically for trapped electrons at GEO. The Aerospace Corporation published a report in 2009 that suggests the use of IGE2006 for GEO orbits, over the use of AE-8 [*Guild et al.,* 2009]

IGE 2006 and AP8-MIN radiation environment modeling tools are suggested for GEO, and were used to calculate the magnitude of the integral and differential flux of the trapped particle environment at

geostationary orbit [*Guild et al.,* 2009]. Figure 9 shows the integral and differential electron and proton flux at GEO.

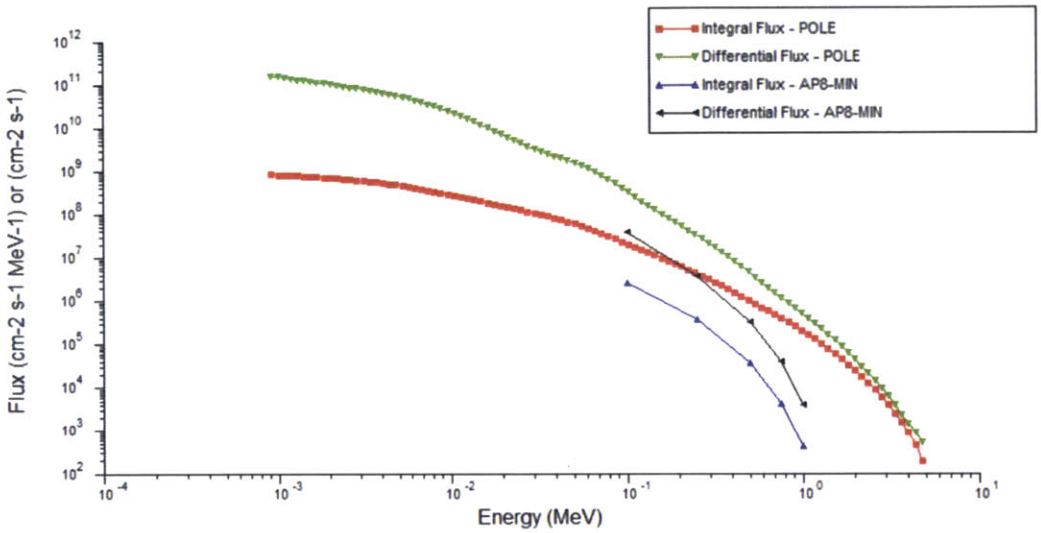

Figure 9. The orbit averaged integral electron flux (shown in red), the differential electron flux (shown in green), the integral proton flux (shown in blue), and the differential electron flux (shown in black) for the trapped particle environment at geostationary orbit

It is clear that geostationary orbit is dominated by trapped electrons ranging from approximately 1 keV to 6 MeV. The figure also shows that a trapped proton population exists with protons ranging from 0.1 to 1 MeV in energy. Additional modeling of the GEO environment will be shown in Chapter 4, yet the purpose of the figure above is to provide the reader with a visual description of the electron and proton spectra at geostationary orbit.

The second type of particles contained within the GEO environment are protons generated from solar events. Using the Emission of Solar Proton (ESP) model at geostationary orbit with a 90% confidence level and for 8.9 active solar cycle years, described in Section 2.4.2, it is found that solar protons are present at energies ranging from 1 MeV to approximately 300 MeV. On average, these protons have an integral flux ranging from 4.8E-01 to 2.2E+03 protons/cm^2/sec. During a severe solar proton event (SPE) the integral flux increases by several orders of

magnitude and the total dose at GEO can equal the dose accumulated over periods of months or longer [*O'Brien,* 2009].

Using the model SHIELDOSE2 shown in Figure 10, the TID over a fifteen-year GEO mission, launched in 2017, behind 2.5 mm of Al is 100 krad.

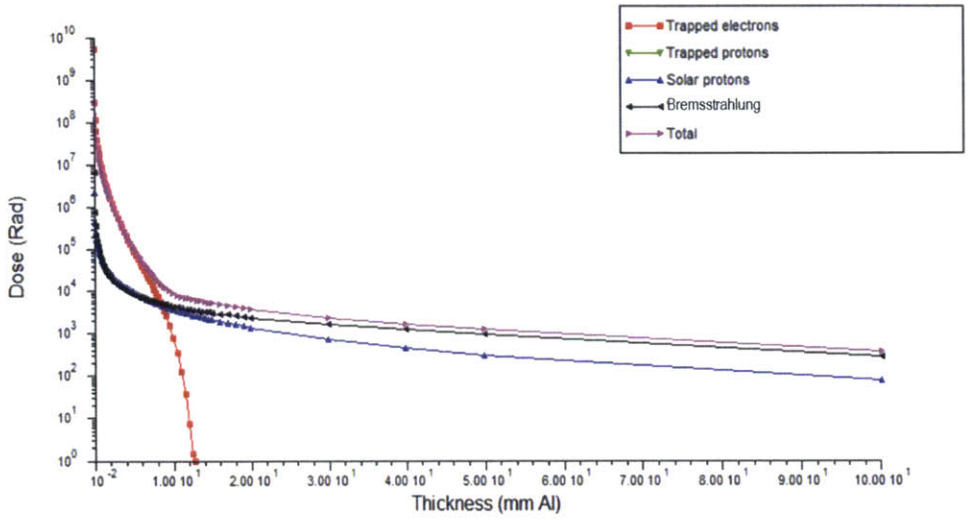

Figure 10. TID computed using SHIELDOSE2 for a 15 year GEO mission launching in 2017. The total TID is shown in magenta, and the contributions from trapped electrons, trapped protons, solar protons, and Bremsstrahlung, are shown in red, green, blue and black respectively.

Bremsstrahlung (*bremsen* meaning "to brake" and *Strahlung* meaning "radiation") occur when part of the energy from fast electrons that interact in matter is converted into electromagnetic radiation in the form of a photon [*Knoll*, 2010]. At a shielding thickness of 2.5 mm of Al, trapped electrons contribute primarily to the total dose. While dose rate is dependent on shielding thickness, typical annual average dose rates at GEO are ~0.2 mrad [*Bogorad et al.*, 2010].

2.5 Space Environment Indices

This section defines three commonly referenced space environment indices: the *Kp* Index, the Disturbance Storm Time index (*Dst*), and Auroral Electrojet (*AE*).

2.5.1 *Kp* Index

The *Kp* index is a qualitative planetary index that characterizes short-term (3-hour periods) geomagnetic disturbances caused by variations in the solar wind. The subscript p stands for planetary, because the index is composed by combining measurements from ground-based magnetometers at various geomagnetic latitudes around the globe. [*Hastings and Garrett,* 1996; *Horne et al.,* 2013]. The *Kp* scale ranges from zero to nine, with 27 one-third steps, where nine designates the highest level of severity for geomagnetic storms [*O'Brien*, 2009]. Between 1996 and 2012, only 2.2% of the *Kp* measurements were recorded as greater than a *Kp* of five, severe geomagnetic activity.

The *Kp* geomagnetic disturbance index is often used as a proxy to quantify the relationship between surface charging and magnetospheric convection [*Gubby and Evans,* 2002; *Thomsen*, 2004]. Magnetospheric convection causes low-energy electron enhancements near geostationary orbit, and is often used to characterize relativistic electron activity [e.g. *Fennell et al.,* 2001; *O'Brien,* 2009; *Choi et al.,* 2011]. *Reeves et al.,* [2003] notes that the disturbance storm time index (*Dst*) is not well related to relativistic particles or to the lower energy electron population responsible for surface charging anomalies. Unfortunately, the *Kp* index can be difficult to interpret physically because variations in the index can be caused by any geophysical current system (magnetopause currents, field aligned currents, and auroral electrojets).

2.5.2 Disturbance Storm Time Index (*Dst*)

The *Dst* Index measures the hourly average of the global variation in the horizontal component of the Earth's magnetic field. This index is constructed from the normalized values of the horizontal component of the Earth's magnetic field, averaged from four low-latitude magnetic field observation stations located in Hermanus (South Africa), Honolulu (HI, USA), Kakioka (Japan), and San Juan (Puerto Rico) [*Mursula et al.*, 2008]. A negative *Dst* value, <-50 nT, indicates that Earth's magnetic

field is weakened, the main defining property of a geomagnetic storm [*Gonzalez et al.,* 1994; *Mursula et al.*, 2008; *Gopalswamy et al.*, 2006]. *Dst* classifications vary, but generally -50 nT > *Dst* > -100 nT is considered moderate, -100 nT to -250 nT is considered intense and -250 nT to -600 nT is considered severe [*Riley*, 2012].

As previously described, the equatorial ring current is formed primarily from proton drifts due to the magnetic field gradient and curvature, and induces a magnetic field counter to that of the Earth's that in turn weakens the Earth's magnetic field. The *Dst* Index is directly proportional to the ring current, as major negative disturbances in the index correspond to an increase in the number of energetic particles forming the ring current [*Mursula et al.,* 2008]. To create a notable variation in the *Dst* Index, energetic particles from the tail must travel close enough to the Earth such that they experience a gradient and curvature force strong enough to completely orbit the Earth. Thus *Dst* is often used to indicate the strength of the ring current around Earth [*Russell and McPherron*, 1973; *Fennell et al.*, 2001].

Positive variations in the *Dst* index are mostly caused by magnetospheric compression due to interplanetary shocks often occurring in the initial phases of magnetic storms. In this phase, an abrupt increase in the solar wind dynamic pressure is often measured on the Earth's surface as a sudden increase in magnetic intensity called the sudden storm commencement (SSC) [*Mursula et al.,* 2008]. A corresponding large decrease in *Dst*, known as the "main phase", due to the ring current encircling the Earth in the westward direction, followed by slow recovery represents a geomagnetic storm [*Gonzalez et al.,* 1994; *Riley,* 2012]. Therefore, the *Dst* Index is particularly useful at identify the strength of geomagnetic storms and the ring current at geostationary orbit. The *Dst* envelope corresponds with the eleven year geomagnetic cycle, with the minimum and maximum corresponding to solar minimum and maximum [*Riley,* 2012].

2.5.3 Auroral Electrojet (*AE*)

The *AE* index represents electric currents, which travel around the Earth's ionosphere near the Northern and Southern Polar Circles

[*Kamide and Akasofu*, 1983]. The *AE* index is due to Hall currents (perpendicular to the Earth magnetic field) induced by the Earth's magnetic field and the electric fields present in the ionosphere. While relatively unperturbed during magnetic quiet periods, the electrojet increases in strength during disturbed periods and expands to both higher and lower latitudes. The *AE* index represents the overall electrojet activity and is formally defined as $AU - AL$, where AU and AL are the largest and smallest values eastward and westward electrojets, respectively.

The increase in *AE* is a result of enhanced particle precipitation, substorm activity and enhanced ionospheric electric fields that inject low energy particles into the inner regions of the magnetosphere [*Neil and Sugiura*, 1966]. Thus, the *AE* index is an indicator of severe surface charging for satellites in the low Earth orbit (LEO) altitudes (less than approximately 600 km), but is not a primary index used for geostationary satellites.

2.6 Space Weather Data Acquisition and Management

Comprehensive measurements of energetic particle populations using in situ spacecraft are vital in understanding decreased satellite performance and the occurrence of satellite anomalies [*Baker,* 1998]. Observations of the space environment covering complete solar cycles are publicly available.

For this analysis, The OMNI2 data set is used and obtained from the Goddard Space Flight Center/Space Physics Data Facility OMNIWeb interface at http://web.gsfc.nasa.gov. OMNI2 contains hourly measurements of near-Earth solar wind magnetic field and plasma parameters, as well as *Kp* index, Disturbance Storm Time index (*Dst*), auroral electrojet (*AE*), and proton flux values. The OMNI2 data comes from numerous satellites such as the Advanced Composition Explorer (ACE) Satellite, the International Monitoring Platform (IMP) satellites and the Geostationary Operational Environmental Satellite (GOES), as well as from the Data Analysis Center for Geomagnetism and Space Magnetism at Kyoto University in Japan [*King and Papitashvili*, 2004].

2.6.1 Sunspot Number Data

Sunspot data, including smoothed and raw sunspot numbers, were obtained from the Solar Influences Data Analysis Center (SIDC) of the Royal Observatory in Brussels, Belgium. This data was used to plot the solar cycle over which the communications satellites were in operation to determine at what point the anomalies tend to occur.

2.6.2 High-Energy Electron Flux Data

High-energy electron flux data were obtained from two sources: Los Alamos National Labs (LANL) and GOES. 1.8–3.5 and 3.5–6 MeV electron flux data were obtained from the Los Alamos National Laboratory (LANL) geosynchronous charged particle instruments, namely the GEO Energetic Sensor for Particles (ESP) [*Reeves et al.,* 2011]. These values are daily averages of the electron flux, and are shown to be nearly identical to the distribution of the GOES >2 MeV electron flux [*Reeves,* 2011]. The NOAA National Geophysical Data Center was additionally used to obtain GOES Space Environment Monitor (SEM) data, >2 MeV integral electron flux, and to assess relativistic electrons at the time of SSPA anomalies.

This GOES SEM sensor suite has provided continuous magnetometer, particle and X-ray data since the mid-1970s, and is a primary source for public, military and commercial space weather warnings [*GOES,* 1996]. The GOES >2 MeV integral electron flux data, with a five second interval, was obtained from the GOES 8 – GOES 15 satellites. In Chapter 6 and Chapter 7, all comparisons and analyses of power amplifier anomalies onboard geostationary satellites were conducted using the GOES >2 MeV integral electron flux data from the GOES satellite that was longitudinally closest to the respective GEO satellite that experienced the anomaly.

At any point between 1996 and 2012 at least two of the GOES 8 – GOES 15 satellites were collecting data. During this time, several of the GOES satellites were either decommissioned into a parking orbit or experienced technological difficulties and are thus not included in this study. Nonetheless, of the remaining GOES satellites, GOES 12 is the primary satellite used for gathering SEM data. GOES 8, 10, 13 and

GOES 14 were also used when one of these satellites was located closer to the anomalous satellite and for dates outside of the and GOES 12 coverage time span. The SEM consists an energetic particle sensor/high-energy proton and alpha detector (EPS/HEPAD), which contains two energetic proton, electron and alpha detectors (EPEADs), a magnetospheric proton detector (MAGPD), a magnetospheric electron detector (MAGED), and a HEPAD [*NSWPC*, 2007].

Chapter 2 has provided an introduction into the space environment, the impacts of radiation on satellite components in LEO and GEO, modeling tools used to predict the impact of the space environment during a spacecraft mission, a description of space environment observations, and the acquisition of space environment data. These topics are fundamentally the basis for the research presented in this thesis.

The following chapter analyzes the space environment observations discussed in Chapter 2 (*Kp* Index, *Dst* Index, *AE* index, high-energy protons and high-energy electrons) throughout four solar cycles, Solar Cycle 20 – Solar Cycle 23.

Chapter 3. Assessment of Space Weather Observations

3.1 Context of this Analysis

Understanding the impact effects of space weather on satellite performance requires data from the satellite, observations of the space environment, and models of the space environment. In this chapter, we discuss our selection of space environment observations and our analysis of the frequency and likelihood of hazardous space weather events. When spacecraft anomalies occur, the time series of the anomaly is often compared to the radiation environment. The use of space weather observations and metrics of the baseline space weather environment must be understood before any connection between the environment and the anomaly can be made. It is helpful to know the historical values of the space weather metrics during the phases of the solar cycle to help determine whether the space environment data are unusually active or variable. Once this analysis is available for reference, it is simpler to assess whether there might be a relationship between space weather conditions and the occurrence of an anomaly.

We analyze three space weather activity metrics (*Kp*, *Dst*, *AE* Index) as well as proton and electron in-situ measurements for Solar Cycles 20 to 23 (1964 to 2008). We develop baseline reference of space weather activity at GEO that we present in terms of the four phases of the solar cycle (maximum, minimum, declining or ascending). Note that the Los Alamos National Lab (LANL) electron flux set referenced in this study only extends from 1989 to 2009, which affects the $\log_{10}$(1.8-3.5 MeV) electron flux analysis. The actual distribution of the electron measurements analyzed, $\log_{10}$(1.8–3.5 MeV Electron flux), can be approximated as equal to 2 MeV electron flux for the purposes of understanding the effects of space environment on satellite performance. Additional detail about the space weather metrics and in-situ measurements can be found in Chapter 2.

We expect that *Kp* Index (a proxy for surface charging), and $\log_{10}$(1.8–3.5 MeV Electron flux) will be most useful for the analysis presented in Chapter 5 and Chapter 7 on the radiation impact on solar cells and high power amplifiers onboard geostationary communications satellites. This is expected because the radiation environment at GEO is dominated by energetic electrons. It is likely that the *Dst* Index may also prove useful as it describes geomagnetic activity and the ring current. The high

energy protons will be useful for the solar cell degradation analysis in Chapter 5, but are not expected to depict a relationship with the high power amplifier anomalies analyzed in Chapter 7. The lack of relationship with the amplifier failures is expected because of low penetration depth of protons with respect to electrons, both at energies less than a few hundred MeV, and the relatively large shielding thickness around the amplifiers. However, as previously mentioned, the *AE* index is not a metric used to describe phenomena in geostationary orbit, and was only included for reference during LEO mission design.

With this data analysis, we do not intend to completely revisit well-understood findings from earlier researchers about how space weather activity varies in the different phases of the solar cycle [*e.g., Russell and McPherron*, 1973; *Miyoshi and Kataoka*, 2008]. *Rather, this analysis is to generate a resource for characterizing space weather activity that is consistent with our satellite telemetry and anomaly analysis so that we can consider space weather and compare activity with any satellite anomaly or telemetry findings.*

3.1.1 Identifying Periods of Increased Activity

"Increased space weather activity" is defined in this work as activity greater than two median absolute deviations (MADs) above the median activity for each phase. MAD is used, rather than standard deviation, because it is more resilient to outliers. The median and MAD values for the four solar cycle phases (solar maximum, solar minimum, the ascending phase of the solar cycle and the descending phases) are tabulated in Table 5, 6, 7 and 8. To determine activity level variation over shorter periods of time, the median and MAD values are also calculated over periods of 3, 14 and 30 day periods of time.

Analysis of the variability of space environment activity over shorter periods of time is useful in anomaly root-cause analyses because anomalies can result due to impacts of the environment over periods of days. Contrary to popular belief, anomalies are not always purely the result of instantaneous phenomena like solar flares and galactic cosmic rays that induce SEEs, but can occur after charge accumulates over a period of time.

Part of this work involves figuring out whether increased exposure to higher space weather activity/energetic particles than usual (for a certain period of time) is related to anomalies or telemetry variability. To do this, we look at the probability that increased activity occurs 3, 14, or 30 days before a random day. (This helps to determine whether the satellite anomaly occurrences are consistent with random behavior, or whether there is a bias that could be due to sensitivity to certain types of space weather events or environmental variation).

3.2 Analysis Approach

We quantify the median value of three space weather metrics and two in situ measurements for each of the four phases of the solar cycle for Solar Cycles 20 to 23 (years 1964 to 2008). We then determine whether any of these metrics and measurements are statistically more likely to be high in any particular phase of the solar cycle. We point out here that while our analysis identifies when metrics/measurements are higher than the median value that it does not necessarily mean that the metrics are elevated to the point of being considered a significant event. Our findings focus on how metrics vary in any phase of the solar cycle given the median of the metric for that phase, without making any assessment of whether an event occurred.

3.2.1 Solar Cycle Definition

One complicating factor for this type of analysis is that a Solar Cycle is not always the same length of time. As shown in Table 3, Solar Cycles 20–23 are not all 11 years long, but 13, 11, 11, and 13 years, respectively. Instead of partitioning the cycles into four equal phases, we base our definition of phases on the solar cycle start and end year, and solar maximum defined by *Kane* [2002]. The period of solar maximum, shown in Table 4, is defined as starting one year before the year of solar maximum in *Kane's* [2002] study and extending to include one year after. The ascending phase of the solar cycle is defined as the number of years from the start of the cycle before the solar maximum phase; this ranges from 2—3 years, depending on the overall length of the solar cycle. Solar minimum is the last three years of the cycle, consistent with *Kane* [2002], and the declining phase is the period of time between the

end of the solar maximum phase and start of the solar minimum phase. The resulting solar cycle phases are listed in Table 4.

Table 3. Solar cycle definition [*Kane*, 2002]

Solar cycle number	*Start year*	*End year*	*Solar maximum year*
20	1964	1976	1968
21	1976	1986	1979
22	1986	1996	1989
23	1996	2008	2000

Table 4. Solar cycle phases for Solar Cycles 20 – 23

Solar cycle number	*Ascending period*	*Solar maximum period*	*Declining period*	*Solar minimum period*
20	1964–1966	1967–1969	1970–1973	1974–1976
21	1976–1977	1978–1980	1981–1983	1984–1986
22	1986–1987	1988–1990	1991–1993	1994–1996
23	1996–1998	1999–2001	2002–2005	2006–2008

3.2.2 Data Analysis and Use of Median Absolute Deviation

The *Kp, AE, Dst* and 10 MeV Proton flux data were obtained from the OMNI2 dataset from 1963 to 2012 [*King and Papitashvili*, 2013]. The OMNI2 dataset does not contain electron flux values, so electron flux data from LANL charged particle instruments from 1989 to 2009 were used [*Reeves et al.*, 2011].

As seen in Figure 11(a-e), it is clear that each of the observations do not follow a strict Gaussian distribution. In the case of skewed distributions, particularly Figure 11(a-d), the MAD is more resilient to outliers in data than the standard deviation. This is because the distance from the mean are squared when calculating the standard deviation, and the large outliers are weighted more heavily, which can potentially skew the results [*Draghici*, 2001]. Therefore, the MAD will be used of the standard deviation for the analysis presented in the remainder of this chapter.

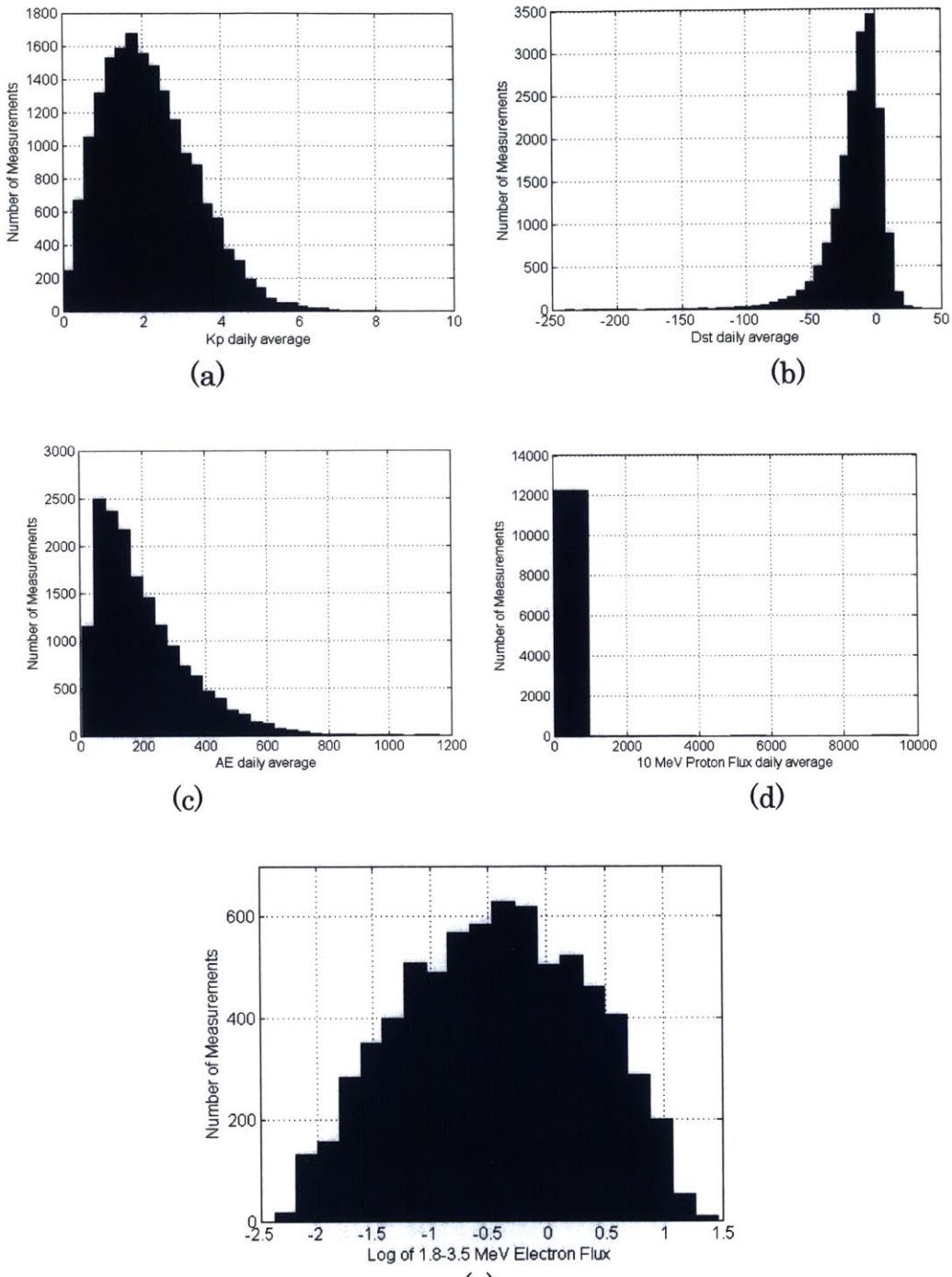

Figure 11(a-e). Distribution of the daily average values of (a) *Kp* index (b) *Dst* Index (c) *AE* Index, (d) 10 MeV Protons, and (e) $\log_{10}$(1.8-3.5 MeV Electrons) for Solar Cycle 20 - 23

In comparison, for the computation of the MAD, the magnitude of a relatively small number of outliers will not skew the results. MAD is computed by finding the median of the absolute residuals:

$$MAD = median(|X_i - median_j(X_j)|) \quad (9)$$

where i is a unit in the set and j is the median of the set. Using the MAD means that we also do not need to eliminate outliers (*e.g.* measurements perhaps do to sensor error) from the dataset.

Table 5, 6, 7 and 8 contain the median and MAD for the metrics and measurements (*Kp, Dst, AE,* 10 MeV Protons, and $\log_{10}$(1.8-3.5 MeV Electrons)) used in this study for Solar Cycles 20, 21, 22, and 23, respectively. We determined the median and the MAD of each space weather metric and in situ measurement for each phase of the solar cycles. These values were then used to determine when the measurements exceeded two MADs above the median value for each cycle's solar maximum, descending, minimum, and ascending phases.

Table 5. Solar Cycle 20 (1964 - 1976)

	Units	Ascending Phase	Solar Max Phase	Declining Phase	Solar Minimum
Kp median	-	1.3	2	2	2.3
Kp MAD	-	0.7	1	1	1
AE median	-	70	126	126	178
AE MAD	-	40	79	79	118
Dst median	nT	0	-10	-13	-10
Dst MAD	nT	8	10	10	10
10 MeV Proton Flux median	p/cm²/sec	N/A	0.35	0.45	0.34
10 MeV Proton Flux MAD	p/cm²/sec	N/A	0.06	0.11	0.02
$\log_{10}$(1.8-3.5) MeV Electron flux median	e/cm²/sec	N/A	N/A	N/A	N/A
$\log_{10}$(1.8-3.5) MeV Electron flux MAD	e/cm²/sec	N/A	N/A	N/A	N/A

Table 6. Solar Cycle 21 (1976 - 1986)

	Units	Ascending Phase	Solar Max Phase	Declining Phase	Solar Minimum
Kp median	-	2	2.3	2.7	2.3
Kp MAD	-	1	1	1	1
AE median	-	NaN	136	197	156
AE MAD	-	NaN	85	126	102
Dst median	nT	-12	-12	-16	-13
Dst MAD	nT	9	13	15	10
10 MeV Proton Flux median	$p/cm^2/sec$	0.36	0.31	0.23	0.31
10 MeV Proton Flux MAD	$p/cm^2/sec$	0.02	0.07	0.04	0.04
Log_{10}(1.8-3.5) MeV Electron flux median	$e/cm^2/sec$	N/A	N/A	N/A	N/A
Log_{10}(1.8-3.5) MeV Electron flux MAD	$e/cm^2/sec$	N/A	N/A	N/A	N/A

Table 7. Solar Cycle 22 (1986 - 1996)

	Units	Ascending Phase	Solar Max Phase	Declining Phase	Solar Minimum
Kp median	-	2	2.3	2.7	2
Kp MAD	-	1	1	1	1
AE median	-	118	152	167	132
AE MAD	-	75	101	111	89
Dst median	nT	-11	-18	-17	-13
Dst MAD	nT	10	15	14	10
10 MeV Proton Flux median	$p/cm^2/sec$	0.35	0.37	0.57	0.72
10 MeV Proton Flux MAD	$p/cm^2/sec$	0.02	0.08	0.1	0.04
Log_{10}(1.8-3.5) MeV Electron flux median	$e/cm^2/sec$	N/A	N/A	-0.51	-0.21
Log_{10}(1.8-3.5) MeV Electron flux MAD	$e/cm^2/sec$	N/A	N/A	0.55	0.68

Table 8. Solar Cycle 23 (1996 - 2008)

	Units	Ascending Phase	Solar Max Phase	Declining Phase	Solar Minimum
Kp median	-	1.7	2	2.3	1.3
Kp MAD	-	1	1	1	1
AE median	-	108	138	167	69
AE MAD	-	69	91	113	45
Dst median	nT	-11	-12	-17	-6
Dst MAD	nT	9	13	12	7
10 MeV Proton Flux median	p/cm²/sec	0.76	0.57	0.24	0.2
10 MeV Proton Flux MAD	p/cm²/sec	0.04	0.11	0.07	0.02
Log_{10}(1.8-3.5) MeV Electron flux median	e/cm²/sec	-0.67	-0.63	-0.17	-0.15
Log_{10}(1.8-3.5) MeV Electron flux MAD	e/cm²/sec	0.54	0.52	0.51	0.58

Table 9. Summary of phase averages and MAD values for the five metrics and in situ measurements

Metric/measurement	*Min phase average*	*Max phase average*	*Min MAD*	*Max MAD*
Kp	1.518	2.810	1.001	1.187
Dst (nT)	–22.555	–2.431	8.835	20.777
AE	128.149	271.238	101.142	183.932
10 MeV proton flux (pfu)	0.735	25.849	0.753	47.381
Log_{10} (1.8–3.5 MeV electron flux)	–0.627	–0.215	0.585	0.705

	Units	Min. phase median	Max. phase median	Min. MAD	Max. MAD
Kp	-	1.3	2.7	0.7	1
AE	-	69	197	40	126
Dst	nT	-18	0	7	15
10 MeV Proton Flux	p/cm²/sec	0.2	0.76	0.02	0.11

Log_{10}(1.8-3.5) MeV Electron flux	e/cm²/sec	-0.67	-0.17	0.51	0.68

3.3 Results: Space Environment Baseline

In this section, we describe the median values and variability of our space weather metrics and measurement data over different periods of time. Section 3.3.1 covers annual activity, Section 3.4 considers variability with respect to phases of the solar cycle, and Section 3.5 considers even shorter timelines: 3 days, 14 days, and 30 days. For all analyses, we defined "increased activity" as values greater than 2 MAD over a given period of time (e.g. one measurement, three days, one year, a solar cycle phase).

3.3.1 Annual Median Values of the Space Environment Metrics and Measurements between 1963 and 2012

We calculate the annual median value for the space weather metrics and measurements, and compare the morphology of these annual median values with the annual median sunspot count, the metric that is used to represent the 11-year solar cycle [*SIDC*, 2003].

Figures 12(a) to 12(e) show the progression of the solar cycles (using the average sunspot number, the blue dashed curve), and the (a) *Kp* Index, (b) *Dst* Index, (c) *AE* index, (d) 10 MeV Proton Flux, and (e) $\log_{10}$ (1.8-3.5 MeV Electron Flux) for Solar Cycles 20–23 (1964 to 2008). These space weather indices are represented with a solid red curve. For the *AE* index, shown in Figure 12(c), data for 1977 is not available.

3.3.1.1 Annual Median of the *Kp* Index

Figure 12(a) shows that from Solar Cycle 21 (1976 to 1986) onwards, the *Kp* index lags behind the solar cycle by a single solar cycle phase, and generally reaches a maximum during the declining phase. As previously mentioned, the *Kp* scale goes from 0 (representing geomagnetically quiet activity) to 9 (representing intense geomagnetic activity). From our

analysis, all of the *Kp* annual median values are less than or equal to 3.0.

3.3.1.2 Annual Median of the *Dst* Index

Figure 12(b) shows the *Dst* index along with the sunspot cycle. The *Dst* index is known as the best societal impact parameter for geomagnetic storms [*Riley*, 2012]. *Dst* can be difficult to interpret because of fluctuations and due to outliers form geomagnetic storms. The scale of *Dst* becomes increasingly more negative during geomagnetic storms, with intense storms classified as Dst < –100 nT. Geomagnetic storms are most likely to occur during solar maximum, when coronal mass ejections (CMEs) that drive magnetic shocks are most common, as these shocks produce geomagnetic storms [*Mursula et al.*, 2008; *Kamide et al.*, 1998]. Figure 12(b) shows annual *Dst* and there are times where *Dst* is more negative during solar maximum, but this is not consistent, and there is less of an overall trend with the solar cycle for *Dst* than for the *Kp* index. This was also noted in *Riley's* [2012] analysis of elevated space weather events.

3.3.1.3 Annual Median of the *AE* Index

The *AE* index is known to significantly vary over short timescales, which can affect the use and interpretation of median values of the *AE* index over shorter timescales. Shown in Figure 12(c), the *AE* index appears to stay in phase with the sunspot curve after Solar Cycle 21. Data for the *AE* index is not available for 1977, so we do not include the ascending phase of Solar Cycle 21 in this study and a gap can be seen in Figure 12(c).

3.3.1.4 Annual Median 10 MeV Proton Flux

The annual median 10 MeV Proton flux curve, shown in Figure 12(d), varies between ~0.1 – 0.8 pfu throughout Solar Cycle 20 – 23. Generally, high energy proton flux fluctuates in phase with the solar cycle, increasing in magnitude during solar maximum, and decreasing in magnitude during solar minimum. Figure 12(d) suggests that the high energy proton flux peaks in antiphase with the solar cycle. The small

range of median 10 MeV Proton flux values prevents conclusions from being made about the variability of the flux over time.

The National Oceanic and Atmospheric Administration (NOAA), the entity responsible for broadcasting space environment warnings, alerts subscribers of 10 MeV proton flux measured greater than 10 pfu, 100 pfu, 1,000 pfu, 10,000 pfu and 10,000 pfu, classified as S1–S5, respectively. The highest warning for 10 MeV protons is a flux of 10,000 pfu, and is considered to cause extreme biological effects (passengers and crew in high flying aircraft at high altitudes) and extreme effects to satellite operations (complete failures, memory impacts, and permanent damage to solar cells). A description of the warning levels is provided at http://www.swpc.noaa.gov/NOAAscales/index.html#SolarRadiationStorms.

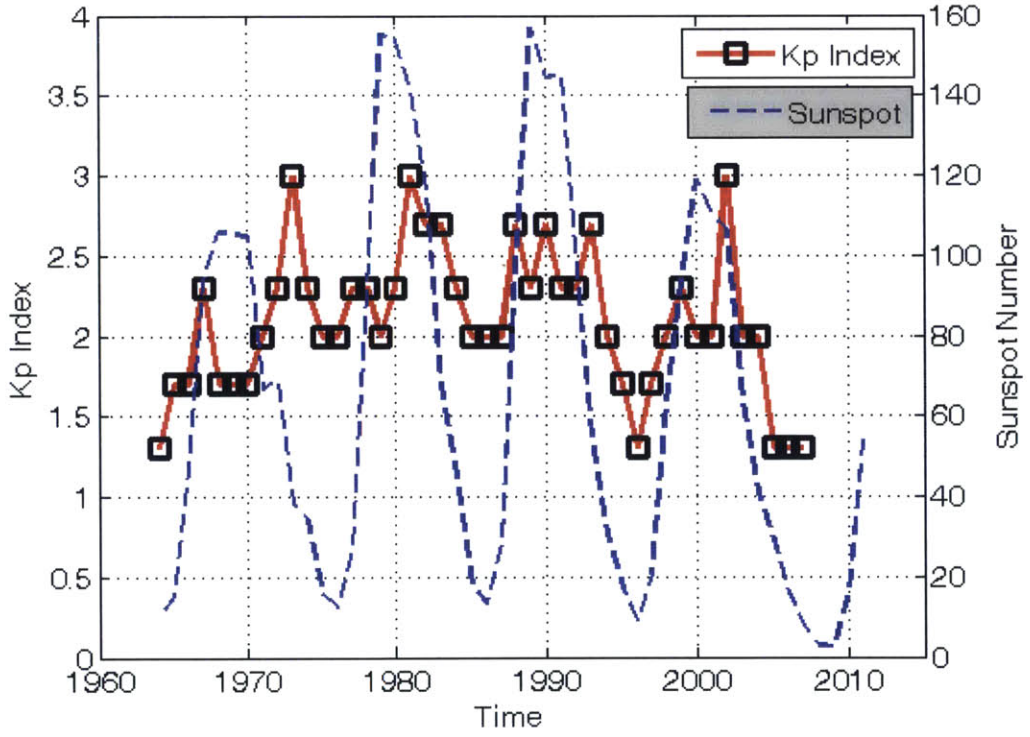

(a)

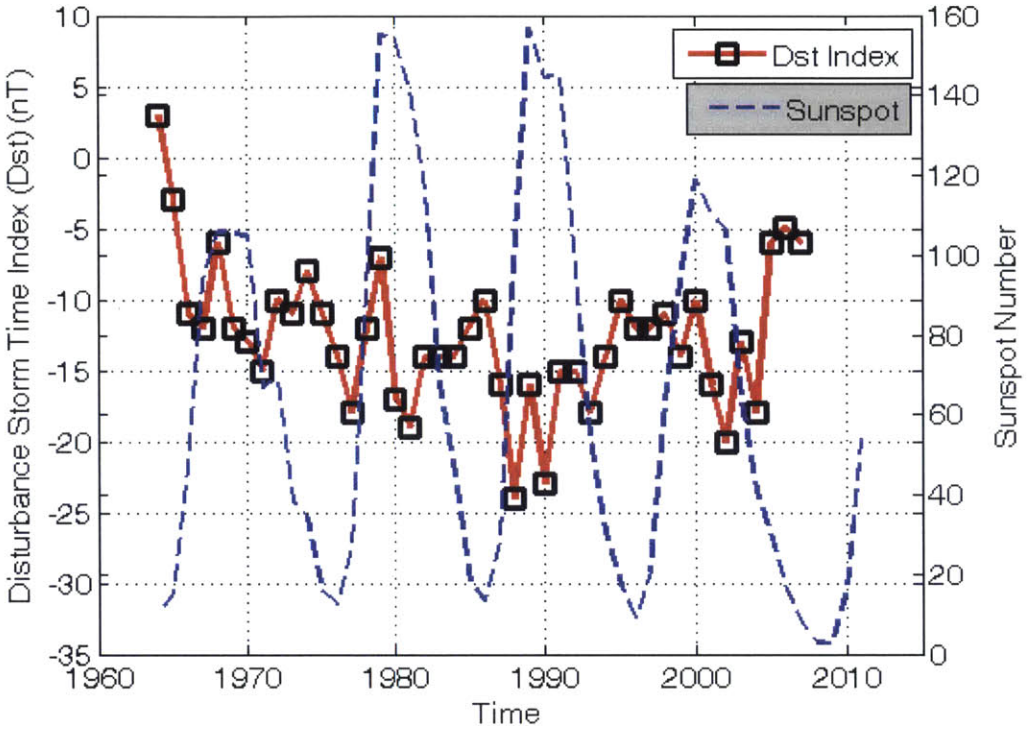
Dst Index
Sunspot
Disturbance Storm Time Index (Dst) (nT)
Sunspot Number
Time
10
5
0
-5
-10
-15
-20
-25
-30
-35
160
140
120
100
80
60
40
20
0
1960
1970
1980
1990
2000
2010

(b)

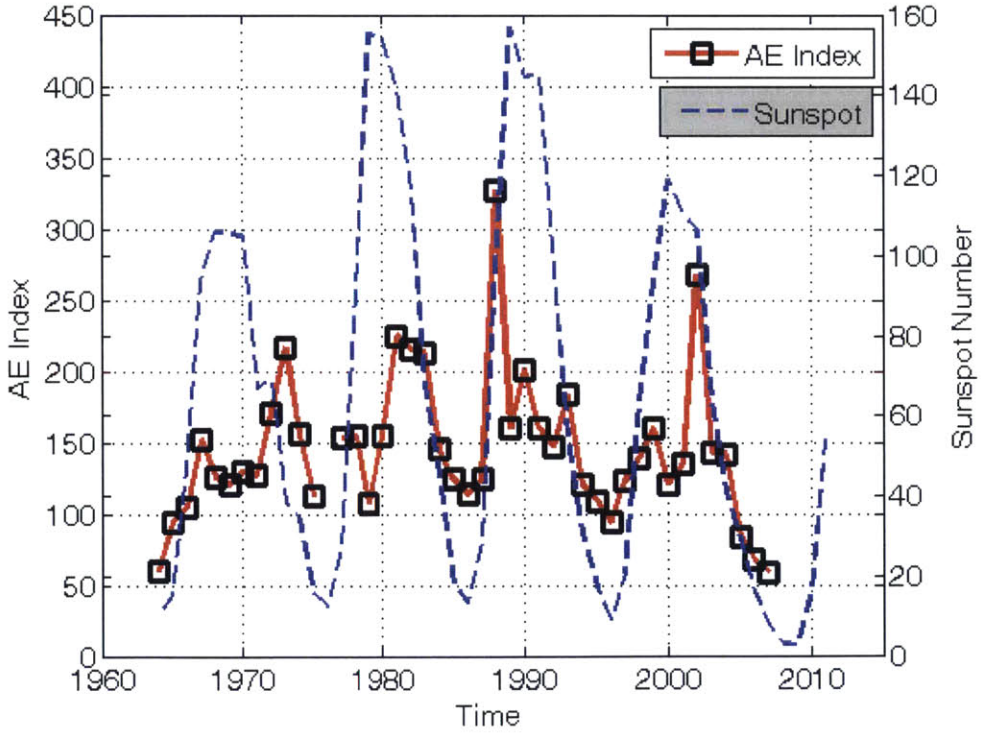
AE Index
Sunspot
AE Index
Sunspot Number
Time
450
400
350
300
250
200
150
100
50
0
160
140
120
100
80
60
40
20
0
1960
1970
1980
1990
2000
2010

(c)

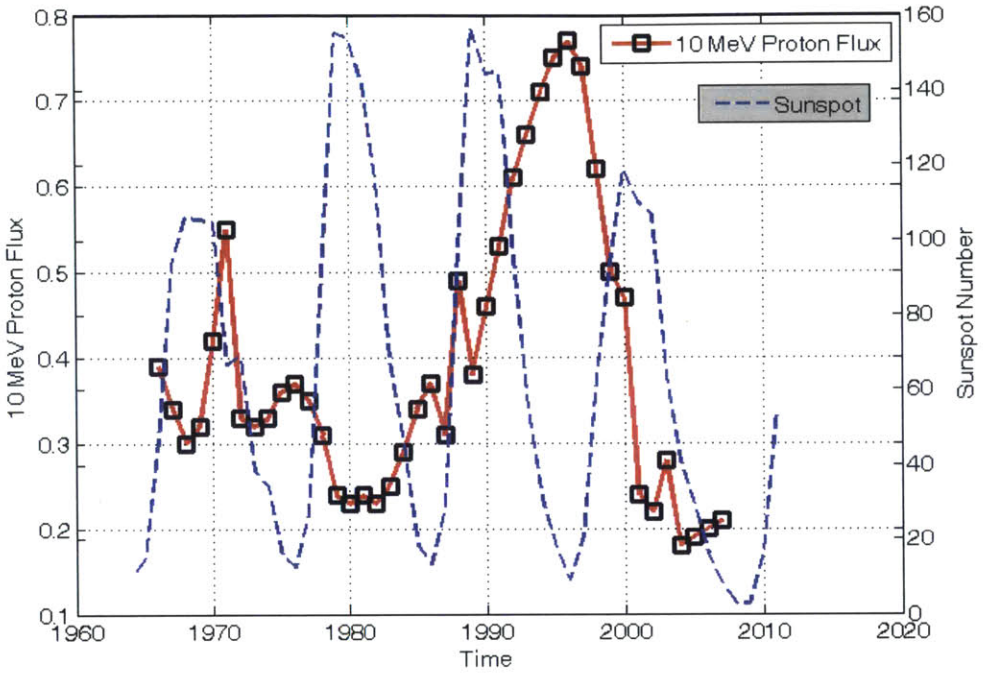
10 MeV Proton Flux
Sunspot
10 MeV Proton Flux
Sunspot Number
Time
0.8
0.7
0.6
0.5
0.4
0.3
0.2
0.1
160
140
120
100
80
60
40
20
0
1960
1970
1980
1990
2000
2010
2020

(d)

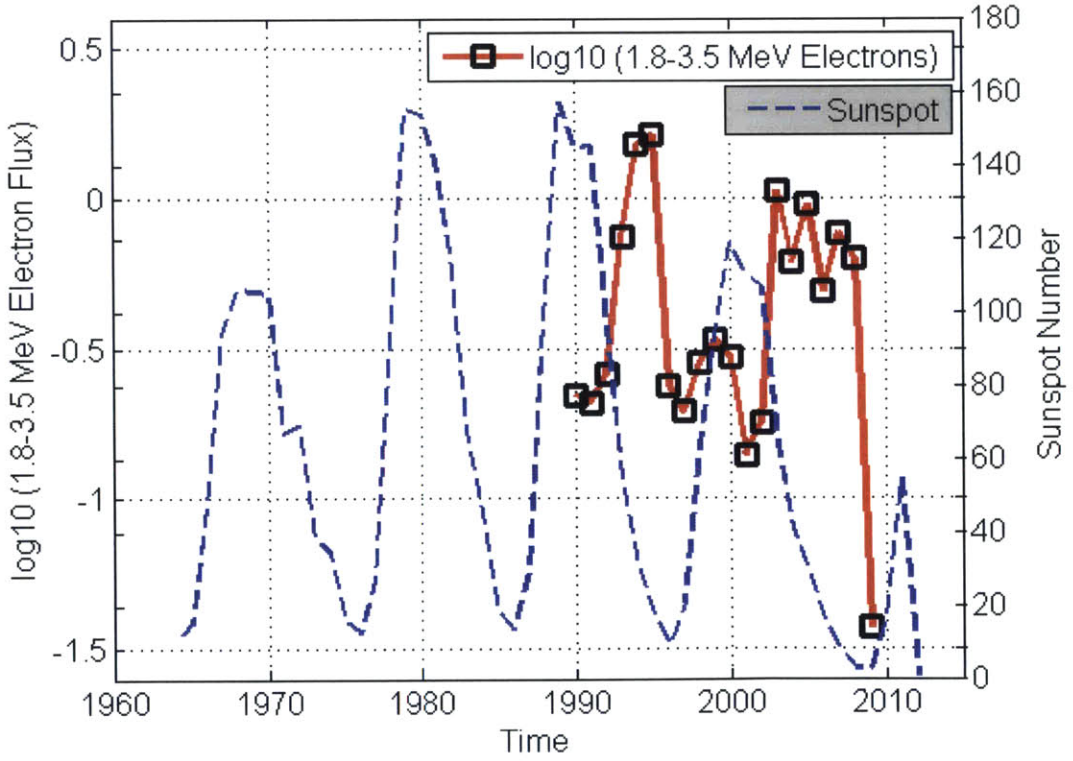
log10 (1.8-3.5 MeV Electrons)
Sunspot
log10 (1.8-3.5 MeV Electron Flux)
Sunspot Number
Time
0.5
0
-0.5
-1
-1.5
180
160
140
120
100
80
60
40
20
0
1960
1970
1980
1990
2000
2010

(e)

Figure 12(a-e). Annual mean values of the sunspot number (blue dashed curve) and annual median values of each dataset (solid red curve) for (a) *Kp* index, (b) *Dst* index, (c) *AE* index, (d) 10 MeV proton flux for Solar Cycles 20-23 (1964 - 2008), and (e) $\log_{10}$(1.8-3.5 MeV electron flux). Data is not available, and thus not included in the figure, for 1977 in 3(c) *AE* Index and before 1989 in 3(e) $\log_{10}$(1.8–3.5 MeV electron flux).

3.3.1.5 Annual Median High Energy Electrons

Figure 12(e) shows the solar cycle as well as the distribution of the annual medians of the LANL $\log_{10}$(1.8–3.5 MeV electron flux) data. This dataset starts at Solar Cycle 22 (1989 – 2009), and although it is much shorter in duration (20 years) than the others (49 years), it is clear that the maxima and minima of the $\log_{10}$(1.8–3.5 MeV electron flux) are slightly out of phase with the sunspot cycle, peaking during the declining phase of the solar cycle. High-energy electrons trapped in the outer belt are known to peak during the declining phase of the solar cycle, when high-speed solar wind streams from CIRs tend to occur [*Shea and Smart*, 1998; Miyoshi and Kataoka, 2008].

3.4 Solar cycle Phase Median Values of the Space Environment Metrics & Measurements for Solar Cycles 20-23

The 'phase' of the solar cycle in which that satellite anomalies occur is often mentioned in investigation reports (*e.g.,* anomaly X occurred at solar maximum). In this section, we discuss the median values of our space weather metrics and measurements for the four different phases of a solar cycle for each Solar Cycle, 20 through 23. The median values for each phase are tabulated in Tables 5, 6, 7, and 8 (for Cycle 20, 21, 22, and 23). Note that each of the four phases are not quite even periods of time per 11-year cycle, as shown in Table 4.

Figures 13(a) to 13(e) shows the median values per phase of the solar sunspot cycle (blue dashed curve), and the (a) *Kp* index, (b) *Dst* index, (c) *AE* index, (d) 10 MeV proton flux, and (e) $\log_{10}$(1.8–3.5 MeV electron flux) for Solar Cycle 20–23 (1964 to 2008). These median values per phase are taken over the periods defined in Table 4. Unfortunately, as with Figures 12(a) to 12(e), data is not available, and thus not included

in the figure, for 1977 in 13(c) *AE* Index and before 1989 in 13(e) $\log_{10}$(1.8–3.5 MeV electron flux).

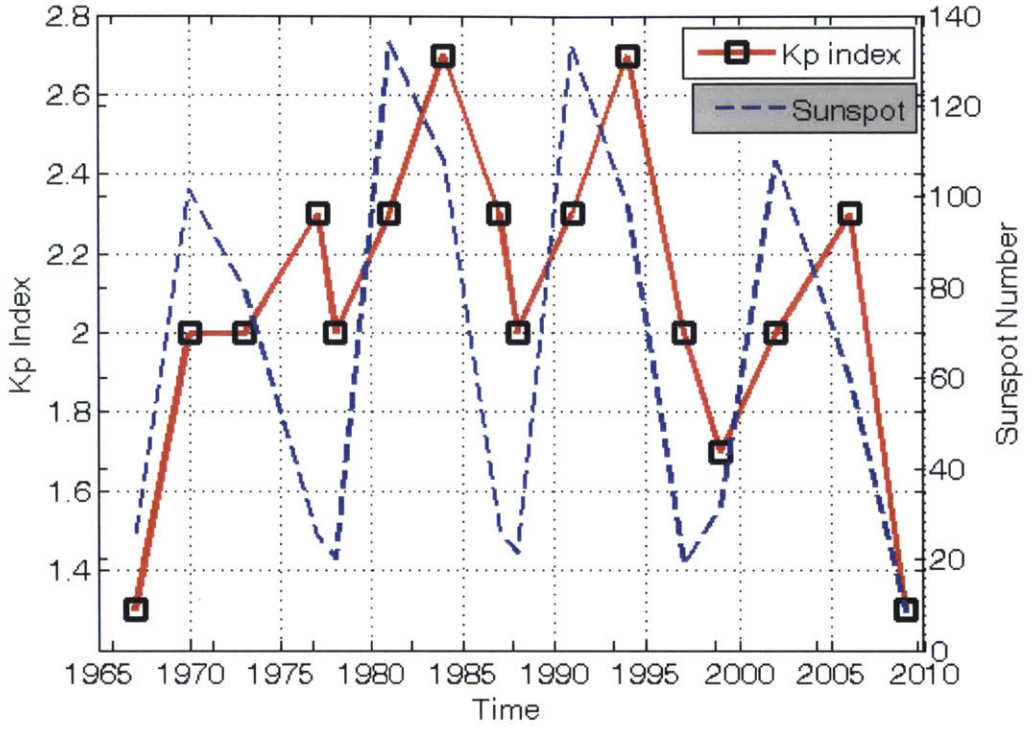

(a)

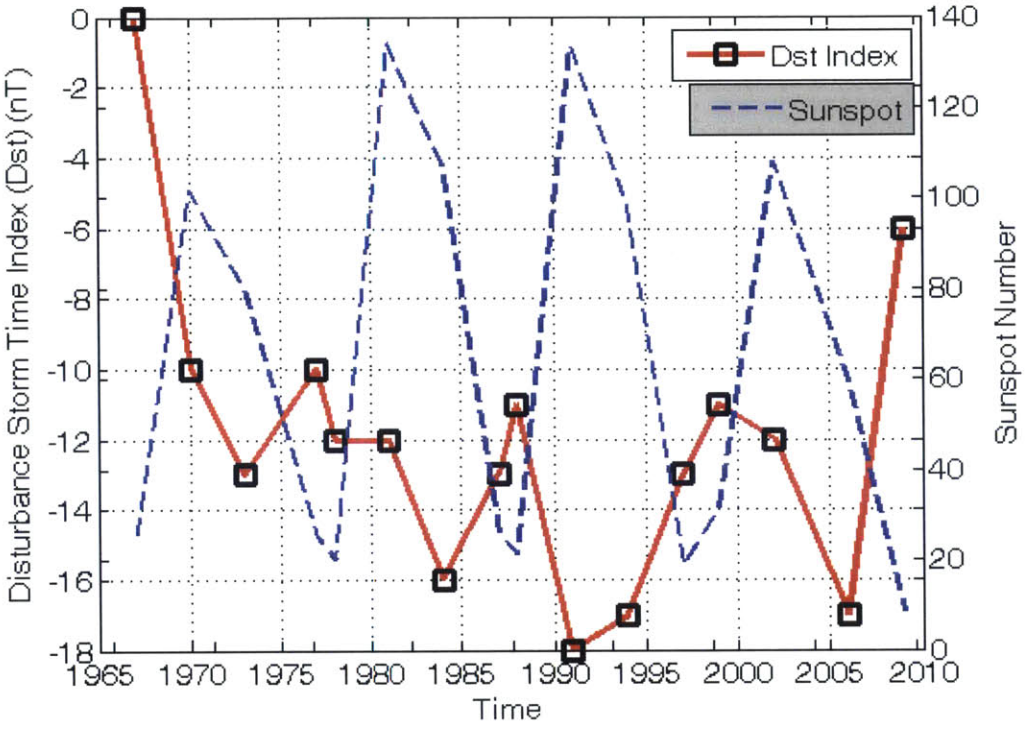
Dst Index
Sunspot
Disturbance Storm Time Index (Dst) (nT)
Sunspot Number
Time
0
-2
-4
-6
-8
-10
-12
-14
-16
-18
140
120
100
80
60
40
20
0
1965
1970
1975
1980
1985
1990
1995
2000
2005
2010

(b)

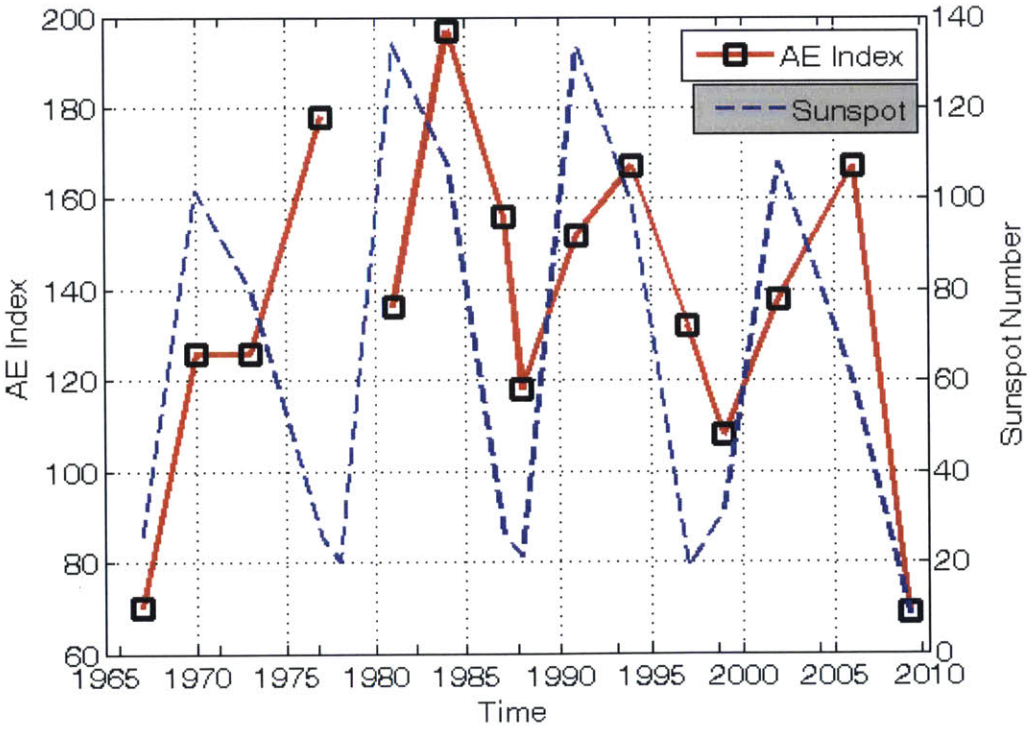
AE Index
Sunspot
AE Index
Sunspot Number
Time
200
180
160
140
120
100
80
60
140
120
100
80
60
40
20
0
1965
1970
1975
1980
1985
1990
1995
2000
2005
2010

(c)

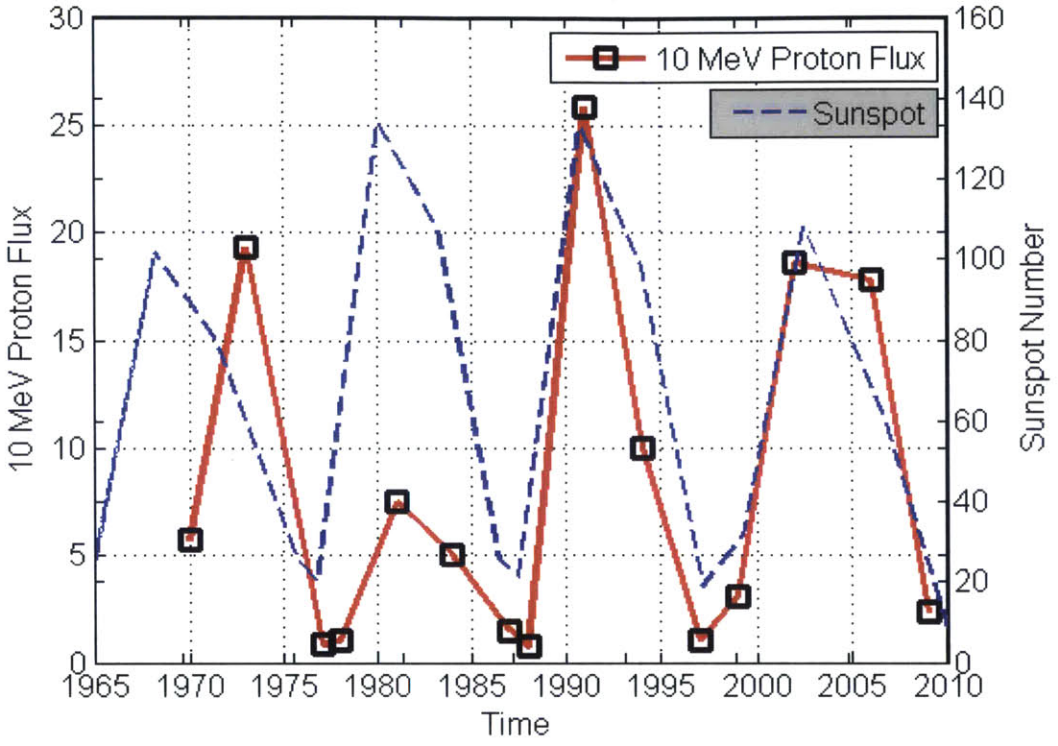
10 MeV Proton Flux
Sunspot
10 MeV Proton Flux
Sunspot Number
Time
30
25
20
15
10
5
0
160
140
120
100
80
60
40
20
0
1965
1970
1975
1980
1985
1990
1995
2000
2005
2010

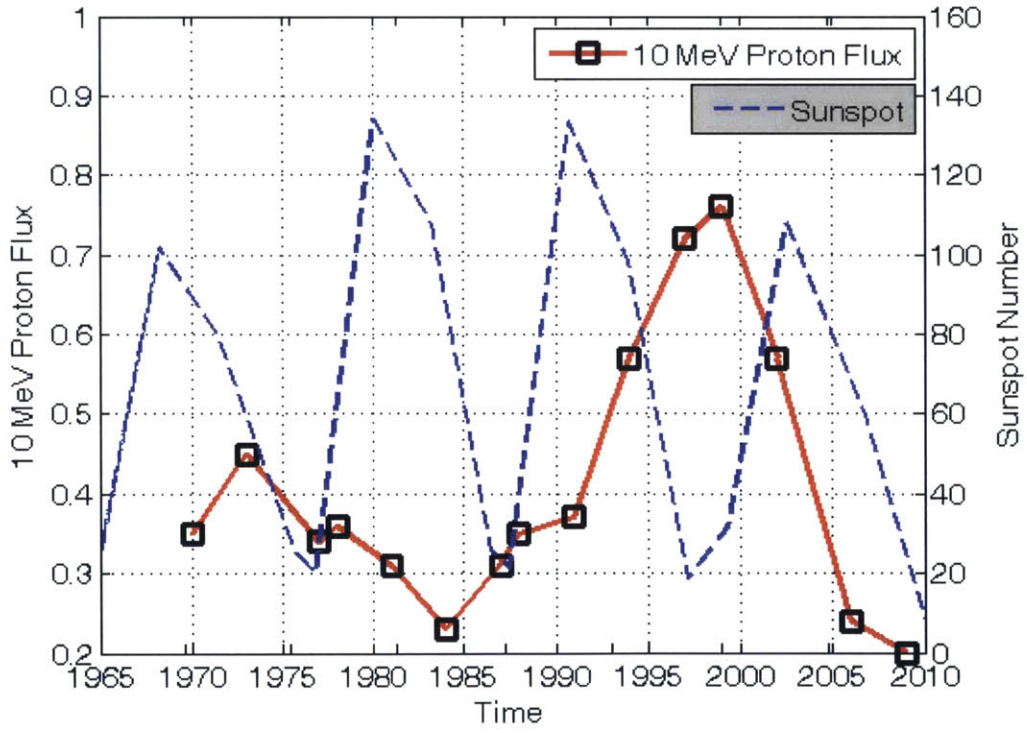
10 MeV Proton Flux
Sunspot
10 MeV Proton Flux
Sunspot Number
Time
1
0.9
0.8
0.7
0.6
0.5
0.4
0.3
0.2
160
140
120
100
80
60
40
20
0
1965
1970
1975
1980
1985
1990
1995
2000
2005
2010

(d)

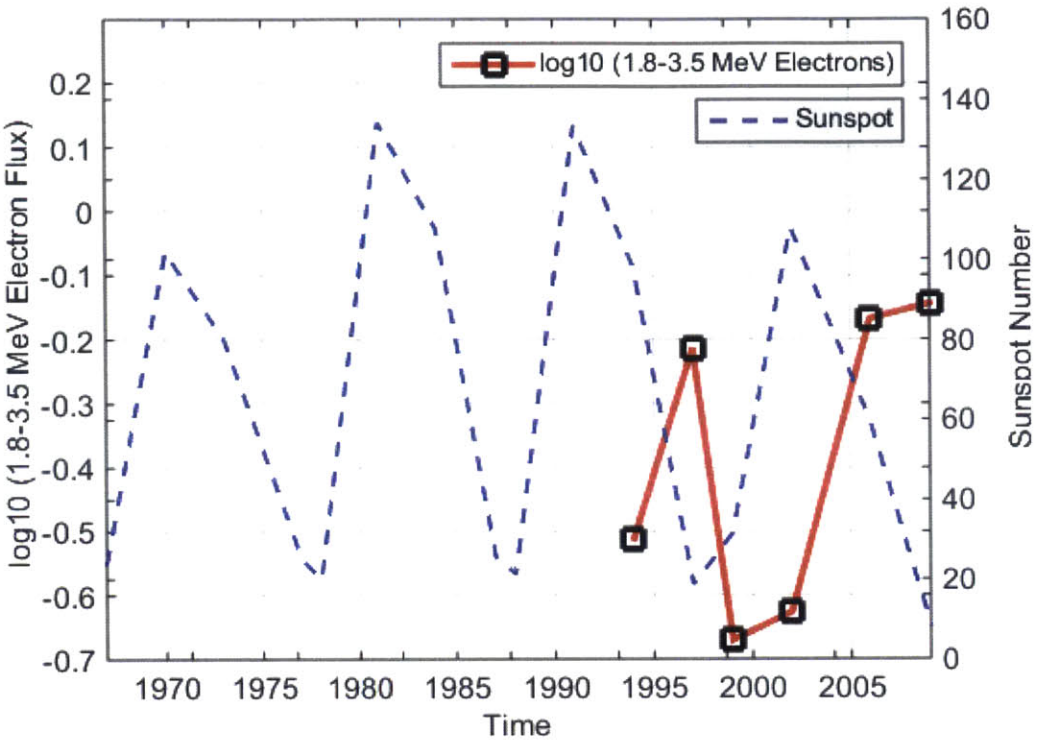

(e)

Figure 13(a-e). Mean values for the solar cycle (solid red curve), and (a) *Kp* index, (b) *Dst* index, (c) *AE* index, (d) 10 MeV proton flux for Solar Cycle 20–24 (1964–2008), and (e) $\log_{10}$(1.8–3.5 MeV electron flux). Data is not available, and thus not included in the figure, for 1977 in 13(c) *AE* Index and before 1989 in 3(e) $\log_{10}$(1.8–3.5 MeV electron flux).

3.5 Likelihood of Increased Activity in the Space Environment

Space weather forecasters analyze observational data and broadcast alerts to the space community, such as commercial satellite operators, of approaching storms or other potentially hazardous activity [*O'Brien et al.,* 2013]. While these space weather warnings are valuable, a more detailed understanding of the likelihood of hazardous space weather would aid the goal of a more causal and quantitative understanding of how the space environment relates to spacecraft anomalies. If a satellite operator systematically observes component anomalies occurring after increases in the space environment per some metric or measurement,

then the environment could be considered a contributing factor to degraded satellite performance and future mitigation may be possible.

Without concurrent in situ measurements of the space environment proximal to a component experiencing an anomaly, it is incredibly difficult to establish causality. Using large amounts of spacecraft housekeeping telemetry (ideally augmented in the future by proximal in-situ measurements) it may be possible to identify the space environment as a contributing factor by considering its effects on many similar components and platforms. To do this, we need to understand the environment both at disturbed and quiet activity levels, as well as the likelihood of increased activity as a function of time (*e.g.* the solar cycle).

In addition to understanding space weather variability over a year, we are also interested in its variability over shorter periods of time. For example, this is useful for considering the possibility of internal charging as a cause (and assessing how long it would take for a component to charge to a level at which damage is sustained).

The period of time over which the impacts of the space environment could affect satellite performance or lead to a component anomaly is not well understood. We consider several time intervals (3 days, 14 days, and 30 days) to investigate near-daily, biweekly and monthly variability of the environment throughout each phase of Solar Cycles 20-23. As shown in Table 4, each phase is between 1-3 years (12-36 months). It is better to use space environment metrics and measurements over shorter time spans as a baseline reference (e.g. annual median or solar cycle phase) than longer time spans (e.g. decades or the duration of the measurement record, 1963 to 2012), as the resulting baselines significantly differ, in some cases by as much as 50%, which affects the interpretation of the space environment.

To understand the likelihood of increased space weather activity we calculate the probability that increased activity, which we define as >2 MADs of the median of a given space weather metric, occurs within a certain period of time (3 days, 14 days, and 30 days) of the first day of each month in each phase of Solar Cycles 20–23. The probability was calculated by dividing the total number of observations recorded above

2 MADs of the median before a period of 3-, 14- or 30-days of the first day of each month in the phase by the total number of months in the phase. The choice of the first day of the month serves as a uniformly random selected day.

The values for both the medians and the MADs are tabulated for the different phases of the solar cycle in Tables 5 to 8. Figures 14(a), 14(b), 14(c), 14(d), and 14(e) show the probability of increased space weather for the *Kp*, *Dst*, *AE* metrics and measurements of protons and electrons for Solar Cycle 20, 21, 22, and 23 over periods of three days (red), 14 days (green), and 30 days (black). When the green line does not appear, as is the case in the 10 MeV proton plot, it is because the green line is equal to the red line, and the red line is plotted over the green line. Probabilities are expected to be higher for the 30-day periods, compared to the 3-day and 14-day periods because the duration of time is longest and there is therefore more time for the observations to exceed 2 MAD.

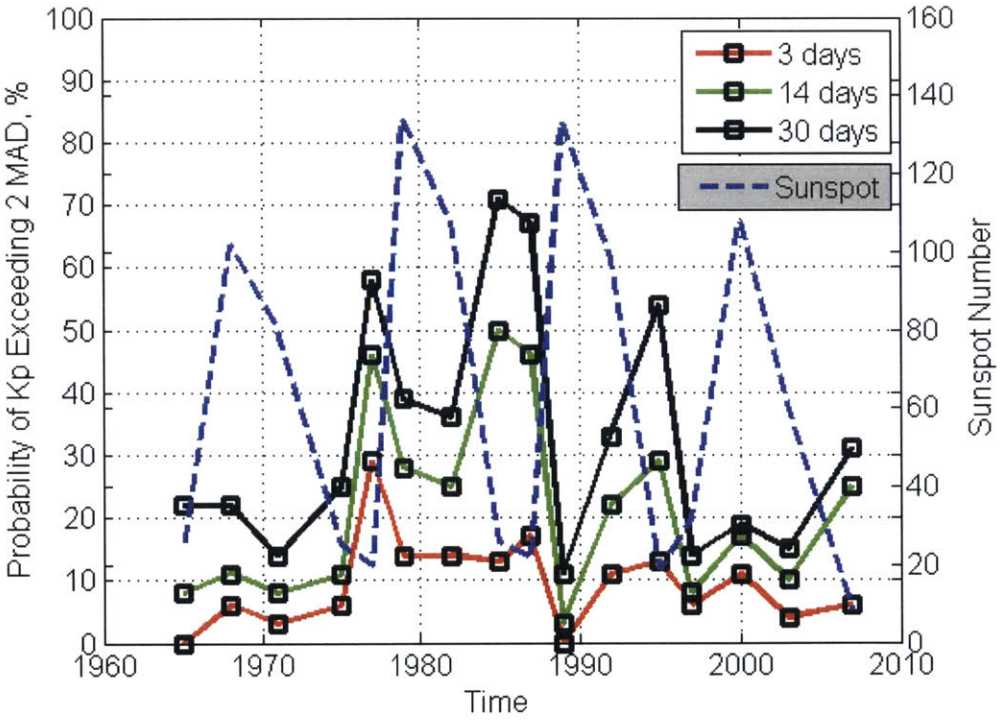

(a)

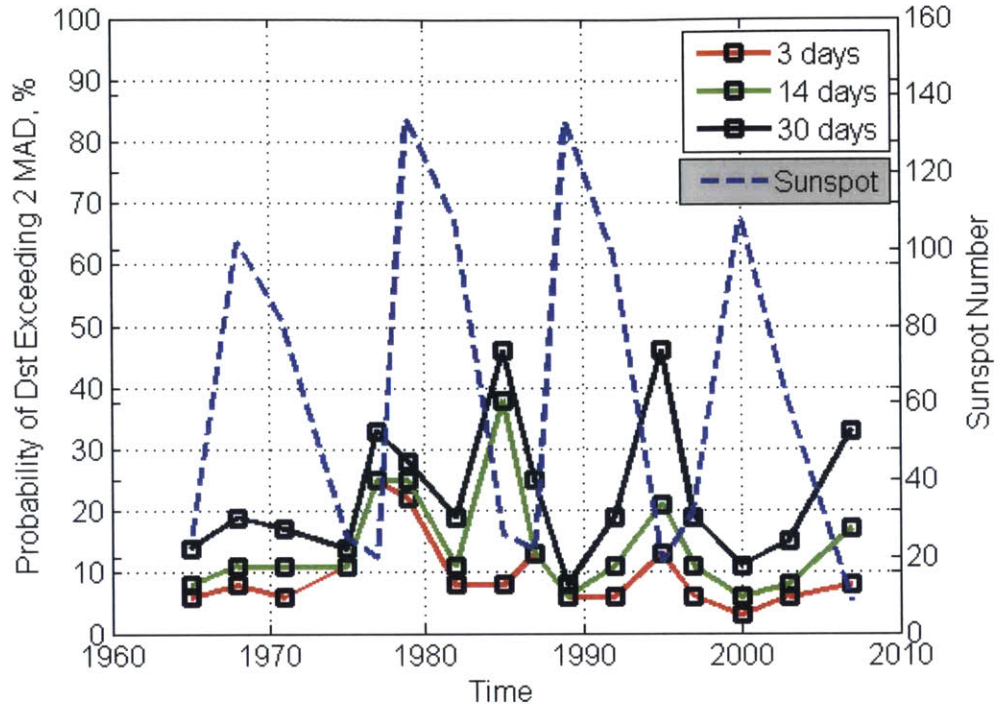
3 days
14 days
30 days
Sunspot
Probability of Dst Exceeding 2 MAD, %
Sunspot Number
Time
0
10
20
30
40
50
60
70
80
90
100
120
140
160
1960
1970
1980
1990
2000
2010

(b)

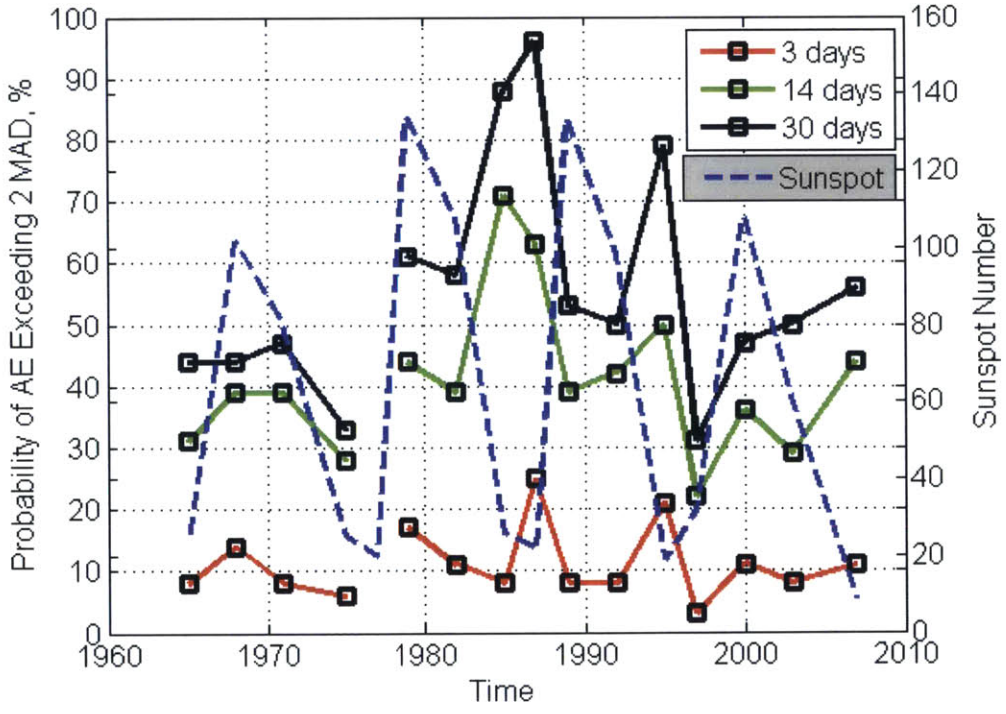
3 days
14 days
30 days
Sunspot
Probability of AE Exceeding 2 MAD, %
Sunspot Number
Time
0
10
20
30
40
50
60
70
80
90
100
120
140
160
1960
1970
1980
1990
2000
2010

(c)

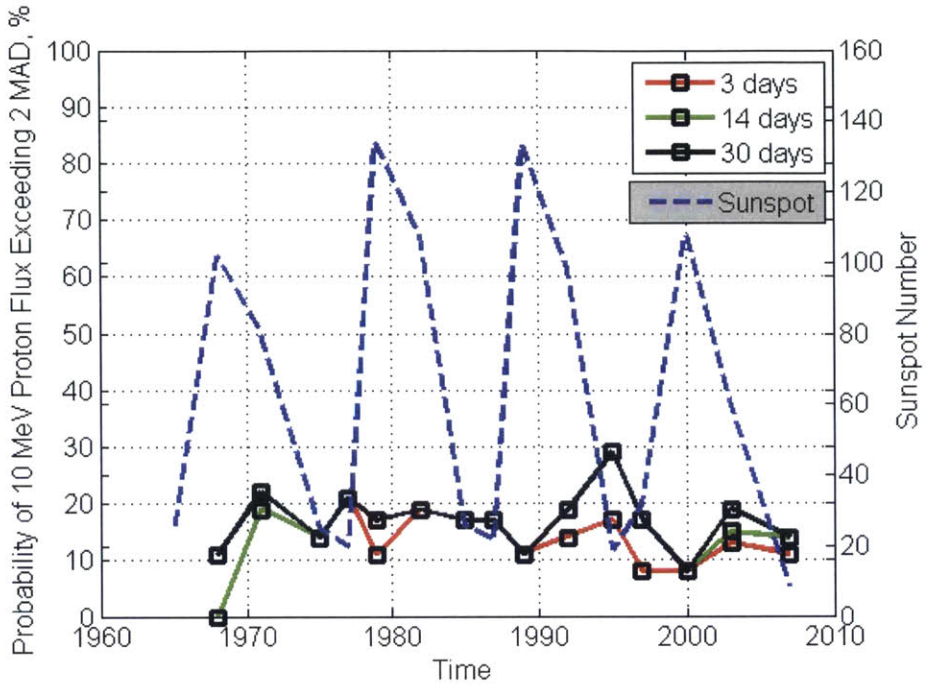

(d)

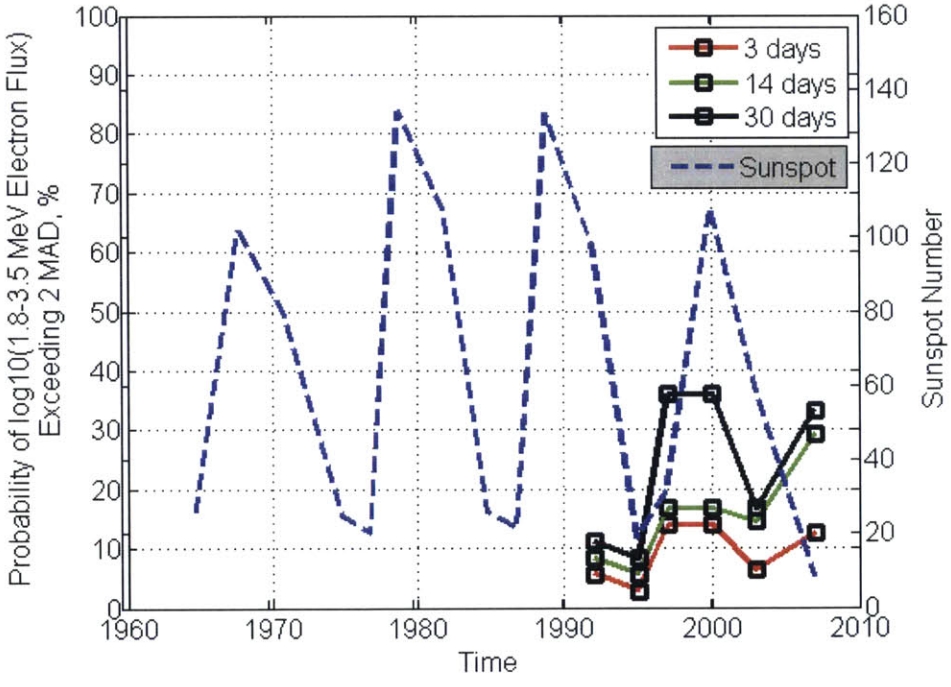

(e)

Figure 14(a-e). The probability (%) that (a) *Kp* index, (b) *Dst* index, (c) *AE* index, (d) 10 MeV proton flux, and (e) $\log_{10}$(1.8–3.5 MeV electron flux) exceeds greater than 2 MAD of the median for 3-day (red), 14-day

(green) and 30-day (black) intervals before the first day of a given month for each of the respective (a–e) space weather metrics for Solar Cycle 20–23. Data is not available, and thus not included in the figure, for 1977 in 14(c) *AE* Index and before 1989 in 14(e) $\log_{10}$(1.8–3.5 MeV electron flux).

3.5.1 Likelihood of Increased *Kp* Index over short time intervals

Figure 14(a) shows the probability (%) that the *Kp* index exceeds 2 MAD above the median *Kp* values for the respective phases of Solar Cycles 20–23. For these four solar cycles, the highest probability for increases in the *Kp* index above 2 MAD does not consistently occur for the same phase although they tend to happen in the declining and minimum phases of the solar cycle.

The highest probability of *Kp* exceeding 2 MAD above the median *Kp* index for a 3-day interval in Solar Cycle 20 occurred during both the solar minimum phase and solar maximum phase with a probability of 6%. For the 14-day interval before the first day of the month, the highest probability was 11% also during solar minimum and maximum phases. For the 30-day interval before the first day of the month, the highest probability was 25% during solar maximum.

Along the same lines, the highest probability of *Kp* exceeding 2 MAD above the median *Kp* for Solar Cycle 21 for the 3-day interval was 29% during the ascending phase, for the 14-day interval it was 50% during solar minimum, and for the 30-day interval it was 71% during solar minimum. These values are much higher for Solar Cycle 21 than they were for Solar Cycle 20.

The overall maximum probability of increased *Kp* occurred in the ascending phase of Solar Cycle 22, with a likelihood of 46%, and 67% for the 14- and 30-day periods before the first day of the month, nearly three times that of Solar Cycle 20.

Solar Cycle 23 had the highest probability of *Kp* exceeding 2 MAD above the median *Kp* index for the 3-day interval at 11% during solar maximum. For the 14-day interval the highest probability was during

solar minimum at 25%, and for the 30-day interval the highest probability was 31% also at solar minimum.

For the *Kp* index, across Solar Cycles 20 – 23, the declining and minimum phase of the solar cycles were the phases in which the highest probability of *Kp* exceeding 2 MAD occurred.

3.5.2 Likelihood of Increased *Dst* Index across short time intervals

Figure 14(b) shows the likelihood of increased *Dst* measurements for 3 day, 14 day, and 30 day time intervals before the first day of the month along with the sunspot number. The maximum probability of *Dst* measuring greater than 2 MAD above the median *Dst* for a given phase consistently occurred during the solar minimum phase for all four solar cycles. For the 30-day time interval before the first day of the months in Solar Cycle 21 and 22, the probability reached as high as 46%

If we were determining the maximum likelihood of severe *Dst* we would expect this to occur at solar maximum, when the most negative and most extreme *Dst* measurements are typically recorded. In this analysis, we are not determining when the most severe observations occur, but when notable variability in observations is most likely. As tabulated in Tables 3 through 6, the median *Dst* for solar minimum and solar maximum are within 10 nT of each other for all four cycles. In Solar Cycle 21, the median *Dst* for the solar maximum and solar minimum phase were even closer, within 1 nT of each other.

3.5.3 Likelihood of Increased *AE* over short time intervals

The maximum likelihood of increased *AE* measurements did not consistently occur during the same phase of each solar cycle, rather it occurred in a different phase for each of the solar cycles. This is most likely due to the short-term variability of the *AE* metric. This may be explained because the *AE* index measures the convection in the space environment which brings in low-energy electrons.

In Solar Cycle 20, the maximum probability (14%) occurred during solar maximum for the 3-day interval and in the declining phase for the 30-

day interval (48%) before the first day of the month. The maximum probability for the 14-day interval (39%) the same for both the maximum and declining phases. Data for the year 1977 were not available, so there is a gap in the analysis in Solar Cycle 21. In the remaining phases of Solar Cycle 21, the maximum probability of increased *AE* occurred during solar maximum for 3-day intervals (18%) and solar minimum for 14-day (71%) and 30-day (88%) intervals before the first day of a given month. In Solar Cycle 22, the maximum likelihood of increased *AE* occurred during the ascending phase of the solar cycle for all intervals, and peaked at 96% for the 30 day interval. For Solar Cycle 23, the highest probability (79%) for 30-day interval of increased *AE* activity occurred during solar minimum.

3.5.4 Likelihood of Increased 10 MeV Proton Flux Over Short Intervals

Figures 14(d) shows the probability of increased 10 MeV proton flux. The probabilities for increased 10 MeV proton flux never exceed 30% for all time periods throughout the four solar cycles. The maximum probability of increased proton flux never occurred at solar maximum, but did occur in all other phases of the solar cycle. For Solar Cycle 20 the maximum probability (22% for the 30-day period) occurred during the declining phase. Solar Cycle 21 experienced a maximum probability of 21% across all time intervals (3 days, 14 days, and 30 days before the first day of the month) during the ascending phase of the cycle. The maximum probability for Solar Cycle 22 (29% for the 30-day period) occurred during solar minimum. The maximum probability of proton flux greater than 2 MADs above the median for Solar Cycle 23 (19%) occurred during the declining phase of the solar cycle.

It is important to remember that the probabilities specified here are not metrics of severe activity, but are rather measurements for the likelihood of variability during a given period of time. For example, high energy protons are known to peak during solar maximum, as was shown in Figure 12(d) and 13(d). Therefore, if the probabilities shown in Figure 14(a-e) were detecting the likelihood of severe activity the probabilities would peak at solar maximum. However, the likelihood of increased high-energy proton flux greater than 2 MAD above the median value never occurred during solar maximum throughout the four solar cycles analyzed. What is important to assess in combination with the

likelihood for increased observations is the median value of the observation itself. If that value is high and the likelihood of increased observations greater than 2 MAD above the median is also high, there can be large impacts on component performance.

3.5.5 Likelihood of increased $\log_{10}$(1.8-3.5 MeV Electron Flux) Over Short Intervals

Shown in Figures 14, we only have electron flux data for 1.5 solar cycles, instead of four complete solar cycles for the indices and proton measurements shown in Figures 14(a) to 14(d). Figure 14(e) shows the distribution of the probability of experiencing increased $\log_{10}$(1.8–3.5 MeV electron flux) for phases of Solar Cycles 22 and 23, from 1989 to 2009. In Solar Cycle 22, probabilities were only calculated for the declining and minimum phases. The 30-day interval highest probability of exceeding 2 MAD of median was 11% and occurred during the declining phase. The probability of increased activity was as low as 5% for the 3-day time interval before the first day of each month. Interestingly, the minimum probability of increased $\log_{10}$(1.8–3.5 MeV electron flux) during Solar Cycle 23 occurred in the declining phase of the solar cycle, suggesting the electrons flux during that phase was high with little variability [*Li et al.*, 2005; *Miyoshi and Kataoka*, 2008]. The probability was 36% for a 30-day interval before the first day of each month in both the ascending and maximum phase of Cycle 23.

3.6 Summary and Discussion of Space Environment Baseline

We analyzed space weather metrics and in situ measurements [*Kp*, *AE*, *Dst*, 10 MeV Proton flux and $\log_{10}$(1.8–3.5 MeV electron flux)] for Solar Cycles 20–23 (1964 to 2008). These data provide a reference for understanding how space weather activity changes annually, throughout the four phases of the solar cycle (maximum, descending, minimum, ascending), and over shorter time intervals. Table 10 summarizes the findings and shows the median likelihood of the five observations across a particular solar cycle phase (ascending (Asc.), maximum (Max.), descending, (Dec.), and minimum (Min.)) and time period (3-, 14- and 30-day)

Table 10. Summary of Likelihood of Increased Observations greater than 2 MAD above the median of each observation

Phase & Time Period	*Kp* Index	*Dst* Index	*AE* Index	10 MeV Protons	$\log_{10}$(1.8–3.5 MeV electron flux)
Asc. 3-day	0.13	0.13	0.12	0.15	0.14
Asc. 14-day	0.27	0.14	0.39	0.18	0.17
Asc. 30-day	0.40	0.23	0.57	0.18	0.36
Max. 3-day	0.08	0.10	0.13	0.08	0.14
Max. 14-day	0.15	0.12	0.40	0.09	0.17
Max. 30-day	0.23	0.17	0.51	0.12	0.36
Dec. 3-day	0.08	0.07	0.09	0.16	0.06
Dec. 14-day	0.16	0.10	0.37	0.18	0.11
Dec. 30-day	0.25	0.18	0.51	0.20	0.14
Min. 3-day	0.09	0.1	0.12	0.15	0.08
Min. 14-day	0.29	0.22	0.48	0.19	0.17
Min. 30-day	0.45	0.35	0.64	0.19	0.21

For years 1963 to 2012, the median values of the space weather metrics and measurements over the nearly 50 years analyzed versus the medians over the individual phases of the four solar cycles between 1963 to 2012 differ by more than 28% for the *Kp* index, 37% for the *AE* Index, 84% for the *Dst* Index, and 200% for both the 10 MeV proton flux and $\log_{10}$(1.8–3.5 MeV electron flux) measurements. Therefore, to limit excessive error, it is important when describing median behavior of space environment observations that the median is assessed over as short of period as relevantly possible. For this study, that period is a given solar cycle phase.

One of the desired applications for this analysis and these space weather data are to understand whether a particular anomaly has been preceded by an anomalous increase in particle fluxes or space environment conditions. Such analysis is complicated by the fact that sudden or short-term increases preceding a particular anomaly may be simply a result of a coincidence. To try to understand whether an increase occurred and

assess whether this occurrence could be related to any observed anomalies, it is important to understand probability of such an increase to occur for a random day as a basis for comparison. In this study, we chose the first of each month as a random day and calculated these probabilities. We used the MAD for the space weather metrics and measurements, and defined increased space weather activity as greater than 2 MADs above the median activity for the particular phase of the solar cycle. Using the calculated MADs we found the probability that increased metrics or measurements occur within 3-, 14- and 30 days before the first day of each month in any particular solar cycle phase.

3.6.1 *Kp* Index Summary

Of the metrics and in situ measurements we identified that increases in *Kp* typically occur in the declining phase of the solar cycle, when the median *Kp* generally reaches a maximum. The declining phase is known to be potentially dangerous for satellite operations as geomagnetic activity is most active during this phase [*Miyoshi and Kataoka*, 2008]. The *Kp* metric is often used to augment understanding of the space weather environment with other metrics and in situ measurements.

3.6.2 *Dst* Index Summary

The *Dst* index is used to measure the severity of geomagnetic storms, which are most common during solar maximum. We find that the maximum likelihood of increased *Dst* before the first day of a given month always occurs during solar minimum. Again, the maximum likelihood of increased *Dst* does not match with the occurrence of highly-negative *Dst*, or the most severe geomagnetic storm, but when variability, defined as increases greater than 2 MAD is most likely to occur.

3.6.3 *AE* Index Summary

With respect to satellite anomalies, *AE* shows the conductivity of the space environment, which can be used as a proxy for low-energy electrons in LEO altitudes (less than approximately 600 km) that could potentially contribute to surface-charging related anomalies or ESD

arcs on solar cells. The *AE* index is not a primary index used for geostationary satellites. The maximum probability of increased *AE* does not occur consistently in a particular phase, but did reach the highest probability, 96%, during the ascending phase of Solar Cycle 22 (years 1986 – 1996). The fact that the maximum probability of increased *AE* occurred in a different phase for each of the solar cycles is most likely due to the sporadic, variable nature of the metric.

3.6.4 10 MeV Proton Summary

The median 10 MeV proton flux behavior was consistently low throughout the cycles, ranging from 0.735 to 25.849 pfu. Flux values of this level (~10 pfu) are considered the lowest class, S1, for which NOAA broadcasts warnings. High-energy protons are known to peak at solar maximum, and are notoriously known to cause solar cell degradation and single event effects. The probabilities for 10 MeV proton flux increasing above 2 MAD never exceed 30% for all time periods (3 days, 14 days and 30 days) throughout all four solar cycles, and maximum probability of proton flux above 2 MAD never occurred in the solar maximum phase, but did occur in all other phases of the solar cycle. While this may seem contradictory, it simply means that fluxes are steadier during times when fluxes are elevated.

3.6.5 High Energy Electron Summary

The median annual flux and median phase electron flux, shown in the Figures 12(e) and 13(e), respectively, reach maximum flux during the declining phase of the Solar Cycle, which is known as the phase when elevated high-energy electrons in the outer radiation belts occur [*Li et al.*, 2005; *Miyoshi and Kataoka*, 2008]. The declining phase is considered particularly hazardous for satellite operations with respect to high-energy electron induced internal charging of dielectric components. The $\log_{10}$(1.8–3.5 MeV electron flux) data is only present for 1.5 solar cycles (half of Cycle 23 and all of Solar Cycle 24), yet we find that the likelihood of increased $\log_{10}$(1.8–3.5 MeV electron flux) occurs in the declining phase of Cycle 22 and the minimum phase of Cycle 23.

3.6.6 Chapter 3 Closing Remarks

The approach and results of this chapter provide resources for the satellite operator and engineering community for understanding how space weather activity changes over different time intervals, including annually, over phases of the solar cycle, and over short time intervals lasting days to weeks in duration. The probability that the environmental observations are elevated over short time intervals, compared with normal activity, was also quantified. Understanding whether observed variation in a given metric or in-situ measurement is typical or not is useful for satellite operators responsible for monitoring the performance and component health of spacecraft throughout the duration of the mission (e.g., launch and maneuvers). For the purpose of our research, this analysis also helps us to determine the contribution of the environment for satellite component anomalies.

Solar cells are an example of a particular component that are known to degrade due to the space environment. Solar cells are particularly important to satellite operators and designers, because they are the primary power source for the satellite and the components working to ensure the mission will operate with sufficient power throughout the entire lifetime. Unfortunately, solar cells can be damaged by energetic protons and electrons like the 10 MeV protons and the $\log_{10}$(1.8–3.5 MeV electron) that are used for in-situ measurement data in this chapter. Chapter 5 contains detailed analysis of solar cell degradation onboard eleven GEO satellite launched, operated by Inmarsat, Telenor, and ARABSat. The following chapter, Chapter 4, details the approach used and provides background information on the physical mechanisms of solar cell degradation, models used for predicting solar cell degradation, and the data acquired for the analysis presented in Chapter 5.

Chapter 4. On-Orbit Solar Cell Degradation: Approach

Solar cells have been used as a primary power source for satellites since the launch of the Vanguard I in 1958 [*Walker and Statler*, 1988; *Bailey and Raffaelle*, 2003]. Today, satellites, including geostationary communications satellites, generate kilowatts (kW) of power with solar cells and must incorporate systems designed to allow normal operations through end of life (EOL) of 10-15 year long missions.

In this chapter, we describe space-based photovoltaic power systems, the methods for monitoring solar cell degradation, and effect of radiation on solar cells. We present the current methods for modeling solar cell degradation over mission lifetimes, and describe our approach to using on-orbit data to compare with these models. The chapter ends with a description of the plan for analysis of solar cell degradation using on-orbit telemetry and space environment data. The analysis and its results are presented in Chapter 5.

4.1 Space-based Photovoltaic Power Systems

Space-based photovoltaic power systems consist of photovoltaic panels that generate power to a load. Solar panels consist of parallel strings of cells, and each of these strings has multiple cells in series [*Taherbaneh et al.,* 2011]. Solar cells are semiconductor devices that convert solar light energy into direct electric current [*Ibrahim et al.,* 2011]. Incoming photons generate minority carriers on the front surface of the cell that diffuse into the cell junction to produce photocurrent output. In space, these systems are constantly exposed to radiation, which causes defects that prevent the carriers from reaching the cell junction and decrease the generated current [*Tauke et al.,* 1967; *Hacke et al.,* 1994; *de Angelis et al.*, 2001].

Due to their function, solar cells are one of the least shielded satellite components [*O'Brien*, 2009]. A thin transparent coverglass is used to shield the front surface of the cell and the cell substrate material and the panel structure are used to shield the back surface. The coverglass is coated with antireflection and conductive coatings, and bonded to the solar cell using a form of transparent adhesive [*Messenger et al.*, 2011]. Low-energy protons and electrons are absorbed in the coverglass because the glass causes the incident particles to slow down, preventing

the particles from reaching the active volume of the cell and causing degradation [*Bailey and Raffaelle,* 2003].

The thickness of the coverglass is one of the most important parameters in designing missions for EOL power requirements. Coverglass thickness of ~3 mils has the capacity to stop all incident protons of energies less than ~2.8 MeV and electrons with energies less than ~200 keV [*Messenger et al.,* 2010]. For GEO missions, the coverglass thickness is generally between 3 to 6 mils (75 and 150 microns) [*Messenger et al,* 2006]. At least three of the satellites analyzed in this work use a coverglass of 100 microns in thickness (the equivalent of 3.94 mils of Al).

The actual solar cells also vary in thickness. Silicon cell thicknesses are often on the order of 100 microns, while GaAs cell thicknesses are on the order of a few microns. Protons with energy as low as 0.3 MeV can penetrate into greater than 1 micron of the solar cell, and in doing so transfer energy into the active area of the cell [*Messenger et al.,* 2001]. In comparison, 10 MeV protons can penetrate more than 400 and 700 microns into GaAs and silicon cells, respectively, and travel directly through the active region of the cell with little deceleration [*Rong et al.,* 2003; *Alurralde et al.,* 2004].

4.2 Solar Cell Performance Parameters

The main solar cell parameters used to monitor cell performance and indicate the occurrence of degradation are the short circuit current (I_{sc}), open circuit voltage (V_{oc}) and maximum power (P_{max}) [*Rauschenbach,* 1980]. Solar cell efficiency is a parameter used to characterize the ability of the cell to convert incoming photons into electricity, but is not used to monitor solar cell performance once the cells are operational.

I_{sc} is the current through the cell when the load resistance, or voltage, across the cell is zero or when the cell is short-circuited. I_{sc} is the largest current that can be drawn from the cell, and is produced from the collection of light-generated carriers in the cell structure [*Ibrahim et al.,* 2011]. For GaAs-based triple junction solar cells grown monolithically, the I_{sc} is the lowest current output of the three subjunctions in the cell

stack, because the sub-cells are connected in series in a monolithic growth [*Sumita et al.,* 2003].

V_{oc} is the voltage produced by the cell for infinite load resistance or zero current [*Walker and Statler,* 1988]. V_{oc} corresponds to the sum of the voltages generated at each cell for a series connected device, and is directly influenced by any damage on each subcell [*Sumita et al.,* 2003]. V_{oc} is also the most sensitive parameter to cell temperature [*Walker and Statler,* 1988; *Ibrahim et al.,* 2011]. For analysis of V_{oc} one should isolate the impacts of the cell temperature from the degradation of the cell. P_{max} is the point on the current-voltage (I-V) curve when the product of the current and voltage is maximized [*Walker and Statler,* 1988]. The I-V curve is shown in the Figure 15, with the values of I_{sc}, V_{oc}, and P_{max} designated.

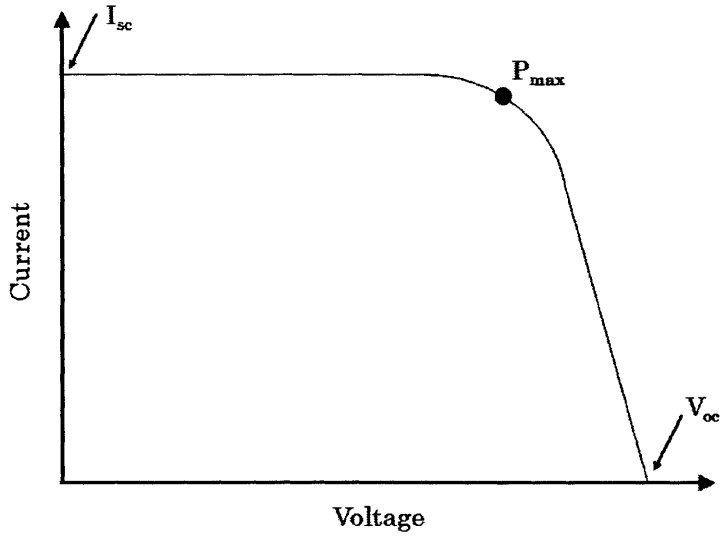

Figure 15. The I-V Curve

The degradation rates of I_{sc}, and V_{oc} depend on the type of cell material and device structure [*Walters et al.,* 1996; *Alurralde et al.,* 2004]. As fluence increases, the observed degradation in *Isc,* V_{oc}, and P_{max} increases, but a decrease in degradation occurs with increasing proton energy after a cell-specific proton energy for the same fluence [*Rong et al.,* 2003]. This is because the thickness of the cell plays a role. Protons at energies that are high enough to pass through the solar cell, instead of become trapped in it, result in a decrease in degradation that

ultimately depends on whether the high-energy particle has sufficient energy to transverse through the cell completely without depositing energy in the active region of the solar cell. These parameters, I_{sc}, V_{oc} and P_{max}, are monitored carefully through satellite telemetry, especially in GEO communications satellites to ensure the payload will have enough power at end of life (EOL).

4.3 The Effects of Radiation on Solar Cells

Silicon (Si) and gallium arsenide (GaAs) are two semiconductor materials commonly used in solar cells for satellite applications. In previous decades, silicon cells were the state of the art solar cell for space. Today, Si cells are still operating onboard numerous satellites, including GEO COMSATs, but GaAs cells, first launched in 1996 on COMSAT PAS-5, are now the most advanced cells in flight [*Oldenwald and Green,* 2007]. Both cell types experience degradation due to radiation in the space environment.

Over the past fifty years, significant progress has been made in advancing the overall cell efficiency and radiation resistivity through the use of ground based radiation damage experiments [*Tauke et al.,* 1967; *Bielle-Daspet, et al.,* 1980; *Walker and Statler*, 1988; *Walters et al.,* 1998; *Hismatsu et al.*, 1998; *de Angelis et al.,* 2001; *Rong et al.*, 2003; *Sumita et al.,* 2003; *Alurralde et al.*, 2004]. As demand for power increases at GEO, GaAs cells are increasingly used because of their high efficiency and radiation tolerance [*Hacke et al.*, 1994; *Fatemi et al.,* 2000; *Rong et al.,* 2003; *Laiadi et al.*, 2013].

As charged particles in the space environment traverse material, they lose energy through both ionizing and non-ionizing means. For solar cells, the primary energy loss mechanism is through non-ionizing effects that lead to the displacement of atoms in the semiconductor lattice. The displacement of atoms results in lattice defects such as vacancies, interstitials (displaced atoms moving to non-lattice positions) and the formation of defect energy levels in the semiconductor material [*Weinberg*, 1991; *Sumita et al.,* 2003]. These defects produce carrier-trapping centers (e.g. recombination centers and compensation centers) in the semiconductor bandgap, as well as generate carriers. Carrier

generation leads to an increases in the forward bias dark I-V curve and degrades V_{oc}. [*Walters et al.,* 2005].

Recombination centers reduce minority carrier diffusion length, or minority carrier lifetime, and decrease the photovoltaic output of the cell [*Srour and McGarrity,* 1988]. For GaAs and Si cells, radiation-induced recombination centers serve as the primary mechanism for cell performance degradation. The decrease in the minority carrier diffusion length degrades I_{sc}, and leads to an increased forward biased dark I-V curve, which also degrades V_{oc} [*Walters et al.,* 2005]. In order to generate photocurrent output, charge carriers must diffuse to the junction before recombination occurs [*Hacke et al.*, 1994; *Yamaguchi,* 2001]. Degradation of the minority carrier diffusion length reduces the cell's efficiency [*Walters et al.,* 2005]. For GaAs solar cells, the average diffusion length of the photo-generated carrier is large in comparison to the junction distance; for silicon cells, the average diffusion length is comparable to the thickness of the photo-carrier generating region. Thus, the decrease in diffusion length of carriers in silicon corresponds to a decrease in efficiency, whereas for GaAs solar cells, carrier diffusion length degradation contributes to a smaller decrease in efficiency [*Hacke et al.*, 1994]. A schematic of a Si cell and a GaAs cell are shown in Figure 16 (a,b) below.

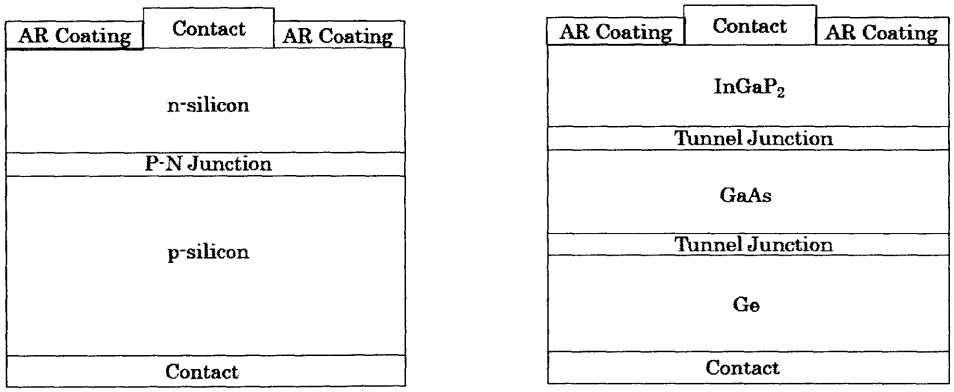

Figure 16 (a,b). Schematic diagram of (a) Si solar cell structure and (b) multijunction GaAs solar cell structure. Solar illumination penetrates the top of the structure, AR coating designates anti-reflective coating. Tunnel junctions are required to maintain device polarity. The images are not to scale.

Compensation centers remove majority carriers, which change the structure of the pn junction eventually leading to type conversion [*Walters et al.,* 2000]. Similar to the Bragg's peak in ionization, a displacement damage peak exists for a specific range of incident proton energies. Significant damage in the active region of the cell occurs when the displacement damage peak occurs in the active region of the cell [*Messenger et al.,* 2006]. For GaAs cells, protons of 300 keV penetrate into the junction region and produce damage in the critically sensitive photo generation region of the cell [*Anspaugh,* 1996]. Figure 17 provides a schematic of a solar cell, which consists of a pn junction.

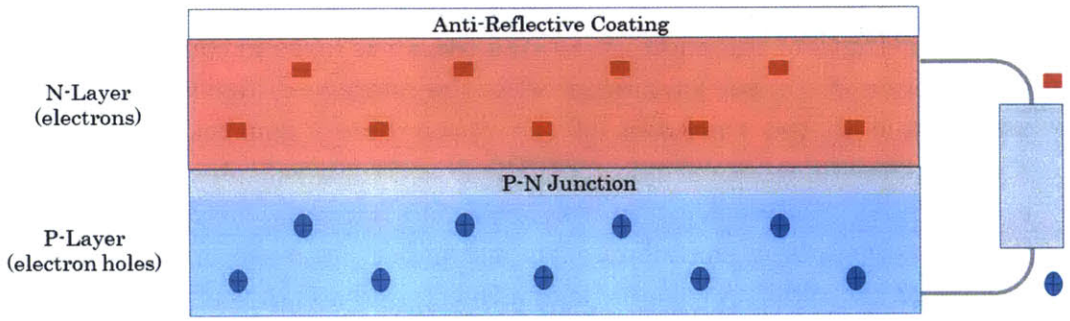

Figure 17. Schematic of a photovoltaic cell with an external load. The PN Junction occurs when P- and N-layers are in contact and forms a depletion region. The external load is connected to the P- and N-layers to allow electrons to flow through in order to generate electricity

Ionization occurs when incident particles collide with orbital electrons of the cell, which ultimately alters properties of the cell, and leads to an increase in leakage currents. Ionization can also cause the development of color centers, which darken adhesives and coverglass, and thus reduces the transmittance of the coverglass [*Bailey and Raffaelle*, 2003]. Ionizing radiation is not the largest contributor to solar cell degradation, as it only accounts for approximately 4% of cell degradation over the mission lifetime [*Messenger et al.,* 2011].

As shown in Chapter 2, given a proton and an electron of equivalent energy, the proton range or penetration depth into a given material is less than the range of an electron. The proton deposits energy into a

smaller volume and at a specific depth, which is marked for ionization by Bragg's peak; this leads to a higher maximum energy density deposited in the material [*Messenger et al.,* 2006; *Lai,* 2012]. As the energy and bombardment fluence of protons increases, there is a decrease in the degradation rate of the cell's performance parameters (I_{sc} and V_{oc}). Thus, high-energy protons produce less disruption in the periodic lattice structure [*Bielle-Daspet et al.*, 1980; *Rong et al.,* 2003].

4.4 Solar Cell Degradation in Geostationary Orbit

Geostationary orbits (GEO) are in the outer radiation belt, which is dominated by high-energy electrons and bombarded with energetic solar protons from solar events [*Baker*, 1998]. The primary sources of solar cell degradation for geostationary orbit are trapped electrons and solar protons. As the typical thickness of coverglass is 3-4 mils (75-100 microns) it completely blocks out the harmful effects of low-energy electrons and trapped protons in GEO, which have energies less than 1 MeV [*Tauke et al.,* 1967; *Messenger et al.,* 2001].

4.5 Current Models of Solar Cell/Panel Performance

Satellite designers predict solar cell degradation using radiation environment models (trapped-environment and transient solar proton environment) in order to quantify the required power of a system in a specific orbit at EOL. Unfortunately, there have been cases when anomalously high particle irradiation has been observed to degrade the performance of satellite solar cells to a greater extent than the predicted exposure rates. While the cause of satellite anomalies are rarely publicly disclosed, several have been attributed to solar array failures. In 2012, AMC-16 experienced a solar array circuit failure. In 2010, INSAT 4B had a 50% power loss due to a solar array anomaly, and in 2008, NigComSat 1 experienced a total loss due to solar array failure. Additionally, in 1995, GOES 7 experienced solar panel degradation that reduced the expected lifetime of the satellite by three years [*Bedingfield et al.,* 1996].

In 2009, the Aerospace Corporation published a report stating that for geostationary orbits POLE now known as IGE2006 was most

appropriate for simulating the trapped electron environment and that ESP 90th is most appropriate for simulating the long-term solar protons environment [*Guild et al.*, 2009].

Figure 18 shows the integral electron and proton flux at GEO using the ONERA/DESP-LANL code (previously known as POLE) and AP8-MIN. It is clear that geostationary orbit is dominated by trapped electrons ranging from approximately 1 keV to 6 MeV. Figure 18 also shows that a trapped proton population exists with protons ranging from 0.1 to 1 MeV in energy. Three solar proton event models (ESP 90%, ESP 95% and JPL91 Extended) were also modeled and compared. The ESP model was run with 8.9 active solar years. Solar protons are present at geostationary orbit with energies ranging from 1 MeV to approximately 300 MeV. During a severe solar proton event (SPEs), the integral flux increases by several orders of magnitude and the total dose at GEO can equal the dose accumulated over periods of months or longer [*O'Brien*, 2009].

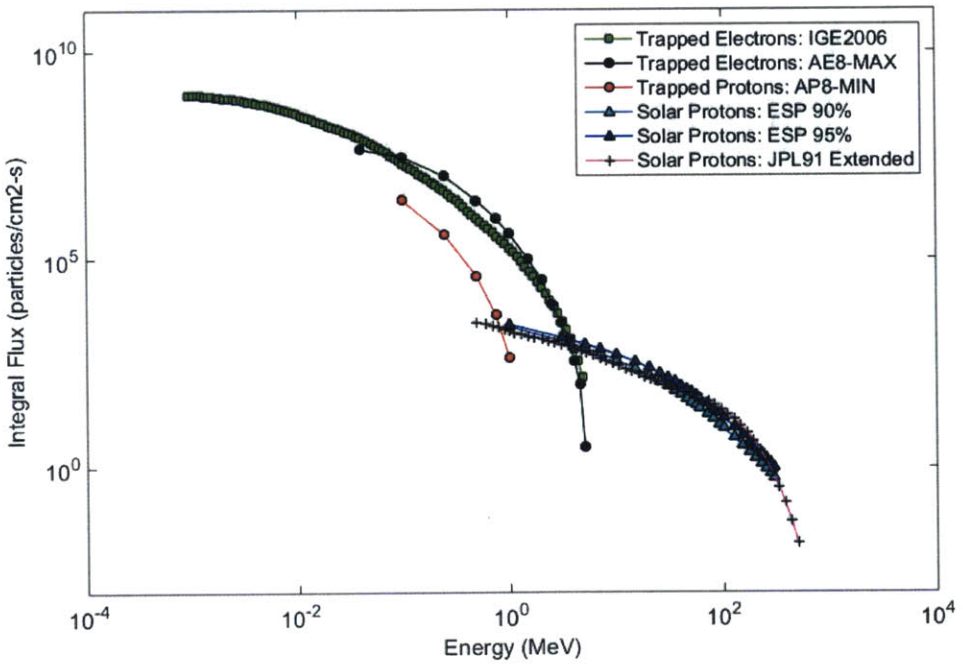

Figure 18. The orbit averaged integral IGE2006 electron flux (shown in green), the integral AE8-MAX electron flux (shown in black), the integral proton flux (shown in red), and the integral SPE fluxes (ESP

90% shown in cyan; ESP 95% shown in blue, and JPL91 Extended shown in magenta) for a fifteen-year geostationary orbit.

4.6 Analysis Approach

Satellite engineers, satellite operators and space weather scientists all want to better understand the relationship between the space environment and solar cell degradation, using on-orbit data to validate models and ground-based testing. Investigation of solar cell degradation through the analysis of on-orbit solar array health monitoring telemetry for understanding solar array degradation is not common, due to the proprietary nature of the satellite telemetry [*Walker and Statler*, 1988; *Messenger et al.*, 2011]. In this work, we overcome the typical road-block of proprietary data by partnering with geostationary satellite operators to investigate solar cell degradation through the analysis of on-orbit solar cell telemetry. We first analyze solar cell telemetry in order to quantify the magnitude of annual solar cell degradation experienced onboard eleven geostationary satellites.

Satellite operators, such as Inmarsat, ARABSAT, and Telenor, continuously track performance with real-time telemetry downlinked from the satellite. However, a universal standard for telemetry format does not exist. There is also not a standardized approach toward monitoring solar panel performance. One approach for monitoring solar cell performance is to analyze the V_{oc} and I_{sc} of a set of diagnostic cells on the cells. The diagnostic cells are generally located towards the middle of the array so that they provide a measurement representative of the entire array, and are not contaminated from thruster firings. Two other approaches used are to either monitor the bus load or to monitor the Power Supply Regulator (PSR) shunt currents. The PSR shunt currents represent the array power that is shunted into a load, and not required by the bus or payload. As an array degrades over time less excess power is generated, or shunted, and the degradation of the array can be estimated.

Assessing the performance and degradation of solar arrays is particularly difficult unless the solar array systems are configured to monitor diagnostic cells in the array. The complexities of calibrating out

fluctuations in the bus load required to assess performance do not provide specific knowledge of the degradation mechanism. The only way to understand the changes in the solar cell parameters is to monitor them through the use of diagnostic test cells.

Satellite operators receive space environment warnings from agencies such as the National Oceanic and Atmospheric Association (NOAA), but these warnings are not accompanied by predictions of expected solar array degradation for a given event. For example, solar proton events (SPEs) of 10 MeV >10,000 pfu (protons/cm^2/sec/sr), the highest threshold of SPE warning for NOAA, are thought to cause instantaneous solar array degradation [*Koons et al.,* 2000; *Oldenwald and Green,* 2007]. These events are among the most difficult environmental phenomena to predict, but are most frequent during solar maximum [*Lohmeyer et al.,* 2013]. The SPEs of 1989 caused GOES-7 solar panels to degrade during one day by the expected loss over half the mission lifetime of nominal radiation aging. These events also lead to the failure of CS-3b and operational problems of MARECS-1 [*Allen and Wilkinson,* 1993].

We next obtain dates of SPEs to quantitatively compare with the solar cell telemetry, and to determine if the SPEs lead to increased degradation. We investigate whether or not there is a functional relationship between SPE 10 MeV proton fluence and degradation for both Si and GaAs cells. Finally, we compare the degradation measured from solar cell telemetry to validate commonly used models for predicting solar cell degradation. We assess the performance of nine combinations of trapped and solar particle models commonly used as input to quantifying the expected solar cell degradation.

4.7 Solar Cell Telemetry Acquisition and Radiation Environment Database

To compare solar cell performance among these different measurement approaches, we present our annual degradation findings in terms of a percent change in the monitored performance metric used. Any day of the year could have been selected for the annual degradation calculations, as long as the same day was used as a baseline for all annual degradation calculations. The telemetry used for the annual

degradation analysis is taken during vernal equinox, assumed to be March 21 of each year. During vernal and autumnal equinox the Sun directly crosses over the celestial equator, and the lengths of day and night are equivalent [*Wertz and Larsen*, 1999].

For the degradation during SPEs, we calculate the percent change in the performance parameter over the event. To identify SPE periods of interest for our analysis of degradation, we use the highest NOAA defined threshold of SPEs of 10 MeV Proton Flux > 10,000 pfu, for which dates can be found at http://umbra.nascom.nasa.gov/SEP/. Table 11 provides information for the six instances where SPEs of 10 MeV Proton Flux > 10,000 pfu have occurred since 1990. The table includes the start date and time of the event, the date and time of the maximum flux reached, the value of the maximum 10 MeV Proton Flux > 10,000 pfu, and the fluence accumulated from the start of the event until the maximum 10 MeV Flux > 10,000 pfu was reached. The length of the SPEs tabulated below range from 0.75 to 1.5 days. The fluences are based on 4π fluxes measured onboard the GOES satellites [*Reedy*, 2002; *Oldenwald and Green*, 2007].

Table 11. NOAA Solar Proton Events (10 MeV Proton Flux > 10,000 pfu)

SPE	SPE Start Date and Time	SPE Maximum Flux Date and Time	Maximum 10 MeV Proton Flux > 10,000 (pfu)	Fluence over SPE (10^9 particles/cm^2)
1	July 14, 2000 10:45	July 15, 2000 12:30	24,000	11.5
2	Nov. 8, 2000 23:50	Nov. 9, 2000 15:55	14,800	9.1
3	Sept. 24, 2001 12:15	Sept. 25, 2001 23:35	12,900	7.4
4	Nov. 4, 2001 17:05	Nov. 6, 2001 2:15	31,700	15.0
5	Nov. 22, 2001 23:20	Nov. 24, 2001 11:15	18,900	8.1
6	Oct. 28, 2003 12:15	Oct. 29, 2003 6:15	29,500	~14.0

Chapter 5. On-Orbit Solar Cell Degradation: Analysis

In this chapter, we address two goals: (i) to quantify the solar cell degradation through analysis of solar cell telemetry (I_{sc} and V_{oc}) from eleven geostationary (GEO) communication satellites launched between 1990 and 1998, and (ii) to quantify the accuracy of models used for predicting solar cell degradation for satellite designers by comparing observed degradation measured with on-orbit telemetry to predictions of solar cell degradation. The solar cell telemetry is from eleven GEO communication satellites that all have mission lifetimes between 7 and 20 years. The satellites are operated by three GEO COMSAT operators: Inmarsat, headquartered in London, ARABSAT, headquartered in Saudi Arabia, and Telenor, headquartered in Norway.

In Section 5.1, we quantify and compare the annual degradation of two different solar cell categories, silicon (Si) and gallium arsenide (GaAs), In Section 5.2 we examine the degradation of both solar cell categories during NOAA-defined 10 MeV Solar Proton Events (SPEs) of flux >10,000 pfu. Based on the results of Section 5.2, in Section 5.3 we investigate whether or not there is a functional relationship between SPE 10 MeV proton fluence and degradation for both Si and GaAs cells. We compare measured on-orbit degradation to model predictions in Section 5.4 and Section 5.5. The model analysis uses nine different combinations of environmental models as input to the solar cell degradation code which compares their predictions with observed solar cell degradation of Si and GaAs cells behind 4 mils of coverglass. To consider the effect of adhesives, we repeat this type of analysis again for cells behind both 4 mils of coverglass and 2 mils of adhesive.

5.1 Annual Degradation of Solar Cells

We calculate the annual degradation of solar cells on each of the eleven satellites using their reported performance on the vernal equinox, March 21, of each year as a reference. In addition to the annual degradation, we also calculate the total degradation as percent change in performance between March 21st of the first year of operation and March 21st of the last year of operation.

Of the eleven satellites considered in this study, seven satellites are equipped with silicon solar cells, and four satellites are equipped with

GaAs solar cells. We acknowledge that there are different types of both silicon and GaAs cells, but for the purpose of this analysis, we group them into their larger categories of silicon and GaAs, which should have fairly common bandgap structures. To maintain confidentiality, the solar arrays are referred to using alphanumeric identifiers, for example, silicon cells are analyzed on-board what will be referred to as Solar Array A, Solar Array B, to Solar Array L, and GaAs cells are on-board what will be referred to as Solar Array AA, BB to Solar Array FF. Unfortunately, several satellites experienced solar array failures, such as failures in the solar array drive mechanisms, or had long-term anomalous performance and were not considered in all parts of this analysis.

5.1.1 Annual Degradation of Silicon Cells

Table 12 shows the total percent degradation and the average annual percent degradation of ten silicon solar arrays. The total % degradation is calculated by taking the difference in performance on March 21st of the first and last year of operation and dividing by the performance of the March 21st of the first year. The time-normalized average annual percent degradations are also tabulated; these were calculated by dividing the total percent degradation by the total number of years of operation.

We also include a column that describes the performance measurement used. This column captures how the operator monitors the degradation of the solar arrays. "Unique algorithm" means that the operator monitors solar array performance through the use of a proprietary algorithm that accounts for multiple telemetered measurements, including I_{sc} and V_{oc}. "I_{sc}/ V_{oc}" designates that solar array degradation is monitored through the I_{sc} and V_{oc} telemetry only.

Table 12. Degradation of silicon solar arrays. Average % degradation over life and annually.

Solar Array	Years of Operation	Total % Degradation	Average Annual % Degradation	Performance Measurement
A	7	8.16	1.17	Unique algorithm
B	7	10.90	1.56	Unique algorithm
C	14	11.85	0.85	Unique algorithm
D	14	14.11	1.01	Unique algorithm
E	10	16.92	1.69	Unique algorithm
F	20	16.13	0.81	I_{sc}/V_{oc}
G	20	17.78	0.89	I_{sc}/V_{oc}
H	20	14.18	0.71	I_{sc}/V_{oc}
I	20	24.47	1.24	I_{sc}/V_{oc}
J	14	14.92	1.07	I_{sc}/V_{oc}
K	18	13.27	0.74	I_{sc}/V_{oc}
L	18	14.17	0.79	I_{sc}/V_{oc}

In the 1980's, a typical Si cell could expect between 19 – 25% total cell degradation for a seven year GEO mission [*Rauschenbach,* 1980]. Since that time, a common design rule-of-thumb is that silicon solar cells in GEO will experience approximately 25% degradation over 10 years in orbit. While this may have been true in the mid-1990s, we show that this design assumption no longer holds [*Bailey and Flood,* 1998]. ***Our results show that degradation rates for silicon cells have decreased and are now approximately 10% over a 10 year mission (approximately 1.04% per year, as can be seen in Table 12).*** The decrease in the observed degradation compared with predicted appears significant enough to suggest an update to the design rule-of-thumb for Si solar cell degradation (25% cell degradation over 10 years at GEO). This difference is likely due to the developments in silicon solar cell technology, such as improvements in surface passivization, bulk lifetimes, contact passivization and light trapping in the cell. These improvements all contribute to an overall increase in the cell efficiency and could also reduce degradation [*Green,* 2009].

From our analysis, we observe that solar array degradation per year can be as high as 5% per year, even if the average annual percent

degradation over the full mission is lower. Figure 19 shows the variation in the annual percent degradation for twelve silicon solar arrays, plotted along with the 11-year solar cycle measured in Sunspot Number gathered from the Solar Influences Data Center in Brussels, Belgium. SPEs of 10 MeV Protons > 10,000 pfu occurred in 2000, 2001 and 2003, but did not occur in 2002. These twelve solar arrays are onboard the seven satellites equipped with Si solar cells. The seven satellites are of two different manufactured bus types, designated as Bus Make 1 and Bus Make 2.

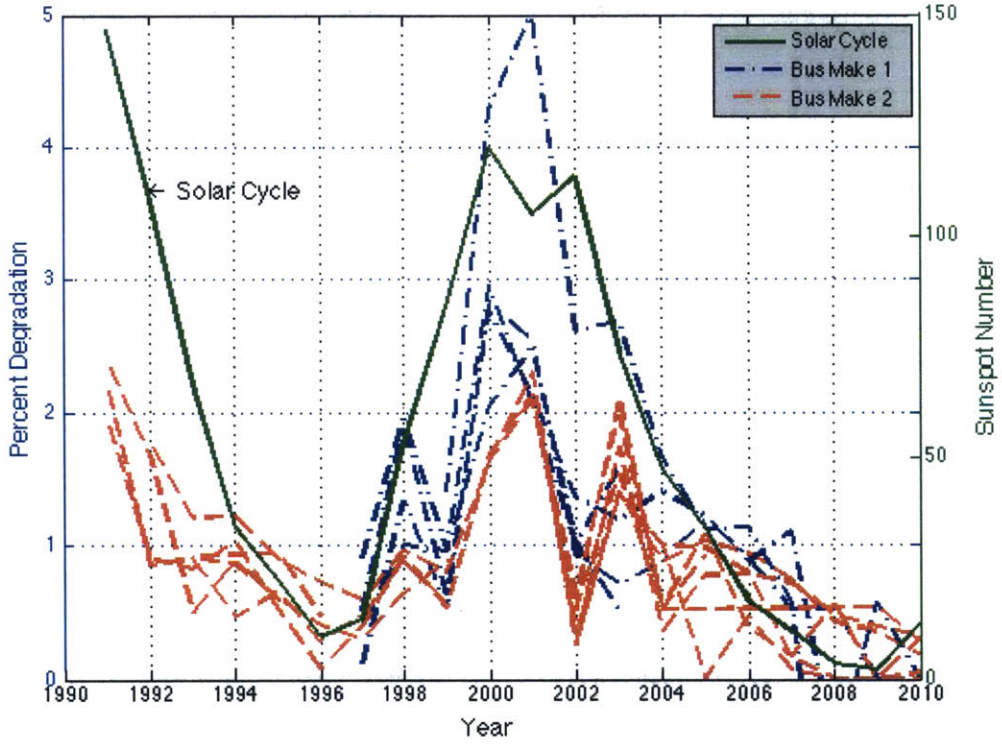

Figure 19. Silicon solar arrays' annual percent degradation. Annual average degradation (red, blue) is plotted with the eleven-year solar cycle (green). The solar arrays are onboard satellites of two different bus types: Bus Make 1, shown in blue and Bus Make 2, shown in red. Two different performance measurements were used on the different bus makes. The magnitude of the solar cycle is quantified with the Sunspot Number shown on the right y-axis. SPEs occurred in 2000, 2001 and 2003, but did not occur in 2002.

It is important to note that the two different bus makes, Bus Make 1 and Bus Make 2, use different methods for monitoring solar array degradation (one bus make uses a unique algorithm where the other uses I_{sc} and V_{oc}. It is possible that there are small biases in the resulting degradation that could be due to differences in the way the performance is measured.

The percent degradation in the solar array performance appears to follow the same trend as the 11-year solar cycle, peaking during solar maximum. Solar maximum is the phase of the solar cycle when SPEs, which are known to contribute to solar array degradation, are most severe. Interestingly, there is a clear decrease in the solar array degradation in 2002 and 2004. As noted in Table 11, 2002 and 2004 were years that had no recorded 10 MeV SPEs > 10,000 pfu. In Section 5.2, we further analyze the relationship between solar array degradation and SPEs.

5.1.2 Annual Degradation of Gallium Arsenide Cells

GaAs cells are more resistant to damage caused by radiation because unlike Si, they do not require long diffusion lengths and can withstand more diffusion length degradation before cell performance decreases [*Hacke et al.,* 1994; *Anspaugh,* 1996]. Four of the eleven satellites in this study are equipped with GaAs solar arrays. Table 13 shows the total percent degradation, the average annual percent degradation, and the performance measurement for the GaAs solar arrays.

Table 13. Degradation of GaAs cells onboard the six GaAs solar arrays. Average % degradation over life and annually.

Solar Array	Years of Available data	Total % Degradation	Average Annual % Degradation	Performance Measurement
AA	14	10.30	0.74	I_{sc}/V_{oc}
BB	14	7.27	0.52	I_{sc}/V_{oc}
CC	14	6.13	0.44	I_{sc}/V_{oc}
DD	14	7.66	0.64	I_{sc}/V_{oc}
EE	13	13.41	1.03	Unique Algorithm
FF	12	10.44	0.87	Unique Algorithm

For GaAs arrays, total degradation ranged from 6.13% to 13.4% for 12-14 year operating periods. The average annual percent degradation ranged from 0.44% to 1.03%. The total average degradation, or the average of all of the individual average annual GaAs array degradations, is approximately 0.67%, which is roughly 0.37% less than the total average annual degradation of silicon solar cells.

Figure 20 shows the annual degradation of GaAs solar cells onboard six satellites. There were two bus types, designated as Bus Make 3 and Bus Make 4. Figure 20 also shows the solar cycle, which is measured with the Sunspot Number on the right y-axis.

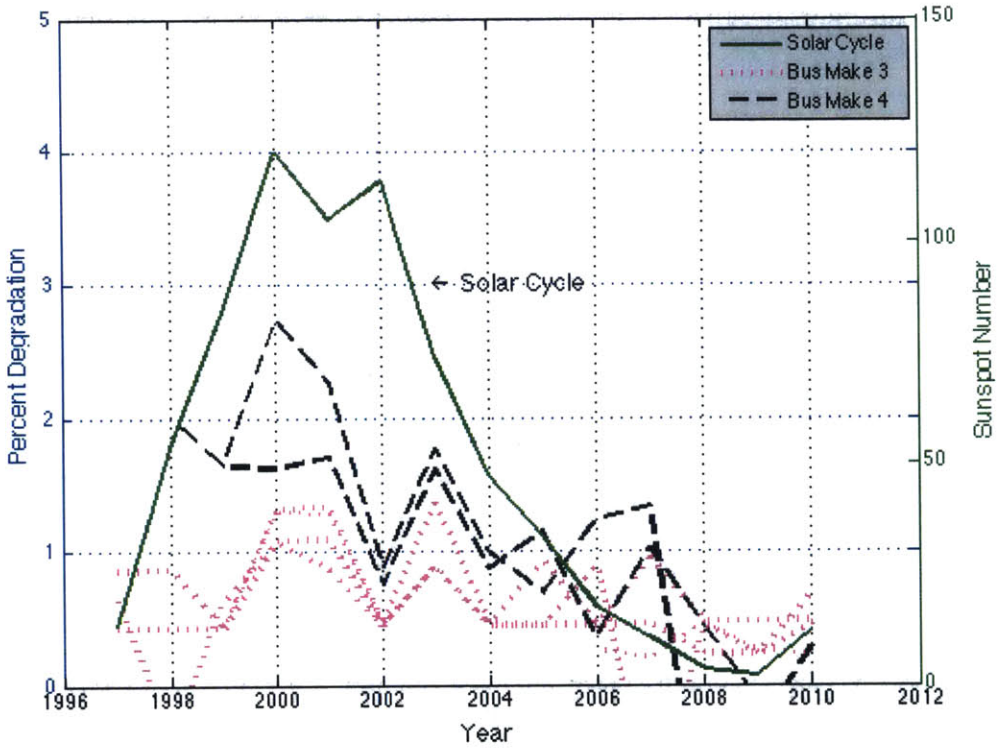

Figure 20. GaAs solar arrays' annual percent degradation. Annual average degradation (magenta, black) is plotted with the eleven-year solar cycle (green). Bus Make 3 is shown in magenta and Bus Make 4 in black. The magnitude of the solar cycle is quantified with the Sunspot Number shown on the right y-axis. SPEs occurred in 2000, 2001 and 2003, but did not occur in 2002.

The decrease in degradation during years 2002 and 2004, when no 10 MeV SPEs > 10,000 pfu occurred is consistent with the results shown in Figure 19. The maximum annual average percent degradation of GaAs is 1.03%, which is 0.66% less than silicon. Overall, the annual average degradation for the GaAs cells is less than that of the silicon cells.

5.2 Solar Cell Degradation During SPEs

There were six SPEs with 10 MeV protons greater than 10,000 pfu during the period that we have data from the eleven satellites, from 1990 to 2013. Table 14 shows the degradation for the silicon solar cells during the six SPEs, and Table 15 shows the degradation for the GaAs cells only over the days during which the six SPEs occurred. The SPE is defined from the start time to the time at which max flux occurs, as NOAA does not record an SPE end time. Only the arrays that were monitored with V_{oc} and I_{sc} are included in following two tables. Cell monitored purely with V_{oc} and I_{sc} were only considered for consistency in comparison, and because the unique algorithms often incorporate other aspects of solar cell performance that are not calibrated to degradation in V_{oc} and I_{sc}.

The degradation in V_{oc} and I_{sc} over the six SPEs listed in Table 11 was calculated as the total degradation from the start day/time of the SPE to the end day/time of the SPE. The SPEs range in from 0.75 to 1.5 days. The degradation over the six SPEs was also computed normalized to an hour. These values are not tabulated but are analyzed in the next section, Section 5.3. Both tables, Table 14 and Table 15 also show the average degradation experienced over each of the SPE events in gray. The classification and description of the six SPEs can be found in Table 11.

Table 14. Silicon solar array percent degradation during the six NOAA SPE events of 10 MeV Protons > 10,000 pfu

Solar Array	SPE 1	SPE 2	SPE 3	SPE 4	SPE 5	SPE 6
A	0.62	0.72	0	1.11	1.27	0.79
B	0.58	0.98	0	0.93	1.21	0.74
C	1.62	0.51	0.52	0.53	0	0.58
D	1.20	0.15	0.15	1.54	1.57	0.58
E	1.08	0.51	0	1.04	1.06	1.10

F	0.53	0.51	0	0.51	1.05	1.04
G	0.53	0	0	0.52	0.53	1.05
H	0.56	0.54	0	0.54	0	0.56
I	0.52	N/A	0	1.01	0.52	1.03
Degradation over each SPE	0.81	0.49	0.06	0.86	0.80	0.83

As shown in Table 11, SPEs 1, 4, and 6, occurred on July 14-15, 2000, November 4-6, 2001, and October 28-29, 2003, and were the three SPEs with the highest 10 MeV proton fluence. These were also the three SPEs that on average coincided with the most solar array degradation, 0.81%, 0.86% and 0.83%, respectively.

Table 15 shows degradation for the GaAs solar cells during the six SPEs. Not all of the satellites with GaAs solar cells were in operation during all six SPEs of 10 MeV Protons > 10,000 pfu. These cells were, however, included in the average annual degradation previously presented. Additionally, multiple arrays used shunted power for the performance metric, and were not included in this analysis because they could not be compared directly with the degradation of the Si cells monitored with I_{sc} and V_{oc}.

Table 15. GaAs solar cell percent degradation during the six NOAA SPE events of 10 MeV Protons > 10,000 pfu

Solar Array	SPE 1	SPE 2	SPE 3	SPE 4	SPE 5	SPE 6
AA	0.50	0.46	0	0.92	0.47	0.47
BB	0.49	0.45	0.44	0.91	0.46	0.47
CC	0.48	0.44	0	0.44	0.46	0.45
DD	0.49	0	0	0.45	0	0.46
Degradation over each SPE	0.49	0.38	0.11	0.68	0.35	0.46

Similar to the results of the SPE degradation for silicon cells, the three SPEs, shown in Table 11, with highest fluence (SPE 1, 4, and 6) produced the highest amount of degradation in the GaAs cells (0.49%, 0.68%, and 0.46% respectively). The fact that the GaAs arrays

experienced less degradation than the silicon arrays is consistent with expectations. *Oldenwald and Green* [2007] assumed in their study that GaAs based panels were half as susceptible to SPE damage as Si panels.

5.3 Solar Array Degradation vs. Solar Particle Event Flux

In this section we investigate whether or not there is a clear functional relationship between SPEs of 10 MeV protons >10,000 pfu and the amount of solar cell degradation for both Si and GaAs cells. Figure 21(a,b) show the average percent degradation of I_{sc} for each of the six SPEs with 10 MeV protons > 10,000 pfu. Error bars show one standard deviation above and below the average percent degradation.

Figure 21(a) shows the average percent degradation from the start day/time to the end day/time of each of the six SPEs in Table 11. Data for Si cells are shown in blue and data for GaAs are shown in green. Figure 21(b) shows the average percent degradation from the start day/time to the end day/time of each of the SPEs in Table 11, normalized for the length of time in hours of the respective SPEs.

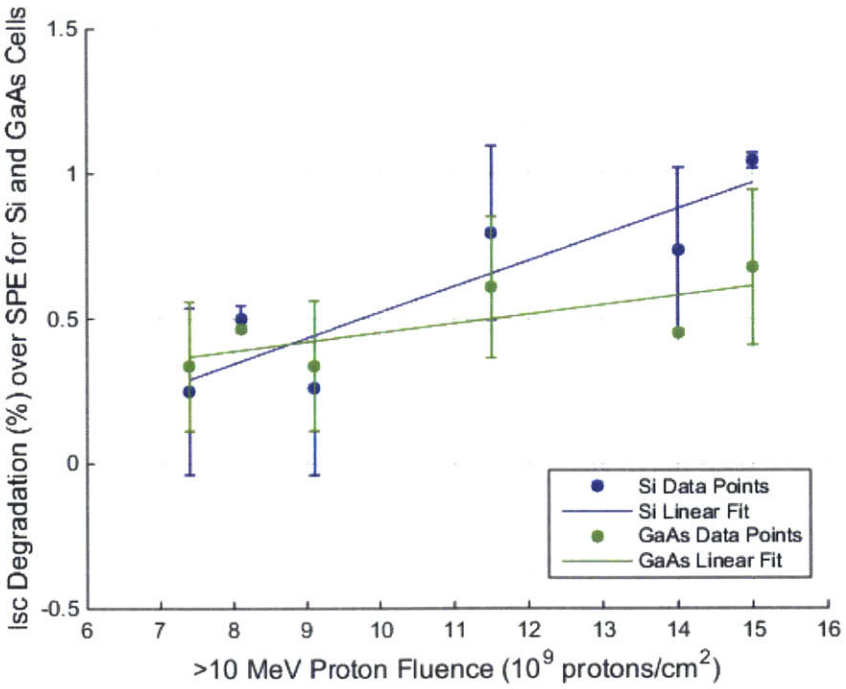

(a)

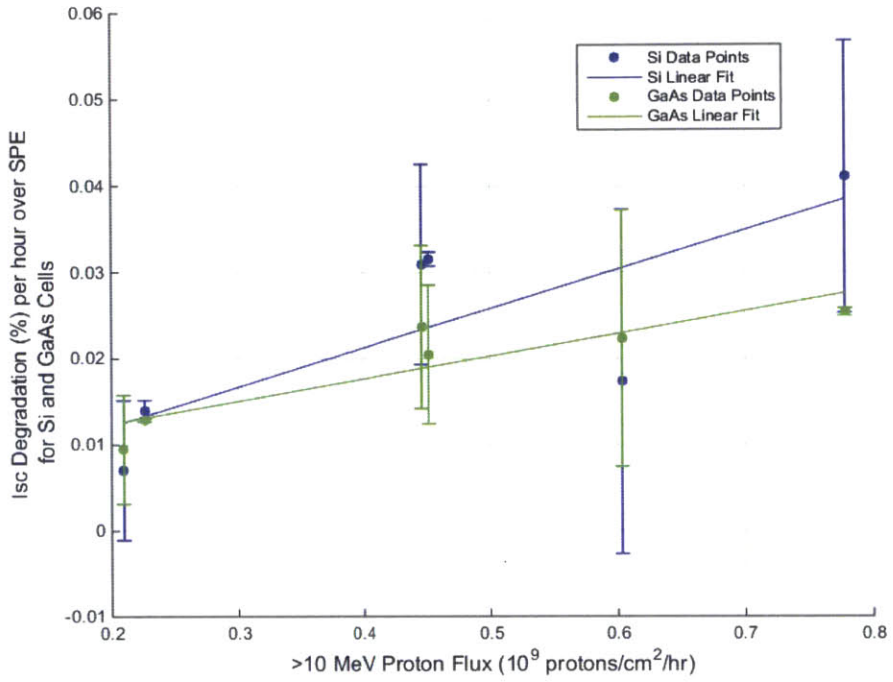

(b)

Figure 21 (a,b). Percent Degradation of (a) Si Solar Cells and (b) GaAs Solar Cells over SPEs of 10 MeV Protons > 10,000 pfu. The error bars designate a standard deviation above and below the mean degradation.

Higher degradation occurs at higher fluences for both Si and GaAs cells. For Figure 21(a), which is not normalized to an hour of time, the Si curve fit is $y = 0.089*x - 0.375$, which has a goodness of fit of $R^2 = 0.798$. The GaAs curve fit is $y = 0.033*x + 0.125$, which has a goodness of fit of $R^2 = 0.540$.

The normalization presented in Figure 21(b) was included to account for the duration and strength of the SPEs. We wanted to specifically account for the fact that the degradation over a weaker SPE that lasts longer may be different than the degradation over a severe SPE that lasts hours. For Figure 21(b), which is normalized to an hour of time, the Si curve fit is $y = 0.046*x + 0.003$. The goodness of fit for the Si curve is equal to $R^2 = 0.599$. The GaAs curve fit is $y = 0.026*x + 0.007$. The goodness of fit for the GaAs curve is equal to 0.800.

Higher fits occurred for the degradation over the SPEs normalized to an hour, but only marginally higher. None of the R^2 values were greater

than 0.8, which does not describe a close fit. Improvements to our assessment of the functional relationship between SPE strength and percent solar array degradation could be made using additional solar array degradation data from other geostationary satellite operators that monitor cell performance parameters with a diagnostic cell.

5.4 Comparison of On-Orbit Measurements with Models for Computing Solar Cell Degradation

Solar cell degradation is predicted using a model that outputs the expected 1 MeV electron equivalent fluence (JPL's EQFLUX is used in this analysis) of a mission to make predictions of percent degradation expected over the entire mission. The high-level model that predicts degradation is itself dependent on two models that it uses internally, one for the trapped particle environment and one for the long-term solar proton environment. So to determine the expected solar array degradation of a given mission the 1 MeV equivalent electron fluence model takes as input a mission's orbital information, launch date, mission duration, and then a model for the trapped particle environment and a model for long-term solar proton environment. Available trapped particle models include AE8/AP8, IGE2006 (formerly POLE), and AP9/AE9, which were discussed in Section 2.4.1. There are also several long-term solar proton environment models. ESP 90%, ESP 95%, and JPL91 Extended are among the most commonly used long-term solar particle models.

With so many possible combinations of possible trapped particle and long-term solar proton models, it is challenging to answer the question, *"Which combination of models will most accurately predict the solar array degradation for my mission orbit and duration?"* The analysis in Section 5.5 and Section 5.6 addresses this question by comparing more than 300 years of on-orbit solar cell performance telemetry with model predictions of expected degradation using JPL's EQFLUX model for equivalent 1 MeV electron fluence. JPL's EQFLUX model inputs a trapped environment model for protons and electrons along with a solar proton event model, which is important to note for the analysis presented in the following section.

5.5 Analysis Approach for Quantifying Solar Cell Degradation

First, we quantify the expected degradation of short circuit current (I_{sc}) for silicon and GaAs solar cells onboard a 15 year mission in GEO for nine different combinations of models tabulated below. The nine model combinations consist of trapped environment models alone, solar proton models alone, and a combination of both trapped and solar proton models. All of these models are either default inputs in modeling tools such as SPENVIS (www.spenvis.oma.be) and OMERE (www.trad.fr/OMERE-software), and/or are suggested for use in The Aerospace Corporation's Report "Space Environment Model Recommendations for Geosynchronous Orbit" [*Guild et al.,* 2009]. The ESP model was run for 8.9 solar cycle active years.

The expected solar cell performance degradation from the nine model combinations is then compared with the degradation of the short circuit current experienced on seven Si cells and four GaAs cells as recorded on-orbit. AP8-MIN was not modeled alone because its fluence contribution behind 4 mils of coverglass is zero.

Table 16. Model Combinations

Trial Number	Trapped Electron Model	Trapped Proton Model	Solar Proton Model
1	IGE2006	AP8-MIN	-
2	AE8-MAX	AP8-MIN	-
3	-	-	ESP 90th
4	-	-	ESP 95th
5	-	-	JPL91 Extended
6*	IGE2006	AP8-MIN	ESP 90th
7	IGE2006	AP8-MIN	ESP 95th
8	IGE2006	AP8-MIN	JPL91 Extended
9**	AE8-MAX	AP8-MIN	JPL91 Extended

*The Aerospace Corporation [*Guild et al.,* 2009] recommended combination for GEO
**Manufacturer's commonly used model combination for GEO.

To clearly capture the possible effect of coverglass adhesive on the outcome, we perform the model comparison study twice. The first time we use 4 mils of SiO_2 coverglass (density = 2.32 g/cm^3) on top of the solar

cell. The second time we use 4 mils of SiO_2 coverglass and 2 mils of DC 93-500 coverglass silicone adhesive (density = 1.08 g/cm^3) on top of the solar cell [*Messenger et al.,* 2010]. The cell structures modeled should be realistic as possible, and account for solar cell adhesive. In running this analysis twice we can quantify the deviation with and without the inclusion of adhesive, and can determine which of the two scenarios more closely matched reality based on on-board solar cell telemetry.

5.5.1 Model predictions of Si Cell I_{sc} Degradation for a 15 year GEO mission with 4 mils of coverglass

To model the expected degradation in I_{sc} over a given mission life we first need the 1 MeV *equivalent* electron fluence, which includes contributions from the trapped proton and electron environments and the transient solar proton environment. The 1 MeV equivalent electron fluence, which is output from JPL's EQFLUX, is used as a way to describe radiation in the space environment (due to a variety of particle types and energies) when simulated under laboratory conditions. Damage coefficients are generated during cell testing at several energy levels for protons and electrons, and these are then used to describe the damage produced from that particle/energy in terms of a 1 MeV electron [*Tada and Carter,* 1977].

Equation 11 is then used to determine the degradation of the Si cells due to radiation. A different approach is used for GaAs cells.

$$\frac{Isc}{Isc_o} = 1 - C \cdot log\left(1 + \frac{\phi}{\phi_x}\right) \tag{11}$$

In Equation 11, C represents the decrease in I_{sc} per decade in radiation fluence in the logarithmic region and ϕ_x refers to the radiation fluence at which I_{sc} starts to change to a linear function of the logarithm of the fluence [*Anspaugh,* 1996]. For this analysis, a value of $C = 0.173$ and a value of ϕ_x = 8.90E+13 e/cm^2 were used [*Anspaugh,* 1989]. The 1 MeV equivalent fluence for the mission was determined using the nine combinations of models in Table 16 as input. Table 17 shows the 1 MeV equivalent electron fluence, the degradation in I_{sc} over the fifteen year

mission, and the average annual percent degradation for a Si cell behind 4 mils of coverglass. The average annual percent degradation for the fifteen year GEO mission is determined using the equation below:

$$\%_{deg,avg.annual} = \frac{100\left(1-\frac{Isc}{Isc_0}\right)}{15\ years} \quad (12)$$

Table 17. Solar cell degradation predictions for a 15-year GEO mission for Si cells with 4 mils of coverglass

Trial Number	Models Included	1 MeV Equivalent Electron Fluence (ele/cm^2)	I_{sc}/I_{sco}	Average Annual Percent Degradation (%)
1	IGE2006	1.45E+14	0.928	0.48
2	AE8-MAX	3.83E+14	0.875	0.83
3	ESP 90th	6.54E+14	0.841	1.06
4	ESP 95th	7.93E+14	0.828	1.15
5	JPL91 Extended	4.67E+14	0.863	0.92
6*	IGE2006, AP8-MIN, ESP 90th	7.99E+14	0.827	1.15
7	IGE2006, AP8-MIN, ESP 95th	9.38E+14	0.816	1.22
8	IGE2006, AP8-min, JPL91 Extended	6.12E+14	0.845	1.03
9**	AE8-MAX, AP8-MIN, JPL91 Extended	8.54E+14	0.823	1.18

*The Aerospace Corporation [*Guild et al.*, 2009] recommended combination for GEO
**Manufacturer's commonly used model combination for GEO.

Section 5.5.2 compares the expected average annual percent degradations presented in Table 17 with the on-orbit I_{sc} telemetry of seven Si solar cells.

5.5.2 Comparison of Measured Si Cell I_{sc} Degradation and Modeled Solar Cell Degradation for a Si Cell behind 4 mils of coverglass

The color scale in Table 18 scales with the difference between the modeled and measured annual average degradation. The model results used nine different combinations of models, and the actual annual average degradation is measured by on-orbit telemetry. The minimum deviation (0 ± 0.1) between the modeled performance and the measured performance from on-orbit telemetry is shown in green, yellow designates a deviation between 0.1 and 0.2 and -0.1 and -0.2, light orange designates a deviation between 0.2 and 0.3 and -0.2 to -0.3. The second highest deviation is shown in dark orange (0.3 to 0.4 and -0.3 to -0.4), and the maximum deviation is shown in red, where the difference is >0.4% or <-0.4%.

Table 18. Reference for Degradation Stoplight Tables

Magnitude of Deviation	Color
0 ± 0.1	
0.1 + 0.1 -0.1 – 0.1	
0.2 + 0.1 -0.2 – 0.1	
0.3 + 0.1 -0.3 – 0.1	
>0.4 <-0.4	

Table 19 shows the difference between the observed average annual percent degradation of Si cells F-L and modeled average annual percent degradation produced from the nine model combinations for cells behind 4 mils of coverglass is presented in the stoplight chart below. As mentioned in Table 12. Arrays A – E use an operator unique algorithm for monitoring degradation, rather than I_{sc} or V_{oc}. It would be inappropriate to include Arrays A – E in the analysis.

Table 19. Difference between On-Orbit Measurement vs. Predicted Si Cell Average Annual Percent Degradation for Cells with 4 mils coverglass. The far right column is the average of the absolute value of the deviations.

Trial Number	F	G	H	I	J	K	L	Ave-rage
1	0.33	0.41	0.23	0.76	0.59	0.26	0.31	0.41
2	-0.02	0.06	-0.12	0.41	0.24	-0.09	-0.04	0.14
3	-0.25	-0.17	-0.35	0.18	0.01	-0.32	-0.27	0.22
4	-0.34	-0.26	-0.44	0.09	-0.08	-0.41	-0.36	0.28
5	-0.11	-0.03	-0.21	0.32	0.15	-0.18	-0.13	0.16
6*	-0.34	-0.26	-0.44	0.09	-0.08	-0.41	-0.36	0.28
7	-0.41	-0.33	-0.51	0.02	-0.15	-0.48	-0.43	0.33
8	-0.22	-0.14	-0.32	0.21	0.04	-0.29	-0.24	0.21
9**	-0.37	-0.29	-0.47	0.06	-0.11	-0.44	-0.39	0.30

*The Aerospace Corporation [*Guild et al.,* 2009] recommended combination for GEO
**Manufacturer's commonly used model combination for GEO.

The specific deviation between the modeled and the on-orbit measured average annual degradation ranged from 0.01% to 0.76%. The lowest deviation, 0.01% occurred using the transient solar particle model ESP90% model alone. The highest deviation, 0.76%, occurred using the IGE2006 model for trapped electrons in GEO alone. Model combination 2, AE8-MAX alone, produced the least deviation, on average of 0.14%, compared with the other model combinations. The average deviation in the absolute value of the predicted and on-orbit average annual degradation, shown on the far right of the table, was a minimum at 0.14% and a maximum of 0.41%. The maximum deviation coincides with the model combination that produced the maximum specific deviation, but the minimum occurred for a different model combination than the model that produced a specific deviation of 0.01%.

Given the variable nature of the space environment, it is interesting that the expected average annual degradations are accurate to within <0.8% for Si cells behind 4 mils of coverglass. While the accuracy of the models

for the cells considered in this study are actually quite good, a 0.76% difference every year over a 15 year mission could result in a total difference of nearly 11.5% at EOL. It is likely that the discrepancy is not solely due to the models, but may also be due to the deviation in the actual cell flown and the ASEC GaAs/Ge cell used as a baseline in this analysis. However, operators could still benefit from improved modeling and or cell testing improvements (cheaper and more efficient methods for testing cells) to further reduce this difference.

The next section, Section 5.5.3, includes analyses similar to those presented in Sections 5.5.1 and 5.5.2, but for GaAs cells behind 4 mils of coverglass, rather than Si cells behind 4 mils of coverglass.

5.5.3 Model predictions of GaAs Cell I_{sc} Degradation for a 15 year GEO mission with 4 mils of coverglass

Equation 13 is used to determine the degradation in I_{sc} for the GaAs cells rather than Eq. 11 for Si cells [*Anspaugh,* 1996]. The equation for the degradation in I_{sc} for the GaAs cells is shown below and is based on least-square polynomial fits of GaAs test data.

$$\frac{Isc}{Isc_o} = \sum_{i=0}^{m} a_i [ln(\phi)]^i \qquad (13)$$

Here ϕ is the total 1 MeV electron fluence, m is the degree of polynomial, and a_i are the parameters determined by least square fits. The least square fits are considered to agree well with the cubic spline fits to the average values of the electrical cell parameters after various levels of irradiate fluence [*Anspaugh,* 1996]. The least-square fits for the ASEC GaAs/Ge cell (now Emcore) are from the GaAs Solar Cell Handbook and are presented in Table 20, and are used in Equation 13 above. The ASEC GaAs/Ge cell is used as a standard example for the GaAs cells in this study because this cell was a primary GaAs cells launched in the 1990s.

Table 20. Least-Square Fits to the Normalized Electrical Parameters of ASEC GaAs/Ge Cells Irradiated with 1 MeV Electrons [*Anspaugh,* 1996]

Fit Coefficient	I_{sd}/I_{sco}
a_0	-3.21E+01
a_1	2.87
a_2	-7.17E-03
a_3	-6.15E-03
a_4	2.13E-04
a_5	-2.19E-06

The predicted GaAs solar cell degradation of I_{sc} for a 15 year GEO mission is shown in Table 21, along with the 1 MeV equivalent electron fluence for the mission and the calculated average annual percent degradation computed using Eq. 12.

Table 21. Solar Cell Degradation Predictions for 15-year GEO Mission for GaAs cells with 4 mils of coverglass

Trial No.	Models Included	1 MeV Equiv. Elec. Fluence 4 mils cg (ele/cm^2)	I_{sd}/I_{sco}	Average Annual % Degradation
1	IGE2006	1.40E+14	0.937	0.42
2	AE8-MAX	3.84E+14	0.896	0.70
3	ESP 90th	1.81E+14	0.928	0.48
4	ESP 95th	2.09E+14	0.923	0.51
5	JPL91 Extended	1.42E+14	0.936	0.42
6*	IGE2006, AP8-MIN, ESP 90th	3.21E+14	0.905	0.64
7	IGE2006, AP8-MIN, ESP 95th	3.48E+14	0.901	0.66
8	IGE2006, AP8-MIN, JPL91 Extended	2.82E+14	0.911	0.59
9**	AE8-MAX, AP8-MIN, JPL Extended	5.26E+14	0.878	0.82

*The Aerospace Corporation [*Guild et al.*, 2009] recommended combination for GEO

**Manufacturer's commonly used model combination for GEO.

In the table above, the IGE2006 model (Trial #1) produced the least degradation in I_{sc} equal to 93.7%, and the 9th trial, which includes AE8-MAX, AP8-MIN, and JPL Extended predicted the most amount of degradation in I_{sc} equal to 87.8%. The 9th trial is commonly used by manufacturers for modeling GEO. The difference in the 1st and 9th trial is 5.9%.

Section 5.5.4 compares the expected average annual percent degradations in Table 21 with the on-orbit I_{sc} telemetry of four GaAs solar arrays, designated as AA, BB, CC and DD.

5.5.4 Comparison between On-Orbit Measurements and Models of GaAs Cell I_{sc} Degradation behind 4 mils of coverglass

The difference between the observed average annual percent degradation of GaAs cells AA-DD and modeled average annual percent degradation produced from the nine model combinations for cells behind 4 mils of coverglass is presented in Table 22.

Table 22. Differences between On-orbit measurements vs. Model predictions of GaAs Cell Average Annual Percent Degradation for Cells with 4 mils coverglass. The far right column is the average of the absolute value of the deviations.

Trial No.	AA	BB	CC	DD	Average
1	0.32	0.10	0.02	0.22	0.17
2	0.04	-0.18	-0.26	-0.06	0.14
3	0.26	0.04	-0.04	0.16	0.13
4	0.23	0.01	-0.07	0.13	0.11
5	0.32	0.10	0.02	0.22	0.17
6*	0.10	-0.12	-0.20	0	0.11
7	0.08	-0.14	-0.22	-0.02	0.12
8	0.15	-0.07	-0.15	-0.05	0.11
9**	-0.08	-0.30	-0.38	-0.18	0.24

*The Aerospace Corporation [*Guild et al.,* 2009] recommended combination for GEO
**Manufacturer's commonly used model combination for GEO.

The range of differences between measurements and the model for the GaAs cells is 0.00% – 0.38%, which is roughly half the range of the Si cells presented in Table 22 (0.01% to 0.76%.). The smallest difference between measurements and model for the GaAs cells, 0.00% occurred using the trapped electron model IGE2006, the AP8-MIN trapped proton model, and the long term solar proton model ESP 90th (Trial #6). The largest difference, 0.38%, occurred using the AE8-MAX, AP8-MIN, JPL Extended models, which is the typical model combination used by manufacturers for GEO missions (Trial #9). The average deviation of the absolute value of the predicted and on-orbit average annual degradation, shown on the far right of the table, was a minimum at 0.11% and a maximum of 0.24%. The maximum and minimum average deviation both coincide with the model combinations that produced the maximum specific deviation, 0.38%, and the minimum specific deviation of 0.01%.

5.6 Comparison between On-Orbit Measurements and Models of GaAs Cell I_{sc} Degradation behind 4 mils of coverglass and 2 mils of adhesive

Dow Corning (DC) 93-500 is a clear space-grade encapsulant that is commonly used for bonding coverglass to solar cells. A thickness of 2 mils is typical and should be included in solar cell degradation modeling to accurately portray the geometry and characteristics of the full cell [*Messenger et al.,* 2011]. In this section, we perform the same analysis as in Sections 5.5.1 to 5.5.4, but for cells not only behind 4 mils of coverglass, but also including an additional 2 mils of adhesive. The purpose of this analysis is to quantify the difference in modeling the cells with and without adhesive.

5.6.1 Model predictions of Si Cell I_{sc} Degradation for a 15 year GEO mission with 4 mils of coverglass and 2 mils of adhesive

Table 23 shows the 1 MeV equivalent electron fluence, the degradation in I_{sc} over the fifteen year mission, and the average annual percent degradation for a Si cell behind 4 mils of coverglass and 2 mils of

adhesive. These values were computed using the same equations presented in Section 5.5.1 for the I_{sd}/I_{sco} and the average annual percent degradation.

Table 23. Solar Cell Degradation Predictions for a 15-year GEO Mission for Si cells with 4 mils of coverglass and 2 mils of adhesive

Trial Number	Models Included	1 MeV Equivalent Electron Fluence (ele/cm^2)	I_{sd}/I_{sco}	Average Annual Percent Degradation (%)
1	IGE2006	1.35E+14	0.931	0.46
2	AE8-MAX	3.56E+14	0.879	0.81
3	ESP 90th	5.80E+14	0.849	1.01
4	ESP 95th	7.10E+14	0.835	1.10
5	JPL91 Extended	4.04E+14	0.872	0.86
6*	IGE2006, AP8-MIN, ESP 90th	7.15E+14	0.835	1.10
7	IGE2006, AP8-MIN, ESP 95th	8.45E+14	0.824	1.18
8	IGE2006, AP8-min, JPL91 Extended	5.39E+14	0.853	0.98
9**	AE8-MAX, AP8-MIN, JPL91 Extended	7.60E+14	0.831	1.13

*The Aerospace Corporation [*Guild et al.*, 2009] recommended combination for GEO
**Manufacturer's commonly used model combination for GEO.

Section 5.6.2 compares the difference in on-orbit measured degradation and modeled degradation of I_{sc} for Si cells behind 4 mils of coverglass and 2 mils of adhesive.

5.6.2 Comparison of On-orbit Si Cell I_{sc} Degradation and Expected Modelled Solar Cell Degradation for a Si Cell behind 4 mils of coverglass and 2 mils of adhesive

The deviation in the observed average annual percent degradation of Si cells F-L and expected average annual percent degradation produced from the nine model combinations for cells behind 4 mils of coverglass and 2 mils of adhesive is presented in the stoplight chart below.

Table 24. Comparison between On-Orbit Measurements and Models of Si Cell I_{sc} Degradation behind 4 mils of coverglass and 2 mils of adhesive. The far right column is the average of the absolute value of the deviations.

Trial No.	F	G	H	I	J	K	L	Average
1	0.35	0.43	0.25	0.78	0.61	0.28	0.33	0.43
2	0	0.08	-0.10	0.43	0.26	-0.07	0.02	0.14
3	-0.20	-0.12	-0.30	0.23	0.06	-0.27	-0.22	0.20
4	-0.29	-0.21	-0.39	0.14	-0.03	-0.36	-0.31	0.25
5	-0.05	0.03	-0.15	0.38	0.21	-0.12	-0.07	0.14
6*	-0.29	-0.21	-0.39	0.14	-0.03	-0.36	-0.31	0.25
7	-0.37	-0.29	-0.47	0.06	-0.11	-0.44	-0.39	0.30
8	-0.17	-0.09	-0.27	0.26	0.09	-0.24	-0.19	0.19
9**	-0.32	-0.24	-0.42	0.11	-0.06	-0.39	-0.34	0.27

*The Aerospace Corporation [*Guild et al.*, 2009] recommended combination for GEO
**Manufacturer's commonly used model combination for GEO.

The difference between the modeled and measured average annual degradation ranges from 0% to 0.78%. The lowest difference, 0% was for the trapped electron model AE8-MAX alone. The highest deviation, 0.78%, was for the IGE2006 model for trapped electrons in GEO alone. The model combination with the least deviation, 0.14% on average, compared with the observed degradation for all of the cell cases was Trial #2, AE8-MAX alone. The average of the absolute value of the deviation in the predicted and on-orbit average annual degradation, shown on the far right of the table, was a minimum at 0.137%, shown as 0.14% in the table above) and a maximum of 0.43%. The maximum and minimum absolute value of the deviation coincide with the model

combinations that produced the maximum deviation, 0.78%, and the minimum deviation of 0%.

Based on the comparison of the overall average of the absolute value of the deviation in the modeled and observed solar array degradation, the addition of 2 mils of adhesive more accurately predicted the observed degradation by 0.02% - 0.04% for model combinations 3 - 9. The addition of adhesive predicted the same overall average deviation in model 2, AE8-MAX alone, and caused more deviation for the first model combination, IGE-2006 alone.

In Section 5.6.3 and 5.6.5 we present a similar analysis to that presented in Sections 5.5.3 and 5.5.4, but for GaAs cells behind 4 mils of coverglass behind 4 mils of coverglass and 2 mils of adhesive.

5.6.3 Comparison of On-orbit Si Cell I_{sc} Degradation and Expected Modelled Solar Cell Degradation for a GaAs Cell behind 4 mils of coverglass and 2 mils of adhesive

The predicted GaAs solar cell degradation of I_{sc} behind 4 mils of coverglass and 2 mils of adhesive for a 15 year GEO mission is shown in Table 25, along with the 1 MeV equivalent electron fluence for the mission and the calculated average annual percent degradation computed using Eq. 12.

Table 25. Solar Cell Degradation Predictions for 15-year GEO Mission for GaAs cells with 4 mils of coverglass and 2 mils of adhesive

Trial No.	Models Included	1 MeV Equiv. Elec. Fluence (ele/cm^2)	I_{sd}/I_{sco}	Average Annual % Degradation
1	IGE2006	1.31E+14	0.939	0.41
2	AE8-MAX	3.57E+14	0.899	0.67
3	ESP 90th	1.51E+14	0.934	0.44
4	ESP 95th	1.75E+14	0.930	0.47
5	JPL91 Extended	1.14E+14	0.943	0.38
6*	IGE2006, AP8-MIN, ESP 90th	2.82E+14	0.911	0.60

7	IGE2006, AP8-MIN, ESP 95th	3.06E+14	0.907	0.62
8	IGE2006, AP8-MIN, JPL91 Extended	2.45E+14	0.917	0.56
9**	AE8-MAX, AP8-MIN, JPL Extended	4.71E+14	0.884	0.77

*The Aerospace Corporation [*Guild et al.*, 2009] recommended combination for GEO
**Manufacturer's commonly used model combination for GEO.

The 1 MeV equivalent fluence for the nine trials presented in the table above, Table 25, are less than those presented in Table 21 for cells behind only 4 mils of coverglass. This is expected because the addition of adhesive simulated in Table 25 will absorb more particles than compared to coverglass alone.

Section 5.6.4 compares the modeled average annual percent degradations of four GaAs solar cells behind 4 mils of cg and 2 mils of adhesive presented in Table 25 with the on-orbit I_{sc} telemetry of four GaAs solar cells behind 4 mils of cg and 2 mils of adhesive (the authors are certain that several arrays incorporate 4 mils of coverglass and 2 mils of adhesive, but were not able to obtain this information from all operators) The four GaAs cells are designated as AA, BB, CC and DD. It is important to remember that the cells on-board these arrays are diagnostic cells that are used as a proxy of degradation for the entire array.

5.6.4 Comparison of On-Orbit GaAs Cell I_{sc} Degradation and Expected Modelled Solar Cell Degradation for a GaAs Cell behind 4 mils of coverglass and 2 mils of adhesive

The difference in the observed average annual percent degradation of GaAs cells AA-DD and modeled average annual percent degradation produced from the nine model combinations for cells behind 4 mils of coverglass and 2 mils of adhesive is presented in Table 26.

Table 26. Comparison between On-Orbit Measurements and Models of GaAs Cell Average Annual Percent Degradation for Cells with 4 mils

coverglass and 2 mils of adhesive. The far right column is the average of the absolute value of the deviations.

Trial No.	AA	BB	CC	DD	Average
1	0.33	0.11	0.03	0.23	0.18
2	0.07	-0.15	-0.23	-0.03	0.12
3	0.30	0.08	0	0.20	0.15
4	0.27	0.05	-0.03	0.17	0.13
5	0.36	0.14	0.06	0.26	0.21
6**	0.14	-0.08	-0.16	0.04	0.11
7	0.12	-0.10	-0.18	0.02	0.11
8	0.18	-0.04	-0.12	0.08	0.11
9*	-0.03	-0.25	-0.33	-0.13	0.19

*The Aerospace Corporation [*Guild et al.,* 2009] recommended combination for GEO
**Manufacturer's commonly used model combination for GEO.

The range of differences for the GaAs cells behind 4 mils of cg and 2 mils of adhesive was 0% – 0.36%. The lowest deviation of 0% used the transient solar particle model ESP90% alone. The highest difference, 0.36%, was using the JPL Extended models alone. The average of the absolute value of the deviation in the predicted and on-orbit average annual degradation, shown on the far right of the table, was a minimum at 0.11% and a maximum of 0.21. The maximum deviation did coincided with the model combination that produced the maximum specific deviation, 0.36%, but the minimum did not correspond with the minimum specific deviation.

Based on the comparison of the overall average of the absolute value of the deviation in the modelled and observed solar array degradation, for GaAs the inclusion of adhesive yields less deviation, or a more accurate prediction of 0.01 – 0.05%, for model combinations 2, 7, and 9. The models predicted the same value with the inclusion of coverglass for model combinations 6 and 8, and the inclusion of adhesive yields more

deviation of 0.01 – 0.04%, or a less accurate prediction, for model number 1, and 3-5.

For the analysis that includes coverglass adhesive in the modeling scenario for GaAs cells, model combinations 6-8 produced the smallest difference between observed measurement and model, on average of 0.11% across the four cells, compared with the other model combinations.

5.7 Summary

A common design rule-of-thumb is that silicon solar cells in GEO will experience approximately 25% degradation over 10 years in orbit. While this may have been true in the mid-1990s, we show that due to the development of solar cell technology today this design assumption no longer holds [*Bailey and Flood*, 1998]. Our results show that degradation rates for silicon cells have decreased and are now approximately 10% over a 10 year mission. The decrease in the observed degradation compared with predicted appears significant enough to suggest an update to the design rule-of-thumb for Si solar cell degradation (25% cell degradation over 10 years at GEO). This difference is likely due to the developments in silicon solar cell technology, such as improvements in surface passivization, bulk lifetimes, contact passivization and light trapping in the cell. These improvements all contribute to an overall increase in the cell efficiency and could also reduce degradation [*Green*, 2009].

The average annual percent degradation for Si cells ranges from 0.71% to 1.69% per year over the mission life, with an overall average of the "average annual percent degradation" equal to 1.04%. As expected, our analysis showed that GaAs cells experience less degradation than Si cells. The average annual percent degradation for GaAs cells ranged from 0.44% to 1.03%. The total average degradation, or the average of all of the individual average annual GaAs array degradations, is approximately 0.67%, which is roughly 0.37% less than the total average annual degradation of silicon solar cells.

The eleven GEO satellites used in this analysis launched between 1990 and 1998. Interestingly for both GaAs and Si, the years in which maximum degradation occurred coincided with the years of the six largest 10 MeV Proton SPEs of > 10,000 pfu between 1990 and 2014. These sixe SPEs occurred in years 2000, 2001, and 2003. To determine if the degradation experienced over the SPEs had functional relationship with the accumulated fluence or fluence/hour (flux), we plotted the degradation over the accumulated fluence and the degradation over the SPEs normalized to the time length of the SPEs measured in hours. Linear fits were applied to the four data sets (Si and GaAs degradation over the SPEs and Si and GaAs degradation normalized to an hour of the SPE). Equations for linear curve fits reached a maximum R^2 value of 0.8. Analysis of additional on-orbit solar cell telemetry, for Si and GaAs cells that were operational during a minimum of years 2000 to 2004, could help develop a functional relationship between SPE proton flux and solar array degradation.

We also compared the difference between solar array degradation models and on-orbit solar array degradation measured from satellite telemetry. The results show that the models predicted an average annual percent degradation in I_{sc} to within <0.8% accuracy of the observed on-orbit value for Si cells and to within <0.4% accuracy of the observed on-orbit value for GaAs cells. When looking at the overall average across all of the satellites of the absolute value of the deviations in the modeled and observed solar array degradation, the models predict within <0.43% accuracy for Si and within <0.36% for GaAs.

Table 27 summarizes the models that provided the largest and smallest overall average of the absolute value of the deviation of the model and observed solar array degradation for all four simulated scenarios: Si and GaAs cells with 4 mils of coverglass and Si and GaAs cells with 4 mils of coverglass and 2 mils of adhesive. The values in Table 27 have been normalized to the observed degradation.

Table 27. Summary of Differences Between the Overall Average of the Absolute Value of the Expected Annual Average Degradation On-orbit and models, normalized to the observed degradation.

	Min. Difference (%)	Model for Min. Difference	Max Difference (%)	Model for Max. Difference
Si with 4 mils cg	0.14	AE8-MAX	0.44	IGE-2006
Si with 4 mils cg, 2 mils adhesive	0.13	AE8-MAX	0.47	IGE-2006
GaAs with 4 mils cg	0.17	ESP 95%	0.46	AE8-MAX, AP8-MIN, JPL Extended
GaAs with 4 mils cg, 2 mils of adhesive	0.18	IGE2006, AP8-MIN, JPL91 Extended	0.37	AE8-MAX, AP8-MIN, JPL91 Extended

For simulations behind 4 mils coverglass and for 4 mils coverglass with 2 mils of adhesive, AE8-MAX alone produced the closest output from a model compared amongst the nine combination of models for Si cells. Model combination 8, IGE2006, AP8MIN, JPL91 Extended, and model combination 4, ESP 95th alone produced the least deviation amongst the nine combination of models for GaAs cells. More telemetry is required before it is appropriate to conclusively prescribe which model combination is the "best" model combination to use.

For Si cells, the smallest deviation in predicted and observed degradation occurred using trapped electron models alone. Future work pertaining to the solar cell degradation could also involve the investigation of the role of high energy electrons in cell degradation at GEO, and whether or not trapped electron models alone should be used in degradation modeling.

Chapter 7 and Chapter 8 present and discuss the root-cause analysis of solid state power amplifier anomalies onboard eight of Inmarsat's geostationary communications satellites.

Chapter 6. GEO COMSAT Power Amplifiers: Context and Telemetry Data Description

Despite market uncertainty and the bankruptcy of several commercial satellite companies in the 1980's and 1990's, telecommunications represents the most profitable commercial satellite application today. Future growth is predicted to accommodate the high demand for video and multimedia content distribution [*Aloisio et al., 2010*]. Geostationary communication satellite designs continue to evolve to meet the demand for higher bandwidth, data rates, smaller process features, higher power satellites, higher efficiency components, and reduced mass and size [*Robbins et al.,* 2005; *Rapisarda et al.,* 2010; *Murthy et al.,* 2011; *Bijeev et al.,* 2011]. As satellite systems increase in capability, complexity, and introduce higher efficiency and smaller process-size components, they may become more susceptible to environmental effects [*Baker,* 2000; *Denig et al.,* 2010]

Improving the efficiency of a communications satellite means improving the primary RF high power amplifier technologies onboard the payload [*Rapisarda et al.,* 2010]. RF power amplifiers are used to amplify an uplinked signal prior to retransmission (downlink). The uplinked signals experience substantial losses (free-space path loss, transmission line loss, and polarization loss) and must be amplified to survive similar losses during downlink for sufficient receiver detection [*Robbins et al.,* 2005, *Kaliski,* 2009; *Colantonio,* 2009]. RF power amplifiers consume 80-90% of the spacecraft bus power [*Illokken,* 1987; *Strauss,* 1993]. Therefore, amplifier DC to RF power conversion efficiency is of primary importance. Increased efficiency means decreased waste power in the form of heat which affects thermal management, payload capability, and spacecraft size and mass [*Kaliski,* 2009; *Strauss,* 1993, *Komm et al.,* 2000].

Traveling wave tube amplifiers (TWTAs) and solid-state power amplifiers (SSPAs) are the two primary types of high power amplifiers onboard communications satellites. Demand for higher power at higher frequencies has historically favored the use of TWTAs, as traditional SSPA technology at equivalent power, frequency and bandwidth levels was previously unavailable [*Robbins et al.,* 2005, *Weekley and Mangus,* 2005]. Recent technological advancements, such as linearization, miniaturization and new device materials like GaN, have leveled the playing field for SSPAs. These advancements motivate new trades and

analyses of amplifier characteristics during the communications satellite design process [*Kaliski,* 2009, *Strauss,* 1994].

6.1 SSPAs and TWTAs: Current capabilities and Future trends

In this chapter, we review current TWTA and SSPA technologies available for space-based applications, and discuss future directions for these technologies. SSPAs are the focus of the root-cause anomaly analysis presented in Chapter 7. While TWTAs are not thoroughly investigated, the authors find TWTA technology interesting in comparison to SSPAs, and therefore include descriptions of the component in the following subsections. Additionally, Appendix B contains a related analysis of the capabilities of amplifier technologies onboard 565 communications satellites payloads launched between 1982 and 2016.

6.1.1 Traveling Wave Tube Amplifiers (TWTAs)

Traveling Wave Tube Amplifiers, or TWTAs, were the first successful RF power amplifier technology for communication systems [*Strauss,* 1993]. TWTAs were extensively used in satellite payloads at the birth of the space age in the 1960s and were exclusively used on 69% of all geostationary communications satellites between 1992-2006 [*Strauss,* 1993; *Mallon,* 2008]. This section describes the physical amplification process behind TWTA technology and the advantages and disadvantages of these devices.

TWTAs consist of an electronic power conditioner (EPC) and a traveling wave tube (TWT). The EPC consists of several components, including DC-DC and DC-AC converters, protection circuits, and telecommand-telemetry circuits [*Bijeev et al.,* 2011]. Understanding the intricacies of the devices is important in conducting anomaly analyses. The EPC directly interfaces with the satellite bus primary power system and converts the satellite bus voltage to the necessary electrode voltage (kV DC) for the TWT [*Komm et al.,* 2000]. The EPC can supply thousands of volts of regulated voltage for stable TWT output power (minimizing the impact of effects such as intermittent power generation and thermal

variation experienced during periods of sunlight and eclipse) [*Bijeev et al.,* 2011, *Cuignet et al.,* 2013].

The TWT is a vacuum electron device that consists of an electron gun, a slow wave structure (SWS), a magnetic focusing system, RF input and output couplers, and a collector. As noted, the TWT requires a conditioned power source for supplying voltage to the electron gun. When voltage is supplied, the electron gun emits an electron beam from a cathode heated to 1000 degrees Celsius. The electron beam is injected into the SWS, which includes a magnetic focusing system that confines the beam as it travels down the center of the SWS. For space-applications, a simple helix SWS and a coated tungsten matrix (M-type) cathode have typically been used. The helix SWS provides the greatest dispersion control and greatest operating bandwidth; the coated tungsten matrix cathode provides high mean currents and is capable of surviving and functioning under severe vibration and shock levels [*Coaker and Challis,* 2008]. New methods for cathode fabrication can replace the metal composites of the cathode with a micro-fabricated silicon substrate with enhanced electric field features [*Qiu et al.,* 2009].

The RF signal, at the desired power and frequency, is injected through the input coupler onto the SWS. The SWS extends from the RF input coupler to the RF output coupler. An energy exchange occurs between electron beam particles and the RF wave as both travel down the SWS at similar speeds; this energy exchange generates the amplification of the RF signal. Attenuators prevent the wave from traveling back to the cathode, and a collector is located at the end of the helix coil, where the spent electron beam is deposited. Approximately 70% of the total consumed power is converted into RF energy and the remaining 30% is converted to waste heat. The largest fraction of waste heat is in the collector; one of the primary focuses for improving amplifier efficiency is to reduce the fraction of waste heat [*Komm et al.,* 2000]. Passive thermal control including heat pipes and surfaces of high emissivity are used to dissipate the concentrated heat in the payload [*Murthy et al.,* 2011].

TWTAs are uniquely rated in terms of saturated power level, which is the key metric for output power regardless of increased input level. Thus, devices often operate at an RF output backed-off from saturation. When TWTAs are operated in a saturation mode, consumed power

converted into useful RF energy decreases and power converted into waste heat in the collector increases. When operating in saturation, interference can occur due to intermodulation distortion (IMD) that can generate unwanted frequencies outside of the designed channel. The saturation power level and the amplifier operating point, in terms of output back off (OBO), must both be carefully engineered to minimize power consumption and IMD [*Mallet et al.,* 2006]. IMD is not only an issue for TWTAs, but also for solid-state devices (SSPAs) [*Komm et al.,* 2000; *Qiu et al.,* 2009]. Figure 22 shows a schematic of two L-3 Communications Electron Technologies, Inc., TWTA devices.

(a) (b)

Figure 22. L-3 Communications Electron Technologies, Inc. TWTA devices: a) Ku-band TWT [*Menninger et al.,* 2013] and b) V-band TWTA [*Robbins et al.,* 2012]

6.1.1.1 TWTA Failure Mechanisms

The majority of power amplifiers tend to live beyond their expected lifetime of 15-20 years. Amplifier failures do occur. It is generally assumed that these failures are related to the cathode design. A study of ~90 Boeing satellites concluded that TWTA failures were more likely to occur in early years of life [*Nicol et al.,* 2008]. Traveling wave tube (TWT) failures that occur are often due to interface problems, poor workmanship or material defects [*Illokken,* 1987]. Failures have significant impact on the satellite systems, and a single failure can range from gradual power degradation to sudden, unexpected switch off. In the gradual degradation scenario, TWTAs can operate for long periods (on the order of months to years) before failure, as well as experience other anomalies, such as spurious switch offs (SSOs) due to voltage breakdowns, which may be caused by the radiation

environment. Furthermore, TWTAs generally appear to be more robust to the space environment than SSPAs.

6.1.1.2 Advantages and Disadvantages of TWTAs

TWTAs yield higher data rates and greater bandwidth than their alternatives because they have better efficiency at high power and high frequencies with better efficiency [*Bijeev et al.,* 2004; *Robbins et al.,* 2005; *Coaker and Challis,* 2008]. TWTAs can operate at high temperatures, which is an advantage given the challenges of communications satellite thermal management [*Kaliski,* 2009, *Feicht et al.,* 2012].

One of the main concerns cited with TWTA performance is guaranteeing operation for 15-20 years on orbit [*Bijeev et al.,* 2011, *Strauss,* 1993]. Well-designed TWTs have been known to continuously operate more than 100,000 hours and generally reach the 20-year mission lifetime [*Coaker and Challis,* 2008, *Feicht et al.,* 2012]. One disadvantage of the TWTA is the need for kilovolt-level power supplies, which are often heavy and expensive. The power supplies needed for SSPAs are scalable, as SSPAs use 2^N power transistors (e.g., 1, 2, 4, and 8). While this configuration is scalable, it can also lead to significant losses for SSPAs [*Colantonio et al.,* 2009].

6.1.1.3 TWTA Configurations

This section describes approaches to TWTA reconfigurability, current state of the art linearization and modern-day TWTA manufacturing capabilities.

6.1.1.3.1 Flex-TWTAs and Reconfigurability

Currently, increasing payload bandwidth and power is managed by reconfiguration and linearization of the RF power across different beams and channels. The reconfigurable approach uses flexible traveling wave tube amplifiers (flex-TWTAs or bias adjustable TWTAs). These types of TWTAs can redistribute available power in the event of traffic imbalances between multiple beams over time. Flex-TWTAs use a telecommand to modify an amplifier's anode voltage, or bias conditions, which dictates the range of TWT output powers [*Manz,* 2009]. Varying

the anode voltage yields a different cathode current, which produces a different TWT gain and output power. Flex-TWTAs conserve power, which can reduce overall payload scale or allow for additional satellite capacity [*Kaliski,* 2009]. Reconfigurable payloads help manage non-uniform traffic, multi-mission satellites that support both interactive and broadcast data services, and evolving user demands. Reconfigurable designs allow payloads to efficiently combine coverage, power and bandwidth flexibility, while reducing power consumption and cost [*Aloisio et al.,* 2008].

6.1.1.3.2 TWTA Linearization

TWTAs are not inherently linear devices, yet significant progress has been made over the past decade toward their linearization. Linearizers are incorporated in an amplifier system to reduce the distortion of the signal. As saturation is approached, TWTA non-linearity increases and gain compression occurs (an increased input that is not proportional to the increase in output). TWTA nonlinearity can results in power inefficiency and can cause Out of Band Unwanted Spurious (OBUS) emission [*Rapisarda et al.,* 2010].

For TWTAs, predistortion linearizers are commonly used. These linearizers correct non-linearities in the phase and gain of the input/output transfer response [*Cuignet et al.,* 2013]. Digital or hardware predistorters can improve linearity with limited bandwidth and enable higher efficiencies [*Qiu et al.,* 2009]. Linearizer-Channel amplifiers (LCAMPS) have also been implemented in systems to manage the input power. These amplifiers provide either controlled constant gain to the input signal, known as Fixed Gain Mode, or a constant output level over the dynamic range of input power [*Cuignet et al.,* 2013].

6.1.1.3.3 Current TWTA Manufacturer/Supplier Capabilities

While TWTAs are not the focus of the analysis presented in this thesis, we believe it is important to discuss the current status and future plans for both high power amplifier technologies. Determining the current state of TWTA technology is difficult due to restrictions on the publication for proprietary and security reasons. Since the launch of

Syncom II in 1963, TWTA technology has increased RF power output, efficiency and packaging compactness [*Robbins et al.,* 2005; *Bijeev et al.,* 2011]. The current primary space TWTA suppliers are L-3 Communications Electron Technologies, Inc. (headquartered in Torrance, CA, USA), which provides TWTs, EPCs and LTWTAs (which are integrated EPCs, TWTs, and linearizers), L-3 Narda Microwave-West (headquartered in Folsom, CA, USA), which provides LCAMPs, Thales Electron Devices (headquartered in Ulm, Germany), which provides TWTs, and Tesat Spacecom (headquartered in Backnang, Germany), which provides EPCs and LCAMPs.

L-3 Communications Electron Technologies, Inc. provides publicly available data for their EPCs and TWTs [*L-3 Communications,* LTWTA]. The space-qualified EPCs are available with conduction or radiation cooling, and for both regulated and unregulated bus voltages. The EPCs are capable of up to 94% efficiency, with mass ranging from less than 1.2 kg to 1.75 kg, and DC processed power up to 600 W. L-3 Communications Electron Technologies, Inc., also provides space qualified TWTs in all frequency bands between L-band and Ka-band. These TWTs have efficiencies of up to 72% and power ranges from as low as 20 W (C-band, X-band and Ka-band) to as high as 300 W for S-band. TWTA efficiencies are currently about 65%, which is the combined efficiency of the EPC and TWT – each have individual efficiencies up to 94% and 72% respectively for L-3 Communications Electron Technologies [*L-3 Communications,* LTWTA]. In terms of mass and size, the TWT mass ranges from 0.76 kg to 3.2 kg and the size ranges from 11.3 x 3.0 x 2.5 inches for K-band to 28.0 x 6.5 x 6.5 inches for L-band.

6.1.1.4 Future TWTA Technology

Although TWTA technologies have improved significantly in the past, there is not as clear of a potential for future improvement for TWTAs compared with the potential advances using GaN for SSPAs, which we discuss in Section 6.1.2.4.

One potential advancement for the TWTA is the increased use of Mini-TWTs. Mini-TWTs are a shorter (approximately 7 inches long), lighter, and lower-power version of the traditional TWT, but cannot achieve as high of an RF output power. Mini-TWTs are considered advantageous

as they can provide a 5:1 reduction in size and weight as well as a 50% improvement in efficiency. Mini-TWTs also serve as the basis of Microwave Power Modules (MPMs), which are compact units that consist of a solid-state RF power amplifier and a mini-TWT integrated with power and control circuits [*Manz,* 2009].

We expect TWT manufacturers to continue to incrementally improve TWT and power supply integration, increase frequency coverage, improve efficiency and reliability, and reduce size, weight and cost. As previously mentioned, the efficiency is limited by the amount of consumed power that is not converted into RF energy, but that is converted into waste heat. The physical limitations on increasing the efficiency of these devices relates to the practicality of adding collector stages (four stages are used in practice), given the size, mass and cost limits of the system.

6.1.2 Solid State Power Amplifiers (SSPAs)

SSPAs were first used in space in the late 1970's in the form of bipolar junction transistors (BJTs) and GaAs metal-semiconductor field effect transistors (MESFETs) [*Colantonio et al.,* 2009]. SSPAs became more common for communication applications in the 1980s, when the ability of an SSPA to output RF power of 5-10 Watts became a viable alternative to the TWTA. Historically, SSPAs have been used at lower frequencies such as L and S band with output powers of approximately 10 W. Low-frequency SSPAs have lower mass compared with similar-capability TWTAs of the same capability [*Kaliski,* 2009]. While SSPAs are still generally preferred for lower frequency bands and for lower transmitter power applications [*Colantonio et al.,* 2009], SSPAs have also been used for higher power levels (e.g. 20-40 Watts) despite having lower efficiencies (by as much as 30%) than TWTAs at these power levels [*Strauss,* 1993].

Like TWTAs, SSPAs generally have an electrical power conditioner (EPC). Unlike TWTAs, SSPAs use a field effect transistor (FET) as their primary means of RF power amplification. To achieve high power amplification, many power transistors are placed in parallel and the device outputs are combined. Dissipation of the heat generated from this process is a design challenge, and failure to adequately limit heat from

the devices can ultimately destroy the RF system [*Colantonio et al.,* 2009].

For space applications, the two primary types of SSPA technology use field effect transistors (FETs): GaAs MESFETs and GaAs high electron mobility transistor (HEMT) devices. HEMT devices are more commonly used in space today [*Colantonio et al.,* 2009].

Understanding the device physics behind SSPAs is relevant in understanding its susceptibility to radiation damage. MESFETs consist of an n+ source region that is grounded and an n+ drain region that is positively biased, with an n-channel between the two terminals [*Taylor and Bayruns,* 1985]. The channel is connected to the gate by a Schottky junction, which limits trap formation in the gate insulator and enables higher frequency operation [*Sze,* 2001]. When a negative gate source voltage is applied, the metal semiconductor junction is reverse biased. A depletion layer in the channel is formed and enables the control of current flow between the drain and source [*Colantonio et al.,* 2009]. The performance of the device is dictated by the length, width and depth of the channel and by depletion layer width [*Sze,* 2001]. For example, the length of the channel defines the time required for electrons to travel through the channel and determines the cutoff and maximum frequency of the device. MESFETs are generally fabricated with GaAs, a III-V semiconductor, and are capable of operating at frequencies approaching W band [*Colantonio et al.,* 2009].

HEMT devices are variations of MESFET devices and consist of a junction between two materials of different band gaps, known as a heterojunction. The two materials are a highly-doped wide-bandgap n-type donor-supply layer (generally AlGaAs) and an undoped narrow bandgap channel layer (generally GaAs). The heterojunction forms a potential well in the undoped GaAs, where highly mobile electrons are free from colliding with impurities and the electrons cannot escape the potential well. The heterojunction also leads to the formation of the two-dimensional electron gas (2-DEG) in the undoped GaAs layer enabling a 2x higher frequency response, which is why HEMTs are used over MESFETS for microwave applications [*Paylidis,* 1999].

The SSPA shown in Figure 25 was flown onboard ALPHASAT, with a nominal RF output power of 15W with an efficiency of 31% [*Airbus Defence and Space,* L/S-band].

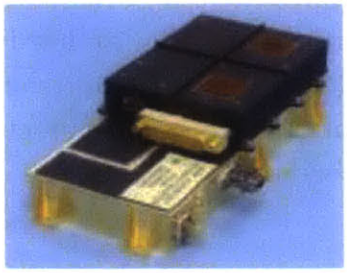

Figure 23. Airbus Defence and Space (formerly Astrium) L/S Band SSPA for mobile communications satellites [*Airbus Defence and Space,* L/S-band]

6.1.2.1 SSPA Failure Mechanisms

SSPAs failures can occur for reasons including extended use (age) and workmanship [*Strauss,* 1993]. Within an SSPA, the EPC and the RF output stage generate substantial heat; stresses and degradation due to thermal forcing can lead to amplifier anomalies as well. SSPAs onboard spacecraft are also susceptible to the harsh radiation environment, which may induce anomalous performance as a result of surface charging, internal charging that could lead to ESD. A more detailed analysis of SSPA failure mechanisms related to the space environment is discussed in Chapter 7.

Operators classify SSPA anomalies as either "soft" or "hard" anomalies failures. Soft anomalies occur in one of the output stages when low current conditions are observed. The "soft" and "hard" anomalies terminology is not commonly used with TWTA anomalies, which are generally assumed to be hard. Soft anomalies are considered recoverable, and do not require the use of a redundant SSPA. Hard anomalies can occur when a drive stage fails or due to extended use. These anomalies are not recoverable, and a redundant SSPA must be turned on to continue providing the required output power [*Lohmeyer and Cahoy*, 2013].

Both hard and soft anomalies are identified when spacecraft health telemetry, such as the SSPA current used in this work, falls below a predefined threshold for nominal performance. Thresholds are established to monitor the health of components and notify operators when the component experiences anomalous performance. The threshold setting is specific to particular hardware; for example, the SSPA current thresholds for Fleet A SSPAs and Fleet B SSPAs are different because the configurations, manufacturers, and/or model of these components are different.

6.1.2.2 Advantages and Disadvantages of SSPAs

The basic SSPA RF module is comparatively smaller in mass, more compact, lower in cost, and has superior intermodulation performance to provide higher linearity [*Escalera et al.,* 2000; *Sechi and Bujatti*, 2009] compared with TWTAs. SSPAs are also considered safer for personnel in comparison to the TWT, and require lower voltage (5-10 V DC for GaAs FET types, compared to kilovolts for the TWTA cathode and collector) [*Raab et al.,* 2009].

The primary disadvantages of SSPAs include high current draws, lower efficiencies at high frequencies (due to the inability to match the load impedance because of parasitics, model differences and device variations), and lower power generation than TWTAs. The power FETs in the SSPAs generate large amounts of heat; this is one of the most challenging SSPA design problems. While the basic RF module is smaller compared with TWTAs, the required heat sinks typically cause the overall SSPA package to be larger than the TWTA [*Colantonio et al.,* 2009].

6.1.2.3 Current SSPA Technology

Several of the leading manufacturers/suppliers of SSPAs for space-based applications are Airbus Defence and Space (headquartered in Toulouse, France), Thales Alenia Space (TAS) (headquartered in Cannes, France), L-3 Communications Narda Satellite Networks (headquartered in New York City, USA), Mitsubishi Electric (Melco) (headquartered in Tokyo, Japan), NEC Toshiba Space Systems Ltd.

(headquartered in Tokyo, Japan), and Tesat Spacecom (headquartered in Backnang, Germany).

Similar to TWTAs, publicly available data sheets and component specifications are often limited, and available information may not capture the full extent of device capability. However, the following information was found. Airbus Defence and Space currently builds SSPAs for L-band, S-band, and C-band. The L- and S-band devices produce output powers of 15 W with 31% efficiency, and have a nominal gain of 67 dB. The mass of these devices is approximately 0.75 kg with an operating temperature range of -20°C to +75°C [*Airbus Defence and Space,* L/S-band]. The Airbus Defence and Space C-band SSPA has an output power capability of 20 W with an efficiency of 37%, and a nominal gain of 70 dB. The mass of this device is 1.285 kg, and it has an operating temperature range of -30°C to +75°C [*Airbus Defense and Space,* C-band]. NEC Toshiba Space Systems also provides L-band, S-band and C-band SSPAs. The output power and nominal gain of the L-band SSPA is 55 W and 61 dB, and the output power and nominal gain of the S-band SSPA is 24 W and 70 dB [*NEC Toshiba,* L-band; *NEC Toshiba,* S-band]. The NEC Toshiba Space Systems C-band SSPA is specified to have an output power of 20 W and 86 dB nominal gain [*NEC Toshiba,* C-band].

Additionally, TAS provides efficiency and mass specifications of their C-band, X-band, Ku-band and Ka-band SSPA. These four devices have efficiencies of 36%, 25%, 15%, and 10%, respectively. The masses of these four devices range from 1 – 1.5 kg, with the Ka-band SSPA at 1 kg, and the X-band SSPA at 1.5 kg. [*NEC Toshiba,* C-band]. Melco provides a C-band SSPA, which is capable of 60 W output power, has 48% efficiency, has a nominal gain of 84 dB, and a mass of 1.9 kg [*Melco,* C-band].

6.1.2.4 Future SSPA Technology

Recent development of GaN HEMT SSPAs is expected to level the playing field with improved efficiency, linearity, power density, and reliability [*Kaliski,* 2009, 15]. SiC is also considered promising for MESFET designs, yet the current material cost has been cited as the limiting factor in the development of SiC devices for space based applications [*Raab et al.,* 2003].

In GaN HEMTs, the heterostructure consists of AlGaN and undoped GaN. Like GaAs, GaN is a III-V semiconductor with a bandgap of 3.2 eV, whereas GaAs has a bandgap of 1.42 eV; the difference in bandgap is indicative of the high power density of the GaN device. The high power density of GaN means smaller devices, which reduces the size, cost and need for thermal management on-board satellite systems [*Colantonio et al.,* 2009]. GaN is also capable of withstanding high temperature environments before performance degradation occurs, whereas GaAs degrades at temperatures greater than 175°C. The EEE-INST-002 quality standard currently prohibits junction temperatures greater than 125°C [*Sahu,* 2008]. GaN also has higher power added efficiency (PAE) and higher breakdown voltage (~100 VDC), which in turn should increase device reliability.

The robustness of GaN HEMT SSPAs in space cannot currently be assessed, as they have yet to be flown commercially, although there are significant efforts from ESA and the DOD to advance their technology development level. Airbus Defence and Space has several data sheets published on their GaN technologies. Their 1.05 kg GaN S-band SSPA is capable of achieving 85 W nominal RF output power with 40% DC to RF conversion efficiency [*Airbus Defense and Space,* 85W S]. Airbus Defence and Space also has a 1.35 kg GaN C-band SSPA capable of a nominal output power of 80 W [*Airbus Defense and Space,* 80W C]. Other vendors, such as NEC, Melco TriQuint, Northrop Grumman, RFH IC, and Sumitomo, have also developed GaN devices, but do not publicly publish specifications for their devices.

6.2 Data Acquisition of GEO COMSAT Amplifier Telemetry

To obtain the desired telemetry and satellite information for the SSPA analysis in this thesis, we collaborated with Inmarsat, a telecommunications company based in London, U.K., to analyze 665,112 operational hours of satellite telemetry data from eight satellites on two of Inmarsat's satellite fleets operating between 1996 and 2012. There are five satellites in what we will call Fleet A and three satellites in Fleet B.

6.2.1 SSPA Telemetry Management and Anomaly Description

The spacecraft health measurements are continuously recorded (e.g., hourly) and saved and then downlinked to the ground where they are monitored and archived. The satellite telemetry databases are used to identify and investigate both nominal and anomalous satellite component performance. Data on high-power amplifiers (SSPAs and TWTAs), eclipse durations, solar panel data, anomaly lists and SEU information were also obtained. Chapter 7 focuses on the analysis of Inmarsat SSPA telemetry: current, temperature, and the SSPA anomaly logs. We consider all known anomalies present in the operator's archive in this study and discuss future work to analyze data to identify previously unknown anomalies or impacts.

As previously mentioned, operators classify SSPA anomalies into two categories: "hard" anomalies and "soft" anomalies. Of the twenty-six SSPA anomalies in the data set used, only four were soft failures, and 22 were hard failures. Only one of the SSPAs that experienced a soft failure was ultimately able to continue nominal operation. Thus 25/26 SSPA anomalies called for a redundant SSPA unit to be switched on. One of the twenty-six SSPA anomalies that called for a redundant SSPA unit did not have a replacement SSPA available because it had already been switched on from a previous anomaly. Manufacturers and operators have a goal of avoiding scenarios and degradation that result when replacement SSPAs are not immediately available.

When the amplifier is irradiated by high-energy particles that transfer more than the radiation ionization energy to the semiconductor, an electron hole pair forms in the semiconductor material (such as silicon or Gallium Arsenide GaAs) [e.g., *Alig et al.*, 1975]. This changes the charge carrying capability and affects the amplification properties of the transistor of the amplifier, which can cause anomalies to occur [*Bhat et al.* 2005]. Similar to those presented in two studies in *Strauss* [1993], which are further discussed in Appendix B, the Inmarsat SSPAs did not experience a single generic amplifier failure mechanism, but experienced abrupt unexpected anomalies.

Chapter 7 presents an attempt at root-cause investigation of SSPA anomalies potentially due to the space environment. In Chapter 7, possible anomaly sources are investigated in detail using analysis and more sophisticated models. Anomaly sources considered include surface charging, internal charging, eclipse timing, and age.

Chapter 7. GEO COMSAT Power Amplifier Analysis and Results

In order to quantify the effect of space weather on geostationary communications satellites, we focus on one type of component, the solid-state power amplifiers (SSPAs). Space weather effects can modify the operation and efficiency of the amplifiers and cause amplifier anomalies, which in turn will limit the operational lifetime of the satellite. To understand and quantify how space weather can damage power amplifiers requires analysis of enough space weather and satellite anomaly data such that valid statistics and relationships can be inferred, along with a detailed understanding of the space environment and specifics about the configuration of the affected spacecraft systems and components [*Baker,* 2002; *Tretkoff,* 2010].

Over time, energetic particles can deposit themselves into an amplifier's material and change the charge mobility that was originally determined by the dopant concentrations of an amplifier's material. The change in charge mobility, which is a radiation dose type mechanism, leads to a change in conductivity that will affect amplifier current, which is a parameter monitored and tracked in housekeeping telemetry. If radiation dose was the sole contributor of an anomaly it would be likely that the anomalies would all occur around the same time, after having received a given amount of dose.

If the current exceeds a predetermined upper threshold, the SSPA will saturate. Non-linear amplification occurs when amplifiers are driven past saturation and this is undesirable as it generates harmonics and distorts the transmitted signal. If the current falls below a predetermined lower threshold, then the SSPA will not provide enough current to adequately amplify the signal.

Weekley and Mangus [2005] note that 80% of SSPA failures disable downlink capability. The general approach to mitigating damage caused by space weather and radiation is to implement high factors of redundancy in design as well as practice conservative operational management. In this work, we use a combination of space weather observation data and on-orbit component telemetry to improve our understanding of the sensitivity of SSPAs to space weather and draw logical conclusions about their probable failure mechanisms.

7.1 Approach

Choi et al. [2011] analyzed the effects of space weather on 95 satellite anomalies from 79 unique satellites archived in the Satellite News Digest between 1997 and 2009. The study noted relationships between anomalies and seasonal dependencies, satellite local time, geomagnetic index *Kp*, and charged particles observed by Los Alamos National Laboratory (LANL) satellites, but did not find any dependence on solar cycle. The study suggested that energetic electrons might contribute to anomalies but noted that the relationship between anomalies and electrons is not well established. *Mazur and O'Brien* [2012] commented on the data population of *Choi et al.* [2011] and emphasized the importance of a careful analysis of the anomaly records. *Thomsen et al.* [2013] analyzed the statistical properties of the surface-charging environment at geostationary orbit and found evidence in support of *the Choi et al.* [2011] conclusions and also noted that an increased probability of surface charging exists during the declining phase of the solar cycle, when the probability of internal charging from relativistic electrons is also elevated.

In this section we will analyze the relationships between anomalies and geomagnetic index *Kp*, magnetic local time, and seasonal dependencies, similar to the study conducted by *Choi et al.* [2011]. We will also study the hazardous particle populations that may affect the components on the geostationary satellites. The particle populations used in this work include low-energy (keV) electrons, which can cause surface charging, and high-energy relativistic electrons, which can cause internal charging, [*Baker,* 2000, 2002; *O'Brien et al.,* 2013]. We focus on electrons because our preliminary analysis does not support an association between the SSPA anomalies and the occurrence of solar flares (as defined in the NOAA warnings for extreme solar flares), or strong ring current (large negative *Dst*) events [*Lohmeyer et al.,* 2012].

The purpose of this analysis is to improve the understanding of the effects of space weather on geostationary satellites and focus on specific types of component anomalies that have multiple occurrences across similarly configured systems. A total of eight Inmarsat satellites are considered in this study. There are five satellites that we will refer to as Fleet A and three satellites in Fleet B. Analyzing data from five

satellites of the same fleet and then comparing the results with a second three-satellite fleet provides insight into both how space weather effects similar components and systems within each fleet, and lets us assess in-family behaviors and trends that are may be the same or different between the two fleets.

As mentioned in Section 6.1.2, power amplifiers are a critical component in all radio frequency satellite communication systems: They amplify the uplink signals received by the satellite from the ground before retransmitting the downlink signals to the users on the ground [*Strauss*, 1993].

Since 1996, the eight Inmarsat satellites have experienced 26 solid-state power amplifier (SSPA) anomalies; individually, each satellite has experienced between zero and eight SSPA anomalies.

SSPA anomalies have occurred as early in a satellite's lifetime as in the first 3 months of operation and as late as nearly 15 years of operation. All known SSPA anomalies present in the Inmarsat archive for these two fleets are considered in this study; none were removed. There is no identified or confirmed cause for any of the 26 anomalies, and thus, they are considered to be "random" failures [e.g., *Weekley and Mangus*, 2005]. Due to the fact that satellites are not returned to Earth for anomaly investigation, the actual cause of the individual SSPA anomalies is challenging to diagnose [*Thomsen et al.*, 2013; *Choi et al.*, 2011; *Baker*, 2000]. However, the effects of high-energy particle radiation from relativistic electrons and low-energy electrons are expected to have a major role [*Baker*, 2000].

7.1.1 Space Environment Data Acquisition for High Power Amplifier Analysis

In this chapter, 26 total SSPA anomalies are compared with observations of the space weather environment to attempt a root-cause investigation. Specifically, the SSPA telemetry is compared at the time of the anomaly to high-energy relativistic electrons, which can cause internal charging, and low-energy electrons, which can cause surface charging. Five of the 26 anomalies unfortunately do not have corresponding science observations (specifically, they do not have

electron flux data in the LANL data set), so part of this study focuses on the 21 anomalies that have corresponding science observations available.

The OMNI2 data set is the primary data set used in this study and was obtained from the Goddard Space Flight Center/Space Physics Data Facility OMNIWeb interface at http://web.gsfc.nasa.gov. OMNI2 contains hourly measurements of near-Earth solar wind magnetic field and plasma parameters, as well as the *Kp* index (which is used as a proxy for low-energy electrons), the disturbance storm time (*Dst*) index, auroral electrojet (*AE*), and proton flux values. The OMNI2 data come from numerous satellites, such as the Advanced Composition Explorer (ACE) satellite, the International Monitoring Platform satellites, and the Geostationary Operational Environmental Satellite (GOES), as well as from the Data Analysis Center for Geomagnetism and Space Magnetism at Kyoto University in Japan [*King and Papitashvili*, 2004]. High-energy electron flux data (1.8–3.5 and 3.5–6 MeV) were obtained from the Los Alamos National Laboratory (LANL) geosynchronous charged particle instruments [*Reeves et al.,* 2011].

We also use the energetic particle data (>2 MeV electron flux) from the GOES satellite that is longitudinally closest to the respective Inmarsat satellite that experienced the anomaly. The closest GOES satellite is located within 60° of longitude from the Inmarsat satellite for 15 of the 26 anomalies. The farthest separation between a GOES satellite and an Inmarsat satellite was for two of the SSPA anomalies, when the closest GOES satellite was located 160° from the Inmarsat satellite. Interpretation of results should keep these longitudinal separations in consideration.

7.1.2 Severity of Amplifier Anomalies

When the amplifier is irradiated by high-energy particles that transfer more than the radiation ionization energy to the semiconductor, an electron hole pair forms in the semiconductor material (such as silicon or gallium arsenide, (GaAs)) [e.g., *Alig et al.,* 1975]. This changes the charge carrying capability and affects the amplification properties of the transistor of the amplifier, which can cause anomalies to occur [*Bhat et al.*, 2005].

The shielding and the mounting location of the satellite hardware play an important role in protecting components from the harmful effects of the space environment [*Strauss,* 1993]. SSPA units are generally mounted inside the satellite in an electronics box or chassis, where they can be monitored in a thermally controlled environment (thermal management of power amplifiers is a substantial part of communications satellite design). The SSPAs are also somewhat protected from space weather hazards via the external shielding of the spacecraft bus and shielding from other internal units. The typical internal shielding of SSPAs in communications satellites ranges between less than 1mm Al equivalent to slightly more than 3mm Al equivalent depending on the geometric distribution of the internal components. High-energy relativistic electrons (> 2 MeV) and galactic particles are still capable of penetrating the shielding for internal components and can cause anomalies [*Hastings and Garrett*, 1996]. Depending on the application (orbit and expected lifetime), some devices may require spot shielding. Manufacturers perform ray tracing to determine the amounts of shielding required to sufficiently protect individual components and reduce their potential exposure to the radiation environment [*Schwank et al.*, 2008]. In the event that spot shielding is required, precautions regarding component grounding are also taken.

Due to the relatively high amounts of shielding used and the typical location of the SSPAs (deep within the spacecraft), we are not concerned with the possibility of internal charging from lower-energy substorm-injected electrons. While these electrons can cause surface charging, they are not expected to present a significant risk to the SSPA units. However, we still investigate surface charging as a potential component hazard in this Section 7.2.1.

7.2. Amplifier Anomaly Analysis

Figure 24 shows the smoothed sunspot number from the Solar Influences Data Analysis Center (SIDC) of the Royal Observatory of Belgium (data available at http://sidc.oma.be/sunspot-data/) and the Inmarsat SSPA anomalies between 1996 and 2012. The two satellite

fleets, Fleet A and Fleet B, are designated with different colors (green and yellow, respectively). This period includes part of solar cycle 23 (May 1996 to December 2008) and part of solar cycle 24 (January 2009 to January 2012). The solar minimum for cycle 23 occurred in 1996, and the maximum for cycle 23 occurred in 2002. The solar minimum for cycle 24 occurred between 2008 and 2009 [*Riley,* 2012].

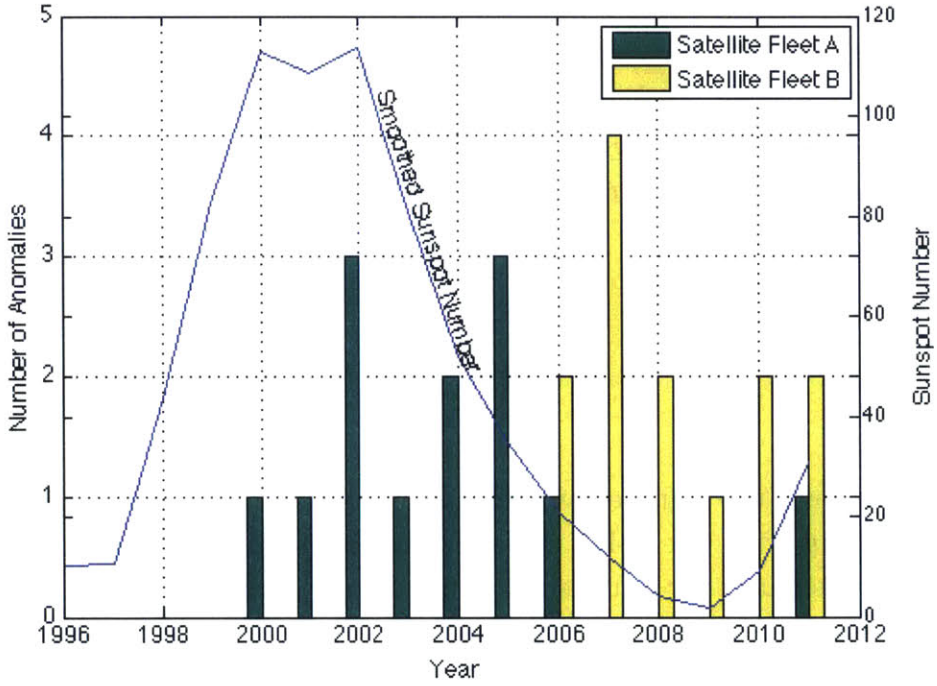

Figure 24. Yearly SSPA anomaly totals per satellite fleet, plotted with the smoothed sunspot number (blue line)

It is important to consider the effects of space weather on Fleet A and Fleet B separately, as they are from different satellite manufacturers. This is because even though the overall function is similar, different components, geometries, shielding, and operational configurations will have different sensitivities to space weather. In theory, we can directly compare "identical" spacecraft within Fleet A and Fleet B, but at the time of analysis Fleet B had not yet experienced a full solar cycle. For the moment, we refrain from drawing conclusions using combined data, we should instead wait until we have enough data such that each fleet has individually experienced a full solar cycle.

There were no SSPA anomalies for either fleet prior to 2000, even though this time period includes launch and the initial years of operation for several of the satellites. The initial operation period is commonly associated with satellite anomalies due to the hazards of the launch environment and orbital repositioning. However, the SSPAs studied here do not appear to have experienced any anomalies during this period. It is important to remember that Fleet A and Fleet B were not launched at the same time. For Fleet A, anomalies occur between 3.5 and 14.5 years of operation, whereas for Fleet B, anomalies occur from less than 0.2 – 7 years of operation. The occurrence of the SSPA anomalies does not show a clear correlation with the satellite or amplifier age [*Lohmeyer et al.,* 2012].

It is interesting to also note that in Figure 24, Fleet A has far fewer SSPA anomalies around solar minimum than Fleet B does; this emphasizes the point that they should be considered on a fleet-by-fleet basis.

Figure 25 shows the number of SSPA anomalies per year per satellite in Fleet A, along with the solar cycle. A similar graph for Fleet B is not shown because data for a full solar cycle do not yet exist.

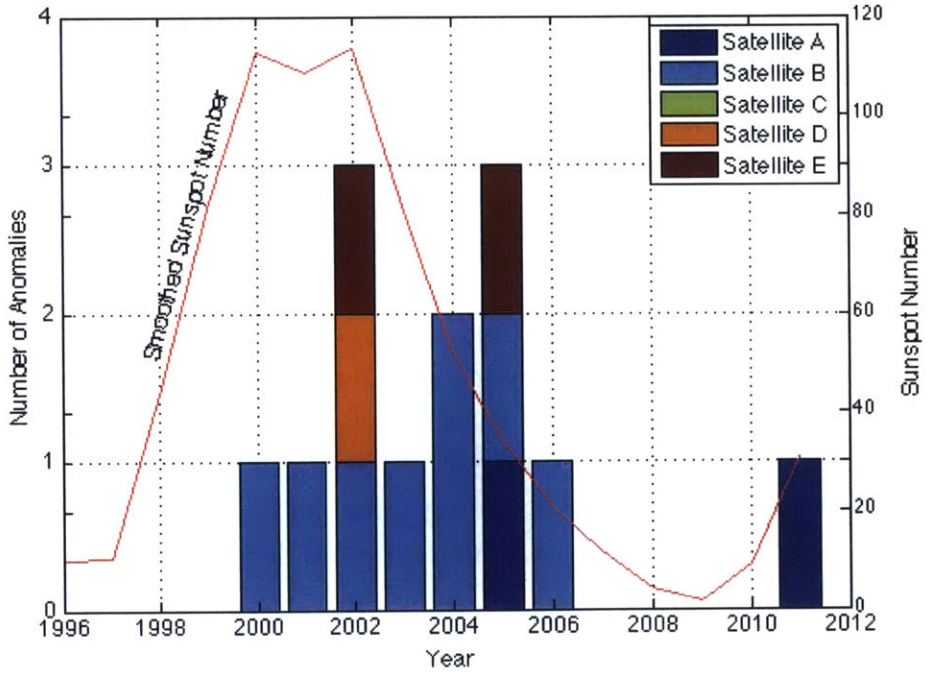

Figure 25. SSPA anomalies per year for Fleet A from 1996 to 2012. Each letter in the legend corresponds to a different satellite in the fleet. Fleet A has data for an entire solar cycle; Fleet B does not.

For Fleet A, no SSPA anomalies occur immediately after launch or even within the first three years of operation. Consistent with *Choi et al.* [2011] study, the SSPA anomalies on Fleet A do not primarily occur at solar maximum, when surface charging anomalies are most likely [*Denton et al.,* 2006], but occur during the declining phase of the solar cycle. The declining phase of the solar cycle is the time when CIRs drive high-speed solar wind streams and produce enhancements of relativistic electrons, notoriously known to cause internal charging [*Shea and Smart*, 1998; *Wrenn et al.,* 2002; *Denton et al.,* 2006; *Miyoshi and Kataoka*, 2008]. Hot electron temperature, which has been found to determine surface-charging levels, also reaches a maximum during the declining phase of the solar cycle [*Denton et al.,* 2006].

It would be useful to be able to tell from the time distribution of the 13 SSPA anomalies aboard Fleet A whether anomalies were due to internal charging caused by higher energy electrons or surface charging caused by low-energy electrons or deep dielectric charging from relativistic electrons. Even if we find a likely relationship for one of these causes in our analysis, we cannot yet completely rule out other causes of anomalies, due to limited data availability. A larger amount of data over a solar cycle would improve our ability to perform a statistical analysis make a clear correlation between SSPA anomalies and space weather. However, we are able to begin this type of approach with the data currently available, with the goal of expanding and improving the analysis in the future. In Sections 7.2.1 to 7.2.3 below, we consider several possible space-weather related causes for the anomalies, and move forward in a more detailed analysis of the most likely space weather related cause.

7.2.1 Low-Energy Electrons, Surface Charging, and the *Kp* Index

Several geostationary satellites have experienced anomalies due to surface charging. For example, the Maritime European Communications Satellite A experienced an uncommanded switching

anomaly believed to be caused by surface charging related to a sudden increase in moderate-energy electrons [*Wrenn,* 1995; *Baker,* 2000]. It is widely acknowledged that surface charging anomalies generally occur between local midnight and dawn [e.g., *Wrenn,* 1995; *Fennell et al.* 2001; *Lanzerotti et al.,* 1998; *Allen,* 2010]. The local time (LT) analysis of the 26 SSPA anomalies is presented in this section.

The *Kp* magnetic disturbance index is often used as a proxy to quantify the relationship between surface charging and magnetospheric convection [*Thomsen,* 2004] which causes hot electron enhancements near geostationary orbit [e.g., *Fennell et al.,* 2001; *O'Brien*, 2009; *Korth et al.,* 1999]. Between 1996 and 2012, only 2.2% of the *Kp* measurements were recorded as greater than a *Kp* of 5, indicating severe geomagnetic activity. However, Denton and Borovsky [2012, Appendix A] found that surface charging still occurs even at relatively low *Kp* values (*Kp* of approximately 2 or 3).

Figure 26 shows the distribution of the *Kp* index from 1996-2012 for (a,b) every *Kp* measurement, (c,d) *Kp* averaged over two days, (e,f) *Kp* averaged over three days and (g,h) *Kp* averaged over two weeks, or fourteen days. The y-axis, labeled Count, represents the number of *Kp* measurements. The *Kp* distributions for Inmarsat Fleet A are shown in Figure 26(a,c,e,g). Each Fleet A anomaly is shown with a green square. The *Kp* distributions for Fleet B are shown in Figure 26(b,d,f,h). Each Fleet B anomaly is shown with a cyan circle. The anomaly placement points are calculated using the respective averaging method of each figure. For example the anomaly points on Figure 26(c) represent the average *Kp* value of the two days prior to the anomaly. Each point represents a single anomaly. The y-axis coordinate of the anomaly point does not correspond to a count value labeled on the y-axis of each plot; these are only offset vertically for clarity.

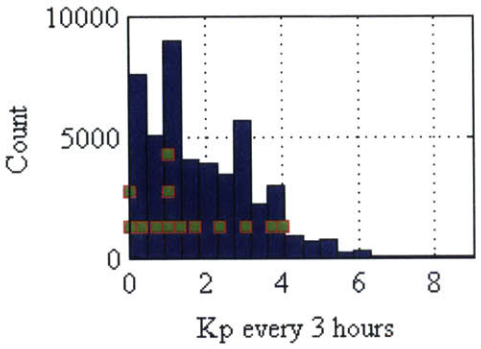
10000
5000
0
Count
0
2
4
6
8
Kp every 3 hours

(a)

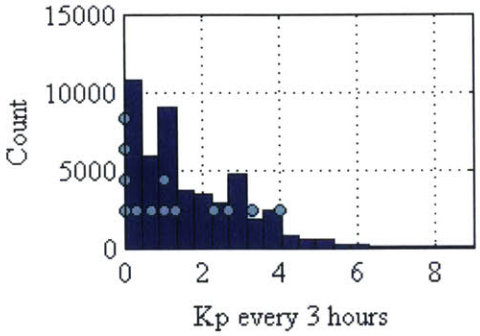
15000
10000
5000
0
Count
0
2
4
6
8
Kp every 3 hours

(b)

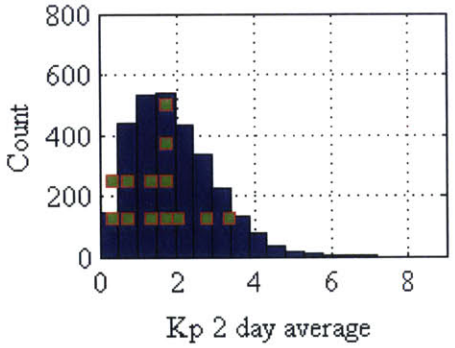
800
600
400
200
0
Count
0
2
4
6
8
Kp 2 day average

(c)

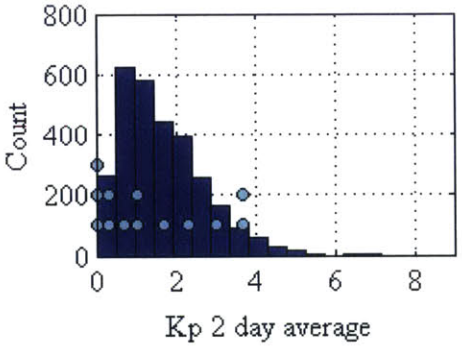
800
600
400
200
0
Count
0
2
4
6
8
Kp 2 day average

(d)

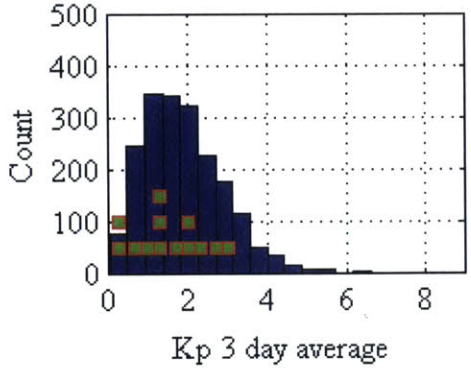
500
400
300
200
100
0
Count
0
2
4
6
8
Kp 3 day average

(e)

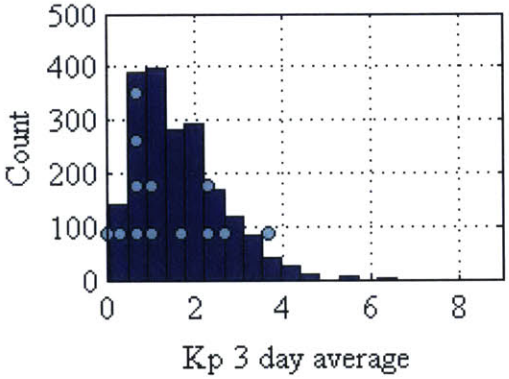
500
400
300
200
100
0
Count
0
2
4
6
8
Kp 3 day average

(f)

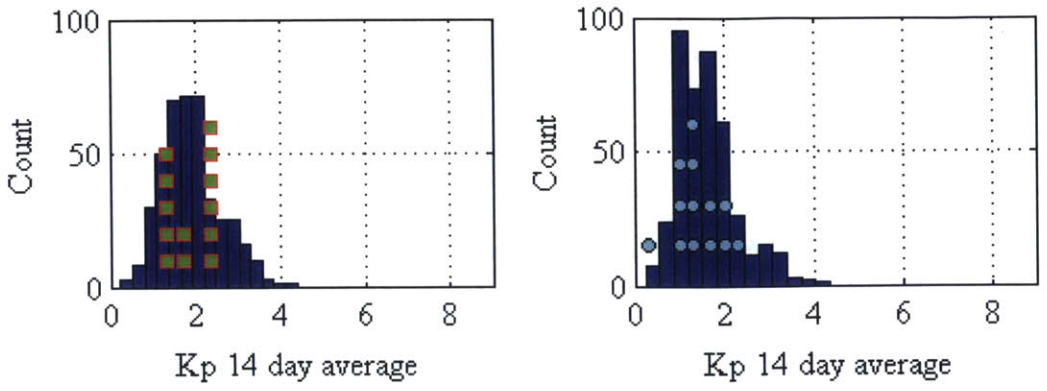

Figure 26 (a-h). The distribution of *Kp* Index for (a,b) every measurement, (c,d) two day average, (e,f) three day average, and (g,h) two-week average with *Kp* index at the time of the SSPA anomalies. The distributions for the time period of operations of Fleet A are shown in Figure 26(a,c,e,g) and the anomalies of Fleet A are represented with green squares. The distributions for the time of period of operations of Fleet B are shown in Figure 26(b,d,f,h) and the anomalies of Fleet B are represented with cyan circles. The specific time periods for each fleet are not distinguished for proprietary reasons, but the analysis only includes *Kp* from periods when the respective satellite fleets were in operation. The *Kp* time series are taken from the Data Analysis Center for Geomagnetism and Space Magnetism at Kyoto University in Japan, accessed through the OMNI 2 web site.

The anomalies do not appear to depend on the *Kp* index. Figure 26(f), for example, shows more anomalies at small *Kp* values, and there appear to be more days with smaller *Kp* during the time of the operation of fleet B. Additional anomaly data would help to refine this preliminary conclusion. A summary of the four *Kp* distributions is provided in the two tables below. For both fleets, the maximum *Kp* at the time of anomaly did not exceed a *Kp* of 4, indicating that none occurred during unusually elevated geomagnetic activity. Twenty-one out the 26 (80%) anomalies occurred when the *Kp* was less than 2.5.

Tables 28 and 29 summarize the mean *Kp*, the standard deviation of the *Kp* distributions, the minimum *Kp*, and the maximum *Kp* for all four distributions (single *Kp* measurement, 2-day *Kp* average, 3-day *Kp* average, and 14-day Kp average). For Fleet A, the average *Kp* of all

anomalies for these four distributions is greater than the respective average *Kp* values for Fleet B. This is because the anomalies for Fleet B occur after 2006, when geomagnetic activity was low. The minimum and maximum *Kp* values at the time of the anomalies are approximately equal for both fleets.

Table 28. Fleet A Summary of *Kp* at Time of 13 SSPA Anomalies

Fleet A	*Kp*	*Kp* 2 Day Average	*Kp* 3 Day Average	*Kp* 14 Day Average
Mean	1.538	1.542	1.567	1.848
Standard deviation	1.335	0.832	0.828	0.425
Minimum value	0	0	0.449	1.287
Maximum value	4	3.248	3.097	2.326

Table 29. Fleet B Summary of *Kp* at Time of 13 SSPA Anomalies

Fleet B	*Kp*	*Kp* 2 Day Average	*Kp* 3 Day Average	*Kp* 14 Day Average
Mean	1.277	1.427	1.387	1.406
Standard deviation	1.371	1.320	1.110	0.540
Minimum value	0	0.072	0.138	0.256
Maximum value	4	3.656	3.776	2.386

To relate these results to charging phenomena, *O'Brien* [2009] found the probability of an anomaly caused by surface charging peaks in the range of *Kp* = 4–6. Similarly, *Thomsen et al.* [2013] found an increased probability of surface charging at higher *Kp* values. Denton and *Borovsky* [2012] found strong surface charging even at relatively low *Kp* (> ~2 or 3). Because we can show that these specific SSPA anomalies occurred at times of quiet geomagnetic activity, we conclude that they are not likely caused by surface charging alone.

7.2.2 SSPA Anomalies and Local Time

Several studies suggest that satellite anomalies caused by surface charging have a dependence on satellite local time, as surface charging

anomalies generally tend to occur between midnight and dawn [e.g., *Wilkinson*, 1994; *Fennell et al.,* 2001; *Iucci et al.,* 2006; *Choi et al.,* 2011]. Surface charging tends to occur between midnight and dawn because as electrons are injected into the Earth's magnetosphere they travel eastward in the midnight to dawn direction, losing energy as they travel. Low-energy electrons that are injected tend to lose energy through collisions with spacecraft and other particles before they can reach dawn, depositing on spacecraft surfaces. Internal charging often occurs at times near local noon, but can also occur outside of this time sector [*Fennell et al.*, 2001; *Wrenn et al.,* 2002]. *Choi et al.* [2011] found that for 95 GEO anomalies, 72% of the anomalies occur between midnight and dawn in local time. However, for *Choi et al.* [2011], the anomalies are not only SSPAs but also include a variety of additional failures.

In Figure 27, we plot the local time of each of the 26 SSPA anomalies on the eight Inmarsat satellites. Fleet A is represented with red circles, and Fleet B is shown in black asterisks. The radial distance from the center of the graph has no significance but is used for clarity since several anomalies occur at similar local times.

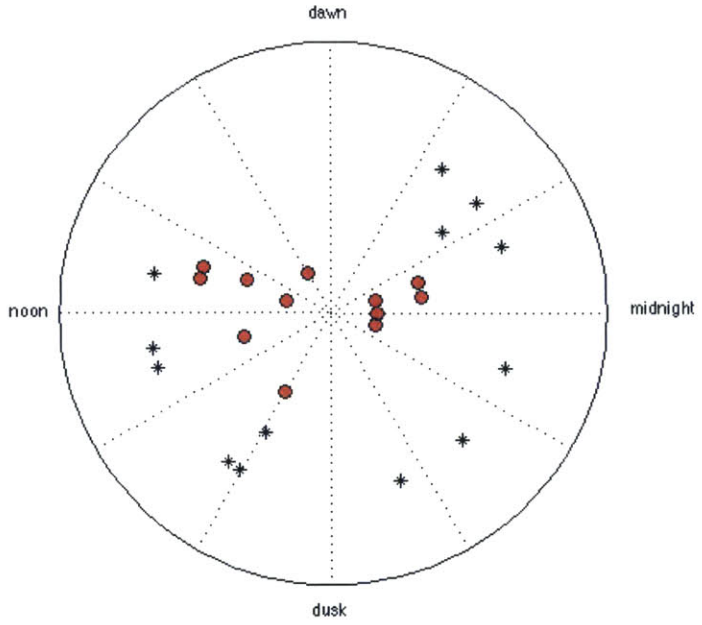

Figure 27. Local time for the twenty-six SSPA anomalies onboard (red circles) Fleet A and (black asterisk) Fleet B. The radial distance from the center of the plot is an offset for clarity and has no other significance.

Of the 13 SSPA anomalies in Fleet A, six (46%) occurred around local midnight, and the remaining seven (54%) occurred more loosely around local noon (one each closer to the dawn and dusk sectors than to local noon). For Fleet B, five of the thirteen occur in the approximately midnight to dawn sector (38.5%), and six (46%) occur in the local noon to dusk sector. *Thomsen et al.* [2013] showed that there is essentially zero chance that anomalies between 12:00 and 17:00 local time (LT) are caused from surface charging. Seven of the 26 anomalies occur between 12:00 and 17:00 LT and are thus not considered to have resulted from surface charging. The local time distribution of the Inmarsat anomalies indicates that surface charging could not have been the causative agent for all of the SSPA anomalies.

7.2.3 SSPA Anomalies and Eclipse Data

In the event of an eclipse, the Earth blocks sunlight from reaching the solar arrays and requires satellite operators to monitor and control power use. The two eclipse seasons are late February to mid-April (spring eclipse season) and late August to late October (fall eclipse season). The longest eclipses generally last between 68 min and 73 min [*Lohmeyer et al.*, 2012]. The eclipse seasons coincide with the vernal and autumnal equinox, because it is during equinox that the Earth blocks the Sun's light from reaching the satellites.

Choi et al. [2011] found that more of the geostationary satellite anomalies occurred in spring (March, April, and May) and fall (September, October, and November) than in summer and winter. Spring and fall are known as periods when geomagnetic activity is at a maximum, formally attributed to the Russell McPherron Effect [*Russell and McPherron*, 1973]. Although other researchers observed semiannual variation in geomagnetic activity as well as in GEO anomalies [*Wilkinson*, 1994; *Iucci et al,* 2006], we did not observe this relationship for the 26 SSPA anomalies on board the Inmarsat satellites. Table 30 shows the season in which each of the 26 SSPA anomalies occur.

Table 30. The number of SSPA anomalies per season on each of the Inmarsat satellites

Satellite	Winter	Spring	Summer	Fall
A	1	1	0	0
B	1	3	0	4
C	0	0	1	0
D	2	0	0	0
E	2	1	1	1
F	1	2	1	2
G	1	0	0	1
Total	8	7	3	8

There is not a clear seasonal trend for the SSPA anomalies. More than half of the anomalies (16/26) occurred in winter and fall, and the fewest number of anomalies occurred in summer. Interestingly, January was the month with the most anomalies, even though January is a time when geomagnetic activity is at a minimum [*Russell and McPherron*, 1973]. One possible explanation of these results is that the geometry of the Earth eclipsing the Sun, in addition to the measures taken by the operators during eclipse seasons for power management, seems to reduce the number of SSPA anomalies. The local time distribution suggests that an eclipse effect is rather unlikely. Additional anomaly data would help determine if the SSPAs are susceptible to the previously noted seasonal dependencies of geostationary anomalies [*Iucci et al.*, 2006; *Wilkinson*, 1994; *Choi et al.*, 2011].

7.3 Discussion of the Initial Space Environment Analysis of Amplifier Anomalies

Based on the Inmarsat SSPA data alone, we cannot generalize that all geostationary communications satellite anomalies have a causal relationship with the sunspot cycle (11 year solar cycle). More Fleet A SSPA anomalies occur during the declining phase of the solar cycle, when relativistic electron fluxes reach their highest values, but also when surface charging is most likely to occur [*Thomsen et al.*, 2013].

To understand the relationship of the SSPA anomalies and surface charging, the *Kp* index was analyzed. The anomalies do not appear to have a clear relationship with the *Kp*. Twenty-one out of the 26 (80%) anomalies occurred when the *Kp* was less than 2.5 at the time of the anomaly, and all 26 (100%) of the anomalies occurred with a two-week

average *Kp* value of less than 2.5. This suggests that the anomalies occurred at times of relatively quiet geomagnetic activity and that the anomalies are likely not caused by surface charging. It should be noted that relativistic electron fluxes, which are discussed in more detail below, are often weaker during the time of low *Kp*. Furthermore, 7 of the 26 SSPA anomalies occur at a local time between 12:00 and 17:00 LT when surface charging is not likely to occur [*Thomsen et al.,* 2013]. More anomalies occur in the noon to dusk sector (54% for Fleet A and 46% for Fleet B) than at the midnight to dawn local time sector (46% and 38.5%). The frequency of occurrence is slightly less at midnight, which indicates that other space weather impacts than surface charging alone play a role.

Additionally, we considered the occurrence rate of SSPA anomalies with geostationary eclipse season (during the equinoxes). No obvious seasonal distribution exists, yet more than half of the anomalies (16/26) occur in winter and fall. The month with the highest number of anomalies is January, when geomagnetic activity is typically low [*Russell and McPherron*, 1973].

7.4 Internal Charging Analysis: >2 MeV Electron Flux

The >2 MeV electron flux is typically used as the representative electron population capable of penetrating spacecraft structures [e.g., *Love et al.,* 2000]. These relativistic electrons are accelerated during geomagnetic storms and deposit into the dielectric materials of the satellites (semiconductors and circuit boards). If the rate of charge buildup exceeds the rate at which charge can escape from the internal components, an ESD or arcing will occur [e.g., *Shea and Smart*, 1998; *Baker,* 2000; *Fennell et al.,* 2001; *Bodeau,* 2010; *Lai,* 2012].

As previously mentioned, the anomalies on ANIK E1, ANIK E2, the Japanese BS- 3a satellite, Intelsat K, Galaxy 4, and Telstar 401 have been attributed by several previous studies to internal charging [*Baker,* 2000; *Love et al.,* 2000; *Allen,* 2010; *Horne et al.,* 2013]. However, at the time of the ANIK and Telstar anomalies, the >2 MeV electron flux was very weak [*Baker*, 2000]. Some of these anomalies, such as those on the Japanese BS-3a and the ANIK satellites, did experience periods of high

flux levels of energetic electrons 1–2 weeks before the anomalies occurred [*Shea and Smart*, 1998; *Love et al.*, 2000].

Figure 28(a-d) shows the distribution of the $\log_{10}$ of 1.8-3.5 MeV daily averaged electron flux from 1996-2009 measured on LANL SOPA [*Reeves et al.,* 2011] for (a) every measurement, (b) averaged over two days, (c) averaged over three days and (d) averaged over two weeks, or fourteen days. The distribution of the $\log_{10}$ of 1.8–3.5 MeV electron flux at the time of the anomaly, approximated to the nearest 0.2 pfu (pfu = (#/(cm^2 s sr keV)), is shown for Fleet A with green squares and Fleet B with cyan circles. These points represent the $\log_{10}$(1.8–3.5 MeV electron flux) value averaged to the same extent of the respective distribution. The offset vertical location of the anomaly markers is for clarity only and does not correspond to the count values on the y-axis, which designate the number of daily electron flux measurements. For Fleet B, five anomalies occurred when flux data from LANL is not available, but this does not appear to affect the distribution. Given the reduced size of the Fleet B data, both fleets are shown on the same figure, rather than separated, which should be done for large data sets.

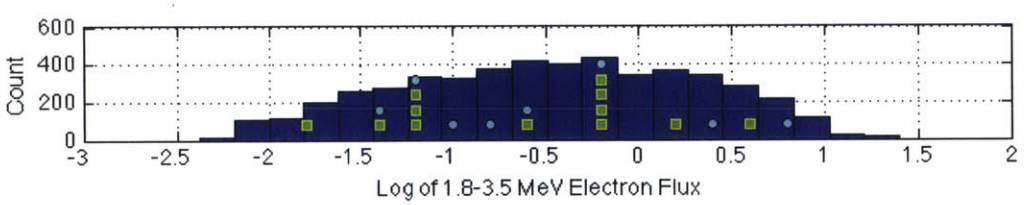

(a)

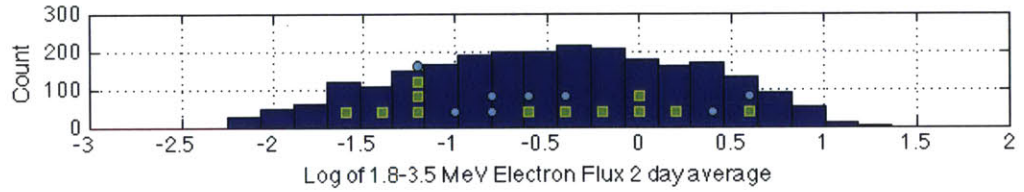

(b)

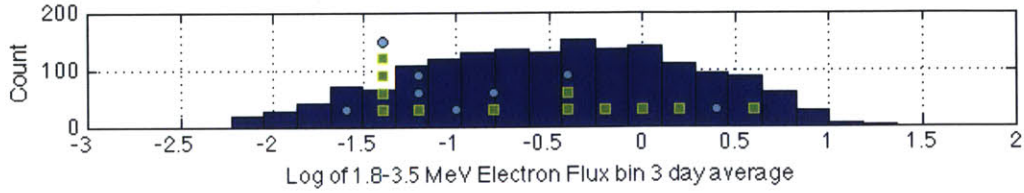

(c)

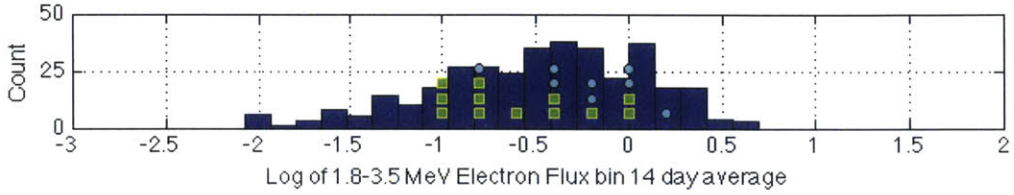

(d)

Figure 28 (a-d). The distribution of the $\log_{10}$ of 1.8-3.5 MeV Electron fluxes in units of #/(cm^2 s st keV) from 1996-2009 for (a) every measurement, (b) two day average, (c) three day average, and (d) two-week average with electron flux at the time of the SSPA anomalies on Fleet A (green squares) and Fleet B (cyan circles).

From 1996-2009 (LANL data is not available after 2009), the average log of 1.8-3.5 MeV Electron flux was -0.489 $\log_{10}$(#/(cm^2 s st keV)) with a standard deviation of 0.75 $\log_{10}$(#/(cm^2 s st keV)). Anomalies occur between $\log_{10}$ of electron flux values of -1.81 and 0.55 $\log_{10}$(#/(cm^2 s st keV)) for Fleet A, and -1.47 and 0.85 $\log_{10}$(#/(cm^2 s st keV)) for Fleet B. There does not appear to be an obvious, unique distribution of the electron flux at the time of the anomalies.

Since it is very difficult to evaluate the existence of elevated electron flux using a 14 day average, Figure 29(a-b) shows a superposed epoch of the 21 individual $\log_{10}$ of 1.8–3.5MeV electron flux curves, in gray, for a period of 3 weeks before the anomaly and the curve of the daily average $\log_{10}$ of 1.8–3.5 MeV electron flux during this period. Only 21 of the 26 anomalies occur in periods when LANL 1.8-3.5 MeV electron flux data exist. Figure 29(b) shows the same curve of the daily average $\log_{10}$ of 1.8–3.5 MeV electron flux 21 days before the anomalies, but with a different vertical scale. A peak in electron flux occurs between 7 and 14 days before the SSPA anomalies. The figures below also suggest that either past elevated radiation-belt fluxes or some conditions related to relativistic electron enhancements (either causally or accidentally) are most likely responsible for the SSPA anomalies.

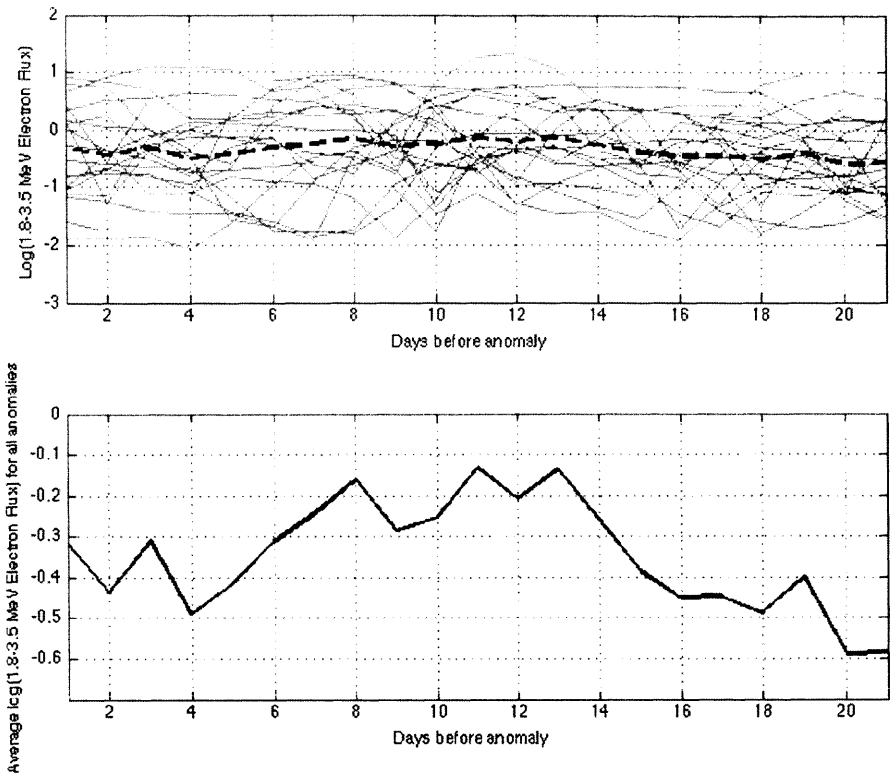

Figure 29 (a,b) Twenty-one individual $\log_{10}$(1.8–3.5 MeV electron flux) 0–21 days before the SSPA anomalies, represented by the thin gray curves, and the daily average shown in the dashed black curve in Figure 29(a). Figure 29(b) shows the same average $\log_{10}$(1.8–3.5 MeV electron flux) 0–21 days before the SSPA anomalies, as shown in black in Figure 29(a), but with higher resolution.

A total of six of the 21 anomalies, or ~29%, experienced a flux level greater than 1.5 standard deviations above the mean $\log_{10}$ of 1.8–3.5 MeV electron flux from 1996 to 2009, or a $\log_{10}$ of 1.8–3.5 MeV electron flux of 0.64 between 7 and 14 days before the anomaly. For the entire period between 1996 and 2009, 365 out of 5110 days experienced a $\log_{10}$ of 1.8–3.5 MeV electron flux greater than 1.5 standard deviations above the mean (note that 365 days here is not related to a calendar year). From the LANL data set, 5110 days were evenly divided into 365 consecutive 14-day intervals with an imaginary "anomaly" on the last day of each 14 day interval (the 365 number of 14 day intervals is also a coincidence and has nothing to do with the days in a year). Of these 365 fourteen day intervals, 78 of them, or 21%, had daily average values greater than 1.5 standard deviations between days 7 and 14 before an anomaly.

7.4.1 Monte Carlo Analysis of $\log_{10}$(1.8-3.5 MeV electron flux)

Figures 30(a–d) display the GOES >2 MeV electron flux rate (solid blue line) and the SSPA current (dotted green line) two weeks before and after four SSPA anomalies. Continuous GOES data was not available for the two week period before two of the six anomalies that experienced a flux level greater than 1.5 standard deviations above the mean $\log_{10}$ of 1.8–3.5 MeV electron flux from 1996 to 2009, or a $\log_{10}$ of 1.8–3.5 MeV electron flux of 0.64 between 7 and 14 days before the anomaly. The time of anomaly is designated with a red vertical line. The periodic higher-frequency variability in both the SSPA and the >2 MeV data is due to the diurnal cycle.

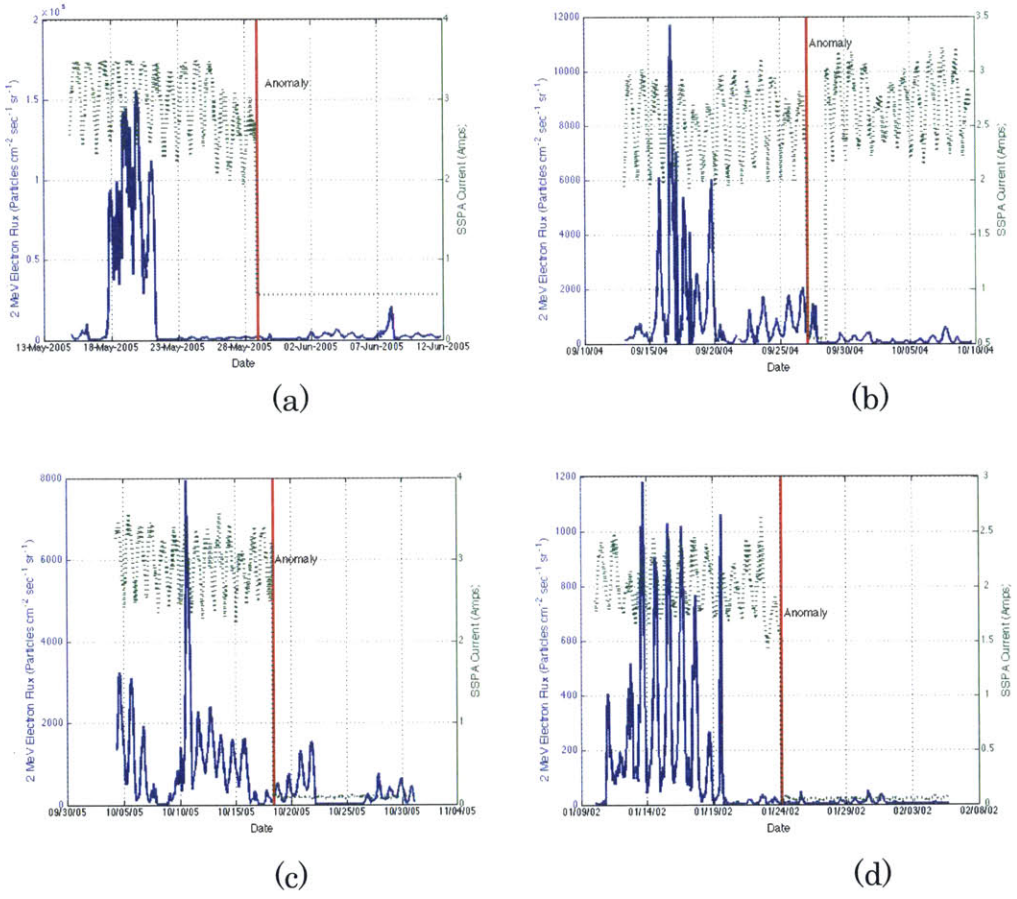

Figure 30(a–d). >2 MeV electron flux during SSPA anomalies for 2 weeks before and after four anomalies. GOES 2 MeV electron flux is plotted on the left vertical axis, and SSPA current is plotted on the right

axis. The GOES >2 MeV electron flux is the blue line, the SSPA current is the dotted green line, and the anomaly is marked with a red line. The higher-frequency variability in both electron flux and current is due to the diurnal cycle.

Figure 30(a-d) clearly shows that there is often a substantial increase of 2 MeV electron flux that occurs approximately one to two weeks before the selected anomalies. The number of days between the peak 2 MeV electron flux and the four anomalies in Figures 30(a–d) is 10.6 days for Figure 30(a), 10.4 days for Figure 30(b), 7.8 days for Figure 30(c), and 10.4 days for Figure 30(d).

To understand the likelihood that a random anomaly occurs between 7 and 14 days after the level of the $\log_{10}$ of 1.8–3.5 MeV electron flux exceeds the mean by 1.5 standard deviations between 1996 and 2009, we conducted a Monte Carlo simulation. This analysis was also used to confirm that peaks like those shown in Figure 30(a-d) do not occur every two weeks. Specifically, we determined the likelihood that 21 random anomalies would occur between 7 and 14 days after a level of the $\log_{10}$ of 1.8–3.5 MeV electron flux that exceeds the mean by 1.5 standard deviations above the mean. For 100,000 iterations of the Monte Carlo simulation, we found that 2.8 out of 21, or ~13%, anomalies occur 7–14 days after a $\log_{10}$ of 1.8–3.5 MeV electron flux greater than 1.5 standard deviations above the mean. With the Monte Carlo approach, instead of the uniform distribution approach, we find that nearly twice as many (29%) anomalies occurred after elevated electron events above 1.5 standard deviations in the data as compared with the Monte Carlo trial (13%).

As previously mentioned, the Japanese BS-3a and the ANIK satellites also experienced enhanced levels of high-energy electron flux 1–2 weeks before an anomaly. *Wrenn* [1995] provided statistical, conclusive evidence that internal dielectric charging was the cause of the ANIK satellite failures. One plausible cause of these 11 SSPA anomalies could be from internal dielectric charging. However, *Bodeau* [2010] questions whether long delays between electron enhancements and anomalies due to internal charging are relevant.

The second space weather–related failure mechanism considered is internal charging caused from high-energy electrons. While most of the anomalies occurred during the declining phase of the solar cycle, when electron fluxes are enhanced, there does not appear to be an obvious relationship in Figure 28 (a-e) between the anomalies and 1.8–3.5 MeV electron fluxes at the time of anomaly or prior to the anomaly. However, 6 of the 21 anomalies, nearly 30% of the anomalies, experienced electron flux greater than 1.5 standard deviations of the long-term average electron flux approximately 1–2 weeks prior to the anomaly. For a uniform distribution of anomalies over 5110 days of LANL electron flux data (in 365 fourteen day intervals with an imaginary anomaly at the end of each interval), we find 78/365 of the 14 day intervals, or 21%, had events with daily average electron flux values above 1.5 standard deviations from days 7 to 14 of each interval. For 21 anomalies randomly distributed across the 5110 days, with 100,000 iterations of the Monte Carlo simulation, we found that 2.8 out of a random set of 21 anomalies, or 13%, would occur 7–14 days after a $\log_{10}$ of 1.8–3.5MeV electron flux greater than 1.5 standard deviations above the mean.

7.5 Internal Charging Analysis: >2 MeV Electron Fluence

From the initial assessment of which types of charging and what energy particles may be contributing to the anomalies, we find that further analysis is needed to determine whether internal charging served as a likely failure mechanism, and this follow-up analysis requires examination of the high-energy electron ***fluence*** (integrated flux over time), not just analysis of the maximum high energy electron flux experienced before the anomalies occur [*Bodeau*, 2010]. In the remainder of this chapter, we expand upon the initial results presented in *Lohmeyer and Cahoy* [2013] and determine the high-energy electron fluence for periods of 1 day, 3 days, 7 days, 10 days, 14 days and 21 days prior to the anomaly.

After calculating the high energy electron fluence, we confirm that an increased >2 MeV electron fluence over a period of fourteen days prior to the observed anomaly exists compared with all >2 MeV electron fluence measurements between 1996 and 2012, and also compared with

a Monte Carlo analysis conducted on daily >2 MeV electron fluence measurements.

Twenty-four of the twenty-six SSPA anomalies had GOES >2 MeV electron fluence available over a period of fourteen days before the anomalies. Eight of the twenty-four anomalies, or 33%, were found to occur with a >2 MeV fourteen day electron fluence between 2E+10 e/cm^2 and 4E+10 e/cm^2. Comparing the fluence related to anomalies with fluence in general, only 14% of all >2 MeV electron fluence measurements between 1996 and 2012 were found to be between 2E+10 and 4E+10 e/cm^2, and an average of 13%, with a standard deviation of 7.5%, of the anomalies experienced a >2 MeV electron fluence between 2E+10 and 4E+10 e/cm^2 in the Monte Carlo analysis of 1000 randomly selected 26 days. Twenty-six days were randomly selected to simulate the twenty-six SSPA anomalies that occurred on twenty-six different days.

7.5.1 Overall Goals for Detailed Internal Charging Scenario Investigation

The overall goal of the upcoming sections is to follow up on the indication that internal charging may be related to the anomalies. We examine in detail a possible internal charging scenario. First, we use ESA's internal charging model, Dielectric Internal Charging Threat Analysis Tool (DICTAT) [*Rodgers,* 2004] to model thirty-five different combinations of six material resistivities and seven temperatures in order to determine whether internal charging is indeed a possible and likely amplifier failure mechanism.

Furthermore, in Section 7.5 the SSPA anomalies are analyzed with respect to the space environment, specifically the GOES >2 MeV electron fluence at different periods of time leading up to the anomaly to determine if internal charging is a possible anomaly mechanism. In Section 7.6, the components of the amplifier system are outlined and the important ones highlighted. Section 7.7 details the internal charging analysis using DICTAT and the results of that analysis. Section 7.8 describes the experimental set up, testing, and results of amplifier components in a simulated worst-case GEO environment. In Section 7.9, the results of this study are summarized and discussed.

7.5.2 Analysis of GOES >2 MeV Electron Fluence and SSPA Anomalies

In this work, we used continuous GOES daily >2 MeV electron fluence data (http://www.swpc.noaa.gov/ftpmenu/indices/old_indices_html) from 1996 to 2012 to quantify the accumulated fluence prior to the anomalies. Figure 1 shows the GOES >2 MeV daily electron fluence measurements from 1996 to 2012, the eleven-year Sun-spot cycle, as well as the times at which the SSPA anomalies occurred. Fleet A and Fleet B were not both launched at the same time; exact launch dates are not discussed in detail for proprietary reasons. However, it is important to note that Fleet A was in operation as early as 1996, and did not experience any SSPA failures until year three of operation. The fleet on which the anomalies occurred is indicated, and the vertical location of the anomaly markers has no meaning, but is selected for clarity.

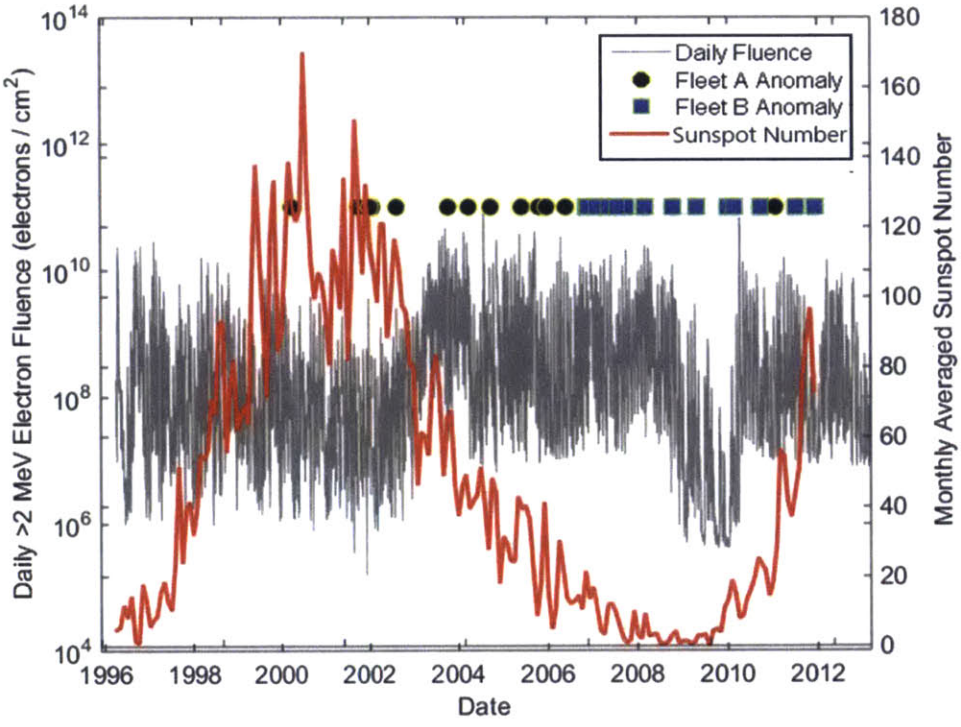

Figure 31. Daily >2 MeV Electron Fluence and the time of SSPA Anomalies. Fleet A anomalies are marked with a black circle outlined in yellow, and Fleet B anomalies are marked with a blue square outlined in green. The GOES Daily 2 MeV Electron fluence, marked in

gray, spans between 1996 and 2012, and the solar cycle is shown in red.

Lohmeyer and Cahoy [2013] found more than 69% of the thirteen anomalies from Fleet A occurred during the declining phase of the solar cycle. Fleet B has yet to operate for a complete solar cycle, so analysis of anomaly occurrence throughout an entire solar cycle was not conducted. The lack of apparent correlation of anomaly occurrence and daily high-energy electron fluence shown in Figure 1 does not clearly indicate that the anomalies are driven by energetic electron flux over a particular day, but motivates the investigation of more persistent flux over longer periods of time prior to the anomaly.

Two sets of design criteria for ESD hazards have been established. First and most commonly cited, is the *NASA-HDBK-4002A* [2011] criterion; the second is defined in *Wrenn and Smith* [1996]. The NASA handbook specifies a safe ***ten-hour*** fluence level of ≤2E+10 electrons/cm^2. The safe fluence level is derived from the Combined Release and Radiation Effects Satellite (CRRES) Internal Discharge Monitor (IDM), which experienced no ESD events when the accumulated fluence *inside the IDM* over a 10 hour orbit was less than 2E+10 e/cm^2 [*Vampola,* 1987]. The safe 10 hour fluence level is not accompanied by a safe fluence energy level, nor does it consider the electrical time constant (leakage rate) of the material. Analysis in *NASA-HDBK-4002A* [2011], using a suggested worst-case environment, suggests that a total shielding of 110 mils aluminum equivalent thickness would reduce the fluence behind the shielding to a level under safe fluence limit. *Bodeau* [2010] finds the 110 mils of Al and the safe fluence limit to be unsafe for materials with long decay time constants [*Bodeau,* 2010].

Wrenn and Smith [1996] define two thresholds for space hazards in their ESD guideline:

- Threshold I states that significant probability of hazard exists when >2 MeV *daily* electron fluence *outside the spacecraft* exceeds 3.8E+09 e/cm^2. (Note: the NASA 4002 criterion is the fluence inside the spacecraft.)

- Threshold II states that an extremely significant probability of hazard exists when >2 MeV *daily* electron fluence exceeds 3.8E+10 e/cm^2 [*Lai,* 2012].

These thresholds are based upon empirical correlations of anomalies with the external electron flux data. However, we must keep in mind that the > 2 MeV electron flux outside the spacecraft is only a proxy for the actual electron fluence reaching the possible source of ESD inside the spacecraft. The range of a 2 MeV electron is about 170 mils (4.3 mm) aluminum [Bodeau, 2010]. If the shielding between the ESD source and external environment is less than that, then lower energy electrons can penetrate the shielding and contribute to the charging of the ESD source. There are far more electrons at energies lower than 2 MeV, so the > 2 MeV external flux level may understate the total flux of electrons reaching the ESD source if the shielding is substantially lower than 170 mils aluminum.

As previously mentioned, *Bodeau* [2010] finds these safe fluence levels inappropriate for materials with electrical time constants much longer than 10 hours, and specifies that the safe-level criterion should be based upon the fluence accumulated for a time interval that reflects a material's electrical time constant. When the CRRES IDM was designed, engineering handbooks gave PTFE Teflon a resistivity at room temperature in the 1E+13 to 1E+17 ohm-cm range [*Robinson*, 1989; *Cotts and Reyes*, 1985], which would give a corresponding time constant between 1 second and 3.3 hours. A 10 hour fluence criterion would reflect three electrical time constants, over which time a material should approach its peak steady state voltage. So the NASA 4002 criterion appears to meet the standard set by Bodeau. However, it was subsequently established [e.g., *Swaminathan*, 2003 and references therein] that the resistivity measurement techniques codified in standards such as ASTM D-257 [2014] and derivative standards such as IEC 93 [1980] are:

> "...typically instrumentation resolution limited to accurate measurements of resistivities of less than 1E+12 to 1E+17 Ω-cm. Inconsistencies in sample humidity, sample temperature, initial voltages and other factors from such tests cause significant variability in results. Further, the duration of standard tests are short enough that the primary

currents used to determine resistivity are often caused by the polarization of molecules by the applied electric field rather than by charge transport through the bulk of the dielectric. Testing over much longer periods of time in a well-controlled vacuum environment is required to allow this polarization current to become small so that accurate observation of the more relevant charged particle transport through a dielectric material is possible."

When improved methods were applied to CRRES IDM samples, the room-temperature resistivity of its PTFE was found to be around 3E+20 ohm-cm and its electrical time constant was 339 days [*Green*, 2005]. Similarly, *Green et al.* found that the electrical time constants of other materials, such as FR4 and alumina, were orders of magnitude higher than the ASTM-based material time constants. Because the actual material time constants are so long, it is possible to accumulate sufficient charge to reach electrical breakdown from much lower average flux levels over longer time periods [*Bodeau*, 2010]. Unfortunately, because these advanced test methods have not yet been applied to most spacecraft materials, material-specific safe fluence criteria cannot be established and a revised fluence threshold of 2E+09e/cm^2 over 10 hours has been suggested in the interim [*Garrett and Whittlesey,* 2011].

The highest >2 MeV *daily* electron fluence on the days on which anomalies occurred was approximately 9E+09 e/cm^2. None of the twenty-six anomalies breached the *NASA-HDBK-4002A* [2011] safe ten-hour fluence level of 2E+10 e/cm^2, or *Wrenn and Smith's* Threshold II of 3.8E+10 e/cm^2. One of the twenty-six SSPA anomalies breached *Wrenn and Smith's* Threshold I of 3.8E+09 e/cm^2. Five of the twenty-six SSPA anomalies experience a daily >2 MeV electron fluence of greater than the more-conservative interim safe ten-hour fluence 2.0E+09 e/cm^2 in *NASA-HDBK-4002A* [2011].

Given that the true risk of deep charging and ESD is from the fluence of electrons accumulated over periods of time comparable to a material's electrical time constant, we first determine the >2 MeV electron fluence accumulated over six time periods: 1, 3, 7, 10, 14, and 21 days, from the daily GOES >2 MeV electron fluence data between 1996 and 2012. In the next section, we isolate the >2 MeV electron fluence before the twenty-six SSPA anomalies over the same six time periods. We will show

that SSPA failures occur with much higher frequency when the fluence accumulated over 14-21 days is high (compared with the typical 14-21 day fluence and compared with the percent of time periods with high fluence).

To verify that a relationship between the observed higher rate of anomalies and high fluence exists, we performed 1000 trials of 26 randomly selected days between 1996 and 2012 and quantified the distribution of 1, 3, 7, 10, 14, and 21-day fluence values prior to the 26 random dates to determine the mean fluence value as well as the standard deviation of fluences. The disproportionate distribution of anomalies in the higher fluence intervals occurs at a rate that is not easily explained by a simple random sampling of the dates, and therefore shows a relationship with high fluence exists.

7.5.2.1 Distribution of GOES >2 MeV Electron Fluence from 1996 to 2012

Figure 2 shows the distribution of the >2 MeV electron fluence from 1996 to 2012 over the six periods previously mentioned (1, 3, 7, 10, 14 and 21 days). The fluence bins shown are differential bins, <2E+10 e/cm^2, 2E+10 – 4E+10 e/cm^2, 4E+10 – 6E+10 e/cm^2, 6E+10 – 8E+10 e/cm^2, and >10E+10 e/cm^2.

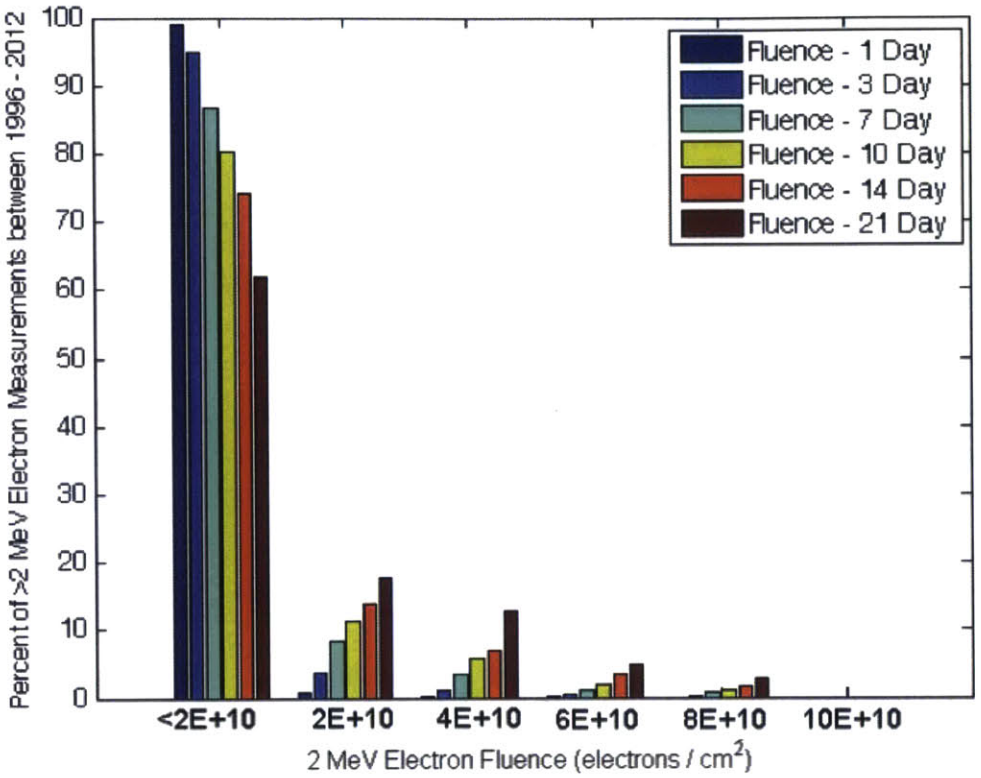

Figure 32. Percentage of >2 MeV Electron Fluence Measurements from 1996 to 2012 over periods of 1, 3, 7, 10 14, and 21 day periods

It is important to note that the longer fluence periods (7, 14, 21 days) at the same fluence interval, for example 2E+10 to 4E+10 e/cm^2, are specifying lower average daily fluxes. All measurements over all time periods were less than 1E+11 e/cm^2. Of the 6,180 total daily >2 MeV electron fluence measurements, 99% of the daily measurements were between 0 and 2E+10 e/cm^2. Similarly, the majority of >2 MeV electron fluence measurements for the 3, 7, 10, 14, and 21 day time periods occurred between 0 and 2E+10 e/cm^2. A total of 49 out of 350, or 14%, of the >2 MeV 14 day electron fluence measurements were in the next higher fluence bin, 2E+10 to 4E+10 e/cm^2. A total of 13% of >2 MeV 21 day electron fluence measurements between 1996 and 2012 occurred in the third fleunce bin (4E+10 to 6E+10 e/cm^2) and 3% occurred in the fourth bin (6E+10 to 8E+10 e/cm^2.) Given this baseline distribution, when we next examine the SSPA failures, if the SSPA failures were random and unrelated to the environment, we would expect the percentile distribution of failures with fluence to look like the percentile distribution of the fluences themselves.

7.5.2.2 Distribution of GOES >2 MeV Electron Fluence Prior to the 26 SSPA Anomalies

Figure 33 shows the percentage of anomalies that occurred at a particular GOES >2 MeV electron fluence for the 1, 3, 7, 10, 14 and 21 day periods of interest. All twenty-six anomalies experienced a daily >2 MeV electron fluence between 0 and 2E+10 e/cm^2 one day prior to the anomaly. Unfortunately >2 MeV electron fluence measurements were not available for all periods of fourteen and twenty-one days prior to the 26 anomalies (GOES electron data history has infrequent gaps of 1 or more days). Of the population of 26 anomalies, 24 have corresponding fourteen day >2 MeV electron fluence measurements, and 17 have twenty-one day >2 MeV electron fluence measurements prior to anomalies.

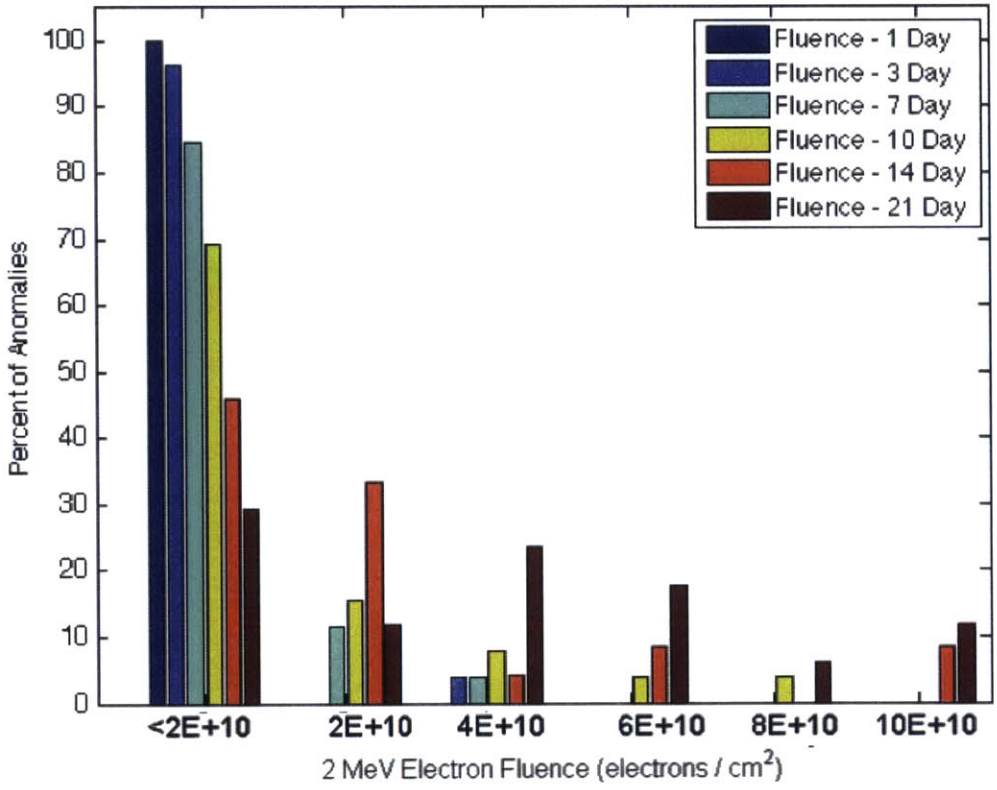

Figure 33. Percentage of SSPA Anomalies that occur for a given total >2 MeV electron fluence over periods of 1, 3, 7, 10, 14 days and 21 day periods prior to the twenty-six SSPA anomalies.

Looking at the distribution for different durations of high electron flux prior to anomalies, we find that a disproportionate number of anomalies occur after 14 days of elevated electron flux: e.g., the height of the 14 day bar in the 2E+10 fluence bin of Figure 33 is much higher than the 14 day bar in the same fluence bin in Figure 32. On the other hand, the 14 day bar in the low flux (<2E+10) bin of Figure 33 is smaller than the 14 day bar in the same fluence bin of Figure 32. Specifically, Figure 33 shows that 33% (8 of 24) with available data occurred with a >2 MeV fourteen day electron fluence of 2E+10 to 4E+10 e/cm^2, compared to 14% of all measurements between 1996 and 2012 shown in Figure 32 in the same fluence bin.

Figure 34 shows the ratio of the % of anomalies that occur in each fluence bin for each time period (shown in Figure 33) to the % of all measurements between 1996 and 2012 for the same fluence bin and time period (shown in Figure 2). Figure 34 shows that the anomaly rate for anomalies that occurred with a >2 MeV fourteen day electron fluence of 2E+10 to 4E+10 e/cm^2 is a factor of ~2.4 times higher (33%/14%) than explainable by random failures (i.e., by the frequency of occurrence for the fourteen day fluence in the 2E+10 to 4E+10 e/cm^2 interval).

Similarly, a disproportionate percentage of anomalies occur after 21 days of elevated fluence. Of the seventeen anomalies with available 21 day fluence measurements, Figure 33 shows that four or 23.5% occurred with a >2 MeV twenty-one day fluence between 4E+10 and 6E+10 e/cm^2, compared to 13% of all >2 MeV 21-day electron fluence measurements between 1996 and 2012 in the same fluence bin, shown in Figure 32. An additional 18% (3 of 17 anomalies) occurred with a fluence between in the third bin (6E+10 and 8E+10 e/cm^2,) which is a factor of 3.7 higher than the 4.8% of all >2 MeV twenty-one day fluence measurements in the same fluence interval.

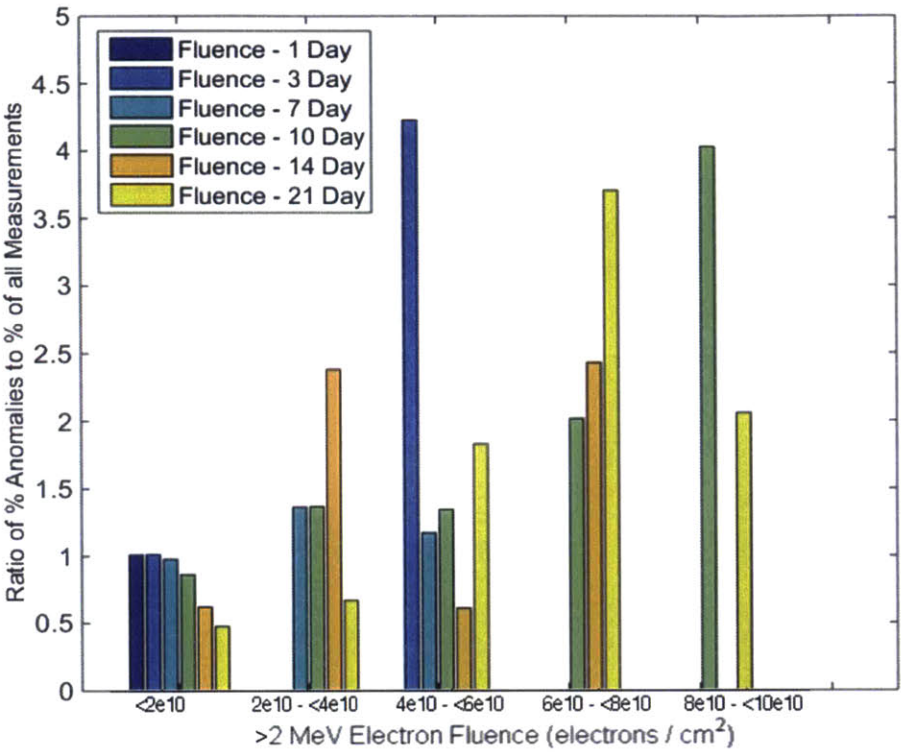

Figure 34. Ratio of the anomaly %'s from Figure 3 to the measurement %'s shown in Figure 2 for each >2 MeV electron fluence and each time period (1, 3, 7, 10, 14, and 21 days)

The three day fluence period between 4E+10 - <6E+10 e/cm^2 has the highest ratio of % anomalies to % of all measurements, but is not considered relevant because it specifies a ratio of 3.85% of anomalies to 0.91% of all measurements. Other than for the three day fluence period between 4E+10 - <6E+10 e/cm^2, the >2 MeV electron fluence for periods of 1, 3, and 7 days prior to the anomalies show approximately the same proportion of anomalies that experience <2E+10 e/cm^2, showing no clear relationship to the environment. The relative increase in the number of anomalies in Figure 33, as compared to Figure 32, for longer-term electron fluence (e.g. 14 day and 21 day periods) indicates that a disproportionate number of anomalies occur during long durations of high electron flux.

7.5.2.3 Distribution of GOES >2 MeV Electron Fluence for 1000 trials of 26 random days between 1996 and 2012

To determine the likeliness of the distribution presented in Figure 33, twenty-six random "anomaly dates" were selected 1000 times and the >2 MeV electron fluence over the six periods prior to the anomalies was quantified. Figure 35 shows the average percentages of twenty-six anomalies that occurred within a given >2 MeV electron fluence interval. The error bars represent a standard deviation above and below the average for the 1000 trials.

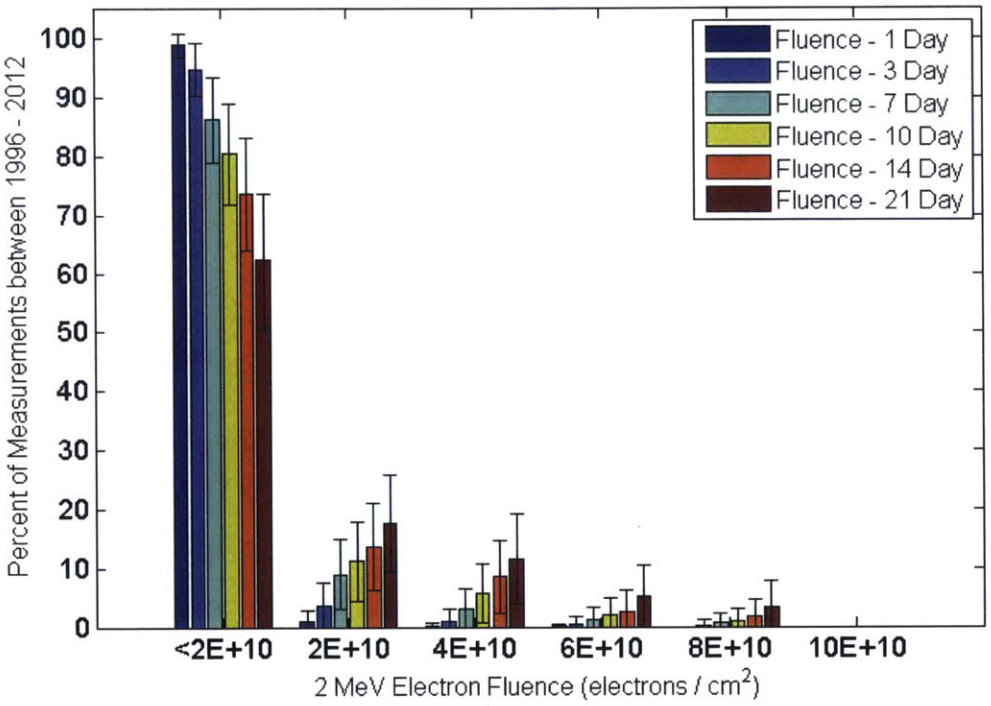

Figure 35. Percentage of 1000 random trials of twenty-six random days that occurred for a given >2 MeV electron fluence of 1 day, 3 days, 7 days, 10 days, 14 days and 21 days prior to the randomly selected twenty-six days

As expected, the distribution of values from the Monte Carlo simulation are similar to distribution of the >2 MeV electron fluence measurements in Figure 32 in all fluence intervals and for all durations. For example, the percentage of measurements with a 14 day fluence in the 2E+10 to 4E+10 interval was 14% (in Figure 32) and is 13.6% in Figure 35. The standard deviation for the % of the 26 randomly chosen dates with 14 day fluence in the 2E+10 to 4E+10 e/cm^2 interval was 7.5% for the 1000 trials The observed 33% of SSPA failures that occurred with a 14 day fluence in the 2E+10-4E+10 interval is 2.62 sigma higher than the mean

[(33.3%-14%)/7.5%], indicating that the higher anomaly rate is not likely due to chance.

Table 31 tabulates the observed anomaly rates (%) expressed as a number of standard deviations from the mean, which shows where the rates are unusually high and unlikely to be produced by a random failure process.

Table 31. The observed anomaly rates (%) expressed as a number of standard deviations from the mean value of the Monte Carlo simulation

	1 day	3 days	7 days	10 days	14 days	21 days
<2E+10	0.50	0.30	-0.23	-1.31	-2.85	-2.85
2E+10 – <4E+10	-0.48	-0.91	0.42	0.63	**2.62**	-0.71
4E+10 – <6E+10	-0.14	1.35	0.23	0.41	-0.69	**1.55**
6E+10 – <8E+10	-0.11	-0.31	-0.48	0.67	**1.58**	**2.34**
8E+10 – <10E+10	0.00	-0.23	-0.38	**1.42**	-0.60	0.58

Unexpected increases in observed failure rate were also compared to the Monte Carlo analysis for elevated periods of twenty-one day fluences before an anomaly. An average of 11.6% with a standard deviation of 7.68% of randomly selected anomalies experienced a >2 MeV electron fluence over twenty-one days prior to the anomaly between 4E+10 and 6E+10 e/cm^2 (third fluence bin). The 24% (four of seventeen) of anomalies that occurred with twenty-one day electron fluence in the same third fluence bin is only 1.55 sigma higher than the expected rate for a random sample of dates. On the other hand, an average of 5.25% (with a standard deviation of 5.3%) of the randomly selected dates experienced a >2 MeV electron fluence over a period of twenty-one days in the fourth fluence bin (6E+10 to 8E+10 e/cm^2). The 18%, (three of the seventeen) of anomalies with twenty-one day electron fluence in the same fluence bin is 2.34 sigma above the expected rate for a random sample of dates. This shows that the anomaly rates at high fluence levels are higher than expected and cannot be reasonably explained by chance alone.

Based on similar statistical evidence showing a correlation of anomalies to high fluences over 14 and 21 day periods [*Balcewicz,* 1998], *Bodeau* [2010] performed a real-time analysis of the accumulation and loss of charge within a dielectric exposed to a GEO energetic flux environment (attenuated by a specified amount of shielding), using an equivalent R-C circuit model. The analysis demonstrated that repeated episodes of high electron flux (expected during the decline from solar max) could charge materials to charge densities and electric fields expected to cause electrical discharges, if the material had very high resistivity (and consequently a very long electrical time constant). So if the amount of shielding is defined and the key material properties are known, then a prediction of charging could be performed to determine if internal charging could plausibly produce ESD and cause the Inmarsat anomalies. However, because the design details for the two fleets are proprietary and unknown to the authors, a Bodeau-like analysis of the charging from launch to failure could not be performed for the hardware in each of the individual spacecraft. Instead, a typical RF amplifier system is surveyed in the next section to identify the most likely locations for charging and ESD in preparation for a generic charging analysis to determine if sufficient fluence could be accumulated inside the key hardware to produce the failures.

7.6 RF Power Amplifier Systems

The increased rate of anomalies following exposure to elevated energetic electron fluence over a period of fourteen to twenty-one days prior to the anomalies suggests the failures may have been caused by deep dielectric charging in materials with very high resistivity and long electrical time constants (electrical time constant equals the product of dielectric constant and resistivity), and which has high electron flux exposure. Consequently, we investigate the components of the RF power amplifier system and their susceptibility to internal charging. The overall amplifier configuration consists of a coaxial cable that carries the RF signal to the amplifier input and another coaxial cable from the amplifier output to an antenna. Between the RF input and output of the SSPA are the transistors that are responsible for the power amplification, and numerous passive components like resistors, switches, and capacitors.

The coaxial cables utilize low loss conductors, such as silver plated copper, and low RF loss insulators (such as Teflon), to minimize the RF absorption at the operating frequency. The alternative to coax is waveguide, which has no insulator or floating center conductor, and therefore no ESD risk. Putting a coax and waveguide in series, may DC-isolate the coax center conductor at their interface. It is common practice to DC isolate the transistors by inserting a blocking capacitor before the transistor at the input and output coax interfaces. At high RF operating frequencies, the capacitor acts as a short circuit and freely passes the intended signal, while at lower frequencies, the capacitor has high impedance and blocks/reflects the undesired signal. The SSPAs also have a secondary power supply that converts the primary spacecraft power to the lower voltages needed to operate the internal circuits, and a command and telemetry section that is used to set the operating levels (e.g., gain) of the SSPA and to monitor operating levels (e.g., temperature, voltages, RF power output). Since the telemetry from the failed units points to the RF circuitry as the location of the failure, we do not pursue the DC power and command and telemetry circuits as potential sources of the failure.

To assess the credibility of deep charging as a possible cause of the SSPA anomalies, we investigate the component of the amplifier system that is likely most exposed to charging: the coaxial cable, and the component most susceptible to experience voltages above their specified voltage ratings: the DC blocking capacitor. Other dielectrics and electrically isolated conductors within the SSPA RF section could potentially cause the anomalies. The spacecraft shielding around a coax cable and the SSPA it connects to should be the similar, so both would be exposed to similar electron flux levels. But the extra shielding provided by a typical unit chassis to potential ESD sources inside is greater (by at least 20mils) than the shielding provided by the coax shield and outer jacket to the coax center conductor and internal dielectric. Consequently, the lower electron flux exposure inside a unit chassis makes potential ESD sources within a unit a less likely source of the anomalies.

Coaxial cables are made of an inner conductor, surrounded by an insulating dielectric layer surrounded by a conducting shield. There additionally may be an outer insulating dielectric jacket. Charging and

discharging of the coax dielectric outer jacket was not of interest, since the internal RF transmission line is well isolated from an external electrical transient by the coax shield. The geometry and properties of the inner dielectric material control most of the electrical properties of the cable (e.g., impedance, RF loss). For RF applications, the dielectric material must have low loss. Teflon (polytetrafluoroethylene, PTFE) is a commonly used dielectric material for coax cables in satellite systems. Investigation of the possibility of internal charging of the dielectric material in the coax cables is provided in Section 4.

The other component of RF communication system that we may consider cause SSPA anomalies is the DC blocking capacitor. DC blocking capacitors are used to block the flow of DC current while passing desired RF signals, and are typically found at the SSPA RF input and output connections to the coaxes. A typical DC blocking capacitor is a fixed single-layer microwave capacitor placed at the RF connection between a coax cable center conductor and FET amplifier. Consequently, the coax center conductor may be DC isolated from ground by the blocking capacitors. A DC blocking capacitor is typically rated at 50 V to 100 V for safe operation, and in some cases is as low as 15 V. The voltage rating for safe operation is not the voltage at which absolute breakdown of the capacitor will occur, as one can operate the capacitor with AC signals of 100 V indefinitely and have little to no impact on the lifetime of the capacitor. The breakdown voltage of the DC blocking capacitor is unknown.

When the center conductor of the coax is isolated, internal charging within the coax cables in the communications system may charge the DC blocking capacitor to voltages exceeding their maximum voltage rating, compromising the capacitor and making it susceptible to failure. A fast transient breakdown of the blocking capacitor, plus isolated coax center conductor, would immediately cause overstress of the inner circuit components (e.g. most FET transistors) leading likely to failure and the consequent loss of RF output. The magnitude of damage depends on the energy released in the breakdown, as well as the voltage and current level and the duration of the breakdown.

In the subsequent analysis, the likelihood of internal charging for a typical Teflon based RF coaxial cable is modeled and the voltage across

the cable is quantified. The modeled voltages are compared to the voltage rating of the DC capacitor to assess whether the voltage across the cable is high enough to compromise or damage the DC blocking capacitor. If the cables experience a voltage that exceeds the rating of the DC blocking capacitor, an anomaly would likely occur.

7.7 Internal Charging Analysis of the Coaxial Cables in an SSPA System

In this section, we analyze the likelihood of internal charging in the coaxial cables leading to the power amplifiers to determine if the cause of anomalies could be due to dielectric breakdown (induced electric field exceeds the breakdown threshold). The susceptibility of a material to internal charging depends on the flux and energy spectrum of the incident electrons and the material properties, specifically the conductivity, or bulk resistivity, and the electrical-decay time constant for the material [*Wrenn,* 1995; *Sorensen et al.,* 1999]. Prior tests of Teflon cables [*Green et al.*, 2009] showed that discharge pulses can occur from the coax cable outer insulation jacket, but were not set up to measure charging or ESD pulses inside the coax. Other tests showed charging of coax cables with isolated center conductors up to multi kV levels, but no ESD [*Payan et al.,* 2005].

The RF payloads in this study incorporate low-loss coaxial cables. Low-loss cables were used in the Fleet A and Fleet B payload designs, but the specific coax cables are unknown to the authors. RG-141 is a common RF coaxial cable with characteristics that are typical of low loss RF coaxes generally (low-loss silver plated copper conductors with low-loss tangent Teflon inner dielectric), so it was used as a representative model for all RF cables. We analyze a Teflon cable, RG-141 [*Ref. Data for Radio Engineers*, 1956; *MIL-C-17/170A*, 1985], to determine if it is liable to breakdown due to internal charging in a worst-case GEO environment. The worst-case GEO environment will be described in further detail in Section 7.7.2. The material properties of RG-141 are found in Table 31.

Table 32. Material Properties of RG-141 Coaxial Cable [*Ref. Data for Radio Engineers*, 1956; *MIL-C-17/170A*, 1985]

Class of cable	high temperature, single braid
Inner conductor	0.09 cm diameter silvered copper weld
Dielectric material	solid polytetrafluoroethylene (PTFE) - Teflon
Nominal diameter of dielectric	0.2946 cm
Protective covering	Polytetrafluoroethylene- (Teflon-) tape moisture seal
Outer conductor diameter	0.371 cm (max)
Jacket	.432 cm (max)
Nominal impedance	50.0 ohms
Nominal capacitance	28.5 picoFarads/ft
Maximum operating voltage	1900 Vrms

As shown in the table above, the maximum safe operating voltage for the coaxial cable is 1900 V rms. The real breakdown threshold for the coaxial cable is not known, but is expected to be greater than 1900 V rms. The bulk conductivity of Teflon is typically cited at 1E-18/ohm-m [*ASTM D257*, 2014] in air, but can range from 1E-20/ohm-m [*Sessler,* 1975; *Bodeau,* 2010] to 1E-16/ohm-m. Ionizing radiation creates additional electron-ion carriers in the material, which increases the conductivity. This Radiation Induced Conductivity (RIC) depends upon the specific material and the radiation dose rate. The parameters that describe the RIC of PTFE are not well known, and vary with aging (total dose) of the dielectric material [*Hanna et al.,* 2013]. This wide range of conductivities has been demonstrated experimentally as a result of radiation dose (and therefore, time on orbit). In addition, conductivity is a strong function of temperature. The SSPA temperature recorded in the acquired telemetry ranges from approximately 5 to 50 C. Coaxial cable temperature is not monitored, so the SSPA temperature range was used as an estimation for the temperature range of the coaxial cable,

with the additional inclusion of 0 C. In our analysis, we parametrically vary conductivity and temperature, covering conductivities 1E-16/ohm-m to 1E-20/ohm-m and temperatures of 0 to 50 C.

7.7.1 ESA's Internal Charging Tool - DICTAT

ESA's Internal Charging Tool, DICTAT (Dielectric Internal Charging Threat Analysis Tool), is used to determine if the coaxial cables leading to the power amplifiers are likely to experience breakdown [*Rodgers,* 2004]. DICTAT is a 1-D internal charging code that determines radiation transport through various shielding to identify the maximum internal electric field in a component on orbit and compares it with a suitable breakdown threshold in order to determine whether the component is susceptible to ESD. To determine this, DICTAT calculates the electron current using analytical approximations to quantify the electron transport through a shield and the charge deposited inside the dielectric. From this deposited charge, the maximum electric field within the dielectric is found. This field is then compared with the dielectric breakdown field. Assessments of breakdown thresholds are generally empirical and vary widely. DICTAT has adopted a generic material-independent breakdown threshold value of 1E+07 V/m, derived from *Frederickson* [1980] that is consistent with known experimental results and is commonly accepted.

DICTAT accounts for the effects of temperature (T) on bulk conductivity, and the increase in conductivity due to radiation ($\dot{D}$) as shown in Equations 14 and 15 below. The radiation induced conductivity parameters, k_p and Δ, and the Arrhenius activation energy, Ea, parameter are given in Table 3 in the next section. The other parameter is Boltzmann's constant, k_B.

$$\sigma(T,\dot{D}) = \sigma_{bulk}(T) + k_p \cdot (\dot{D})^{\Delta} \tag{14}$$

$$\sigma_{bulk}(T) = \sigma_{bulk}(298K) * exp\left[\frac{-Ea}{k_B} \cdot \left(\frac{1}{T} - \frac{1}{298}\right)\right] \tag{15}$$

DICTAT divides the dielectric into "subzones" or layers of equal thickness, and calculates the charge deposited within and the current passing through each zone. The code defines the "charging current" to

be the net current flowing into each layer minus charge leakage out of the layer. The electric field is found at the boundary of each layer of the dielectric from the cumulative charge, and the surface voltage is found by summing the electric field for all zones.

The rate of charge leakage and electric field decay is controlled by the material's characteristic time constant, τ, which is defined as the product of the resistivity and dielectric constant. A wide range of electric time constants for Teflon are cited, ranging from fractions of an hour (0.9 hours [*Sorensen et al.*, 1999]), to days (2.1 days [*NASA HDBK 4002A*, 2011]), to almost a year (339 days [*Swaminathan*, 2003, *Sessler*, 1975]). However, these values are typically based on room temperature resistivity and no radiation induced effects. DICTAT's approach is to take the total conductivity accounting for operating temperature and dose rate when calculating the conductivity of the dielectric (effective resistivity) and also when calculating the time constant. Since the dose rate is varying through the material, the conductivity, electrical time constant and rate of charge leakage out of each layer vary. DICTAT derives and effective conductivity and time constant by integrating across the dielectric thickness. The DICTAT reports the charging time, which is the time it takes for the electric field that is enhanced from the environment, to decay to the equilibrium electric field.

7.7.2 DICTAT Simulations

Fluence Model for Internal Charging (FLUMIC) is the worst-case electron environment model used in DICTAT. FLUMIC gives the integral electron spectra between L=3 and L=8 (between approximately 19,000 km and 50,000 km), and is valid for energies >200 keV [*Rodgers et al.*, 2004]. The AE8 model was not used as it only provides the orbit-averaged spectrum, rather than the worst-case spectrum. The FLUMIC model was found to overestimate the observed GOES >2 MeV Integral Electron Flux by an average factor of four over six time periods (1 to 21 days) prior to the anomalies, so the FLUMIC spectrum is assumed to be an appropriate worst-case spectrum for our analysis.

A cylindrical geometry is assumed, and the DICTAT default maximum field of view of 90 degrees (hemispherical exposure) is selected. Table 33 provides a summary of the coaxial cable parameters input to

DICTAT. The dielectric and shield thickness, shield and core material, and core radius were obtained from the material properties for the RG-141 coaxial cable. To account for aluminum spacecraft shielding, the outer copper shielding is increased. A shielding thickness of 68 mils was assumed for the spacecraft structure, which includes 4 mils aluminum shielding equivalent for a thermal blanket close out and the 28 mils of aluminum equivalent of a structural honeycomb panel. The total copper shielding input to DICTAT, 0.077 cm, is the outer copper shield surrounding the dielectric summed with the approximate contribution from spacecraft shielding – totaling to 0.077 cm (30.31 mils) of copper shielding, or 100 mils of equivalent Al shielding. Typical values for the density, dielectric constant, k_p, delta constant, and thermal activation energy for Teflon electrical conductivity were also input [*Sessler*, 1979; *Frederickson et al.*, 1986; *NASA HDBK 4002A*, 2011].

Table 33. DICTAT Input Parameters for the Dielectric and the Conductor

Dielectric Parameters	**Input to DICTAT**
Dielectric material	Teflon
Thickness [cm]	0.1003
Density [g/cm^3]	2.17
Dielectric constant	2.15
Breakdown electric field [V/m]	1E+07
RIC dose rate factor k_p	2E-14
Delta	0.695
Activation energy [eV]	1.4
Conductor Parameters	**Input to DICTAT**
Shield material	copper
Shield thickness [cm]	0.077
Core material	copper
Core radius [cm]	0.047

A total of thirty-five simulations were run, with a range of resistivities (1E+18, 1E+19, 1E+20, 1E+21, and 1E+22 ohm-cm), and a range of temperatures (0C, 5C, 10C, 20C, 30C, 40C, 50C). The range of resistivities is chosen to cover the wide range of room-temperature bulk resistivities quoted in literature, as discussed previously.

7.7.3 DICTAT Simulation Results

The comprehensive results from DICTAT for a single worst-case GEO orbit (23.93 hours) are tabulated in Table 34. None of the thirty-five trials exceeded the coax insulation breakdown threshold (the calculated maximum electric field did not exceed the 1E+07 V/m threshold for any of the simulations) during one orbit.

Table 34. DICTAT Results over one worst-case GEO orbit – The calculated maximum electric field did not exceed the 1E+07 V/m breakdown threshold for any of the simulations

DICTAT Input Parameters			DICTAT Derived Parameters		
Effective Conductivity	Bulk Resistivity @ 25 C	Temperature	E-max	Charging Time	Peak Voltage
[1/ohm-m]	*[ohm-cm]*	*[C]*	*[V/m]*	*[days]*	*[V]*
1E-16	1.00E+18	0	3.87E+06	1810	3393
1E-17	1.00E+19	0	5.70E+06	3170	5766
1E-18	1.00E+20	0	6.12E+06	3660	6567
1E-19	1.00E+21	0	6.17E+06	3730	6681
1E-20	1.00E+22	0	6.18E+06	3740	6694
1E-16	1.00E+18	5	2.65E+06	1125	2148
1E-17	1.00E+19	5	5.11E+06	2650	4890
1E-18	1.00E+20	5	6.03E+06	3540	6369
1E-19	1.00E+21	5	6.16E+06	3720	6658
1E-20	1.00E+22	5	6.18E+06	3740	6691
1E-16	1.00E+18	10	1.56E+06	599	1170
1E-17	1.00E+19	10	4.19E+06	2000	3744
1E-18	1.00E+20	10	5.81E+06	3280	5959
1E-19	1.00E+21	10	6.14E+06	3680	6600
1E-20	1.00E+22	10	6.17E+06	3740	6685
1E-16	1.00E+18	20	3.62E+05	122	243
1E-17	1.00E+19	20	1.97E+06	782	1519
1E-18	1.00E+20	20	4.64E+06	2290	4266
1E-19	1.00E+21	20	5.94E+06	3420	6182
1E-20	1.00E+22	20	6.15E+06	3700	6634
1E-16	1.00E+18	30	6.64E+04	21.6	43.5
1E-17	1.00E+19	30	5.63E+05	193	384.5
1E-18	1.00E+20	30	2.59E+06	1080	2073
1E-19	1.00E+21	30	5.13E+06	2650	4897
1E-20	1.00E+22	30	6.04E+06	3540	6382
1E-16	1.00E+18	40	1.26E+04	4.06	8.235
1E-17	1.00E+19	40	1.22E+05	39.7	80.04
1E-18	1.00E+20	40	9.31E+05	332	657.2
1E-19	1.00E+21	40	3.40E+06	1510	2864
1E-20	1.00E+22	40	5.56E+06	3030	5531
1E-16	1.00E+18	50	2.70E+03	0.842	1.765
1E-17	1.00E+19	50	2.60E+04	8.39	16.96
1E-18	1.00E+20	50	2.47E+05	80.3	161.3
1E-19	1.00E+21	50	1.56E+06	590	1156
1E-20	1.00E+22	50	4.31E+06	2060	3854

There is a strong conductivity and temperature dependence for the maximum electric field, charging time, and voltage. As conductivity decreases, we expect longer charging times, higher electric fields, and higher voltages. At higher temperatures, we expect shorter charging times, lower electric fields, and lower voltages. Figure 36 shows the voltage accumulated over one orbit for the range of Teflon resistivities (1E+18 to 1E+22 ohm-cm) at temperatures between 0 and 50 C (per equation 14 above).

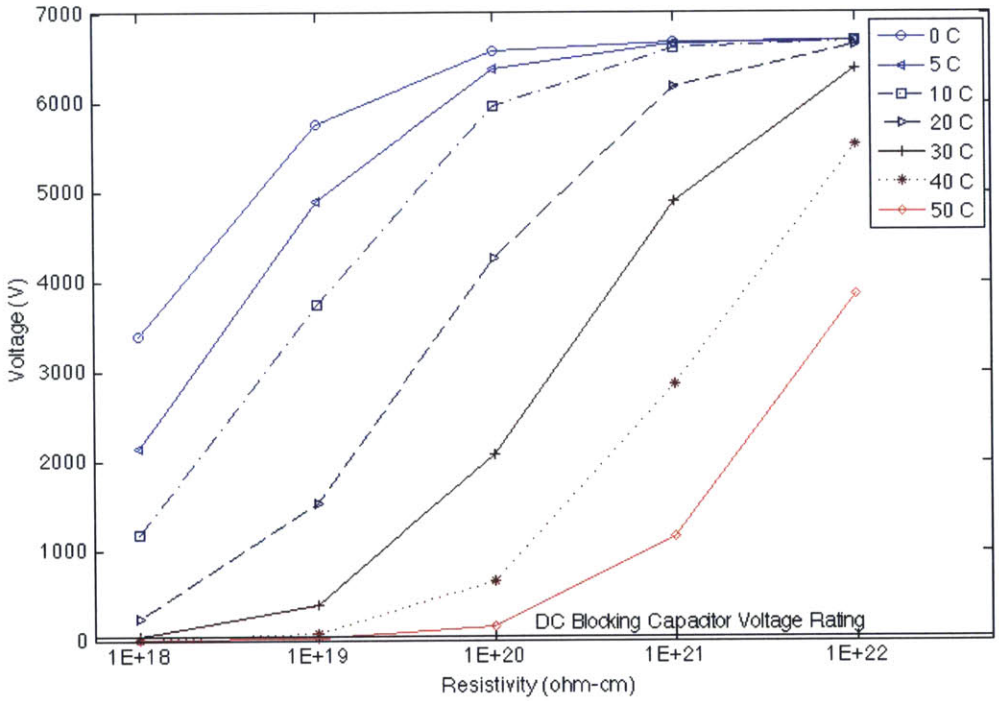

Figure 36. Voltage reached for thirty-five simulated scenarios of seven temperatures (0 to 50 degrees C) and five resistivity values (1E+18 to 1E+22 ohm-cm) for a single GEO orbit (1 day).

As seen in Figure 36, none of the cases exceeded the breakdown E-field and corresponding voltage threshold of the dielectric material for one orbit, but the voltage exceeded the blocking capacitor maximum voltage (>50 V) on thirty-two of the thirty-five simulations. The voltage was <50 V for temperatures of 30, 40 and 50 C at the highest conductivity of 1E-16 1/ohm-m (1E+18 ohm-cm resistivity). The actual capacitor breakdown threshold, which should exceed the rated by a significant amount, is unknown.

7.7.4 Electric Field and Voltage Approximations after 1, 3, 7, 10, 14, and 21 days

FLUMIC is not efficient to run for long time intervals. Therefore, the average electric field and accumulated voltage for the six periods of interest (1, 3, 7, 10, 14, 21 days) is approximated using the electric field and voltage values output from the DICTAT simulations for one orbit. The purpose of this analysis is to determine if hazardous voltages could be reached under any plausible subset of material properties. We assume that the worst-case flux is and temperature are constant over the extended time period, so the RIC, total conductivity, electrical time constant and charge accumulated per day would remain constant.

To find the electric field beyond one day, we calculate the average electric field, E_0, of the ten sections of the dielectric cylinder that DICTAT partitions for the first day. Ignoring charge leakage, each day would add an identical increment of trapped charge and increase the electric field by E_o. However, the accumulated charge and electric field from the previous day has exponentially decayed based on the time constant, τ.

Table 33 tabulates the maximum E-field of the ten sections and the charging time. Using Equation 16, along with the constant daily incremental electric field, E_0, charging time, τ, and orbit duration of 23.9 hours, Δt, we determine the electric field for each day, n.

$$E_n = E_{n-1}\left(exp\frac{-\Delta t}{\tau_n}\right) + E_0 \qquad (16)$$

The average electric field, E_n, is then multiplied by the dielectric thickness, 0.1003 cm, to calculate the accumulated voltage. The accumulated electric field and voltages are tabulated in Table 35 and Table 36, respectively, for periods of 1, 3, 7, 10, 14, and 21 days.

Table 35. Accumulated Electric Field over periods of 1, 3, 7, 10, 14 and 21 days in a worst-case GEO orbit – The calculated average electric field exceeded the 1E+07 V/m breakdown threshold for the majority of the 3, 7, 10, 14, and 21 day simulations.

DICTAT Inputs		Average E-Field after N days					
Effective Conductivity	**Temp.**	**1 day**	**3 days**	**7 days**	**10 days**	**14 days**	**21 days**
[1/ohm-m]	*[C]*	*[V/m]*	*[V/m]*	*[V/m]*	*[V/m]*	*[V/m]*	*[V/m]*
1E-16	0	3.29E+06	9.74E+06	2.21E+07	3.10E+07	4.23E+07	6.07E+07
1E-17	0	5.75E+06	1.71E+07	3.93E+07	5.56E+07	7.67E+07	1.12E+08
1E-18	0	6.55E+06	1.95E+07	4.49E+07	6.36E+07	8.79E+07	1.29E+08
1E-19	0	6.66E+06	1.99E+07	4.57E+07	6.47E+07	8.95E+07	1.31E+08
1E-20	0	6.67E+06	1.99E+07	4.58E+07	6.48E+07	8.96E+07	1.32E+08
1E-16	5	2.14E+06	6.29E+06	1.41E+07	1.95E+07	2.62E+07	3.67E+07
1E-17	5	4.88E+06	1.45E+07	3.32E+07	4.68E+07	6.44E+07	9.37E+07
1E-18	5	6.35E+06	1.89E+07	4.36E+07	6.16E+07	8.51E+07	1.25E+08
1E-19	5	6.64E+06	1.98E+07	4.56E+07	6.45E+07	8.92E+07	1.31E+08
1E-20	5	6.67E+06	1.99E+07	4.58E+07	6.48E+07	8.96E+07	1.32E+08
1E-16	10	1.17E+06	3.36E+06	7.27E+06	9.81E+06	1.28E+07	1.69E+07
1E-17	10	3.73E+06	1.11E+07	2.52E+07	3.54E+07	4.84E+07	6.97E+07
1E-18	10	5.94E+06	1.77E+07	4.07E+07	5.75E+07	7.94E+07	1.16E+08
1E-19	10	6.58E+06	1.96E+07	4.52E+07	6.39E+07	8.83E+07	1.30E+08
1E-20	10	6.67E+06	1.99E+07	4.58E+07	6.48E+07	8.95E+07	1.31E+08
1E-16	20	2.43E+05	6.07E+05	1.02E+06	1.17E+06	1.28E+06	1.34E+06
1E-17	20	1.51E+06	4.41E+06	9.69E+06	1.32E+07	1.75E+07	2.38E+07
1E-18	20	4.25E+06	1.26E+07	2.89E+07	4.06E+07	5.57E+07	8.06E+07
1E-19	20	6.16E+06	1.84E+07	4.23E+07	5.97E+07	8.25E+07	1.21E+08
1E-20	20	6.61E+06	1.97E+07	4.54E+07	6.43E+07	8.88E+07	1.30E+08
1E-16	30	3.73E+04	5.36E+04	5.56E+04	5.57E+04	5.57E+04	5.57E+04
1E-17	30	3.84E+05	1.02E+06	1.91E+06	2.34E+06	2.72E+06	3.06E+06
1E-18	30	2.07E+06	6.07E+06	1.36E+07	1.87E+07	2.52E+07	3.51E+07
1E-19	30	4.88E+06	1.45E+07	3.33E+07	4.69E+07	6.45E+07	9.38E+07
1E-20	30	6.36E+06	1.90E+07	4.37E+07	6.17E+07	8.53E+07	1.25E+08
1E-16	40	1.13E+04	1.13E+04	1.13E+04	1.13E+04	1.13E+04	1.13E+04
1E-17	40	7.98E+04	1.47E+05	1.74E+05	1.76E+05	1.76E+05	1.76E+05
1E-18	40	6.55E+05	1.83E+06	3.73E+06	4.84E+06	5.99E+06	7.35E+06
1E-19	40	2.86E+06	8.43E+06	1.91E+07	2.66E+07	3.61E+07	5.14E+07
1E-20	40	5.51E+06	1.64E+07	3.77E+07	5.32E+07	7.34E+07	1.07E+08
1E-16	50	2.56E+03	2.56E+03	2.56E+03	2.56E+03	2.56E+03	2.56E+03
1E-17	50	2.07E+04	2.20E+04	2.20E+04	2.20E+04	2.20E+04	2.20E+04
1E-18	50	1.61E+05	3.69E+05	5.47E+05	5.93E+05	6.15E+05	6.24E+05
1E-19	50	1.15E+06	3.32E+06	7.17E+06	9.67E+06	1.26E+07	1.66E+07
1E-20	50	3.84E+06	1.14E+07	2.60E+07	3.65E+07	4.99E+07	7.20E+07

Table 36. Accumulated Voltage over a period of 1, 3, 7, 10, 14, and 21 days – The voltage threshold of the DC Blocking capacitor (50 V) was exceeded for all of the simulations except for four of the 1 day accumulated voltage simulations

DICTAT Inputs		Accumulated Voltage after N days					
Effective Conductivity	Temp.	1 day	3 days	7 days	10 days	14 days	21 days
[1/ohm·m]	*[C]*	*[V]*	*[V]*	*[V]*	*[V]*	*[V]*	*[V]*
1E-16	0	3,298.87	9.77E+03	2.22E+04	3.11E+04	4.24E+04	6.09E+04
1E-17	0	5,765.85	1.72E+04	3.95E+04	5.57E+04	7.69E+04	1.12E+05
1E-18	0	6,566.24	1.96E+04	4.51E+04	6.38E+04	8.81E+04	1.29E+05
1E-19	0	6,681.44	1.99E+04	4.59E+04	6.49E+04	8.98E+04	1.32E+05
1E-20	0	6,692.62	2.00E+04	4.60E+04	6.50E+04	8.99E+04	1.32E+05
1E-16	5	2,148.33	6.31E+03	1.41E+04	1.96E+04	2.63E+04	3.68E+04
1E-17	5	4,889.63	1.45E+04	3.33E+04	4.70E+04	6.46E+04	9.40E+04
1E-18	5	6,368.55	1.90E+04	4.37E+04	6.18E+04	8.54E+04	1.25E+05
1E-19	5	6,658.01	1.98E+04	4.57E+04	6.47E+04	8.94E+04	1.31E+05
1E-20	5	6,691.72	1.99E+04	4.60E+04	6.50E+04	8.99E+04	1.32E+05
1E-16	10	1,169.97	3.37E+03	7.29E+03	9.84E+03	1.28E+04	1.70E+04
1E-17	10	3,743.10	1.11E+04	2.53E+04	3.55E+04	4.85E+04	6.99E+04
1E-18	10	5,958.62	1.77E+04	4.08E+04	5.77E+04	7.96E+04	1.16E+05
1E-19	10	6,599.94	1.97E+04	4.53E+04	6.41E+04	8.86E+04	1.30E+05
1E-20	10	6,685.00	1.99E+04	4.59E+04	6.50E+04	8.98E+04	1.32E+05
1E-16	20	243.55	6.08E+02	1.02E+03	1.18E+03	1.28E+03	1.35E+03
1E-17	20	1,518.54	4.42E+03	9.72E+03	1.33E+04	1.76E+04	2.39E+04
1E-18	20	4,266.16	1.27E+04	2.89E+04	4.07E+04	5.59E+04	8.09E+04
1E-19	20	6,181.79	1.84E+04	4.24E+04	5.99E+04	8.27E+04	1.21E+05
1E-20	20	6,633.84	1.98E+04	4.55E+04	6.44E+04	8.91E+04	1.31E+05
1E-16	30	37.36	5.38E+01	5.58E+01	5.58E+01	5.58E+01	5.58E+01
1E-17	30	385.54	1.03E+03	1.92E+03	2.35E+03	2.73E+03	3.06E+03
1E-18	30	2,072.90	6.08E+03	1.36E+04	1.88E+04	2.52E+04	3.52E+04
1E-19	30	4,896.65	1.46E+04	3.34E+04	4.70E+04	6.47E+04	9.41E+04
1E-20	30	6,382.39	1.90E+04	4.38E+04	6.19E+04	8.55E+04	1.25E+05
1E-16	40	11.28	1.13E+01	1.13E+01	1.13E+01	1.13E+01	1.13E+01
1E-17	40	80.04	1.48E+02	1.74E+02	1.77E+02	1.77E+02	1.77E+02
1E-18	40	657.19	1.84E+03	3.75E+03	4.86E+03	6.01E+03	7.38E+03
1E-19	40	2,863.67	8.46E+03	1.91E+04	2.67E+04	3.62E+04	5.16E+04
1E-20	40	5,530.84	1.65E+04	3.78E+04	5.34E+04	7.36E+04	1.07E+05
1E-16	50	2.57	2.57E+00	2.57E+00	2.57E+00	2.57E+00	2.57E+00
1E-17	50	20.80	2.21E+01	2.21E+01	2.21E+01	2.21E+01	2.21E+01
1E-18	50	161.32	3.70E+02	5.49E+02	5.95E+02	6.17E+02	6.25E+02
1E-19	50	1,155.83	3.33E+03	7.19E+03	9.70E+03	1.26E+04	1.67E+04
1E-20	50	3,854.43	1.14E+04	2.61E+04	3.66E+04	5.01E+04	7.23E+04

As expected, the largest accumulated electric fields and voltages occur for the trials with the lowest operating temperatures and lowest bulk room-temperature conductivities (highest resistivities). The largest electric field, 1.32E+08 V/m, occurred after 21 days at 0 degrees Celsius and a room temperature conductivity of 1E-20 1/ohm-m. The electric field is greater than the dielectric breakdown threshold, 1E+07 V/m; therefore this trial, as well as all other trials, was liable to experience breakdown. The values in Appendix C that are bolded are greater than the maximum safe operating voltage (1900 V rms) of the coaxial cable. A total of 161/210, or 76.7%, of the voltages in Appendix C were greater than 1900 V, which would indicate the coaxial cable was in an unsafe operation mode.

We acknowledge the non-realistic aspect of using a short duration worst-case flux for multi-week time frames, and that we may be predicting voltages capable of breaking down the capacitors or even the coaxial cables in some cases when a more realistic environment could possibly not have such a risk. Given the uncertainty in material properties, the unknown capacitor breakdown voltage and our pessimistic environment, we deemed the analysis insufficient to *prove* a hazard existed. The results were sufficient motivation to undertake lab tests to assess risk.

Electron tests were conducted in collaboration with Space Systems/Loral (SSL) to better understand the implications of the high voltages reached inside the coaxial cable, and whether resulting damage would occur on the DC blocking capacitor. Section 7.8 describes the experiments in further detail.

7.8 High-Energy Electron Beam Experiments with Coaxial Cable and a DC Blocking Capacitor

The Pelletron accelerator at NASA Marshall Space Flight Center, capable of emitting electrons from 300 keV to 2.5 MeV, was used to test a coax cable connected to an RF front-end circuit (DC blocking capacitor circuit). The accelerator is connected to a sample test chamber that is maintained below 1E-05 Torr (vacuum). Thick shielding inside the test

chamber prevents electrons from discharging material inside the chamber other than the intended test sample. The overall goal of the test was to determine whether any discharges were observed under irradiation, and if any damage resulted from breaching the voltage rating for safe operation of the DC blocking capacitor.

Payan et al., *[2005]* similarly tested coax cables with DC isolated ("floating") center conductors. In their test, a coax cable was charged to 1200 V (center conductor to shield) without spontaneous breakdown. The coax core was then switched to allow the current transient that occurred when the charge core was grounded to be measured. None of the SSPA failures we are assessing were associated with any commanded coax switching events. The lack of breakdown is consistent with the voltage rating of the RG-141 (1900 Vrms). Clearly, if a DC blocking capacitor had been attached to the coax, it would have experienced breakdown before the cable reached 1200 V. In this experiment, a small square of material, referred to as a "flag", was placed facing an electrostatic potential meter, such as a TREK probe and meter, a method commonly used to monitor the potential of the floating core. Payan et al., *[2005]* suggest providing shunt resistance to prevent coaxial cables from accumulating charge.

The impacts of not providing shunt resistance to an RF circuit were observed in the Galileo testing of a coax cable (RG-142/U) performed at JPL [*Leung et al.*, 1985]. For this experiment, coax cables with inner conductors terminated in 50 ohms, were tested at high Jovian e-flux levels and energies. The 50-ohm termination acted as the electrical probe of the coax for ESD event detection. In this configuration peak voltages of 4-6 V, and 8 V worst case were observed, showing that electrical breakdown of the internal dielectric was inconsequential to the health of any connected components, like a DC blocking capacitor. Wire bundles with one or more floating coax center conductor, representing "abandoned" wires after modifications and repairs in the harness, were also tested. Measurements were taken of the ESD transients from the electrically isolated wires in the harness, cross-coupled to another line terminated in 50 ohms. Discharges in the 10s of Volts were observed when measuring peak voltages cross-coupled into other cables. While this serves as further evidence that ungrounded coax would charge and discharge, measurements of the center conductor

voltage or the ESD currents from the ungrounded coax breakdown were not collected [*Leung et al.*, 1985].

We planned a charging test using an RG-141 coax connected with a DC blocking cap to determine if the coax would charge and cause the blocking cap to breakdown, and to measure the resulting current pulse (into a 50 ohm load) to determine if the pulse was sufficient to damage downstream RF components. For this experiment, a 2.18-meter RG-141 coaxial cable rated to 1900 Vrms with a capacitance of 28.5 pF/ft (total capacitance of ~205 pF) and a DC blocking capacitor of ~15 pF rated to 50 V for safe operation, were tested at two different electron beam energies (300 keV and 1 MeV). The lengths of coaxial cables vary significantly throughout the actual spacecraft, although satellite designers make every attempt to minimize lengths to reduce loss, weight and cost. A cable length of 2.18 m was chosen as representative of a typical coax length. The cable was exposed to a respective worst-case GEO test fluence for both energies. A beam energy of 300 keV primarily charges the dielectric in the vicinity of the coax shield, while a 1 MeV beam charges the dielectric closer to the center conductor. Worst case GEO fluences of 3.6E+12 e/cm^2 for 300 keV and 8.4E+11 e/cm^2 for 1 MeV were reached using a flux of 1.9E+08 e/cm^2/s (approximately 0.03 nA/cm^2).

A Pearson current probe was used to measure and record the total arc count and a second current probe was used to monitor current on the coax. Arcs were defined by a trigger level of 20 mA across a 50 ohm resistor beyond the blocking capacitor. Figure 37 shows a diagram of the RF circuit test configuration that includes a flight-like chip blocking capacitor built on RF substrate that is common to GEO communications satellites. The coax is open at one end in the chamber; the center conductor of the other end of the coax connects directly to the DC blocking capacitor (the RF input) through a monitor box. Both the DC blocking capacitor and coaxial cable are electrically connected, and the center conductor of the coax and the input side of the blocking capacitor are at the same voltage. The coax shield is grounded at the chamber wall feedthrough. There is also another extension coaxial cable from the chamber wall to the monitor box. The outer shield of the extension coaxial cable is grounded at one end of the chamber wall and the other end is connected to the monitor box chassis that is hard grounded to the

facility ground, like the chamber wall. It is assumed that the in-orbit coaxes are an open circuit at both ends, however, the satellite SSPA manufacturers and satellite owners have not confirmed the assumption.

In the experiment, the electron beam strikes the coaxial cable, and charge begins to accumulate in the dielectric material and center conductor within the coax. As tested, most of the cable was in the electron beam since the coax was coiled. The charge accumulation results in a voltage between center conductor and shield and across the capacitor to the 50 ohm load. The monitor box is a Faraday cage through which the center conductor is routed, so that current probes can be used to measure current flowing along the center conductor. The current measurement is taken on the exposed center conductor of the coax, and not around the shield of the coax.

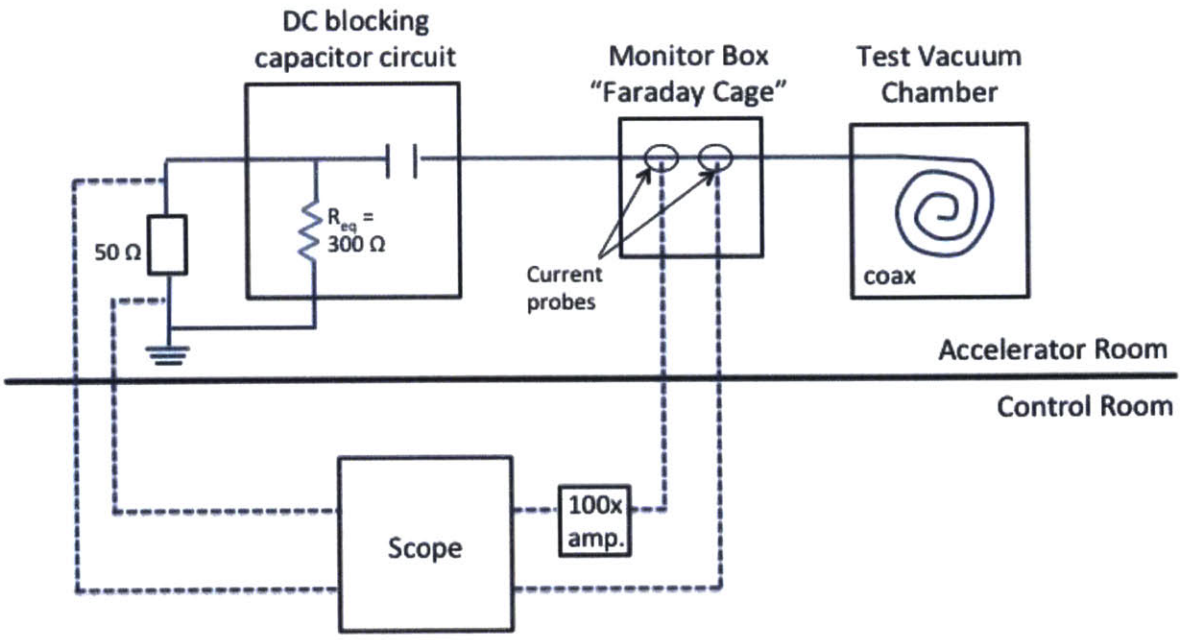

Figure 37. Test configuration for electron experiments for DC blocking capacitor and coaxial cable. Dashed lines are probes where data is read by the scope.

A total of two arcs were observed, both at a beam energy of 1 MeV with a steady current of 0.03 nA/cm^2. The first arc occurred at 1.46E+11 e/cm^2, and had a peak of ~6A and a duration of ~0.25 µs. This level and duration is similar to the findings of *Green et al.* [2009]. The second arc

occurred at 2.35E+11 e/cm^2 had a ~4A peak and lasted for ~0.25 μs. A visual inspection and a DC resistance check were performed after each arc. The corresponding peak voltages across the 50 ohm resistor reached 200 V and 300 V. The total pulse energy delivered to the 50 ohms would be up to ~200 -450 uJ. The peak voltages and pulse energy are more than sufficient to damage the SSPA RF FETs (damage thresholds for JFETs are cited at ~1 uJ in *Rudie* [1981] and *Davis* [1992]), however, ESD pulse injection tests of the specific devices and circuits used in the SSPAs would be required to confirm this.

The RG-141 is rated to approximately 1.9 kV RMS [*Ref. Data For Radio Engineers*, 1956], far above the 50 V rating for safe operation of the DC blocking capacitor. The DC blocking capacitor represents <10% of the total capacitance of the RF circuit, so most of the stored charge and energy delivered by the breakdown comes from the coax, not the DC blocking capacitor. While the blocking capacitor can be considered the "weak link" from a voltage standpoint, it is the combined charge and energy that is being dumped and which would cause failure of downstream RF components.

Post arc inspections at the irradiation site revealed that after both arcs the blocking capacitor was still an open circuit from the RF input (coax connection) to the 50 ohm load, and from the RF input to the facility ground. The equivalent resistor (R_{eq}) continued to show ~300 ohms to ground. An additional test was done with a Gohm-meter, which showed >20 Gohms across the coax shield to center conductor, indicating no degradation to the coax or the DC blocking capacitor, and no formation of a leakage path as a result of the discharge. One possible explanation why no damage occurred to the coax or DC blocking capacitor could be that energy of the transient arc was too low to cause visible damage. High magnification examination of the DC blocking circuit was challenging to capture due to lighting conditions, but is presented in Figure 38, which shows no damage or burn mark.

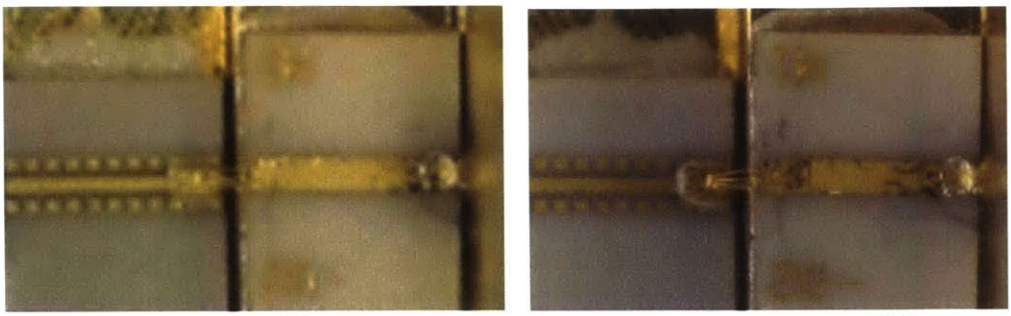

(a) (b)

Figure 38 (a,b). High magnification of (a) pre-test and (b) post-test articles. No burn marks appear on the post-test article

Post irradiation RF performance tests of the circuit were conducted by Space Systems/Loral (SSL) RF laboratory. Table 37 summarizes the pre- and post-irradiation RF performance test results.

Table 37. RF Performance Summary of Pre and Post Charging Test

Time of Test	Freq (GHz)	Insertion Loss (dB)	DC Blocking Capacitor (pF)
Pre-test	5	-2.31	16.5 @ 3 kHz
	10	-2.55	16.0 @ 100 kHz
	15	-3.38	14.3 @ 100 MHz
Post-test	5	-4.34	22.2 @ 3 kHz
	10	-4.65	21.8 @ 100 kHz
	15	-5.54	19.6 @ 100 MHz

The post-test showed a 2 dB degradation in insertion loss and a 5 pF (33%) increase in the DC blocking capacitor, which is significant given that the precision of the measurement is better than 5% in capacitance. Insertion loss is an S-parameter measurement, S12 parameter, which is performed using a network analyzer in a 50 ohms system. The 2 dB increase in insertion loss indicates resistive degradation occurred, even though it was not evident with visual inspection. The post RF measurement reconfirmed the operability of the RF blocking circuit and specifically that the DC blocking capacitor continued to isolate the input DC voltage applied to the RF input port. Visual inspection found no damage (e.g. broken or fused wire bond) nor discoloration on the thin film substrate. The result that there was a discharge suggests that a device following the capacitor (e.g. LNA) may have been the component that was most overstressed when the breakdown occurs.

7.9 Chapter Summary and Conclusions

Chapter 7 focuses on the idea of going from statistical analysis of on-orbit anomalies to root-cause identification. It is interesting to have the opportunity to utilize spacecraft telemetry to understand the effects of the space weather environment, and to compare like anomalies with environmental data to enable pattern identification and the establishment of a plausible cause. In this work analysis of data from satellites of components across similar fleets, and then comparing those data with results from other fleets provides insight into how the space environment impacts similar components within each fleet as well as general trends that may be common amongst different fleet.

After calculating the >2 MeV electron fluence for periods of 1, 3, 7, 10, 14, and 21 days before anomalies, we find that the occurrence of anomalies after 14 days of >2 MeV electron fluence between 2E+10 and 4E+10 e/cm^2 is 2.62 standard deviations greater than 1000 Monte Carlo trials of twenty-six randomly selected anomaly dates. This demonstrates the anomaly rate is well above a random failure rate. Similarly we find that the number anomalies that occur after 21 days of >2 MeV electron fluence between 6E+10 – 8E+10 e/cm^2 is 2.34 standard deviations greater than 1000 Monte Carlo trials of twenty-six randomly selected anomaly dates, demonstrating the anomaly rate is well above a random failure rate.

The high correlation with 14 day and 21 day fluence suggests deep charging may be occurring in materials with a long electrical charging time constant, which in turn requires a very high electrical resistivity. A survey of the RF payload design suggested that the RF coaxes connected to the SSPA inputs and outputs is the most likely source of ESD, because of the very high resistance dielectrics (PTFE Teflon) and high electron flux exposure. This is another reason, that the charge mobility effect of energetic electrons was not pursued. The coax center conductors were assumed to be DC isolated by DC blocking capacitors, commonly used at RF interfaces to coaxes.

DICTAT charging analyses with a bounding GEO electron flux environment predicted electrical breakdown over a wide range of operating temperatures and dielectric (room temperature) resistivities, lending credence to internal charging of the coax and DC blocking cap as a possible cause of the failures. Given the uncertainty in the coax and blocking capacitor properties and breakdown thresholds, we went the next step and conducted an electron beam test to show we could reach breakdown in a representative coax and dc blocking capacitor. The pulses delivered to a 50 ohm load, which was a stand in for the RF transistor next in line, was of sufficient voltage and energy to likely cause failure of the transistor. The combination of the charging analysis and ground test show that internal charging is a plausible explanation for at least some of the reported SSPA failures:

(1) the statistically significant elevated anomaly rate correlated with high 14 day and 21 day fluences preceding the anomalies;
(2) the DICTAT analysis that predicts hazardous charging of a coax over a wide range of possible bulk resistivities and operating temperatures,
(3) a demonstration by electron beam exposure that a representative coax (RG-141) isolated by a representative DC blocking circuit would discharge, and
(4) the discharge peak voltage and energy appears more than sufficient to damage RF FETs

To make the case that internal charging of RF coax was the root-cause more solid would require a much more detailed analysis using the specific coax connected to each SSPA, exposed to the specific flux inside the shielding provided by the specific satellite configuration, using the external electron flux environment accumulated following the unique launch dates of the 8 satellites. This level of detail makes both the analysis and ground test more expensive. Internal charging is a sufficiently credible explanation of at least some of the SSPA failures that adopting the recommendation of *Payan* to incorporate a shunt resistance to prevent charging of the coax and blocking cap appears to be a more practical investment.

Chapter 8. Conclusions and Future Work

In this chapter, we review the main topic of each of the preceding chapters. Section 8.1 and 8.2 summarize the results and findings, and synthesize these into contributions for the solar array degradation analysis and solid state power amplifier anomalies, respectively. Ultimately, this chapter ends with a discussion of future work.

The overall goal of this work is to better understand the impacts of the space environment on geostationary satellite component performance. We focus on two geostationary satellite components, solar arrays and high power amplifiers. Solar arrays are the primary source of power, and power amplifiers enable data transmission (including communications such as news and entertainment media as well as tracking and emergency-response data).

The competitive nature of the satellite communications business makes it difficult to access proprietary telemetry data, even for scientific purposes. It is also difficult to obtain high fidelity space weather data in close proximity to a particular satellite, because the environmental data is currently only measured onboard large satellites that are sparsely located throughout the GEO belt. With limited data, it is challenging to perform failure analyses that can identify the cause of an anomaly.

Satellite operators maintain archives of component telemetry and housekeeping data for the purpose of monitoring the satellites' primary system functions. Satellite performance and component anomalies are detected with thresholds used to trend the real-time data transmitted from orbit. Outside of fleet maintenance, scientific analyses to understand the physical causes of historic component anomalies are generally limited or non-existent.

In this work, our strategy to overcome the barrier of acquiring on-orbit data is to partner with geostationary satellite operators, who own the satellite telemetry. We were able to acquire over a million hours of on-orbit geostationary communications satellite telemetry, from Inmarsat, headquartered in the U.K., Telenor headquartered in Norway, and ARABsat headquartered in Saudi Arabia. We demonstrated a new approach toward understanding space weather effects on space components by obtaining and using this telemetry for scientific analysis. While we were able to make new contributions using these data, the

amount we were able to collect and analyze is only a tiny percentage of the total amount of geostationary satellite telemetry that could be utilized.

For GEO satellite operators, telemetry is generally stored in archives after a period of approximately a week. Obtaining archived telemetry data is a time-intensive, non-user friendly process that is unique for each of the operators and sometime unique to each spacecraft. Acquiring the telemetry for this work required a considerable amount of data management and conditioning before analysis could begin.

Once the telemetry data was in a workable state, we proceeded to gather space weather data from the OMNI2 database, the Geostationary Operational Environmental Satellite (GOES), the Solar Influences Data Center, and Los Alamos National Labs (LANL) geostationary satellites. The space weather data also required a substantial amount of management and conditioning. Once we began our analysis, we mapped each satellite under analysis to the closest available space weather monitoring satellite's data.

In Chapter 2, we provide a description of the space weather environment and the particle populations that were measured in the acquired space weather data. Chapter 2 also includes information on radiation degradation metrics and mechanisms, such as total ionizing dose, charging and single event effects. We also describe current environmental models of the LEO and GEO radiation environment, as well as environmental metrics used to describe the space weather environment (*Kp* Index, *AE* Index, and *Dst* Index) that are relevant to the analyses conducted in later chapters.

Chapter 3 presents an analysis of the GEO space weather environment in terms of environmental metrics, *Kp* and *Dst* indices, and in situ measurements such as $\log_{10}$(1.8-3.5 MeV electrons) and >10 MeV protons. The results from this assessment provide a clearer understanding of the likelihood of increased activity, defined as greater than 2 median absolute deviations (MADs) above the median activity during a particular solar cycle phase (ascending, maximum, descending, and declining), as well as during shorter time periods (3-, 14-, and 30-days). In addition to being useful for analyses in this work, our

tabulations, which capture baseline variability over the past four solar cycles, can also be used for operational decisions during space weather related warnings.

In Chapter 3 we find that increased variability in the *Kp* index typically occurs in the declining phase of the solar cycle, when the average *Kp* generally reaches a maximum. The maximum likelihood of increased *Dst* always occurs during solar minimum. It is important to remember that the maximum likelihood of increased *Dst* does not coincide with the occurrence of highly-negative *Dst,* associated with severe geomagnetic storms, but when variability peaks. High-energy protons are known to peak in flux at solar maximum, yet we find that their variability does not peak at solar maximum. While this may seem contradictory, it simply means that fluxes are steadier during times when fluxes are also elevated. Lastly, the average annual electron flux reaches a maximum flux during the declining phase of the solar cycle, which is known as the phase when elevated high-energy electrons in the outer belt is most prevalent. We find that the maximum likelihood of increased high-energy electron flux occurs in the declining phase of Cycle 22 and the minimum phase of Cycle 23.

8.1 Summary of the Solar Cell Degradation Analysis

Chapter 4 and Chapter 5 address the following research question that was posed in Chapter 1:

> How does geostationary communications satellite telemetry improve our understanding of the impact of solar particle events on solar cell degradation during solar proton events (SPEs)?

Chapter 4 begins with an introduction to space-based photovoltaic power systems and an explanation of the primary solar cell performance parameters used to monitor solar array performance. The physics behind the mechanisms of solar cell radiation damage are also explained. Chapter 4 ends with a discussion of the environmental models used to calculate solar cell degradation, which are required to ensure that satellites will meet their EOL power levels.

In the first half of Chapter 5, we quantify the annual degradation experienced on-board eleven geostationary satellites with either Si or GaAs cells is quantified. As expected, our analysis shows that GaAs cells experience less degradation than Si cells. The average annual percent degradation of the Si cells was calculated to be between 0.71% and 1.69% per year over the mission life. The average annual percent degradation for GaAs cells ranged from 0.44% to 1.03%. The total average degradation, or the average of all of the individual average annual GaAs array degradations, is approximately 0.67%, which is roughly 0.37% less than the total average annual degradation of silicon solar cells, which was 1.04%. Our results also show that degradation rates for silicon cells have decreased from 25% over a 10 year mission, as is generally assumed in design based off findings in the 1990s, and are now approximately 10% over a 10 year mission (approximately 1.04% per year, as can be seen in Table 12).

The years in which severe SPEs of 10 MeV protons > 10,000 pfu occurred were the years in which the highest annual degradation occurred. We quantified the degradation experienced over the SPEs to determine whether solar cell degradation had a functional relationship with the accumulated fluence or the fluence/hour (flux) of the SPEs.

We plotted the percent degradation vs. the accumulated fluence (protons/cm^2) as well as the degradation vs. SPEs normalized to the duration of each of the SPEs measured in hours. Linear fits were applied to the four data sets (Si degradation over SPES, GaAs degradation over SPEs, Si degradation normalized to one hour of the SPEs, and GaAs degradation normalized to one hour of an SPE). Equations for linear curve fits were found for all four data sets. The maximum R^2 value across all of these fits was only of 0.8. Since the data sets are still currently sparse, we would need additional solar array degradation telemetry to improve our understanding of the functional relationship between SPE strength and solar array degradation. Analysis of additional on-orbit solar cell telemetry for Si and GaAs cells that were operational during a minimum of years 2000 to 2004, could help develop a functional relationship between SPE proton flux and solar array degradation.

The remaining half of Chapter 5 analyzes nine combinations of environmental models for the trapped and transient radiation environment at GEO, which are required as input for predicting solar array degradation. The purpose of the analysis is to determine which combination of environmental models most accurately predicts the experienced on-board solar array degradation of the eleven GEO communications satellites analyzed in this chapter. The results show that the models predicted an average annual percent degradation in I_{sc} to within <0.8% accuracy of the observed on-orbit value for Si cells and to within <0.4% accuracy of the observed on-orbit value for GaAs cells. When looking at the overall average of the absolute value of the deviations the models predict within <0.43% accuracy for Si and within <0.36% for GaAs.

Table 27 summarizes the models that provided the largest and smallest overall average of the absolute deviation in the deviations between the modelled and observed solar array degradation for all four simulated scenarios (Si and GaAs cells with 4 mils of coverglass and Si and GaAs cells with 4 mils of coverglass and 2 mils of adhesive). We have also included Table 27 in this chapter for reference.

Table 27. Summary of Differences Between the Overall Average of the Absolute Value of the Expected Annual Average Degradation On-orbit and models, normalized to the observed degradation.

	Min. Difference (%)	Model for Min. Difference	Max Difference (%)	Model for Max. Difference
Si with 4 mils cg	0.14	AE8-MAX	0.44	IGE-2006
Si with 4 mils cg, 2 mils adhesive	0.13	AE8-MAX	0.47	IGE-2006
GaAs with 4 mils cg	0.17	ESP 95%	0.46	AE8-MAX, AP8-MIN, JPL Extended
GaAs with 4 mils cg, 2 mils of adhesive	0.18	IGE2006, AP8-MIN, JPL91 Extended	0.37	AE8-MAX, AP8-MIN, JPL91 Extended

For simulations behind 4 mils coverglass and for 4 mils coverglass with 2 mils of adhesive. Model combination 2, AE8-MAX alone, produced the closest output from a model compared amongst the nine combinations of models for Si cells. For GaAs, model combination 8, IGE2006, AP8MIN, JPL91 Extended, and model combination 4, ESP 95th alone, produced the least deviation amongst the nine combination of models for GaAs cells. More telemetry is required before it is appropriate to conclusively prescribe which model combination is the "best" model combination to use.

8.2 Summary of the Root-Cause Amplifier Anomaly Investigation

Chapter 6 provides background information on GEO communications satellite high power amplifiers: solid state power amplifiers (SSPAs) and traveling wave tube amplifiers (TWTA). The current and future trends for SSPAs and TWTAs, including details on the underlying technology and physics behind these two types of amplifiers, and discussions of the advantages and disadvantages of both technology types are detailed.

Chapter 7 addresses the last of our research question:

> How does the space environment affect geostationary communication satellite components?

To address this question we investigate whether space weather effects are the likely cause of amplifier anomalies and which effects and causes of failure are the most likely candidates. The actual causes of satellite anomalies are difficult, if not impossible, to identify, because satellites are rarely, if ever, returned to Earth for anomaly investigation. [*Baker,* 2000; *Choi et al.,* 2011]. The effects of high-energy particle radiation from relativistic electrons, low-energy electrons and high-energy protons, as well as galactic cosmic rays are typically blamed for uncharacteristic satellite performance [*Baker,* 2000].

Chapter 7 focuses on understanding the role that space weather may have played in twenty-six high power amplifier anomalies on GEO

communications satellites. After an initial assessment of all possible space weather effects, our findings support a specific focus on the high-energy electron environment. Most SSPA anomalies for Fleet A occurred after solar maximum, during the descending phase of the solar cycle. Fleet B has not yet experienced a full solar cycle, but the analysis should be repeated once those data are available. For both fleets, the average value of *Kp* remained < 2 over time periods of 2 days, 3 days, and 14 days before the time of anomaly, which suggests that the anomalies occurred at times of relatively quiet geomagnetic activity and that they were probably not solely caused by surface charging.

We also examine whether the anomalies had any local time (LT) dependence. Anomalies occurred in all LT sectors, with 46% (Fleet A) and 38.5% (Fleet B) in the midnight to dawn sector and 54% (Fleet A) and 46% (Fleet B) in the local noon to dusk sector. From the local time distribution, surface charging does not appear to be the sole cause of the anomalies.

From 1996 to 2009, the average of the 1.8–3.5 MeV electron flux was 1.98 e/(cm^2 s st keV). Five of the 26 anomalies, unfortunately, do not have corresponding science observations (specifically, electron flux data in the LANL data set), so this part of the analysis uses the 21 anomalies when science observations were available.

Eleven anomalies experienced elevated flux approximately one to two weeks prior to the anomaly. Elevated flux is defined as flux greater than one standard deviation above the average flux from 1996-2009, or a $\log_{10}$ of 1.8-3.5 MeV electron flux of 0.297. The average of the enhanced values that occurred prior to the anomalies was 0.7419 $\log_{10}$(e/(cm^2 s st keV)) or 1.57 standard deviations above the $\log_{10}$ of 1.8-3.5 MeV electron flux. Six out of 21 anomalies experienced a high-energy electron flux greater than 1.5 standard deviations above the mean of the $\log_{10}$ of the flux between 7 and 14 days prior to the anomaly.

Of the total 4949 electron flux measurements between 1996 and 2009, 229 measurements or (4.6% of the measurements) were above 1.57 standard deviations of the $\log_{10}$ of 1.8-3.5 MeV electron flux. These 229 measurements do not occur uniformly between 1996 and 2009. The 229 measurements are clustered around the declining phase of the solar

cycle, when geomagnetic activity is known to increase, and are vary sparse at solar max.

Therefore, to understand the likelihood that a random anomaly occurs one to two weeks after a level of $\log_{10}$ of 1.8-3.5 MeV electron flux greater than 1.57 standard deviations between 1996-2009 we conducted a Monte Carlo simulation. Specifically, we determined the likelihood that twenty-six random anomalies would occur between seven and fourteen days after a level of $\log_{10}$ of 1.8-3.5 MeV electron flux greater than 1.57 standard deviations. For 100,000 iterations of the Monte Carlo simulation we found that on average 2 out of 26 anomalies occur seven to fourteen days after a $\log_{10}$ of 1.8-3.5 MeV electron flux greater than 1.57 standard deviations. *We find that approximately five times that number of anomalies occurred after elevated electron events of the same level in the data.*

This finding suggest that internal charging from either past elevated radiation belt fluxes or some conditions related to relativistic electron enhancements (either causally or accidentally) are most likely responsible for the SSPA anomalies. To investigate whether internal charging is a likely cause of the anomalies, we investigate the accumulation of >2 MeV electron flux over time, or the >2 MeV electron fluence over different time periods before the anomalies.

After calculating the >2 MeV electron fluence for periods of 1, 3, 7, 10, 14, and 21 days before anomalies, we find that half (13 of 26) of the anomalies occur after 14 days of >2 MeV electron fluence greater than 2E+10 e/cm^2. This is a factor of three higher than 1000 Monte Carlo trials of twenty-six randomly selected anomaly dates, demonstrating the anomaly rate is well above a random failure rate. The high correlation with 14 day and 21 day fluence suggests deep charging is occurring in materials with a long electrical charging time constant, which in turn requires a very high electrical resistivity.

To assess whether or not deep charging could cause anomalies, we modeled the charge build up in a representative RF coaxial cable for one orbit using ESA's Internal Charging simulation code, DICTAT. This software determines the electric field and the voltage accumulated in a dielectric material in the GEO environment. In this study, we used

Teflon for the coax dielectric material. We examined the maximum electric field to determine if the dielectric experiences breakdown, and we examined the voltage to determine if other components in the amplifier chain, such as the DC blocking capacitor, experience hazardous voltages. We then estimated the electric field and voltage over larger intervals of time, to assess if dielectric charging and discharge may be responsible for the power amplifier anomalies.

The charging analysis simulation produced the largest electric field (1.32+08 V/m) after 21 days at 0 degrees Celsius and a conductivity of 1E-20 1/ohm-m. The highest electric field is greater than the threshold electric field for dielectric breakdown, 1E+07 V/m. Therefore, this trial, as well as all other trials, shows that dielectric breakdown due to internal charging of the coax is plausible. The accumulated voltages exceed the voltage ratings of typical DC blocking capacitors on all trials except for: 50 degrees C for conductivity of 1E-17 1/ohm-m, as well as 30, 40, and 50 degrees C for a conductivity of 1E-16 1/ohm-m. The highest voltage reached, 1.32E+05 V, occurred after 21 days at 0 degrees Celsius and a conductivity of 1E-20 1/ohm-m, and 1E-19 1/ohm-m. This suggests charging to levels leading to breakdown and discharge of DC blocking capacitors occurs for some ranges of coax temperature and resistivity.

Two *NASA-HDBK-4002A* [2011] handbook specifies a safe ***ten-hour*** fluence level of $\leq$2E+10 electrons/cm^2. The safe fluence level is derived from the Combined Release and Radiation Effects Satellite (CRRES) Internal Discharge Monitor (IDM), which experienced no ESD events when the accumulated fluence *inside the IDM* over a 10 hour orbit was less than 2E+10 e/cm^2 [*Vampola,* 1987]. The safe 10 hour fluence level should be modified to incorporate a safe fluence energy level, as well as consideration of the electrical time constant (leakage rate) of the material.

The Pelletron accelerator at NASA Marshall Space Flight Center was used to test a 2.18-meter RG-141 coaxial cable and a DC blocking capacitor of ~15 pF and rated to 50 V. The devices were irradiated at two different electron energies, both representing worst-case GEO test fluences, respectively: 3.6E+12 e/cm^2 for 300 keV and 8.4E+11 e/cm^2 for 1 MeV, using a flux of 0.03 nA/cm^2 (approximately 1.88E+08 e/cm^2/s).

The energetic electron beam test of a typical RF coax at ambient temperature terminated in a DC blocking capacitor produced two discharges with sufficient peak voltage and energy to damage active RF semiconductors. While these peaks caused degradation in the RF performance of the circuit, they did not cause catastrophic damage to the coax or blocking cap. Unfortunately, there are not straightforward ways to measure and detect charging on coax cables in space due to the thick coax shielding; only discharge can be measured with standard configurations. Future work includes experimental testing of coaxial cables and other key components in the power amplifier system. These tests would include a "flag" connected to the center conductor, similar to *Payan et al.,* [2005], so that a TREK probe could be used to monitor the static voltage build up, from which the voltage breakdown could be determined. Additionally, we highlight *Payan et al.,* [2005]'s design suggestion to provide shunt resistance in an RF circuit to prevent the accumulation of charge in the coaxial cables.

Understanding the connection between the space weather conditions and anomalies on subsystems and specific components on identical and similar geostationary communications satellites for periods of time longer than a solar cycle will help guide design improvements and provide insight on operational strategies during space weather events. The analysis of satellite anomalies together with space weather data will also help bring together the commercial satellite communications industry and space weather science communities to understand the sensitivity of key components to the changes of the space environment [*O'Brien et al.,* 2013]. The goal is to improve both component robustness as well as system performance using design redundancy, operational, and predictive monitoring approaches.

In summary, the contributions of this thesis, which were listed in Chapter 1, are shown below:

- The formation of a strategic academic-satellite operator partnership that led to the acquisition of >1 million operational hours of satellite telemetry.
- The quantification of annual solar cell degradation on-board eleven GEO COMSATs that will aid future design and on-orbit power management.

- The validation of solar cell degradation models to within <0.5% of the observed on-orbit degradation at GEO.
- The characterization of the functional relationship between solar cell degradation and extreme Solar Proton Events for both GaAs and Si cells.
- The substantiation of a plausible relationship between amplifier anomalies and internal charging through statistics of high-energy electron fluence measurements, internal charging simulations, and high-energy electron beam radiation experiments.
- Suggested modification of NASA Internal Charging Guidelines

8.3 Future Work

In 2014 the RAND Corporation published the need for a centralized and up-to-date shared database of satellite anomalies by satellite operators [*Galvin et al.,* 2014]. The authors are in full support of this effort, as it could enable more accurate root-cause anomaly investigations. Anomalies could be quickly deemed space weather related if many satellites in longitudinal range experience similar anomalies around the same time. If it is clear that a single satellite is experiencing a particular anomaly it could likely be the result of a unique hardware or software problem. In order for this database to successfully develop, there would need to be a way for the operators to anonymously and securely share their proprietary information.

With respect to the solar array degradation models, improvements in solar array degradation models could be made. Current models include methods for modeling SPEs, but do not incorporate methods for users to include how a given SPE impacts solar cell damage at particular points during a mission lifetime. The timing of an SPE at a given point in a mission may be important, because the SPE could completely dominate degradation if it occurs early in the mission, before any significant electron induced damage can occur. A way to improve the accuracy and capabilities of current models would be to allow a user to input a given number of SPE events throughout a mission lifetime. One could then see the effect of having multiple SPEs in the beginning of a mission versus at the end, or at any point in time. This added capability would require

the quantification of solar array degradation during SPEs for different technologies, which serves as the motivation for the second half of this study.

The analysis of the solar cell degradation presented in this work can aid in quantifying the required margin needed to size solar arrays to meet EOL power for a given mission. Rather than suggesting a modification of solar cell sizing margin, we suggest that a cost benefit analysis of solar cell sizing margin, mission orbit and mission lifetime be conducted to determine appropriate margins for solar cell sizing.

For Si cells, the smallest deviation in predicted and observed degradation occurred using trapped electron models alone. Future work pertaining to the solar cell degradation could also involve the investigation of the role of high energy electrons in cell degradation at GEO, and whether or not trapped electron models alone should be used in degradation modeling.

Another aspect of future work is related to space environment monitoring. *Wrenn* [1995] suggested, internal dielectric charging sensors for GEO satellites are useful for monitoring the high-energy electron flux at the declining phase of the solar cycle and would help monitor and potentially predict the occurrence of major operational anomalies from internal charging. It is currently challenging to convince satellite operators to convince satellite manufacturers to make the necessary allocations and modifications to fly environmental sensor suites, but single dosimeters usually make the cut and fly. Unfortunately, dosimeters only quantify the accumulated dose, and cannot distinguish between the different particle populations required to conduct root-cause anomaly investigations. *Bogorad et al.,* [2010] suggest that dosimeters can be incorporated into satellite designs to serve as simple real-time internal charging monitors. Regardless of whether the dosimeters are used for accumulated dose or internal charging risk, these instruments could help operators assess the real-time risk of potentially vulnerable components.

Ultimately, the collection of more anomaly data and satellite telemetry from industry providers would enable further examination of the relationships between anomalies and the space weather environment.

Telemetry can also be used to infer characteristics of the space environment. Additionally, the use of anomaly information and satellite telemetry coupled with thorough environmental analysis allows for the development of predictive anomaly detection algorithms and the identification of systems and components that might be best suited for servicing missions. The solar array degradation model validation and root-cause anomaly investigation in this thesis were structured on a foundation of conditioned satellite telemetry and space weather data, to efficiently enable the inclusion of additional data to improve the confidence of these results.

Appendix A. LEO TID Look Up Tables

Appendix A contains look up tables for one year LEO missions, launching January 1, 2017, with aluminum shielding thicknesses of 0.5, 1.0, 1.5, 2.0, 2.5 and 3.0 mm. These orbits are circular (eccentricity = 0), have altitudes from 200 – 2000 km, and inclinations of 0, 15, 30, 45, 60, 75, and 90 degrees. Sun-synchronous orbits are also tabulated.

Table A1. Expected TID over 1 year behind 0.5 mm of Al

0.5 mm of Al Shielding - Expected TID (krads) 1 year								
	Inclination (degrees)							
Altitude (km)	0	15	30	45	60	75	90	Sun-synchronous
200	0.00	0.00	0.00	0.16	4.72	6.18	5.28	5.52
225	0.00	0.00	0.00	0.30	5.12	6.73	5.70	6.00
250	0.00	0.00	0.00	0.50	5.63	7.33	6.19	6.52
275	0.00	0.00	0.00	0.82	6.34	8.16	6.71	7.06
300	0.00	0.00	0.01	1.16	6.99	8.94	7.30	7.73
325	0.00	0.00	0.04	1.59	7.68	9.79	7.98	8.48
350	0.00	0.00	0.09	2.10	8.47	10.73	8.72	9.28
375	0.00	0.00	0.19	2.71	9.36	11.79	9.55	10.19
400	0.00	0.00	0.37	3.45	10.34	12.94	10.47	11.19
425	0.00	0.00	0.64	4.28	11.50	14.22	11.49	12.29
450	0.00	0.01	0.86	5.17	12.50	15.35	12.74	13.54
475	0.00	0.03	1.32	6.29	13.81	16.84	14.00	14.85
500	0.00	0.05	1.93	7.57	15.31	18.46	15.32	16.29
525	0.00	0.08	2.71	8.94	16.90	20.15	16.79	17.82
550	0.00	0.12	3.69	10.50	18.66	21.98	18.33	19.48
575	0.00	0.16	4.86	12.29	20.55	23.92	20.00	21.22
600	0.00	0.22	6.33	14.25	22.67	26.05	21.82	23.17
625	0.01	0.30	8.00	16.51	24.98	28.27	23.75	25.29
650	0.03	0.40	10.07	19.00	27.40	30.67	25.83	27.46
675	0.07	0.54	12.45	21.66	30.08	33.24	28.08	29.85
700	0.13	0.74	15.21	24.71	32.94	35.95	30.49	32.40
725	0.29	1.22	20.61	29.03	36.99	39.74	33.07	35.16
750	0.36	1.42	22.28	31.63	39.40	42.00	35.86	38.16

775	0.50	1.97	26.49	35.73	43.09	45.40	38.88	41.44
800	0.68	2.75	31.51	40.25	46.97	49.00	42.18	44.93
825	0.91	3.86	37.30	45.11	51.32	52.98	45.69	48.77
850	1.22	5.33	43.78	50.55	56.06	57.26	49.65	52.97
875	1.65	7.29	51.04	56.65	61.27	61.92	53.89	57.54
900	2.28	9.83	59.49	63.36	66.85	66.93	58.53	62.46
925	3.21	13.21	68.94	70.74	72.86	72.36	63.54	67.85
950	4.56	17.59	79.60	78.79	79.56	78.28	69.07	73.62
975	6.47	23.19	91.45	87.27	86.84	84.75	75.09	80.15
1000	9.16	30.27	104.60	96.98	94.74	91.80	81.62	87.14
1025	12.87	39.14	118.70	107.60	103.40	99.45	88.80	95.22
1050	17.88	50.14	134.60	119.30	112.90	107.80	96.62	103.50
1075	24.38	63.47	152.40	132.10	123.20	116.90	105.10	112.70
1100	32.73	79.64	172.00	146.10	134.50	126.80	114.50	122.70
1125	43.64	99.11	193.70	161.40	146.90	137.60	124.80	133.50
1150	57.74	122.00	217.40	178.10	160.10	149.40	135.90	145.50
1175	75.27	148.20	243.20	196.20	178.80	166.00	147.90	158.20
1200	109.40	193.50	288.60	220.50	194.60	179.80	160.80	171.90
1225	138.20	227.80	319.60	243.70	211.70	194.60	174.70	186.70
1250	172.90	266.30	353.30	266.70	229.90	210.90	189.60	202.60
1275	192.10	286.10	369.10	283.50	244.00	223.10	205.90	219.70
1300	237.20	330.70	407.70	309.80	264.80	241.30	223.40	238.30
1325	290.30	380.20	449.20	338.60	287.60	261.20	242.30	258.40
1350	351.30	434.90	493.80	370.10	311.70	282.50	262.60	280.20
1375	417.60	495.10	541.90	402.90	337.90	305.50	284.40	303.30
1400	484.40	560.80	593.70	438.20	366.20	330.00	308.00	328.30
1500	820.0	888.50	843.20	606.20	497.60	446.00	419.00	445.90
1600	1,275	1,305	1,156	814.6	661.60	590.00	557.10	592.10
1700	1,903	1,824	1,533	1,066	861.10	764.30	724.00	769.10
1800	2,577	2,450	1,972	1,357	1,090	966.30	917.0	974.2
1900	3,315	3,150	2,462	1,682	1,346	1,191	1,133	1,204
2000	4,213	3,922	2,991	2,032	1,621	1,433	1,366	1,453

Table A2. Expected TID over 1 year behind 1 mm of Al

1.0 mm of Al Shielding - Expected TID (krads) 1 year								
	Inclination (degrees)							
Altitude (km)	**0**	**15**	**30**	**45**	**60**	**75**	**90**	**Sun-synchronous**
200	0.00	0.00	0.00	0.03	2.06	2.65	2.26	2.36
225	0.00	0.00	0.00	0.05	2.21	2.87	2.43	2.54
250	0.00	0.00	0.00	0.09	2.41	3.10	2.61	2.74
275	0.00	0.00	0.00	0.13	2.66	3.42	2.80	2.94
300	0.00	0.00	0.00	0.18	2.89	3.70	3.02	3.18
325	0.00	0.00	0.01	0.26	3.13	4.02	3.25	3.44
350	0.00	0.00	0.02	0.35	3.39	4.36	3.51	3.72
375	0.00	0.00	0.04	0.46	3.69	4.73	3.80	4.03
400	0.00	0.00	0.08	0.60	4.02	5.14	4.11	4.37
425	0.00	0.00	0.14	0.77	4.39	5.58	4.45	4.74
450	0.00	0.01	0.23	1.02	4.74	6.00	4.89	5.16
475	0.00	0.02	0.33	1.26	5.16	6.50	5.31	5.59
500	0.00	0.04	0.46	1.52	5.64	7.05	5.74	6.06
525	0.00	0.06	0.62	1.82	6.14	7.61	6.21	6.54
550	0.00	0.09	0.82	2.15	6.67	8.21	6.69	7.06
575	0.00	0.12	1.05	2.53	7.24	8.83	7.20	7.59
600	0.00	0.17	1.34	2.96	7.87	9.50	7.75	8.18
625	0.01	0.22	1.65	3.44	8.54	10.18	8.32	8.80
650	0.02	0.28	2.04	3.96	9.23	10.90	8.93	9.43
675	0.05	0.35	2.48	4.51	9.98	11.65	9.56	10.10
700	0.10	0.44	2.98	5.14	10.75	12.43	10.22	10.80
725	0.23	0.62	3.94	6.02	11.83	13.49	10.92	11.54
750	0.28	0.69	4.23	6.55	12.46	14.10	11.65	12.32
775	0.39	0.85	4.97	7.37	13.40	15.00	12.42	13.16
800	0.51	1.06	5.84	8.26	14.37	15.93	13.24	14.03
825	0.65	1.32	6.80	9.21	15.43	16.94	14.09	14.96
850	0.82	1.65	7.93	10.25	16.57	17.99	15.03	15.96
875	1.02	2.06	9.15	11.42	17.76	19.09	16.00	17.02
900	1.26	2.57	10.57	12.68	19.03	20.27	17.06	18.14
925	1.57	3.21	12.15	14.07	20.38	21.51	18.16	19.32

950	1.96	4.01	13.93	15.56	21.85	22.82	19.36	20.59
975	2.46	5.00	15.90	17.13	23.41	24.25	20.63	21.97
1000	3.11	6.22	18.08	18.90	25.08	25.75	22.00	23.42
1025	3.92	7.70	20.42	20.82	26.88	27.36	23.46	25.27
1050	4.95	9.50	23.06	22.91	28.82	29.08	25.03	26.98
1075	6.21	11.64	25.99	25.19	30.90	30.93	26.71	28.80
1100	7.75	14.21	29.23	27.66	33.14	32.88	28.54	30.77
1125	9.67	17.26	32.80	30.34	35.55	35.00	30.50	32.86
1150	12.02	20.82	36.72	33.26	38.10	37.27	32.60	35.16
1175	14.79	24.92	41.01	36.41	41.68	40.40	34.87	37.60
1200	19.99	32.21	48.67	40.67	44.71	43.08	37.28	40.19
1225	24.23	37.81	53.95	44.75	47.96	45.91	39.90	43.00
1250	29.25	44.16	59.74	48.78	51.43	48.96	42.70	46.01
1275	31.99	47.44	62.44	51.75	54.10	51.28	45.72	49.24
1300	38.36	54.87	69.10	56.37	57.99	54.68	48.95	52.73
1325	45.76	63.13	76.27	61.40	62.27	58.38	52.43	56.50
1350	54.27	72.27	84.00	66.90	66.77	62.34	56.16	60.49
1375	63.74	82.37	92.38	72.67	71.63	66.56	60.16	64.80
1400	73.93	93.43	101.4	78.86	76.87	71.09	64.45	69.40
1500	127.6	149.0	145.4	108.40	101.20	92.37	84.70	91.06
1600	203.6	221.6	201.6	145.50	131.60	118.90	110.00	118.10
1700	310.3	314.6	270.1	191.00	168.90	151.30	141.00	151.30
1800	434.4	430.7	351.6	245.00	212.70	189.70	177.60	190.60
1900	579.3	566.4	445.3	307.20	263.10	233.60	219.80	235.90
2000	759.5	722.7	549.2	376.30	318.70	282.50	266.70	286.60

Table A3. Expected TID over 1 year behind 1.5 mm of Al

1.5 mm of Al Shielding - Expected TID (krads) 1 year								
	Inclination (degrees)							
Altitude (km)	0	15	30	45	60	75	90	Sun-synchronous
200	0.00	0.00	0.00	0.02	1.19	1.53	1.31	1.36
225	0.00	0.00	0.00	0.03	1.28	1.65	1.40	1.47
250	0.00	0.00	0.00	0.04	1.39	1.78	1.50	1.57
275	0.00	0.00	0.00	0.06	1.53	1.96	1.61	1.68
300	0.00	0.00	0.00	0.08	1.66	2.12	1.73	1.81
325	0.00	0.00	0.01	0.12	1.79	2.29	1.86	1.96
350	0.00	0.00	0.01	0.16	1.94	2.48	2.00	2.11
375	0.00	0.00	0.03	0.22	2.10	2.68	2.15	2.28
400	0.00	0.00	0.05	0.29	2.28	2.91	2.33	2.47
425	0.00	0.00	0.09	0.38	2.49	3.15	2.51	2.67
450	0.00	0.01	0.16	0.54	2.70	3.39	2.77	2.90
475	0.00	0.02	0.22	0.66	2.93	3.67	3.00	3.13
500	0.00	0.03	0.30	0.80	3.19	3.98	3.24	3.39
525	0.00	0.05	0.40	0.97	3.47	4.29	3.49	3.65
550	0.00	0.08	0.52	1.14	3.77	4.62	3.76	3.94
575	0.00	0.11	0.65	1.35	4.09	4.96	4.04	4.23
600	0.00	0.14	0.81	1.59	4.43	5.33	4.35	4.55
625	0.01	0.19	0.98	1.84	4.80	5.70	4.66	4.89
650	0.02	0.24	1.20	2.11	5.18	6.10	4.99	5.23
675	0.04	0.31	1.43	2.41	5.59	6.51	5.33	5.59
700	0.09	0.38	1.70	2.74	6.01	6.93	5.69	5.96
725	0.19	0.53	2.21	3.21	6.60	7.50	6.07	6.36
750	0.24	0.58	2.37	3.48	6.94	7.83	6.46	6.78
775	0.34	0.71	2.74	3.91	7.45	8.32	6.88	7.23
800	0.44	0.87	3.19	4.37	7.97	8.81	7.31	7.68
825	0.57	1.05	3.68	4.86	8.53	9.35	7.76	8.17
850	0.72	1.28	4.25	5.39	9.14	9.90	8.26	8.69
875	0.90	1.55	4.85	5.98	9.76	10.48	8.77	9.24
900	1.10	1.87	5.55	6.62	10.43	11.10	9.32	9.82
925	1.35	2.27	6.33	7.32	11.13	11.74	9.89	10.42

950	1.65	2.74	7.20	8.07	11.89	12.42	10.51	11.07
975	2.03	3.31	8.16	8.86	12.70	13.15	11.16	11.77
1000	2.49	3.99	9.21	9.73	13.55	13.92	11.86	12.50
1025	3.06	4.80	10.35	10.69	14.48	14.74	12.60	13.55
1050	3.74	5.76	11.62	11.72	15.46	15.61	13.40	14.40
1075	4.54	6.88	13.03	12.83	16.52	16.54	14.24	15.33
1100	5.49	8.20	14.58	14.05	17.65	17.53	15.16	16.32
1125	6.62	9.74	16.29	15.35	18.86	18.58	16.14	17.36
1150	7.94	11.52	18.17	16.78	20.14	19.72	17.18	18.51
1175	9.44	13.56	20.22	18.31	21.92	21.29	18.30	19.71
1200	12.16	17.17	23.89	20.39	23.43	22.60	19.50	21.00
1225	14.30	19.94	26.44	22.36	25.04	24.00	20.80	22.40
1250	16.74	23.06	29.24	24.32	26.76	25.51	22.18	23.88
1275	18.06	24.67	30.55	25.76	28.08	26.65	23.67	25.47
1300	21.06	28.30	33.76	27.99	30.00	28.32	25.25	27.19
1325	24.48	32.31	37.20	30.41	32.11	30.13	26.95	29.01
1350	28.37	36.74	40.92	33.05	34.31	32.06	28.77	30.98
1375	32.71	41.60	44.95	35.82	36.69	34.11	30.71	33.07
1400	37.46	46.92	49.28	38.78	39.24	36.31	32.79	35.30
1500	62.50	73.39	70.27	52.82	50.96	46.54	42.52	45.72
1600	98.12	107.90	96.93	70.36	65.52	59.18	54.58	58.66
1700	147.8	152.10	129.4	91.81	83.33	74.61	69.30	74.46
1800	207.5	207.40	168.1	117.3	104.2	92.9	86.72	93.20
1900	278.2	272.80	212.6	146.8	128.4	113.9	106.90	114.90
2000	366.3	348.7	262.0	179.7	155.2	137.3	129.40	139.30

Table A4. Expected TID over 2 year behind 0.5 mm of Al

2 mm of Al Shielding - Expected TID (krads) 1 year								
	Inclination (degrees)							
Altitude (km)	0	15	30	45	60	75	90	Sun-synchronous
200	0.00	0.00	0.00	0.01	0.76	0.98	0.84	0.88
225	0.00	0.00	0.00	0.02	0.82	1.05	0.90	0.94
250	0.00	0.00	0.00	0.03	0.89	1.14	0.96	1.01
275	0.00	0.00	0.00	0.03	0.97	1.24	1.03	1.07
300	0.00	0.00	0.00	0.05	1.05	1.34	1.10	1.15
325	0.00	0.00	0.01	0.07	1.14	1.45	1.18	1.24
350	0.00	0.00	0.01	0.10	1.23	1.57	1.27	1.34
375	0.00	0.00	0.00	0.14	1.33	1.70	1.37	1.44
400	0.00	0.00	0.04	0.19	1.45	1.83	1.47	1.56
425	0.00	0.00	0.07	0.25	1.58	1.99	1.59	1.68
450	0.00	0.01	0.13	0.37	1.72	2.15	1.76	1.83
475	0.00	0.01	0.18	0.46	1.87	2.33	1.91	1.98
500	0.00	0.03	0.25	0.56	2.05	2.52	2.06	2.14
525	0.00	0.04	0.32	0.67	2.23	2.71	2.22	2.30
550	0.00	0.07	0.41	0.79	2.42	2.92	2.39	2.48
575	0.00	0.09	0.51	0.94	2.63	3.14	2.58	2.67
600	0.00	0.13	0.63	1.10	2.85	3.38	2.77	2.87
625	0.00	0.17	0.76	1.27	3.10	3.62	2.97	3.09
650	0.01	0.22	0.92	1.46	3.34	3.87	3.19	3.31
675	0.04	0.28	1.09	1.67	3.61	4.13	3.41	3.54
700	0.07	0.35	1.28	1.89	3.88	4.40	3.64	3.78
725	0.17	0.48	1.65	2.21	4.27	4.77	3.89	4.03
750	0.21	0.53	1.76	2.40	4.49	4.98	4.14	4.30
775	0.30	0.64	2.02	2.69	4.82	5.29	4.41	4.59
800	0.40	0.78	2.33	3.00	5.16	5.61	4.69	4.88
825	0.52	0.94	2.67	3.33	5.53	5.95	4.98	5.20
850	0.66	1.14	3.06	3.69	5.92	6.31	5.31	5.53
875	0.82	1.36	3.47	4.08	6.33	6.68	5.64	5.88
900	1.01	1.62	3.94	4.51	6.76	7.08	5.99	6.25
925	1.24	1.94	4.47	4.97	7.22	7.49	6.37	6.63

950	1.51	2.31	5.04	5.47	7.71	7.93	6.77	7.04
975	1.84	2.75	5.68	5.99	8.24	8.40	7.19	7.49
1000	2.25	3.26	6.38	6.56	8.79	8.90	7.64	7.96
1025	2.73	3.86	7.12	7.19	9.39	9.42	8.12	8.70
1050	3.31	4.56	7.96	7.87	10.03	9.99	8.64	9.26
1075	3.97	5.37	8.88	8.60	10.71	10.71	9.18	9.85
1100	4.73	6.31	9.90	9.40	11.45	11.22	9.77	10.49
1125	5.61	7.39	11.02	10.25	12.23	11.90	10.41	11.20
1150	6.61	8.63	12.25	11.18	13.06	12.63	11.08	11.90
1175	7.74	10.02	13.58	12.18	14.21	13.64	11.81	12.67
1200	9.72	12.49	15.96	13.54	15.19	14.48	12.58	13.50
1225	11.24	14.36	17.62	14.80	16.23	15.39	13.42	14.40
1250	12.94	16.45	19.44	16.08	17.35	16.35	14.31	15.36
1275	13.84	17.53	20.30	17.01	18.20	17.08	15.27	16.38
1300	15.86	19.94	22.37	18.46	19.43	18.16	16.29	17.50
1325	18.14	22.58	24.60	20.02	20.78	19.32	17.38	18.70
1350	20.68	25.48	27.00	21.72	22.20	20.55	18.54	19.90
1375	23.52	28.65	29.59	23.49	23.71	21.86	19.78	21.23
1400	26.62	32.10	32.36	25.39	25.34	23.25	21.11	22.65
1500	42.69	49.02	45.66	34.28	32.75	29.71	27.25	29.22
1600	65.22	70.76	62.33	45.24	41.85	37.59	34.77	37.27
1700	95.99	98.29	82.46	58.52	52.87	47.12	43.87	47.03
1800	132.90	132.50	106.30	74.17	65.74	58.35	54.58	58.54
1900	176.80	172.70	133.60	92.19	80.53	71.18	66.91	71.80
2000	231.00	219.20	163.60	112.20	96.83	85.44	80.62	86.63

Table A5. Expected TID over 1 year behind 2.5 mm of Al

2.5 mm of Al Shielding - Expected TID (krads) 1 year								
	Inclination (degrees)							
Altitude (km)	0	15	30	45	60	75	90	Sun-synchronous
200	0.00	0.00	0.00	0.01	0.50	0.65	0.57	0.59
225	0.00	0.00	0.00	0.01	0.54	0.70	0.61	0.63
250	0.00	0.00	0.00	0.02	0.59	0.75	0.65	0.68
275	0.00	0.00	0.00	0.02	0.64	0.82	0.69	0.72
300	0.00	0.00	0.00	0.04	0.69	0.89	0.74	0.77
325	0.00	0.00	0.00	0.05	0.75	0.96	0.79	0.83
350	0.00	0.00	0.01	0.07	0.81	1.03	0.85	0.89
375	0.00	0.00	0.02	0.22	0.88	1.12	0.91	0.96
400	0.00	0.00	0.04	0.14	0.96	1.21	0.98	1.03
425	0.00	0.00	0.06	0.18	1.04	1.31	1.06	1.11
450	0.00	0.01	0.12	0.28	1.15	1.42	1.18	1.21
475	0.00	0.01	0.16	0.35	1.25	1.54	1.28	1.31
500	0.00	0.02	0.22	0.43	1.37	1.67	1.38	1.42
525	0.00	0.04	0.28	0.51	1.50	1.80	1.49	1.53
550	0.00	0.06	0.36	0.61	1.63	1.94	1.61	1.65
575	0.00	0.09	0.44	0.72	1.78	2.09	1.74	1.78
600	0.00	0.12	0.54	0.85	1.94	2.25	1.87	1.91
625	0.00	0.16	0.65	0.98	2.10	2.41	2.01	2.06
650	0.01	0.20	0.78	1.13	2.28	2.59	2.16	2.21
675	0.03	0.26	0.92	1.28	2.46	2.77	2.31	2.37
700	0.06	0.32	1.08	1.45	2.66	2.95	2.48	2.54
725	0.15	0.45	1.38	1.69	2.93	3.21	2.65	2.72
750	0.19	0.49	1.46	1.84	3.09	3.35	2.83	2.90
775	0.27	0.60	1.68	2.05	3.32	3.57	3.02	3.10
800	0.37	0.73	1.68	2.29	3.56	3.79	3.22	3.31
825	0.48	0.88	2.19	2.54	3.83	4.04	3.43	3.53
850	0.62	1.06	2.50	2.81	4.10	4.29	3.65	3.76
875	0.77	1.26	2.82	3.11	4.40	4.55	3.89	4.01
900	0.95	1.49	3.19	3.43	4.71	4.83	4.15	4.27
925	1.17	1.77	3.59	3.77	5.04	5.12	4.42	4.54

950	1.42	2.09	4.04	4.15	5.39	5.43	4.70	4.83
975	1.73	2.47	4.52	4.53	5.77	5.77	5.01	5.15
1000	2.11	2.91	5.06	4.97	6.17	6.13	5.33	5.48
1025	2.55	3.42	5.63	5.43	6.61	6.50	5.68	6.07
1050	3.07	4.00	6.26	5.94	7.07	6.91	6.06	6.46
1075	3.66	4.67	6.96	6.49	7.57	7.34	6.45	6.90
1100	4.33	5.43	7.74	7.08	8.10	7.80	6.89	7.36
1125	5.10	6.31	8.59	7.72	8.67	8.29	7.35	7.84
1150	5.96	7.30	9.52	8.41	9.28	8.83	7.85	8.38
1175	6.91	8.42	10.53	9.16	10.12	9.56	8.38	8.95
1200	8.57	10.37	12.31	10.18	10.83	10.18	8.94	9.56
1225	9.81	11.84	13.57	11.11	11.60	10.84	9.56	10.21
1250	11.19	13.47	14.93	12.06	12.41	11.54	10.21	10.91
1275	11.91	14.30	15.58	12.76	13.03	12.08	10.91	11.66
1300	13.53	16.16	17.14	13.83	13.94	12.86	11.66	12.46
1325	15.32	18.19	18.80	14.98	14.92	13.71	12.46	13.31
1350	17.30	20.40	20.58	16.24	15.96	14.61	13.31	14.23
1375	19.49	22.81	22.51	17.55	17.06	15.56	14.22	15.19
1400	21.89	25.41	24.56	18.94	18.24	16.57	15.18	16.22
1500	34.06	38.00	34.29	25.42	23.59	21.23	19.62	20.95
1600	50.75	53.87	46.29	33.28	30.08	26.85	25.00	26.69
1700	72.97	73.69	60.62	42.70	37.86	33.58	31.43	33.56
1800	99.19	98.00	77.42	53.69	46.86	41.44	38.93	41.60
1900	130.20	126.20	96.49	66.24	57.14	50.35	47.49	50.79
2000	168.10	158.50	117.30	80.03	68.35	60.17	56.93	60.97

Table A6. Expected TID over 1 year behind 3 mm of Al

3 mm of Al Shielding - Expected TID (krads) 1 year								
	Inclination (degrees)							
Altitude (km)	0	15	30	45	60	75	90	Sun-synchronous
200	0.00	0.00	0.00	0.01	0.34	0.44	0.40	0.41
225	0.00	0.00	0.00	0.01	0.36	0.48	0.42	0.44
250	0.00	0.00	0.00	0.02	0.39	0.51	0.45	0.47
275	0.00	0.00	0.00	0.02	0.43	0.56	0.47	0.49
300	0.00	0.00	0.00	0.03	0.46	0.60	0.50	0.52
325	0.00	0.00	0.00	0.04	0.50	0.64	0.54	0.56
350	0.00	0.00	0.01	0.06	0.54	0.69	0.58	0.60
375	0.00	0.00	0.02	0.14	0.59	0.75	0.62	0.65
400	0.00	0.00	0.03	0.11	0.64	0.81	0.67	0.70
425	0.00	0.00	0.06	0.14	0.70	0.88	0.72	0.76
450	0.00	0.01	0.11	0.23	0.78	0.96	0.81	0.82
475	0.00	0.01	0.15	0.28	0.86	1.04	0.88	0.89
500	0.00	0.02	0.20	0.35	0.94	1.13	0.95	0.96
525	0.00	0.04	0.26	0.42	1.03	1.23	1.03	1.04
550	0.00	0.06	0.33	0.49	1.13	1.32	1.12	1.13
575	0.00	0.08	0.40	0.58	1.24	1.43	1.21	1.22
600	0.00	0.11	0.49	0.69	1.35	1.54	1.31	1.32
625	0.00	0.15	0.59	0.79	1.47	1.66	1.41	1.42
650	0.01	0.19	0.70	0.91	1.60	1.78	1.51	1.53
675	0.03	0.24	0.82	1.04	1.74	1.91	1.63	1.64
700	0.06	0.31	0.96	1.18	1.88	2.05	1.75	1.77
725	0.14	0.43	1.21	1.37	2.08	2.24	1.88	1.90
750	0.17	0.47	1.29	1.48	2.20	2.34	2.01	2.03
775	0.25	0.57	1.47	1.66	2.38	2.50	2.15	2.18
800	0.34	0.69	1.68	1.85	2.56	2.67	2.30	2.33
825	0.46	0.83	1.91	2.05	2.75	2.85	2.46	2.50
850	0.59	1.00	2.17	2.26	2.96	3.03	2.63	2.67
875	0.74	1.19	2.44	2.50	3.19	3.23	2.81	2.85
900	0.91	1.40	2.74	2.75	3.43	3.44	3.01	3.05
925	1.11	1.66	3.08	3.03	3.67	3.66	3.21	3.25

950	1.36	1.95	3.45	3.33	3.95	3.90	3.43	3.47
975	1.65	2.30	3.85	3.64	4.24	4.16	3.67	3.71
1000	2.00	2.69	4.29	3.98	4.54	4.43	3.92	3.96
1025	2.42	3.14	4.76	4.35	4.88	4.72	4.19	4.45
1050	2.91	3.66	5.28	4.76	5.23	5.03	4.48	4.76
1075	3.46	4.25	5.86	5.20	5.62	5.36	4.79	5.09
1100	4.07	4.92	6.49	5.67	6.03	5.72	5.12	5.45
1125	4.77	5.68	7.19	6.18	6.48	6.10	5.49	5.83
1150	5.55	6.54	7.95	6.74	6.95	6.52	5.88	6.25
1175	6.40	7.50	8.78	7.33	7.61	7.09	6.29	6.70
1200	7.87	9.16	10.23	8.16	8.17	7.57	6.74	7.17
1225	8.97	10.41	11.25	8.90	8.77	8.09	7.22	7.69
1250	10.17	11.78	12.35	9.65	9.41	8.65	7.74	8.23
1275	10.79	12.48	12.89	10.21	9.89	9.07	8.29	8.82
1300	12.18	14.03	14.14	11.06	10.60	9.68	8.88	9.45
1325	13.71	15.71	15.48	11.98	11.37	10.34	9.51	10.11
1350	15.39	17.54	16.92	12.98	12.18	11.05	10.18	10.83
1375	17.24	19.51	18.46	14.02	13.04	11.79	10.89	11.59
1400	19.25	21.63	20.10	15.11	13.97	12.59	11.64	12.39
1500	29.29	31.79	27.80	20.20	18.12	16.21	15.11	16.06
1600	42.78	44.36	37.14	26.29	23.10	20.53	19.25	20.46
1700	60.25	59.82	48.14	33.50	29.01	25.65	24.15	25.67
1800	80.44	78.52	60.89	41.81	35.78	31.57	29.80	31.72
1900	104.10	99.93	75.25	51.20	43.43	38.21	36.19	38.56
2000	132.80	124.00	90.76	61.40	51.69	45.46	43.16	46.05

Appendix B. SSPA vs. TWTA Technologies

We begin by summarizing and comparing five previous studies of amplifier technologies. Then, we analyze trends in TWTA and SSPA technologies using payload data from a commercially licensed database and a publicly available database. This data set consists of amplifier technologies onboard 565 communications satellites launched between 1982 and 2016. To the author's knowledge, this is the largest number of satellites and amplifiers included in a power amplifier comparison study to date. Finally, we analyze proprietary amplifier anomaly records onboard 16 satellites, which were equipped with a combined total of 579 amplifiers: 470 SSPAs and 109 TWTAs.

Since the introduction of the SSPA in the 1970s, there have been debates as to which amplifier technology, TWTA or SSPA, is best suited for communication satellite applications. Comparisons of these two satellite components generally focus on the metrics of amplifier reliability, performance, cost, and mass [*Strauss,* 1993; *Kaliski,* 2009]. Conducting an accurate comparison of the two technologies can be difficult, as there are numerous frequency bands and power requirements to consider [*Kaliski,* 2009].

Prior to 1990, there had been very few published studies comparing SSPAs and TWTAs. Since then, only a few major studies have compared the capabilities of the two technologies. These studies took place in 1991, 1993 and 2005. The 1991 study was funded by the European Space and Technology Center (ESTEC) and focused on satellites launched between 1984 and 1992. In 1993, NASA sponsored a study expanding on the 1991 ESTEC study [*Strauss,* 1993, *Weekley and Mangus,* 2005], and in 2005, Boeing supported a study comparing SSPAs and TWTAs onboard satellites launched from the mid-1980s to 2004 [*Weekley and Mangus,* 2005]. Updates to the Boeing 2005 study were made in 2008 and 2013 [*Nicol et al.,* 2008, *Nicol et al.,* 2013].

Table B.1 provides a summary of the findings of these three comparison studies (ESTEC, NASA, Boeing 2005) along with the 2008 and 2013 updates to the 2005 Boeing study. The table includes information on how many satellites and amplifiers were considered, the methods of measuring reliability of the amplifiers, the comparisons of failures in

time (FIT) experienced per billion amplifier operating hours, and additional findings from each of the studies.

Table B.1. Summary of TWTA vs. SSPA Technology and Reliability Comparison Studies

	1991 ESTEC	1993 NASA	2005 Boeing	2008 Boeing	2013 Boeing
Band	C and Ku	C and Ku	L, S, C, Ku, Ka	L, S, C, Ku, Ka	UHF, L, S, C, Ku, Ka
Satellites	75	72	104	~90	101
Operational years	463	497	~1500	~1600	Not specified
TWTAs	1603 64% C-band 36% Ku-band	1860 66% C-band 34% Ku-band	1783 3% S-band 20% C-band 77% Ku-band, 1% Ka-band	1997 7% S-band 20% C-band 71% Ku-band 3% Ka-band	2345 6% S-band 18% C-band 62% Ku-band, 14% Ka-band,
TWTA hours	56.4 million (63.5% C-band	69 million (51.5 C-band 17.5 Ku-band)	80.5 million	129 million	211 million
SSPAs	309 C-band	437 C-band	944 30% L-band 14% S-band, 55% C-band, 1% Ku-band	957 33% L-band 14% S-band 52% C-band 1% Ku-band	1076 1% UHF 38% L-band 14% S-band 46% C-band 1% Ku-band
SSPA hours	11.4 million	59.9 million	30.5 million	64 million	92 million
Method for measuring reliability	FITs, Redundancy	FITs, Output Power vs. FITs	FITs, Watts/FITs	FITs, Failure Age	FITs, Failure Age
FITS Comparisons	TWTAs more reliable: TWTA 680 FITs vs. SSPA 790 FITs	TWTAs more reliable: TWTA 660 FITs vs. SSPA 880 FITs	TWTA FITs lower than SSPA FITs	Overall FITs improvement for both TWTAs and SSPAs between 1998-2005	FITs decrease between 2001-2013, SSPA greater improvement; SSPA FITs constant over entire life, TWTA FITs even over first 10 years then vanish
Failure Analysis	Mentioned possible	Mentioned possible failure	"Graceful degradation" attributed to	Most TWTA failures occurred in	Failure analysis not conducted

	failure mechanisms	mechanisms; Failure rates at Ku-band increased by 8%	SSPA not supported; 80% SSPA failures SSO	first five years. Most SSPA failures occurred after five years of operation	
Additional Findings	SSPAs more reliable in terms of redundancy, SSPA 6:5, TWTA 3:2	Highest output power is 65 W at Ku-band for TWTAs and 17 W at C-band for both SSPAs and TWTAs	SSPAs provided on avg. 66 W less at C-band than equivalent Ku-band TWTAs	SSPA and TWTA FITs appear identical after 2004 due to improved quality of SSPA design	TWTAs advantageous for linear power over all frequencies above C-band
	RF output powers and gains similar for SSPAs and TWTAs	C-band tends to adopt SSPAs for 20-40 W output power requirements and TWTAs for 50-70 W	TWTA 0.456 Watt/FITs vs. 0.078 Watt/FITS (TWTAs 6 x improvement in performance)		

Weekley and Mangus [2005] noted in the Boeing 2005 study that SSPA technology with low enough mass and high enough efficiency was simply not available for high power and high frequency demands. *Strauss* [1993] stated that for output powers of 15 – 50 Watts, either technology can be implemented, but at higher frequencies (Ku and Ka band), TWTAs are historically more common. The five studies all saw an improvement, or decrease of FITs over time, indicating an overall improvement in either amplifier design or integration and test. In terms of FITs, the 1991, 1993 and 2005 studies found TWTA FITs to be lower than that of SSPAs. The 1991 study was the only study to analyze reliability in terms of redundancy, and in that respect found that SSPAs, which had an average redundancy configuration of 6:5, were more reliable than TWTAs with an average redundancy configuration of 3:2. Based on the 1993 NASA study, Strauss [*Strauss,* 1993] predicted a future redundancy of 7:5 for C-band TWTAs and SSPAs.

These five studies motivate our investigation of the current and future status of SSPA and TWTA technologies for communications satellites. Section B.1.2 – B.1.5 contains analysis of 565 communications satellites via payload data from a commercially licensed database and a publicly available database. In this analysis, the frequency, output power, redundancy and bandwidth of more than 18,000 amplifiers is investigated. The last section focuses on a brief failure analysis using satellite anomaly lists from amplifiers on-board sixteen geostationary communication satellites, for a combined total of 579 amplifiers: 470 SSPAs and 109 TWTAs.

B. 1.1 Previous SSPA vs. TWTA Technology and Reliability Comparison Studies

For this study, communications satellite payload data was obtained for 565 communication satellites with launch years from 1982 to 2016. We have used two validated sources of amplifier data from a commercially licensed database, Seradata's Spacetrak (http://www.seradata.com), and a publicly available database, Gunter's Space Page (http://space.skyrocket.de/). The data contained the following information on the satellite and payload: satellite name, launch date, orbit (low earth orbit (LEO) or geostationary orbit (GEO)), manufacturer, bus type, frequency band (UHF to Ka band), amplifier type (SSPA vs. TWTA), redundancy, bandwidth, and output power. Table 2 provides an initial summary of the collected data.

Table B.2. Communications Satellite and Payload Data Summary

Parameter	Value
Total Satellites	565
LEO Satellites	16
GEO Satellites	549
Entirely TWTA Payloads	226
Entirely SSPA Payloads	19
TWTA/SSPA Hybrid Payloads	60

Of the 565 satellites, the 16 LEO satellites are part of the O3b satellite constellation, some of which have a future launch date. The remaining 549 satellites are in geostationary orbit. In total 18,902 amplifiers were considered: 6,428 TWTAs, 2,158 SSPAs, and 10,316 amplifiers of unspecified type.

Of the 565 satellites, the amplifier type (TWTA/SSPA) was not specified for 260 payloads. Of the remaining 305 satellites, 226, or 74%, of the total satellites had payloads that consisted of entirely TWTAs, whereas only 19, or 6%, of the satellites had entirely SSPA payloads, and 20% of the 565 satellites had a combination of both amplifier types onboard. *Mallon* [2008] found that of the GEO communications satellites launched from 1992-2007, 69% used TWTAs exclusively, 24% used a hybrid of SSPAs and TWTAs, and that 6% used SSPAs exclusively. *Mallon* [2008] also found that 1% of the satellites consisted of a phased array, but this payload type is not considered in our study. Unfortunately, we cannot include the 260 satellites with an unspecified payload type in our SSPA vs. TWTA analysis. However, from the specified amplifiers on the remaining 305 satellites, we can infer a 5% increase in exclusively TWTA payloads of GEO communications satellites launched between 1982 and 2016, which consisted of 74% exclusively TWTA payloads compared to the study of GEO communications satellites launched between 1992 and 2007, which consisted of 69% exclusively TWTA payloads [*Mallon,* 2008].

Section B.1.2 provides analysis of the frequency distribution of the amplifiers and satellites considered in this study. Section B.1.3 describes the level of output power achieved for each type of amplifier, and Section B.1.3 presents the level of redundancy designed for the payloads. Finally, Section B.1.4 details the distribution of amplifier bandwidth for the different payload types.

B. 1.2 Frequency Breakdown of Amplifiers and Satellites

While amplifier payload type was not specified for every satellite, the operating frequency band was provided for every satellite and amplifier. Figure 3 shows the operating frequency breakdown of the 18,902 amplifiers. The highest percentage of TWTAs, 68%, and unknown amplifier types, 55%, fall in Ku-band. For SSPAs, the highest

percentage of SSPAs, 60%, operate in C-band. Only 5 UHF amplifiers were recorded amongst the 565 satellites, and these were not designated as SSPA or TWTA.

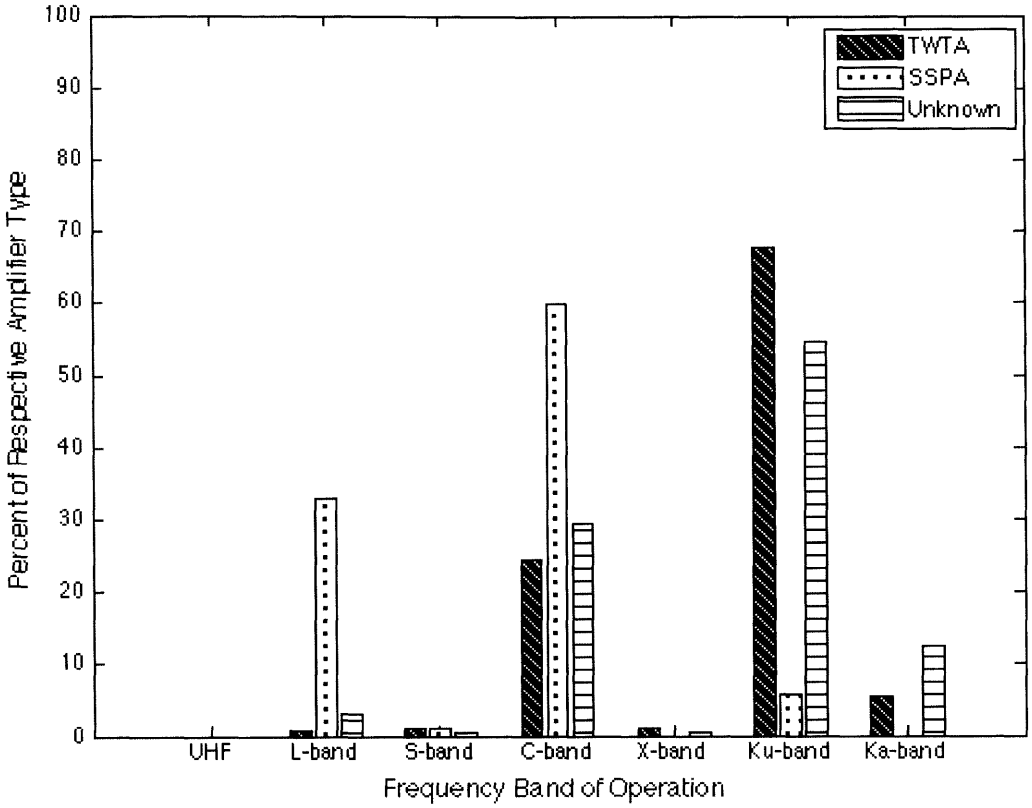

Figure B.2. Frequency breakdown of TWTAs, SSPAs, and amplifiers of unknown type. TWTAs appear to dominate higher frequencies, and SSPAs lower frequencies (C-band and below). We note that there are still SSPAs being used for some high frequency (Ku-band) applications.

As previously mentioned, the Boeing 2005 study, which included 944 SSPAs, found that SSPA technology with low enough mass and high efficiency was not available for high frequency demands [*Weekley and Mangus,* 2005]. The figure above shows that of the 2,158 SSPAs considered here, that SSPAs were in fact used for frequencies as high as Ku-band, and the percentage of SSPAs in Ku-band increased from approximately 1% in Boeing 2005, 2008, and 2013 studies to 6% in this work.

Figure B.3 (a,b) shows the frequency breakdown of the satellites that have a) exclusively SSPA payloads, and b) exclusively TWTA payloads. The significant difference in the number of exclusively SSPA payloads

compared to the number of exclusively TWTA payloads, 19 vs. 226 respectively, also is a reflection of the variety of payload power and frequency band combinations. We note that there were no exclusive SSPA Ka-band payloads. This finding is consistent with the Boeing 2005 study, which claimed SSPAs were not available for high frequencies, but would be a metric to re-examine in future studies. On the other hand, there also were no exclusive TWTA L-band payloads.

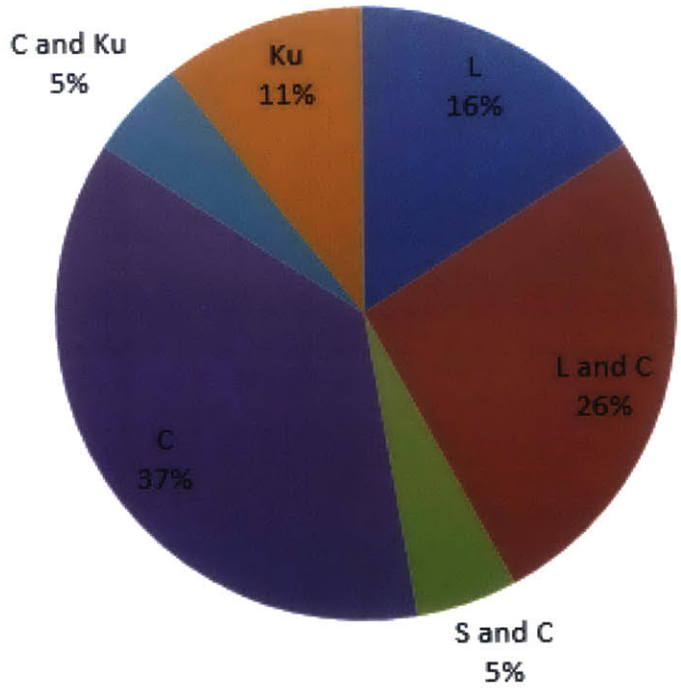

(a)

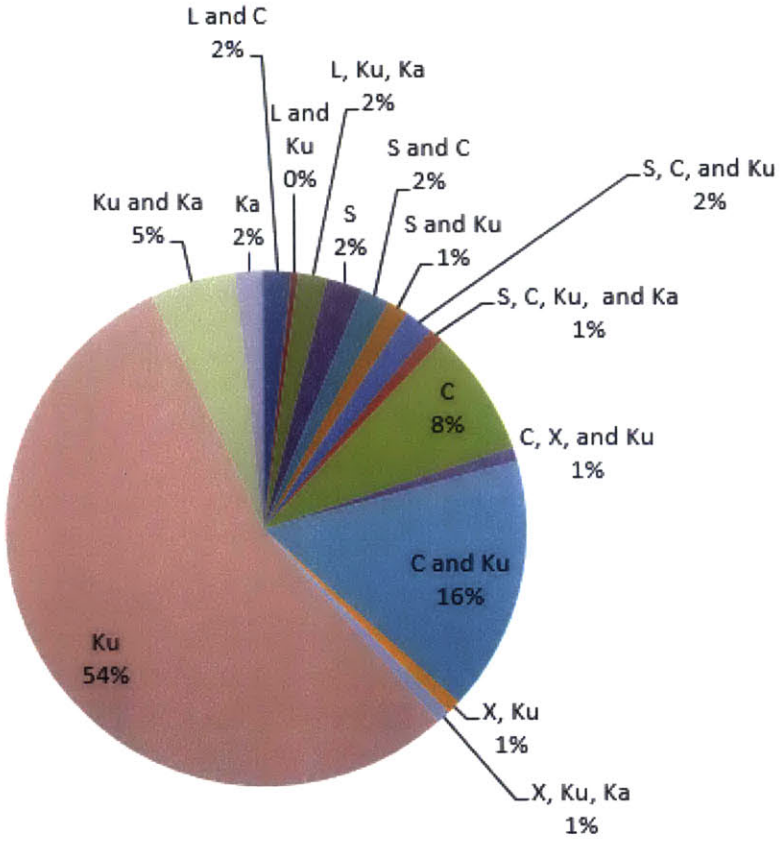

(b)

Figure B.3(a,b). Frequency distribution of a) payloads that are exclusively SSPAs (19 out of 305 payloads) and b) payloads that are exclusively TWTAs (226 out of 305 payloads).

The percentage of exclusively TWTA payloads that consist of a single L-band transponder make up only 4% of all the exclusively TWTA payloads. The largest percentage of exclusively SSPA payloads operates at C band and the largest percentage of exclusively TWTA payloads operate at Ku band. Note that Figure B.3(a) depicts the operating frequency breakdown of all SSPAs, whereas Figure B.3(b) depicts the frequency breakdown of exclusively SSPA payloads.

B.1.3 Amplifier Output Power

The output power of an amplifier is one of the key performance characteristics. Figure B.4 shows the maximum output power of each of the three amplifier types for a particular frequency band. There was no available data for SSPAs that operate at X- or Ka-band.

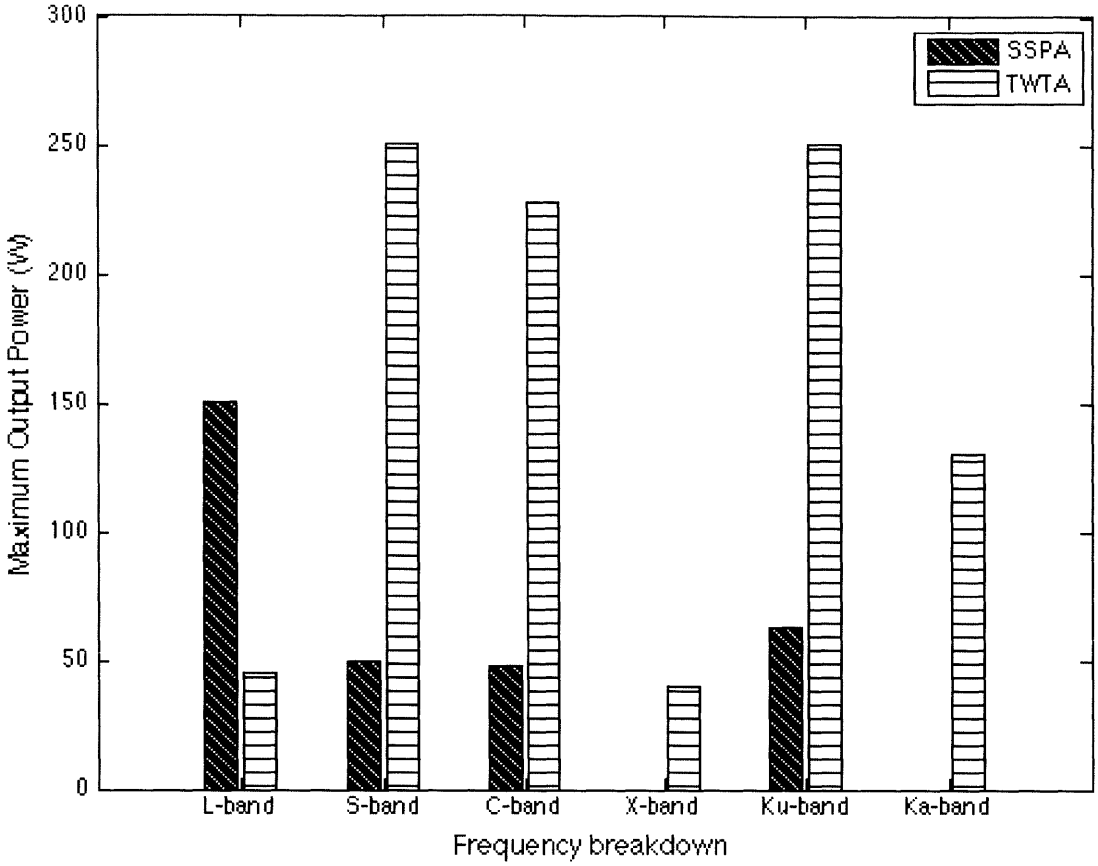

Figure B.4. Frequency breakdown of maximum output power (W) for SSPA and TWTA payloads

The variability in the maximum output power capability of the SSPAs and TWTAs does not support the 1991 ESTEC study, which claimed that RF power output levels were similar for both amplifier technologies. As expected, the TWTAs provide higher output power capabilities at higher frequency bands, and SSPAs generate higher output powers at lower frequency bands. This is evident in L-band, where the SSPA with highest output power produced 150 W, compared to the L-band TWTA with a highest output power of 45 W. The 150 W SSPA was onboard Optus B1, launched in 1992; the second highest output power for SSPAs was 38 W, and was onboard both the AMSC 1 and MSat 1 satellites. It is important to note that the Optus B1 output power is likely an anomalously high data point. It is also evident in the Ku-band, where the SSPA with the highest output power produced 63 W, compared to the maximum output power for the TWTA of 250 W.

The 1993 NASA study found that 66 W was the highest output power for Ku-band TWTAs and that 17 W was the highest output power for both C-band SSPAs and TWTAs. Figure 5 depicts an increase in the maximum output power capability for Ku-band TWTAs to higher than 180 W, more than a 250% increase. We also note an increase in the maximum C-band output power capabilities of both SSPAs and TWTAs. Specifically, there is a 282% increase for C-band SSPAs, which reached a maximum output power of 48 W, and more than a 1000% increase for C-band TWTAs, which reached a maximum output power of 228 W.

Figure B.5 shows the output powers for all TWTAs, SSPAs, and amplifiers of unspecified type with available output power data. The general claim that SSPAs are used for lower output powers compared with TWTAs is supported. We find a general increase in the TWTA output power capability with time for moderately high power TWTAs; the TWTAs with output powers specified above 200 W did not increase. Output power data for SSPAs was not available after 2006.

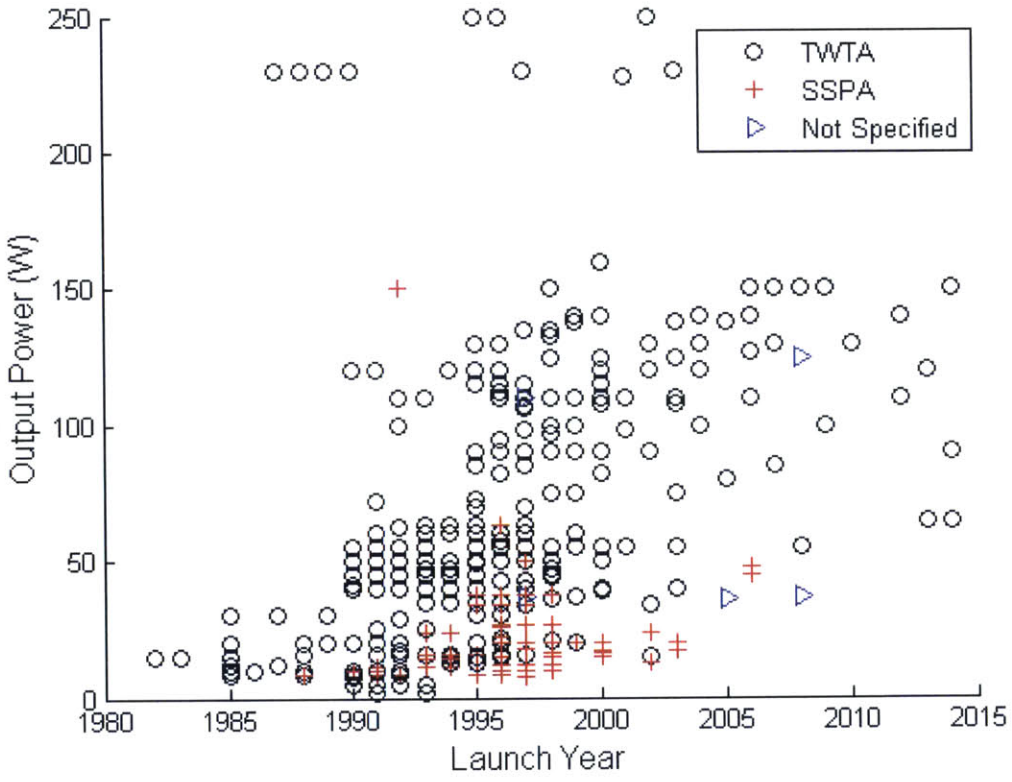

Figure B.5. Output power (W) of amplifiers onboard satellites with TWTAs (marked with a black o), SSPAs (marked with a red +), and unspecified payloads (marked with a blue triangle)

Strauss [1993] noted that both SSPAs and TWTAs could be used for an RF output power of 15-50 W [*Strauss,* 1993]. Figure 9 supports this claim from 1987 to 2006, yet after 2003, the lowest output power cited for a TWTA was 55 W.

The 1993 NASA study suggested that SSPAs were more commonly used in C-band for RF output powers of 20-40 W and that TWTAs were more common for RF output powers between 50-70 W. From the figure above, the highest output power of a C-band SSPA is observed to be 34 W. It is clear that the number of TWTAs with an RF output power between 50-70 W is greater than the number of SSPAs with the same range of output powers.

B.1.4 Amplifier Redundancy

As shown in Table B.1 with the 1991 ESTEC study, the level of amplifier redundancy designed in a system can serve as an indicator for the expected reliability of the component. However, redundancy was not analyzed in any of the other studies included in Table B.1. Figure B.6 shows the number of redundant TWTAs, SSPAs and amplifiers of unspecified type onboard satellites with launch dates from 1982 to 2016. The specific redundancy schemes, such as the one given in the 1991 ESTEC study (SSPA 6:5, TWTA 3:2), are not identified in our analysis. Redundancy data for SSPAs was not available after year 2000.

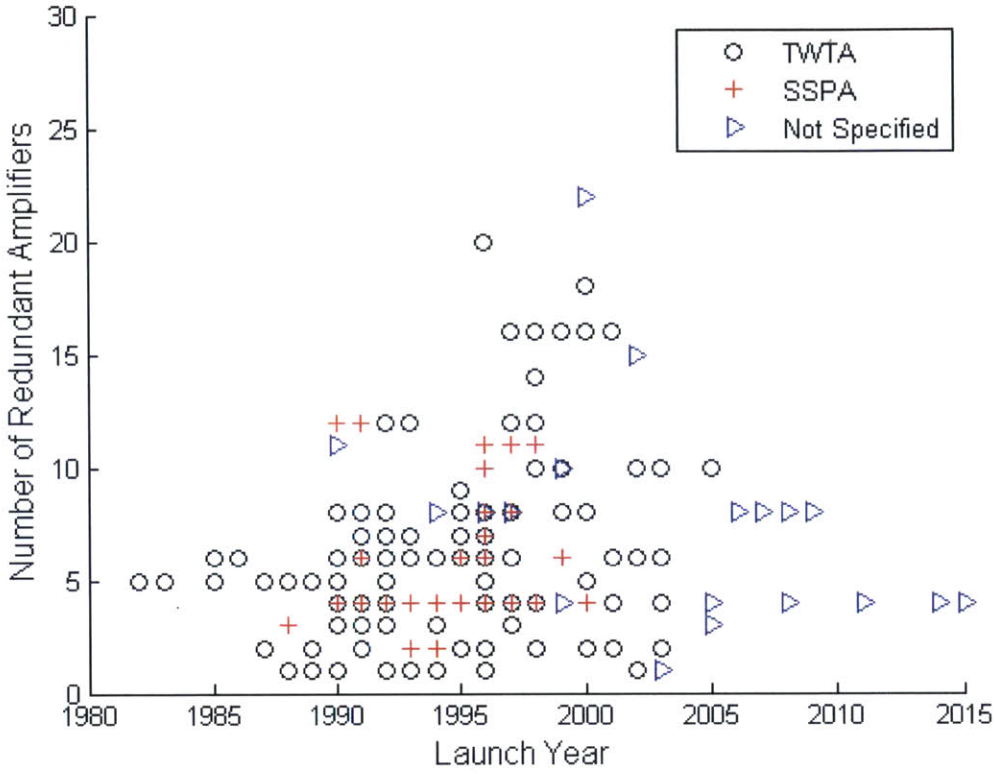

Figure B.6: Number of redundant amplifiers onboard satellites with TWTAs (marked with a black o), SSPAs (marked with a red +), and unspecified payloads (marked with a blue triangle)

The number of SSPA amplifiers shown in the figure above is greater than 19, the total number of exclusively SSPA payloads. This is because data from hybrid payloads, consisting of both SSPAs and TWTAs, was also included in this analysis. It is interesting to note that the highest number of redundant amplifiers reached a total of 20 for TWTAs, 12 for SSPAs and 22 for unspecified amplifier type. The payload equipped with 20 redundant TWTAs consisted of 8 TWTAs that operated in C-band and 12 TWTAs that operated in Ku-band. The payload equipped with 12 redundant SSPAs and the payload equipped with 22 redundant amplifiers of unspecified type both operated in C-band.

Figure B.7 shows the ratio of the number of operational amplifiers to the number of redundant amplifiers for the three amplifier types (SSPA, TWTA, and unspecified). Figure 8 does not include two outlier satellites, Thuraya 1 and Thuraya 2 satellites launched in 2000 and 2003, each

with 125 C-band TWTAs and 2 spares, and thus a ratio of operational TWTA to redundant TWTA equal to 62.5.

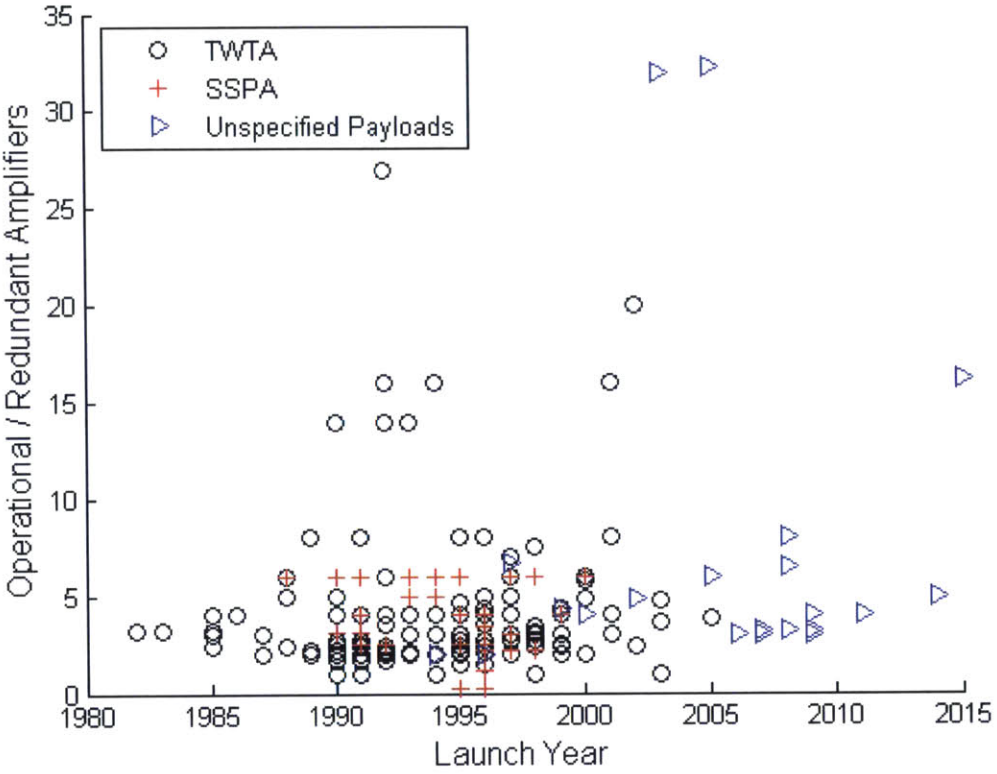

Figure B.7. Ratio of operational to redundant amplifiers onboard satellites with TWTAs (marked with a black o), SSPAs (marked with a red +), and unspecified payloads (marked with a blue triangle)

The ratio of operational to redundant SSPAs never exceeded a ratio of 6, whereas the ratio of operational to redundant TWTAs reached as high as 27 (shown in Figure B.7), with two outlier points of 62.5 that are not shown. Two unspecified payloads were designed with an operational to redundant amplifier ratio of 32. On average the ratio of operational to redundant TWTAs is 5.13 and the ratio of operational to redundant SSPAs is 0.47. Unfortunately, the data gathered for this study does not contain information on redundancy for payloads designated as either SSPA or TWTA after 2005. However, for both the worst-case and average scenario the ratio of operational to redundant amplifiers is ten times higher for TWTAs than SSPAs. This suggests that TWTAs are more considered more reliable, as they are equipped with fewer redundant amplifiers.

B.1.5. Amplifier Bandwidth

The bandwidth of the amplifier is another important performance characteristic for communication satellites since it indicates the range of frequencies over which data is transmitted. Wider bandwidth transponders, currently capable of hundreds of MHz, provide more power and higher data rates, at the expense of increased size and weight.

None of the studies presented in Table B.1. include a comparison of the bandwidth capabilities for the amplifiers. Figure B.8 shows the bandwidth, measured in MHz, for the three amplifier types. One outlier is not included in this figure; the outlier was onboard the Advanced Communications Test Satellite (ACTS) launched in 1993 with four Ka-band TWTAs that operated with a bandwidth of 800 MHz.

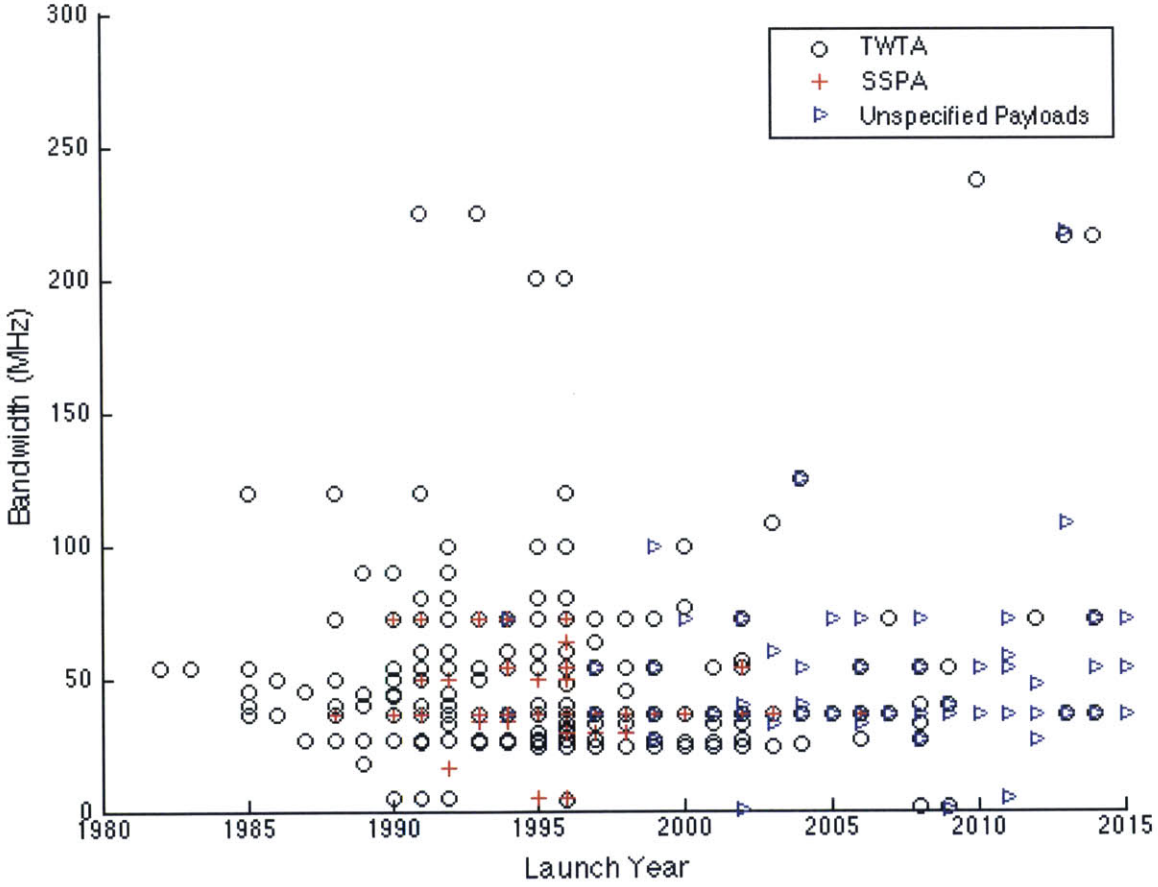

Figure B.8. Bandwidth (MHz) of amplifiers onboard satellites with TWTAs (marked with a black o), SSPAs (marked with a red +), and

unspecified payloads (marked with a blue triangle). The majority of all payloads operate with bandwidths of less than 100 MHz, which is likely due to licensing regulations.

Bandwidth data exists for only one out of the 19 exclusively SSPA payloads and for only 15 out of the 226 exclusively TWTA payloads after 2005. It is difficult to make conclusions on the trends in bandwidth over time. However, the majority of all three amplifier types operate with bandwidths below 100 MHz, which is likely the result technology limitations. Seven SSPAs operated at a bandwidth of 72 MHz, which was the highest bandwidth for an SSPA. As previously mentioned, the highest bandwidth for a TWTA was 800 MHz, but this point was not included in the figure above. The highest bandwidth for a TWTA that is included in Figure B.8 is 237 MHz, which was onboard KA-SAT launched in 2010.

The recent launch of satellites like Europe's KA-SAT, equipped with wide bandwidth transponders, and other programs like the U.S.'s Viasat1, which intends to provide high-speed Internet services, are evidence of a growing trend toward wider band devices. Previously, bandwidth was limited by the available frequency-dependent transponder technologies. Today, transponders with bandwidths of 500 MHz are desired in order to decrease communication burst sizes to microsecond counts. This in turn reduces the amount of time receiving antennas need to be powered up. Wider band transponders are also beneficial for single carrier operation, because they provide high data rates without the intermodulation penalties that arise with multi-carrier mode operation. The disadvantage with wider band transponders operating in single carrier mode is that the terminal demodulators have to use sophisticated waveforms to not overwhelm the demodulation/decoding chain.

Analysis of COMSAT Power Amplifier Failure Rates

In this study, we also analyze spacecraft telemetry from power amplifiers onboard sixteen geostationary communications satellites from the Inmarsat and Telenor satellite fleets. Amplifier reliability is determined through analysis of anomaly logs and analysis of satellite telemetry (specifically amplifier current), prior to the anomaly. Anomaly

logs are consulted for the age of the device at the time of the anomaly, and the amplifier current levels prior to amplifier anomalies are used to distinguish between hard and soft failures.

The sixteen satellites have a combined total of 659 amplifiers: 124 TWTAs and 535 SSPAs. The 124 TWTAs consisted of 92 Ku-band TWTAs, 24 L-band TWTAs, and 8 C-band TWTAs. Of these three Ku-band TWTAs, 8 L-band TWTAs and 4 C-band TWTAs were spares. The 535 SSPAs consisted of 525 L-band SSPAs and 10 C-band SSPAs, of which 33 L-band SSPAs were spares. Of the 124 TWTAs, two TWTA failures occurred, each on separate satellites. The two TWTA anomalies both occurred within the first two years of operation. Of the 535 SSPAs, twenty-six SSPA anomalies occurred, taking place anywhere from within the first three months of operation to fifteen years after launch [*Lohmeyer and Cahoy,* 2013].

In this group, the SSPAs operate at L- or C-band, and the TWTAs operate at either L-, C-, or Ku-band. One of the TWTA failures occurred for a Ku-band amplifier and the other occurred on an L-band amplifier. The Boeing 2005 study found that 100% of their TWTA anomalies were in Ku-band and that the SSPA anomalies were primarily in C-band. Of the 535 SSPAs in our study, twenty-six SSPA failures occurred, with 100% occurring at L-band. This is expected as more than 98% of the SSPAs in this analysis operated at L-band.

The Boeing 2005 study also found that 83% of the satellites experienced zero TWTA anomalies and 80% of the satellites recorded zero SSPA anomalies. Of the 20% of satellites that did experience SSPA anomalies, only 9% experienced more than two SSPA anomalies per satellite. Of the 16 satellites in our study, half of the satellites are exclusively TWTA payloads, and the other half of the satellites are exclusively SSPA payloads. Six out of the eight (75%) exclusively TWTA payloads experienced zero TWTA anomalies, and only one of the eight (13%) exclusively SSPA payloads experienced zero SSPA anomalies. Seven of the eight SSPA payload satellites experienced at least one anomaly, and six of the eight (75%) SSPA payload satellites experienced anywhere from two to eight SSPA anomalies.

Section III.A gives insight into the different failure types for SSPAs: hard and soft failures. TWTAs failures are typically "hard failures", and thus the distinction between hard and soft failures is not common. Hard failures occur when an excessively low or high current measurement breaches a specified current threshold and the device loses ability to operate. The anomaly thresholds are often amplifier and operator specific. For the twenty-six SSPA anomalies, twenty-two of the anomalies or 86% experienced hard failures. Only one of the four SSPAs that experienced a soft failure was recoverable. Therefore twenty-five out of twenty-six of the SSPA anomalies required a redundant amplifier to be switched on [*Lohmeyer and Cahoy,* 2013]. The two TWTA anomalies were hard failures. The Boeing 2005 study stated that a single satellite component failure has essentially zero impact on the communications function. While the ability to turn on redundant amplifiers often alleviates the impact of amplifier failures, issues do arise when a satellite utilizes all available redundant amplifiers. This is has not yet been experienced on any of the sixteen satellites. However, there were three amplifier anomalies for which a redundant amplifier was already in use, and thus not available, due to a previous amplifier failure.

More detailed satellite payload data is necessary for conclusions to be drawn. There is a clear difference between the number of amplifier anomalies described in the 2005 Boeing study of 104 satellites (1783 TWTAs and 944 SSPAs) and the 16 satellites (124 TWTAs and 535 SSPAs) of this analysis. One potential explanation for this difference could be related to the fact that as technological capabilities evolve (e.g. smaller feature sizes), the susceptibility of newer technologies to radiation also increases [*Baker,* 2000; *Love et al.,* 2000].

References

Abel, B. and R.M, Thorne (1998), Electron scattering loss in Earth's inner magnetosphere: 1. Dominant physical processes, *Journal of Geophysical Research: Space Physics (1978-2012),* 103A2, p. 2385-2396.

Airbus Defence and Space, "85W S Band GaN SSPA Data Sheet," *About Amplifiers* [online], http://www.astrium.eads.net/en/equipment/about-amplifiers.html [retrieved 21 Jan 2014].

Airbus Defence and Space, "80W C Band GaN SSPA for communication satellites," *About Amplifiers* [online], http://www.astrium.eads.net/en/equipment/about-amplifiers.html [retrieved 21 Jan 2014].

Airbus Defence and Space, "Airbus Defence and Space L/S Band SSPA Data Sheet," *SSPA - L/S Band for Mobile Communications Satellites* [online], http://www.astrium.eads.net/en/equipment/sspa-ls-band-sspa-for-mobile-communications-satellites.html [retrieved 21 Jan 2014].

Airbus Defence and Space, "C-Band SSPA for communication satellites," *About Amplifiers* [online], http://www.astrium.eads.net/en/equipment/about-amplifiers.html [retrieved 21 Jan 2014].

Alig, R. C., and S. Bloom (1975), Electron-hole-pair creation energies in semiconductors, Phys. Rev. Lett., 35(22), 1522–1524, doi: 10.1103/PhysRevLett.35.1522.

Allen, J. and D.C. Wilkinson (1993), Solar-terrestrial activity affecting systems in space and on Earth, *Workshop Solar-Terrestrial Predictions-IV.*

Allen, J. (2010), The Galaxy 15 anomaly: Another satellite in the wrong place at a critical time, Space Weather, 8, S06008, doi: 10.1029/2010SW000588.

Aloisio, M., Angeletti, P., Colzi, E, D'Addio, S., Balague, R., Casini, E., Coromina, F. (2008), End-to-End Performance Evaluation Methodology for TWTA-Based Satellite Flexible Payloads, IEEE International Vacuum Electronic Conference, 22-24 April 2008, doi: 10.1109/IVELEC.2008.4556438.

Aloisio, M., Angeletti, P., Coromina, F., Deborgies, F., Gaudenzi, R., Ginesi, A. (2010), R&D Challenges for Broadband Satcomes in 2020, IEEE International Vacuum Electronics Conference, 18-20 May 2010.

Alurralde, M., Tamasi, M.J.L., Bruno, C.J., Martinez Bogado, M.G., Pla, J., Fernandez Vazquez, J., Duran, J., Schuff, J., Burlon, A.A., Stoliar, P., and A.J. Kreiner (2004), Experimental and theoretical radiation

damage studies on crystalline silicon solar cells, *Solar Energy Materials and Solar Cells,* 82, 531-542, doi: 10.10106/j.solmat.2003.11.029.

Anspaugh, B.E. (1989), Solar Cell Radiation Handbook Addendum 1: 1982 – 1988, *Jet Propulsion Laboratory.*

Anspaugh, B.E. (1996), GaAs Solar Cell Radiation Handbook, *Jet Propulsion Laboratory.*

Armstrong, T.W., Chandler, K.C. and J. Barish (1973), Calculations of neutron flux spectra induced in the Earth's atmosphere by galactic cosmic rays, *Journal of Geophysical Research,* 78(16), 2715-2726.

ASTM Standard D257 (2014), Standard Test Methods for DC Resistance or Conductance of Insulating Materials, ASTM International, West Conshohocken, PA, 2014, doi:10:1520/D0257, www.astm.org.

Bailey S. and D. Flood (1998), Space photovoltaics, *Progress in Photovoltaics,* 6, 1–14, doi: 10.1002/(SICI)1099-159X(199801/02)6:1<1::AID-PIP204>3.3.CO.

Bailey, S. and R. Raffaelle (2003), Space Solar Cells and Arrays, *Handbook of Photovoltaic Science and Engineering*, John Wiley & Sons, Ltd, doi: 10.1002/0470014008.ch10.

Baker, D.N. (1998), What is Space Weather, *Adv. Space Research,* 22, 1, 7-16, doi: 10.1016/S0273-1177(97)01095-8.

Baker, D. N. (2000), The occurrence of operational anomalies in spacecraft and their relationship to space weather, IEEE Trans. Plasma Sci., 28(6), 2007–2016, doi: 10.1109/27.902228.

Baker, D. N. (2002), How to cope with space weather, Science, 297(5586), 1486–1487, doi: 10.1126/science.1074956.

Baker, D.N. and I.A. Daglis (2007), Radiation belts and ring current, *Space Weather – Physics and Effects*, Springer Berlin Heidelberg, 173-202.

Baker, D.N., Kanekal, S.G., Hoxie, V.C., Henderson, M.G., Li, X., Spence, H.E., Elkington, S.R., Friedel, R.H.W., Goldstein, J., Hudson, M.K., Reeves, G.D., Thorne, R.M., Kletzing, C.A. and S.G. Claudepierre (2013), A long-lived relativistic electron storage ring embedded in Earth's Outer Van Allen Belt, *Science,* 340, 6129, 186-190, doi:10.1126/science.1233518.

Baker, D.N., Kanekal, S.G., Hoxie, V.C., Batiste, S., Bolton, M., Li, X., Elkington, S.R., Monk, S., Reukauf, R., Steg, S., Westfall, J., Belting, C., Bolton, B., Braun, D., Cervelli., B., Hubbell, K., Kien, M., Knappmiller, S., Wade, S., Lamprecht, B., Stevens, K., Wallace, J.,

Yehle, A., Spence, H.E., Friedel, R., (2013), The Relativistic Electron-Proton Telescope (REPT) Instrument on Board the Radiation Belt Storm Probes (RBSP) Spacecraft: Characterization of Earth's Radiation Belt High-Energy Particle Populations, *Space Science Review,* 179, 337-381, doi:10.1007/s11214-012-9950-9.

Balcewicz, P.T., Bodeau, J.M, Frey, M.A., Leung, P.L., and E.J. Mikkelson (1993), Environment on-orbit anomaly correlation efforts at Hughes, *6th Spacecraft Charging Technology Conference.*

Barbieri, L. P., and R. E. Mahmot (2004), October-November 2003's space weather and operations lessons learned, *Space Weather*, 2, S09002, doi: 10.1029/2004SW000064.

Barkas, W.H., and M.J. Berger (1964), *NASA Publ. SP—3013.*

Bedingfield, K.L., Leach, R.D., Alexander, M.B. (1996) Spacecraft system failures and anomalies attributed to the natural space environment, *NASA Reference Publication 1390.*

Benton, E.R. and E.V. Benton (2001) Space radiation dosimetry in low-Earth orbit and beyond, *Advanced Topics in Solid State Dosimetry,* 184(1-2), pp. 255 – 294, doi: 10.1016/S0168-583X(01)00748-0.

Berger, M.J., and S.M. Seltzer (1968), *NASA Publ. SP-169.*

Berger, M.J., and S.M. Seltzer (1970), *Phys. Rev.,* C2, 621,

Bhat, R. B., N. Upadhyaya, and R. Kulkarni (2005), Total radiation dose at geostationary orbit, IEEE Trans. Nucl. Sci., 52(2), 530–534, doi: 10.1109/TNS.2005.846881.

Bielle-Daspet, D., Castaner, L., Gasset, G. and M. Benzohra (1980), Changes in lifetime and diffusion length due to the electron and proton bombardment of silicon solar cells, *Solar Cells,* 2 31-42, doi: 10.1016/0379-6787(80)90096-4.

Bijeev, N.V., Malhotra, A., Kumar, V., Singh, S., Dasgupta, K.S., Motta, R.N., Venugopal, B., Sandhyarani, Jinan, O.K., and B.K. Jayakumar (2011), Design and Realization Challenges of Power Supplies for Space TWT, *IEEE International Vacuum Electronic Conference*, Bangalore, India, doi: 10.1109/IVEC.2011.5747079.

Bodeau, M. (2010), High Energy Electron Climatology that Supports Deep Charging Risk in GEO, paper presented at 48th AIAA Aerospace Sciences Meeting Including the New Horizons Forum and Aerospace Exposition, Orlando, FL, 4-7 January 2010.

Bogorad, A.L., Likar, J.J., Lombardi, R.E., Herschitz, R., and G. Kircher (2010), On-Orbit Total Dose Measurements from 1998 to 2007 Using pFET Dosimeters, *IEEE Transactions on Nuclear Science*, 57(6), 3154-3162, doi:10.1109/TNS.2010.2076832.

Brekke, P., Steen, R., Onsager, T., Wintoft, P., Olaussen, A., Pirjola, R., Stauning, P., Sundelius, B., Ohnstad, T., and L. Marti. (2013), *AGU Space Weather,* 11, 1-2, doi:10.1029/2012SW000881.

Buchen, E. and D. DePasquale (2014), 2014 Nano/Microsatellite Market Assessment, *SpaceWorks Enterprises, Inc.,* Atlanta, GA.

Burt, J. and B. Smith (2012), Deep Space Climate Observatory: The DSCOVR mission, *2012 IEEE Aerospace Conference,* Big Sky, MT, doi: 10.1109/AERO.2012.6187025.

Chapman, S. and J. Bartels (1940), Geomagnetism, *Oxford University Press,* Vol. 1.

Choi, H. S., J. Lee, K. S. Cho, Y. S. Kwak, I. H. Cho, Y. D. Park, Y. H. Kim, D. N. Baker, G. D. Reeves, and D. K. Lee (2011), Analysis of GEO spacecraft anomalies: Space weather relationships, Space Weather, 9, S06001, doi: 10.1029/2010SW000597.

Clette, F., Berghmans, D., Vanlommel, P., Van der Linden, R.A.M., Koeckelenbergh, A. and Wauters, L. (2007), From the Wolf number to the International Sunspot Index: 25 years of SIDC, *Advances in Space Research,* Vol. 40, No. 7, pp.919–928, doi: 10.1016/j.asr.2006.12.045.

Coaker, B. and T. Challis (2008), Traveling Wave Tubes: Modern Devices and Contemporary Applications, *Microwave Journal*, Vol. 51, No. 10, 2008, pp. 32-46.

Cole, D. G. (2003), Space weather: Its effects and predictability, Space Sci. Rev., 107, 295–302, doi: 10.1007/978-94-007-1069-6_27.

Colantonio, P., Giannini, F., and Limiti, E. (2009), High Efficiency RF and Microwave Solid State Power Amplifiers, John Wiley & Sons, Ltd., West Sussex, United Kingdom.

Comparetto, G. and R. Ramirez (1997), Trends in Mobile Satellite Technology, *IEEE*, Cover Feature.

Cotts, D.B. and Z. Reyes (1985), New Polymeric Materials Expected to Have Superior Properties for Space Based Uses, RADC-TR-85-129, Final Technical Report, RADC, Bedford, MA, ADA160285.

Cuignet, E., Tonello, E., Maynard, J., and Boone, P. (2013), Very High efficiency Dual Flexible TWTA, a flexible concept allowing to deal with

performances and schedule constraints of Telecommunication Payloads, *IEEE Vacuum Electronics Conference (IVEC)*, IEEE, pp. 1-2. doi: 10.1109/IVEC.2013.6570951.

Daly, E.J., Lemaire, J., Heynderickx, D. and D.J. Rodgers (1996), Problems with Models of the Radiation Belts, *IEEE Transactions on Nuclear Science*, 43, 2, doi: 10.1109/23.490889.

Davis, V.A. and Gordon, L.W., 1992, Spacecraft Surface Charging Handbook, PL-TR-92-2232, Final Report, Phillips Lab, Hanscomb AFB, MA, Nov 1992, ADA262778;

Davis V.A., Mandell, M.J., and M.F. Thomsen (2008), Representation of the measured geosynchronous plasma environment in spacecraft charging calculations, *Journal of Geophysical Research,* 113, 1-14 , doi: 10.1029/2008JA013116.

de Angelis, N., Bourgoin, J.C., and T. Takamoto, A. Khan, M. Yamaguchi (2001), Solar cell degradation by electron irradiation comparison between Si, GaAs and GaInP cells, Sol. Energy Mater, *Solar Cells,* 66, 495–500, doi:10.1016/S0927-0248(00)00211-7.

Denig W., Cooke, D., and D. Ferguson (2010), Spacecraft Charging and Mitigation, *Space Weather,* 8, 1-2, doi: 10/1029/2010SW000632.

Denton, M. H., J. E. Borovsky, R. M. Skoug, M. F. Thomsen, B. Lavraud, M. G. Henderson, R. L. McPherron, J. C. Zhang, and M. W. Liemohn (2006), Geomagnetic storms driven by ICME and CIR-dominated solar wind, J. Geophys. Res., 111, A07S07, doi: 10.1029/2004JA011436.

Denton, M. H., and J. E. Borovsky (2012), Magnetosphere response to high-speed solar wind streams: A comparison of weak and strong driving and the importance of extended periods of fast solar wind, J. Geophys. Res., 117, A00L05, doi: 10.1029/2011JA017124.

Draghici, S. (2001) 'Data analysis tools for DNA microarray data', Paper presented at the *Pacific Symposium on Biocomputing 2001,* Hawaii, HI, 3–7 January.

Edmonds, L.D., Bames, C.E. and L.Z. Scheick (2000), An Introduction to Space Radiation Effects on Microelectronics, *JPL Publication 00-06*, JPL.

Escalera, N., Boger, W., Denisuk, P., & Dobosz, J. (2000), Ka-band, 30 watts solid state power amplifier. In *Microwave Symposium Digest. 2000 IEEE MTT-S International* (Vol. 1, pp. 561-563). IEEE, doi: 10.1109/MWSYM.2000.861123.

Fatemi, N.S., Polard, H.E., Hou, H.Q., and P.R. Sharps (2000), Solar array trades between very high-efficiency multi-junction and Si space solar cells, *IEEE* 1083-1086, doi: 10.1109/PVSC.2000.916075.

Farthing, W.H. Brown, J.P., and Bryant, W.C. (1982), Differential Spacecraft Charging on the Geostationary Environmental Satellites, NASA TM 83908.

Feicht, J.R., Loi, K.N., Menninger, W.L., Nicolello, J.G., Zhai, X. (2012), Space Qualified 140 W Linearized L-band Helix TWTA, IEEE International Vacuum Electronics Conference, 24-26 April 2012, doi: 10.1109/IVEC.2012.6262193.

Fennell, J.F., Koons, H.C., Roeder, J.L. and Blake, J.B. (2001) Spacecraft charging: observations and relationships to satellite anomalies, Aerospace Rep. TR-2001(8570)-5, Aerospace Corp., Los Angeles, California.

Fennell, J.F., Claudepierre, S.G., Blake, J.B., O'Brien, T.P., Clemmons, J.H., Baker, D.N., Spence, H.E., and G.D. Reeves (2015), Van Allen Probes show the inner radiation zone contains no MeV electrons: ECT/MagEIS data, *Geophysical Research Letters,* doi:10.1002/2014GL062874.

Feynman, J., Spatiale, G., Wang, J., and S. Gabriel (1993), Interplanetary proton fluence model – JPL 1991, *Journal of Geophysical Research,* 98(13), 281.

Frederickson, A.R. (1980), Bulk Charging and Breakdown in Electron Irradiated Polymers, Proceedings of the 3rd Spacecraft Charging Technology Conference, *NASA Report 2182.*

Frederickson, A.R., D. B. Cotts, and J. A. Wall (1986), Spacecraft Dielectric Material Properties and Spacecraft Charging, AIAA Progress in Astronautics and Aeronautics, doi:10.2514/4.865817.

Freeman, J.W. (2001), Storms in Space, *Cambridge University Press.*

Galvin, D.A., Hemenway, B., Wesler, W., Baiocchi, D (2014), Satellite anomalies: Benefits of a centralized anomaly database and methods for securely sharing information among satellite operators, *RAND Corporation.*

Garrett, H.B. and A.C. Whittlesey (2011) Guide to Mitigating Spacecraft Charging Effects, *Jet Propulsion Laboratory.* JPL Space Science and Technology Series.

Ginet, G.P., O'Brien, T.P., Huston, S.L., Johnston, W.R., Guild, T.B., Friedel, R., Lindstrom, C.D., Roth, C.J., Whelan, P., Quinn, R.A., Madden, D., Morley, S., Su, Y. (2013), AE9, AP9, and SPM: New Models for Specifying the Trapped Energetic Particle and Space Plasma Environment, *Space Science Review,* 179, pp. 579-615, doi: 10.1007/s11214-013-9964-y.

GOES I-M Data-book. Palo Alto, CA: Space Systems/Loral, 1996.

Goldman, J.M. (2005), Space Weather & Telecommunications, *The Kluwer International Series in Engineering and Computer Science*, Springer, New York, NY.

Gonzalez, W.D., Joselyn, J.A., Kamide, Y., Kroehl, H.W., Rostoker, G., Tsurutani, B.T. and Vasyliunas, V.M. (1994) What is a geomagnetic storm?, *Journal of Geophysical Research,* Vol. 99, No. A4, 5771–5792, doi: 10.1029/93JA02867.

Gopalswamy, N., Yashiro, S., and S. Akiyama (2006), Coronal Mass Ejections and Space Weather due to extreme events, *ILWS Workshop.*

Green, N.W., Frederickson, A. R. and Dennison, J. R. (2005), Experimentally Derived Resistivity for Dielectric Samples from the CRREs Internal Discharge Monitor, JAXA-SP-05-001E, Japan Aerospace Exploration Agency (JAXA), Tsukuba, Japan, April 4-8, 2005.

Green, N. W., H. Kirkham, W. Kim, and B. McAlpine (2009), Radiation Dose Testing on Juno High voltage Cables, AIAA 2009-353, 47th AIAA Aerospace Sciences Meeting, Orlando, FL, January 5-8, doi: 10.2514/6.2009-353.

Green, M.A. (2009), The Path to 25% Silicon Solar Cell Efficiency: History of Silicon Cell Evolution, *Progress in Photovoltaics: Research and Applications*, 17, pp. 183-189, doi:10.1002/pip.892.

Gubby, R. and J. Evans (2002), Space Environment Effects and Satellite Design, *Journal of Atmospheric and Solar-Terrestrial Physics* 64(16), 1723-1733, doi: 10.1016/S1364-6826(02)00122-0.

Guild, T.B, O'Brien, P., and J.E. Mazur (2009), Space Environment Model Recommendations for Geostationary Orbit, *The Aerospace Corporation*, Report No. TOR-2008(3906)-75.

Gurnett, D.A. and A. Bhattacharjee (2005), Introduction to Plasma Physics, *Cambridge University Press,*

Hacke, P., Uesugi, M., and S. Matsuda (1994), A study of the relationship between junction depth and GaAs solar cell performance under a 1 MeV electron fluence, *Solar Energy Materials and Solar Cells*, 35, 113-119, doi: 10.1016/0927-0248(94)90130-9.

Hanna, R., T. Paulmier, P. Molinie, M. Belhaj, B. Dirassen, D. Payan, and N. Balcon (2013), Radiation Induced Conductivity in Teflon FEP Irradiated With Multienergetic Electron Beam, *IEEE Transactions on Plasma Science*, 41(12), 3520-3525, doi: 10.1109/TPS.2013.2287097.

Hastings, D., and H. Garret (1996), Spacecraft-Environment Interactions, Cambridge Univ. Press, New York.

Heynderickx, D. (2002), Review of Modeling of the Radiation Belts, *International Journal of Modern Physics,* 17(12), 1675-1684, doi: 10.1142/S0217751X02011175.

Hisamatsu, T., Kawasaki, O., Matsuda, S., Nakao, T., and Y.Wakow (1998), Radiation degradation of large fluence irradiated space silicon solar cells, *Solar Energy Materials and Solar Cells*, 50, 331-338, doi: 10.1016/S0927-0248(97)00163-3.

Horne, R. B., S. A. Glauert, N. P. Meredith, D. Boscher, V. Maget, D. Heynderickx, and D. Pitchford (2013), Space weather impacts on satellite and forecasting the Earth's electron radiation belts with 2 SPACECAST, Space Weather, 11, 169–186, doi: 10.1002/ swe.20023.

Ibrahim, A., Ramadan, M.R.I., Aboul-Enein, S., Abdel-Azeem Elsebaii, A., El-Broullesy, S.M (2011), Short circuit current I_{sc} as a real non-destructive diagnostic tool of a photovoltaic modules performance, *International Journal of Renewable Energy Research,* 1(3), 53-59, doi: 10.1016/j.spmi.2013.03.005.

Illokken, E. (1987), TWT Reliability in Space. *Aerospace and Electronic Systems Magazine, IEEE*, *2*(7), 22-24, doi: 10.1109/MAES.1987.5005442.

Iucci, N., Dorman, L.I., Levitin, A.E., Bevlov, E.A, Eroshenko, N.G., Villoresi, G., Chizhenkov, G.V., Gromova, L.I., Parisis, M., Tyasto, M.I. and Yanke, V.G. (2006) Spacecraft operational anomalies and space weather impact hazards, *Advances in Space Research,* Vol. 37, No. 1, pp.184–190, doi: 10.1016/j.asr.2005.03.028.

Kaliski, M., (2009), Evaluation of the Next Steps in Satellite High Power Amplifier Technology: Flexible TWTAs and GaN SSPAs, IEEE International Vacuum Electronics Conference, 28-30 April 2009.

Kamide, Y. and Akasofu, S. (1983), Notes on the Auroral Electrojet indices, *Reviews of Geophysics and Space Physics,* Vol. 21, No. 7, pp.1647–1656, doi: 10.1029/RG021i007p01647.

Kamide, Y., Baumjohann, W., Daglis, I.A., Gonzalez, W.D., Grande, M., Joselyn, J.A., McPherron H.L., Philips, J.L., Reeves, E.D.G., Rostoker, G., Sharma, A.S., Singer, H.J., Tsurutani, B.T. and Vasyliunas, V.M. (1998), Current understanding of magnetic storms: storm-substorm relationships, *Journal of Geophysical Research,* Vol. 103, No. A8, pp.17705–17728.

Kane, R.P. (2002), Some implications using the group sunspot number reconstruction, *Solar Physics,* Vol. 205, No. 2, pp. 282–401.

King, J.H., (1974), Solar Proton Fluences for 1977 – 1983 Space Missions, *Journal of Spacecraft and Rockets,* 11, 401, doi: 10.2514/3.62088.

King, J.H., and N.E. Papitashvili (2004), Solar wind spatial scales in and comparisons of hourly wind and ACE plasma and magnetic field data, J. Geophys. Res., 110, A02209, doi: 10.1029/ 2004JA010804.

King, J. and Papitashvili, N. (2013), *OMNI 2 Preparation,* Goddard Spaceflight Center archives [online] http://omniweb.gsfc.nasa.gov/html.html (accessed 1 October 2012).

Kingsbury, R. W., Schmidt, F. H., Cahoy, K., Sklair, D. A., Blackwell, W. J., Osarentin, I., and Legge Jr, R. S. (2013), TID tolerance of popular cubesat components.

Kivelson, M.G., and C.T. Russell (1995), Introduction to Space Physics, Cambridge University Press.

Knoll, G.F. (2010), Radiation Detection and Measurement 4th Edition, *John Wiley & Sons.*

Komm, D. S., Benton, R. T., Limburg, H. C., Menninger, W. L., and Zhai, X. (2000), Advances in space TWT efficiencies, *IEEE Transactions on Electron Devices,* Vol. 48, No. 1, pp. 174-176. doi: 10.1109/16.892186.

Koons, H.C., Mazur, J.E., Selesnick, R.S., Blake, J.B., Fennel, J.F., Roeder, J.L. and P.C. Anderson (2000), The Impacts of the Space Environment on Space Systems, 6th Spacecraft Charging Technology Conference, Air Force Research Laboratory Science Center, Hanscom Air Force Base, MA.

Korth, H., M. F. Thomsen, J. E. Borovsky, and D. J. McComas (1999), Plasma sheet access to geosynchronous orbit, J. Geophys. Res., 104, 25,047–25,061.

L-3 Communications, "LTWTA Product Sheets", *Space TWTs, LTWTAs, & EPCs,* [online] http://www2.l-3com.com/eti/product_lines_space_twt .htm [retrieved 21 Jan 2014].

Lai, S. T. (2012), Fundamentals of Spacecraft Charging: Spacecraft Interactions with Space Plasmas, *Princeton University Press,* Princeton, NJ.

Laiadi, W., Meftah, Af., Sengouga, N., and Am. Meftah (2013), Irradiation effect on the electrical characteristics of an AlGaAs/GaAs based solar cell: Comparison between electron and proton irradiation and

numerical simulation, *Superlattices and Microstructures,* 58, 44-52, doi: 10.1016/j.spmi.2013.03.005.

Lanzerotti, L. J., C. Breglia, D. W. Maurer, G. K. Johnson III, and C. G. Maclennan (1998), Studies of spacecraft charging on geosynchronous telecommunications satellite, Adv. Space Res., 22, doi: 10.1016/ SO273-1177(97)01104-6.

Lanzerotti, L.J. (2001), Space Weather effects on technologies, *AGU Space Weather,* 11-22, doi: 10.1029/GM125p0011.

Laurenstein, J.M. and J.L. Barth (2005), Radiation belt modeling for spacecraft design: Model comparisons for common orbits. *IEEE Radiation Effects Data Workshop Proceedings,* 102-109.

Leung, P. L., G. H. Plamp, and P. A. Robinson Jr. (1985), Galileo internal electrostatic discharge program, *NASA Lewis Research Center Spacecraft Environ. Interactions Technol.,* 423-433 (SEE N85-22470 13-18).

Li, X., Baker, D.N., Temerin, M., Reeves, G., Friedel, R. and Shen, C. (2005), Energetic electrons, 50 keV to 6 MeV at geosynchronous orbit: their responses to solar wind variations, *Space Weather,* Vol. 3, No. 4, p.S04001, doi: 10.1029/2004SW000105.

Lohmeyer, W., K. Cahoy, and D. N. Baker (2012), Correlation of GEO communication satellite anomalies and space weather phenomena: Improved satellite performance and risk mitigation, paper presented at 30th AIAA International Communications Satellite Systems Conference (ICSSC), Ottawa, Canada.

Lohmeyer, W., K. Cahoy, and S. Liu (2013), Causal relationships between solar proton events and single event upsets for communication satellites, paper presented at the 2013 IEEE Aerospace Conference, Big Sky, Mont., March 2-9.

Lohmeyer, W. Q., Pang, A., Cahoy, K., and Y. Shprits (2013), Quantifying the average and the likelihood of increases in space weather indices and in situ measurements during Solar Cycles 20-23. *International Journal of Space Science and Engineering,* 1(3), p. 230-252. doi: 10.1504/IJSPACESE.2013. 058856.

Lohmeyer, W. Q. and K. Cahoy (2013), Space weather radiation effects on geostationary satellite solid-state power amplifiers, *Space Weather,* 11(8), 476-488, doi: 10.1002/swe.20071.

Love, D. P., D. S. Toomb, D. C. Wilkinson, and J. B. Parkinson (2000), Penetrating electron fluctuations associated with GEO spacecraft

anomalies, IEEE Trans. Plasma Sci., 28, 2075–2084, doi: 10.1109/27.902234.

Lyons, L.R. and R.M Thorne (1973), Equilibrium structure of radiation belt electrons, *Journal of Geophysical Research,* 78(13), p. 2142-2149.

Mallet, A., Anakabe, A., and J. Sombrin (2006), Multiport-Amplifier-Based Architecture Versus Classical Architecture for Space Telecommunication Payloads, *IEEE Transactions on Microwave Theory and Techniques,* Vol. 54, No. 12, pp. 4353 – 4361. doi: 10.1109/TMTT.2006.885904.

Mallon, K.P. (2008), PL.6: TWTAs for Satellite Communications: Past, Present, and Future, *IEEE International Vacuum Electronic Conference*, Monterey, California, 2008, pp. 14-15. doi: 10.1109/IVELEC.2008.4556558.

Mandell, M.J., I. Katz, G.W., Schnelle, P.G. Steen, and J.C. Roche (1978), The decrease in effective photocurrents due to saddle points in electrostatic potentials near differentially charged spacecraft, *IEEE Transactions on Nuclear Science,* NS-25(6), 1313, doi: 10.1109/TNS.1978.4329530.

Manz, B. (2009), Advancing TWT Technology, *Journal of Electronic Defense,* Vol. 32, No. 7, pp. 26 – 30.

Mauk, B.H., Fox, N.J., Kanekal, S.G., Kessel, R.L., Sibeck, D.G., Ukhorskiy, A. (2013), Science Objectives and Rationale for the Radiation Belt Storm Probes Mission, *Space Science Review,* 179, 3-27, doi:10.1007/s11214-012-9908-y.

Mazur, J. E., and T. P. O'Brien (2012), Comment on "Analysis of GEO spacecraft anomalies: Space weather relationships" by Ho-Sung Choi et al, Space Weather, 10, S03003, doi: 10.1029/2011SW000738.

Menninger, W. L., Eze, D. C., Hollister, R. S., and Martin, R. H. (2013), "High-efficiency, 200-W Ku-band traveling-wave tubes for satellite communications downlinks", *IEEE Vacuum Electronics Conference,* IEEE, p. 1-2. doi: 10.1109/IVEC.2013.6571081.

Meredith, N.P., Horne, R.B, Clilverd, M.A., Horsfall, D., Thorne, R.M and R.R. Anderson (2006), Origins of plasmaspheric hiss, *Journal of Geophysical Research: Space Physics (1978-2012),* 111(A9).

Messenger, S.R., Summers, G.P., Burke, E.A., Walters, R.J., and Xapsos, M.A. (2001), Modeling solar cell degradation in space: A comparison of the NRL displacement damage dose and the JPL equivalent Fluences Approach, *Progress in Photovoltaics: Research and applications,* 9, 103-121, doi: 10.1002/pip.357.

Messenger, S.R., Burke, E.A., Walters, R.J., Waner, J.H., Summers, G.P., and T.L. Morton (2006), Effect of Omnidirectional Proton Irradiation On Shielded Solar Cells, *IEEE Transactions on Nuclear Science,* 53(6), doi: 10.1109/TNS.2006.886220.

Messenger, S.R., Jackson, E.M., Warner, J.H., and R.J. Walters (2010), SCREAM: A new code for solar cell degradation prediction using the displacement damage dose approach, *IEEE Photovoltaics Specialist Conference,* doi: 10.1109/PVSC.2010.5614713.

Messenger, S.R., Jackson, E.M, Waner, J.H. and R.J. Walters (2011), Advancements to SCREAM: Multiple Spectrum Input and ShielDDDose Options, *IEEE Photovoltaic Specialist Conference,* doi: 10.1109/PVSC.2012.6318276.

Messenger, S.R., Jackson, E.M., Warner, J.H., Walters, R.J., Cayton, T.E., Chen, Y., Friedel, R.W., Kippen, M., and B. Reed (2011), Correlation of Telemetered Solar Array Data with Particle Detector Data on GPS Spacecraft, *IEEE Transactions on Nuclear Science,* 58(6), 3118-3125, doi: 10.1109/TNS.2011.2172957.

MIL-C-17/170A (1985), Military Specification Sheet: Cables, Radio Frequency, Flexible, Coaxial, 50 Ohms, *U.S. Military.*

Mitsubishi Electric (Melco), C-Band Solid State Power Amplifier 50-70W Class," *Satellite Components* [online], http://www.mitsubishielectric.com/bu/space/products/satellite/rf_equipment/index.html [retrieved 21 Jan 2014].

Miyoshi, Y., and R. Kataoka (2008), Flux enhancement of the outer radiation belt electrons after the arrival of stream interaction regions, J. Geophys. Res., 113, A03S09, doi: 10.1029/2007JA012506.

Mursula, K., Holappa, L. and Karinen, A. (2008), Correct normalization of the Dst index, *Astrophysics and Space Sciences Transactions,* Vol. 4, No. 2, pp.41–45, doi: 10.5194/astra-4-41-2008.

Murthy, H.S., Sharma, A., Badarinarayana, K., and P. Lakshminarasimhan (2011), Thermal Management of GEO Satellite Communication Payload, IEEE International Vacuum Electronics Conference, 21-24 April 2011, doi: 10.1109/IVEC.2011.5747079.

NASA-HDBK-4002A (2011), Avoiding Problems Caused by Spacecraft On-Orbit Internal Charging Effects, *NASA.*

National Weather Service (NSWPC) (2007), NOAA / NWS Space Weather Prediction Center, *NOAA / NWS Space Weather Prediction Center.* National Oceanic and Atmospheric Administration, 5 Nov. 2007. Web. 23 Mar. 2012. http://www.swpc.noaa.gov/.

NEC TOSHIBA Space Systems, Ltd., "High Linearity SSPA Line Up- L-band SSPA," *High Linearity SSPA Line Up* [online], http://www.nec.com/en/global /solutions/space/satellite_communications/images/L-band_SSPA.pdf [retrieved 21 Jan 2014].

NEC TOSHIBA Space Systems, Ltd., "High Linearity SSPA Line Up - S-band SSPA," *High Linearity SSPA Line Up* [online], http://www.nec.com/en/global/ solutions/space/satellite_communications/images/S-band_SSPA.pdf [retrieved 21 Jan 2014].

NEC TOSHIBA Space Systems, Ltd., "C-band SSPA," *C-band SSPA* [online], http://www.nec.com/en/global/solutions/space/satellite_communication s/images/C-band_SSPA.pdf [retrieved 21 Jan 2014].

Neil, T. and Sugiura, M. (1966), Auroral electrojet activity index AE and its universal time variations, *Journal of Geophysical Research,* Vol. 71, No. 3.

Nicol, Eric F., Bill J. Mangus, and J. R. Grebliunas TWTA versus SSPA: Analysis update of the Boeing fleet on-orbit reliability data, *IEEE International Vacuum Electronics Conference,* Monterey, California, 22-24 April 2008. doi: 10.1109/IVELEC.2008.4556435.

Nicol, E. F., Mangus, B. J., Grebliunas, J. R., Woolrich, K., and Schirmer, J. R., "TWTA versus SSPA: A comparison update of the Boeing satellite fleet on-orbit reliability", *IEEE International Vacuum Electronics Conference*, Paris, France, 21-23 May 2013. doi: 10.1109/IVEC.2013.6571087.

NRC (2008), Severe Space Weather Events – Understanding Societal and Economic Impacts Workshop, *National Research Council.* National Academy of Sciences. http://www.nap.edu/catalog/12507.html.

O'Brien, T. P. (2009), SEAES-GEO: A spacecraft environmental anomalies expert system for geosynchronous orbit, Space Weather, 7, S09003, doi: 10.1029/2009SW000473.

O'Brien, T. P., J. E. Mazur, and J. F. Fennell (2013), The priority mismatch between space science and satellite operations, Space Weather, 11, 49, doi: 10.1002/swe.20028.

Oldenwald, S.F., and Green, J.L. (2007), "Forecasting the impact of an 1859-caliber superstorm on geosynchronous Earth-orbiting satellites: Transponder resources", *Space Weather,* 5, doi: 10.1029/2006SW000262.

Olsen, R.C., C.E. McIlwain, and E.C. Whipple Jr. (1981), Observations of differential charging effects on ATS 6, *Journal of Geophysical Research,* 86(A8), 6809, doi: 10.1029/JA086iA08p06809.

Olson, P. and R. Deguen (2012), Eccentricity of the geomagnetic dipole cuased by lopsided inner core growth, *Nature Geoscience Letters,* doi: 10.1038/NGEO1506.

Payan, D., R. Reulet, and B. Diraseen (2005), Charging of Coaxial Lines with Floating Core at Geosynchronous Altitudes, 9th Spacecraft Charging Technology Conference, JAXA-SP-05-001E, Tsukuba, Japan, April 4-8.

Pavlidis, D. (1999), HBT vs. PHEMT vs. MESFET: What's best and why', *Compound Semiconductors,* 5(5), pp. 56-59. doi: 10.1117.12.373015.

Prasanna Swaminathan, A.R. Frederickson, J.R. Dennison, A. Sim, J. Brunson and E. Crapo (2003), Comparison of Classical and Charge Storage Methods for Determining Conductivity of Thin Film Insulators, *Proceedings of the 8th Spacecraft Charging Technology Conference,* NASA Marshall Space Flight Center, Huntsville, Alabama.

Qiu, J. X., Levush, B., Pasour, J., Katz, A., Armstrong, C. M., Whaley, D.R., Tucek, J., Kreischer, K., and D. Gallagher (2009), Vacuum tube amplifiers, *IEEE Microwave Magazine,* Vol. 10, No. 7, pp. 38-51. doi: 10.1109/MMM.2009.934517.

Rauschenbach, H.S. (1980), Solar Cell Array Design Handbook: The Principles and Technology of Photovoltaic Energy Conversion, *Litton Educational Publishing,* New York, NY.

Rapisarda, M., Colzi, E., Angeletti, P., and Aloisio, M. (2010), 4.1: Navigation traveling wave tube amplifiers-trade-off aspects, *IEEE Vacuum Electronics Conference (IVEC),* IEEE, pp. 47-48. doi: 10.1109/IVELEC.2010.5503609.

Raab, F.H., Asbeck, P., Cripps, S., Kenington, P.B., Popovic, Z.B., Pothecary, N., Sevic, J.F., and N.O. Sokal, (2003), RF and microwave power amplifier and transmitter technologies. Part I, *High Frequency Electronics,* Vol. 2, N. 3, pp. 22-36. doi: 10.1109/22.989965.

Reedy R.C. (2002), Recent Solar Energetic Particles: Updates and Trends, *Lunar and Planetary Institute Science Conference Abstracts,* Vol. 33.

Reeves, G.D., McAdams, K.L., Friedel, R.H.W. (2003), Acceleration and loss of relativistic electrons during geomagnetic storms, *Geophysical Research Letters,* 30(10), 1529, doi: 10.1029/2002GL016513.

Reeves, G. D., S. K. Morley, R. H. W. Friedel, M. G. Henderson, T. E. Cayton, G. Cunningham, J. B. Blake, R. A. Christensen, and D. Thomsen (2011),

On the relationship between relativistic electron flux and solar wind velocity: Paulikas and Blake revisited, J. Geophys. Res., 116, A02213, doi: 10.1029/2010JA015735.

Reference Data for Radio Engineers (1956), International Telephone and Telegraph Corporation, Stratford Press Incorporated, NY, NY, 4th Ed., 606-611.

Riley, P. (2012), On the probability of occurrence of extreme space weather events, *Space Weather,* Vol. 10, No. 2, pp.1–12, doi: 10.1029/2011SW000734.

Robbins, N. R., Christensen, J. A., & Hallsten, U. R. (2005), Performance and reliability advances in TWTA high power amplifiers for communications satellites. In *Military Communications Conference, 2005. MILCOM 2005,* Atlantic City, NJ, 17-20 October 2005, 1887-1890 doi: 10.1109/MILCOM.2005.1605948.

Robbins, N., Dibb, D., Menninger, W., Zhai, X., Lewis, D. (2012), Space Qualified, 75-Watt V-band Helix TWTA, International Vacuum Electronics Conference, 24-26 April 2012, doi: 10.1109/IVEC.2012.6262190.

Robinson, P. A. Jr (1989), Spacecraft Environmental Anomalies Handbook, GL-TR-89-0222, Final Report, Air Force Geophysics Laboratory, Hanscom AFB, MA.

Rodgers D. J., K. A. Hunter and G. L. Wrenn (2004), The FLUMIC electron environment model. Proceedings of the 8th Spacecraft Charging Technology Conference, Huntsville, AL, October 20-24.

Rodgers, D. J. (2004), DICTAT Software: Users' Manual v3.0, European Space Agency.

Rong, W., Zengliang, G., Xinghui, Z., and Z. Zuoxu (2003), 5-20 MeV proton irradiation effects on GaAs/Ge solar cells for space use, *Solar Energy Materials & Solar Cells,* 77, 351-357, doi: 10.1016/S0927-0248(02)00354-9.

Royal Observatory of Belgium. SIDC - Solar Influences Data Analysis Center. *SIDC - Solar Influences Data Analysis Center.* 28 Aug. 2003. Web. 25 June 2012. <http://sidc.oma.be/sunspot-data/>.

Rudie, N.J. et al., 1981, Design Support Guide for Radiation Hardening of Space Electronic Systems, IRT Corp, IRT 6409-001

Russell, C.T. and McPherron, R.L. (1973) 'Semiannual variation of geomagnetic activity', *J. Geophys. Res.,* Vol. 78, No. 1, pp.92–108, doi: 10.1029/JA078i001p00092.

Russell, C.T., Wang, Y.L., and J. Raeder (2003), Possible dipole tilt dependence of dayside magnetopause reconnection, *Geophys. Res. Lett., 30*(18), 1937, doi:10.1029/2003GL017725.

Sahu, K., (2008), EEE-INST-002: Instructions for EEE Parts Selection, Screening, Qualification, and Derating, NASA/TP-2003-212242, *NASA.*

Schwabe, H., & Schwabe, H. (1844), Sonnen—Beobachtungen im Jahre 1843. *Astronomische Nachrichten, 21*(15), 234-235.

Schulz, M., and Lanzerotti, L. J. (1974), Particle diffusion in the radiation belts, Springer-Verlag, N.Y.

Schwank, J. R., M. R. Shaneyfelt, and P. E. Dodd (2008), Radiation hardness assurance testing of microelectronic devices and integrated circuits: Radiation environments, physical mechanisms, and foundations for hardness assurance, Sandia Natl. Lab. Doc. SAND-2008-6851P, Albuquerque, New Mexico.

Sechi, F., and M. Bujatti (2009), Solid-State Microwave High-Power Amplifiers, Artech House, Norwood, Mass.

Seltzer, S.M. (1980), SHIELDOSE, A Computer Code for Space-Shielding Radiation Dose Calculations, *National Bureau of Standards,* NBS-IR 74457.

Seltzer, S.M. (1994), Updated calculations for routine space-shielding radiation dose estimates: SHIELDOSE-2, *NIST Publication,* NISTIR 5477.

Sessler, G. M. and West, J.E. (1975), Electrets formed by low-energy electron injection, *Journal of Electrostatics*, 1(2), 111-123.

Sessler, G. M (Ed.) (1979), Electrets, *Topics in Applied Physics*, 33, doi: 10.1007/3-540-17335-8.

Shea, M. A., and D. F. Smart (1998), Space weather: The effects on operations in space, Adv. Space Res., 22(1), 29–38, doi: 10.1016/S0273-1177(97)01097-1.

Sinclair, D. and J. Dyer (2013), Radiation Effects on COTS Parts in SmallSats, *27th AIAA/USU Conference on Small Satellites.*

Singer, S.F. (1958), Trapped albedo theory of the radiation belt, *Physical Review Letters,* 1(5), p. 181.

Singer, H.J., Matheson, L., Grubb, R., Newman, A., and S.D. Bouwer (1996) Monitoring Space Weather with the GOES Magnetometers, *SPIE Conference Proceedings,* 2812, p. 299-308, doi:10.1117/12.254077.

Sorensen, J., Rodgers, D. J. , Ryden, K. A., Latham, P. M., Wrenn, G. L., Levy, and G. Panabiere (1999), "ESA's Tools for Internal Charging", *IEEE Radiation and Its Effects on Components and Systems*, 27-33, doi: 10.1109/RADECS.1999.858540.

Srour, J. R., and McGarrity, J. M. (1988), Radiation effects on microelectronics in space. *Proceedings of the IEEE, 76*(11), 1443-1469, doi: 10.1109/5.90114.

Stassinopoulous, E.G. and J.P. Raymond (1988), The space radiation environment for electronics, *Proceedings of the IEEE,* 76(11), 1423-1442, doi: 10.1109/5.90113.

Strauss, R. (1993), Orbital Performance of Communication Satellite Microwave Power Amplifiers (MPAs), *International Journal of Satellite Communications,* Vol. 11, pp. 279-285. doi: 10.1002/sat.4600110506.

Strauss, R. (1994), Reliability of SSPA's and TWTA's, *IEEE Transactions on Electron Devices* 41(4), 625-626, doi: 10.1109/16.278524.

Sumita, T., Imaizumi, M., Matsuda, S., Ohshima, T., Ohi, A., and H., Itoh (2003), Proton radiation analysis of multi-junction space solar cells, *Nuclear Instruments and Methods in Physics Research,* 206, 448-451, doi: 10.1016/S0168-583X(03)00791-2.

Sze, S.M. (2001), Semiconductor Devices Physics and Technology, New York, John Wiley & Sons, Ltd.

Su, Z., Ziao, F., Zheng, H., and S. Wang (2011), Radiation belt electron dynamics driven by adiabatic transport, radial diffusion and wave-particle interactions, *Journal of Geophysical Research,* 116, doi:10.1029/2010JA016228.

Tada, H.Y. and Carter, J.R. (1977), The Solar Cell Radiation Handbook, *TRW Publ. 21945-6001-RU-00,* Jet Propulsion Laboratory Contract 953362.

Taherbaneh, M., Ghafooifard, H., Rezaie, A.H., Rahimi, K. (2011), Evaluation end-of-life power generation of a satellite solar array, *Energy Conversion and Management,* 52, 2518-2525, doi: 10.1016/j.enconman.2010.12.024.

Tauke, R.V., Faraday, B.J., and R.L. Statler (1967), Annealing of Proton Radiation Damage in Silicon Solar Cells, *Physics Letters*, 24A, 3, doi: 10.1016/0375-9601(67)90731-1.

Taylor, G.W., and R.J. Bayruns, (1985), A comparison of Si MOSFET and GaAs MESFET enhancement/depletion logic performance, *IEEE*

Transactions on Electron Devices, 32(9), pp. 1633-1641. doi: 10.1109/T-ED.1985.22173.

Thomsen, M. F. (2004), Why Kp is such a good measure of magnetospheric convection, Space Weather, 2, S11004, doi: 10.1029/ 2004SW000089.

Thomsen, M.F., Denton, M.H., Lavraud, B., and M. Bodeau (2007), Statistics of plasma fluxes at geosynchronous orbit over more than a full solar cycle, *Space Weather*, 5, doi: 10.1029/2006SW000257.

Thomsen, M. F., M. G. Henderson, and V. K. Jordanova (2013), Statistical properties of the surface-charging environment at geosynchronous orbit, Space Weather, 11, 237–244, doi: 10.1002/swe.20049.

Thorne, R.M. (2010), Radiation belt dynamics: The importance of wave-particle interaction, *Geophysical Research Letters,* 37, doi: 10.1029/2010GL044990.

Tretkoff, E. (2010), Space weather and satellite engineering: An interview with Michael Bodeau, Space Weather, 8, SO3003, doi: 10.1029/2010SW000584.

Tsurutani, B., W. D. Gonzalez, A. L. C. Gonzalez, F. Tang, J. K. Arballo, and M. Okada (1995), Interplanetary origin of geomagnetic activity in the declining phase of the solar cycle, J. Geophys. Res., 100, 21717, doi: 10.1029/95JA01476.

Vampola, A. L. (1987), Thick Dielectric Charging on High Altitude Spacecraft, *Journal of Electrostatics,* 20, 21-30, doi: 10:1016/0304-3886(87)90083-0.

Vaquero, J.M. (2007), Historical sunspot observations: a review, *Advances in Space Research,* Vol. 40, No. 7, pp.929–941, doi: 10.1016/j.asr.2007.01.087.

Vette, J.I. (1991), The AE-8 trapped electron model environment, *NASA STI/Recon Technical Report N*, 92, 24228.

Violet, M.D. and A.R. Frederickson (1993), Spacecraft anomalies on the CRRES satellite correlated with the environment and insulator samples, *IEEE Transactions on Nuclear Science,* 40(6), 1512-1520.

Walker, D.H. and R.L. Statler (1988), A satellite experiment to study the effects of space radiation on solar cell power generation, *Solar Cells*, 23, 243-268, doi: 10.1016/0379-6787(88)90104-4.

Walters, R.J., Messenger, S.R., Cotal, H.L., Summers, G.P., and E.A. Burke (1996), Electron and Proton Irradiation-Induced Degradation of Epitaxial InP solar cells, *Solid-State Electronics*, 39(6), 797-805, doi: 10.1016/0038-1101(95)00342-8.

Walters, R.J., Cotal, H.L., Messenger, S.R., Burke, E.A., Wojtczuk S.J., Serreze, H.B., Sharps, P.R., Timmons, M.L., Iles, P., Yeh, Y.C.M. (1998), Radiation response of InP/Si and InGaP/GaAs space solar cells, *Solar Energy Materials and Solar Cells,* 50, 305-313, doi: 10.1016/S0927-0248(97)00161-X.

Weekley, J. M., and B. J. Mangus (2005), TWTA versus SSPA: A Comparison of on-orbit reliability data, IEEE Trans. Electron Devices, 52(5), 650–652, doi: 10.1109/TED.2005.845864.

Weinberg, I. (1991), Radiation damage in InP solar cells, *Solar Cells,* 31, 331-348, doi: 10.1016/0379-6787(91)90104-W.

Wertz, J.R. and W.J. Larson (1999), Space Mission Analysis and Design.

Wertz, J.R., D.F. Everett, and J.J. Puschell (2011), Space Mission Engineering: The New SMAD, *Microcosm Press,* Hawthorne, CA.

Whipple, E.C. (1976), Observation of photoelectrons and secondary electrons reflected from a potential barrier in the vicinity of ATS 6, *Journal of Geophysical Research,* 81(4), 715, doi: 10.1029/JA081i004p00715.

Wilkinson, D.C., Daugtridge, S.C., Stone, J.L., Sauer, H.H., and P. Darling (1991), TDRS-1 Single Event Upsets and the Effect of the Space Environment, *IEEE Transactions on Nuclear Science*, 38(6), doi: 10.1109/23.124166.

Wilkinson, D. C. (1994), National Oceanic and Atmospheric Administration's spacecraft anomaly data base and examples of solar activity affecting spacecraft, J. Spacecr. Rockets, 31, 160–165, doi: 10.2514/3.26417.

Wilkinson, D.C., Shea, M.A., Smart, D.F. (2000), A Case History of Solar and Galactic Space Weather Effects on the Geosynchronous Communications Satellite TDRS-1, *Adv. Space Res.*, 26(1), 27-30, doi: 10.1016/S0273-1177(99)01022-4.

Wrenn, G. L. (1995), Conclusive evidence for internal dielectric charging anomalies on geosynchronous communications spacecraft, J. Spacecr. Rockets, 32(3), 514–520, doi: 10.2514/3.26645.

Wrenn, G. L., and R. J. K. Smith (1996), Probability factors governing ESD effects in geosynchronous orbit, IEEE Trans. Nucl. Sci., 42(6), 2783–2789, doi: 10.1109/23.556867.

Wrenn, G. L., D. J. Rodgers, and K. A. Ryden (2002), A solar cycle of spacecraft anomalies due to internal charging, Ann. Geophys., 20(7), 953–956, doi: 10.5194/angeo-20-953-2002.

Xapsos, M.A., Summers, G.P., Barth, J.L., Stassinopoulous, E.G., and E.A. Burke (1999), Probability model for worst case solar proton event fluences, *IEEE Transactions on Nuclear Science,* 46, 1481-1485, doi: 10.1109/23.819111.

Xapsos, M.A., Stauffer, C., Gee, G.B., Barth, J.L., Stassinopoulous, E.G., and R.E. McGuire (2004), Model for Solar Proton Risk Assessment, *IEEE Transactions on Nuclear Science,* 51, 3394 – 3398, doi: 10.1109/TNS.2004.839159.

Yamaguchi, M., Taylor, S.J., Yang, M., Matsuda, S., Kawasaki, O., Hisamatsu, T. (1996), High-energy and high-fluence proton irradiation effects in silicon solar cells, *J. Applied Physics*, 80, 4916-4920, doi: 10.1063/1.363534.

Yamaguchi, M. (2001), Radiation-resistant solar cells for space use, Sol. Energy Mater. Sol. Cells, 31–53, doi: 10.1016/S0927-0248(00)00344-5.

Zhao, H., and Q.-G. Zhong (2012), Seasonal and diurnal variation of geomagnetic activity: Russell-McPherron effect during different IMF polarity and/or extreme solar wind conditions, *Journal of Geophysical Research,* 117, A11222, doi:10.1029/2012JA017845.